H24/3566

DEPARTMENT'S RATIFICATION

This is to ascertain that the Department has no objection to the candidate's options regarding access to the Library thesis copy. If so, please sign below and return the completed form to the Monash Graduate School Research Services, Building 3D, Clayton Campus.

Supervisor's signature: ..▮   Date:29./1./3

Please print name)....................................... D.K. MACFARLANE

A STUDY OF PLASTIC CRYSTALS AS NOVEL SOLID STATE ELECTROLYTES

Junhua HUANG

B. Sc.

M. Sc.

A thesis submitted for the fulfillment of the requirements

for the degree of Doctor of Philosophy

School of Chemistry

Monash University

January 2003

TABLE OF CONTENTS

Abstract

This thesis presents the study of the plastic crystals N, N-methyl, methyl pyrrolidinium bis(trifluoromethanesulfonyl)amide (P11TFSA) and N, N-methyl, ethyl pyrrolidinium bis(trifluoromethanesulfonyl)amide (P12TFSA). The purpose of this study is to explore the potential of these plastic crystals to be used as novel solid state electrolyte materials for lithium batteries. The defects, ionic motions, conduction mechanisms and mechanical properties are investigated. Additionally, lithium bis(trifluoromethanesulfonyl)amide (LiTFSA) salt is doped into these plastic crystals in order to achieve high Li^+ ion conductivity.

Both P11TFSA and P12TFSA exhibit plastic crystals behavior. Three solid-solid phase transitions are observed for both materials using differential scanning calorimetry (DSC). Some of the phase transitions accompany crystal lattice expansion and the formation of vacancies. Positron annihilation lifetime spectroscopy (PALS) studies indicate that both the number and size of the vacancies increase substantially with temperature.

Dielectric studies indicate that the rotational motion could occur in phase IV. Nuclear magnetic resonance (NMR) linewidth measurements reveal that, in P11TFSA and P12TFSA, both the cations and anions participate in rotational motion in the solid state. NMR linewidth measurements also suggest that 1% of the cations and anions in P12TFSA begin to diffuse in phase III. The correlation times and activation energies for the rotational motions and diffusional motions are determined by NMR relaxation measurements. 1% of the cations and anions are observed to diffuse at about 10 °C below the melting point for P11TFSA. The diffusional motions of the cations and anions are closely correlated for both P11TFSA and P12TFSA.

The ionic diffusion and the conductivity are revealed to be associated with volumetric expansion and vacancy formation. A Schottky vacancy mechanism probably accounts for the diffusional motion for P11TFSA and P12TFSA in their plastic crystalline phases. The plasticity studies on P11TFSA and P12TFSA reveal better mechanical flexibility than

normal crystals. The good plasticity is attributed to the larger numbers of vacancies and defects present in the materials.

The phase behavior exhibited by LiTFSA doped P12TFSA or P11TFSA mixtures is typical of that of a binary system. The eutectic composition is at about 33 mol% LiTFSA for both systems. The eutectic temperature is observed at 57 ($\pm$ 2) $^{\circ}$C for LiTFSA-P11TFSA or 33 ($\pm$ 3) $^{\circ}$C for LiTFSA-P12TFSA. At room temperature, the highest conductivities observed are 2.5×10^{-4} Scm^{-1} for 33 mol% LiTFSA-P12TFSA and 2.4×10^{-5} Scm^{-1} for 33 mol% LiTFSA-P11TFSA.

Important solid solution phases are observed in both binary systems. The solubility limits are between 4.8 mol% and 9.3 mol% LiTFSA in P12TFSA and between 2.7 mol% and 5 mol% LiTFSA in P11TFSA. The plastic crystal behaviors remain in these solid solution phases, according to the observations of the solid-solid phase transitions and the ionic rotational motions. All the doped Li^{+} ions display liquid like mobility through the solid P11(or P12)TFSA network. As a result, doping with 4.8 mol% LiTFSA into P12TFSA leads to an increase in the conductivity by four orders of magnitude. The diffusional motion of the parent ions is also improved, which could be attributed to the defect-like lattice disruption generated by substituting the P11^{+} (or P12^{+}) cations by the small Li^{+} ions which are unmatched in size.

These materials exhibit relatively constant conductivities over a one week period, suggesting their potential as practical solid state electrolyte materials.

Declaration

This thesis contains no material which has been accepted for the award of any other degree or diploma in any university or other institute and, to the best of my knowledge and belief, contains no material previously published or written by another person, except where due reference is made in the text of the thesis.

Junhua Huang

Acknowledgements

First of all, I would like to thank my supervisors professor Doug MacFarlane and professor Maria Forsyth for their intelligent guidance, enthusiastic encouragement and support throughout this project.

Thanks are also due to:

Iko Burgar, Kate Nairn, Tim Bestow, Hayley Every and Shan Wong for teaching me NMR and letting me use the NMR machines;

Pavla Meakin and Steven Gruenhut for designing the conductivity cell and programming;

Jiazeng Sun and Jake Golding for their help in the synthesis;

Anita Hill and Pavla Meakin for measuring PALS;

Jim Efthimiadis, Mark Greaves and John Ward for obtaining SEM photos;

Craig Forsyth for obtaining the single crystal XRD results and Rod Mackie for measuring the powder XRD;

George Simon for providing the MTA instrument;

Kate Nairn for her patient help and inspiriting discussions during the whole project and in the preparation of this thesis;

And everyone in the Electrolyte Group for the generous help and valuable discussions.

I also appreciate the supports from Monash Graduate Scholarship and Overseas Postgraduate Research Scholarship.

Last but not least, a huge thank you to my family for their love, understanding and support through all these years.

Chapter 1 Introduction

1.1 Lithium Batteries

New electrical devices, such as portable computers and tools, telecommunication equipment and electric vehicles, have been developing rapidly. These electrical appliances require highly reliable rechargeable batteries. A successful battery system should satisfy the "three E" criteria: Energy: high gravimetric and volumetric energy density; Economy: inexpensive materials and manufacturing processes, long service life; Environment: harmless to environment, safe [1].

Widely commercialized rechargeable battery systems include: lead-acid, nickel-cadmium, nickel-metal hydride and zinc-magnesium batteries. The energy density can reach 60-70 $Whkg^{-1}$. The advantages of these batteries are low cost and the ability of overcharge protection. However, cadmium and lead are toxic. Furthermore, the cell voltage and the energy density are limited [1].

The research on lithium batteries has led to a great leap in the rechargeable battery area. Due to the low atomic mass and the very negative electrode potential of lithium, lithium batteries can achieve high cell voltage (ca. 4 V) [1, 2] and high energy density (theoretical value of ca. 2000 $Whkg^{-1}$) [1]. The energy density of the commercial $LiC_6/LiCoO_2$ lithium ion cell is presently 110 $Whkg^{-1}$ [2].

A lithium (or lithium ion) battery is composed of a positive electrode (such as Li_xCoO_2, Li_xNiO_2, $Li_xMn_2O_4$ or conducting polymer) [2, 3], a negative electrode (lithium metal, Li-graphite, Li-Al, Li-Sn, Li-Si and Li-Bi alloys) [2, 3] and the electrolyte. During discharge, the electroactive lithium ions move from the negative electrode to the positive electrode through the electrolyte while the electrons pass through the external circuit with a release of energy. The opposite reaction occurs during charge [2]. The performance of a battery depends not only the properties of the electrodes, but also the electrolyte.
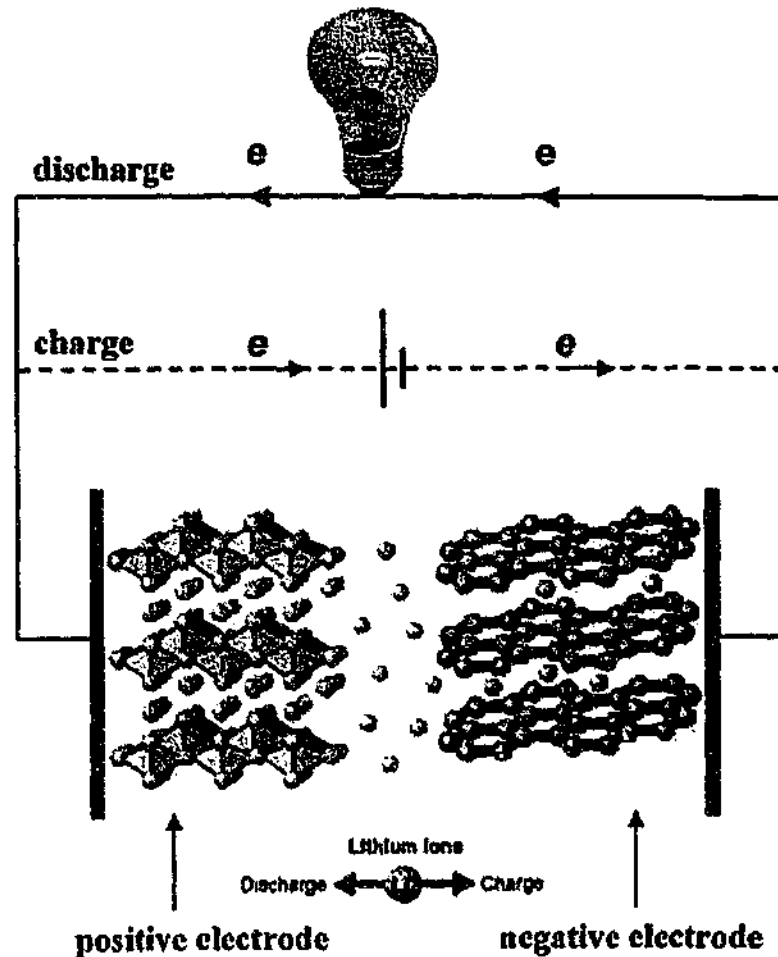
Figure 1.1 The scheme of the battery and the circuit during the discharging or charging.

1.2 Electrolytes

The criteria for ideal electrolyte materials are [2]:

(1) The materials are highly ionically conductive. A poorly conductive electrolyte causes Ohmic loss and power loss in the electrolyte. Ionic conductivity is related to charge carrier concentration n_i, mobility μ_i and charge q_i of mobile species by [4]

$$\sigma = \sum n_i q_i \mu_i$$

Equation 1.1

(2) The charge carrier is lithium ions. Otherwise, the concentration gradients of the ions other than lithium form at the electrolyte-electrode interfaces, which interfere with the

transport of lithium ions, cause phase transitions at these regions and reduce the battery efficiency. The transference number of Li^+ ions t_{Li^+} is given as [5]

$$t_{Li}{}^+ = \frac{\mu_{Li}{}^+}{\sum q_i \mu_i}$$

Equation 1.2

where μ_{Li^+} is the mobility of Li^+ ions. t_{Li^+} is expected to be 1 for an ideal electrolyte.

(3) The electronic conductivity is low to prevent self-discharge.

(4) The materials have mechanical flexibility. Dimensional changes in the electrodes occur during the charge and discharge cycling. The stress produced may result in loss of contact between the electrodes and the electrolyte or fracture of the materials if the electrolyte is not flexible.

(5) The materials should be chemically stable to both electrodes.

(6) The materials are lightweight, safe, environmentally friendly and low cost.

Although it is difficult to satisfy all the requirements, great efforts have been made to improve the performance of the electrolyte materials. Both liquid and solid state electrolyte materials have been studied.

1.3 Liquid Electrolytes

Since lithium reacts with active protons to give H_2, a liquid electrolyte should be aprotic. These liquid electrolytes are generally organic solutions of lithium salts. The organic solvents normally used are carbonate or ether, such as ethylene carbonate (EC), propylene carbonate (PC), dimethyl carbonate (DMC), diethyl carbonate (DEC), 1,2-dimethoxyethane (DME), etc, as well as their mixtures [3, 6]. The lithium salts generally used and studied are: $LiPF_6$, $LiAsF_6$, $LiBF_4$, $LiClO_4$, $LiCF_3SO_3$, $Li(CF_3SO_2)_2N$, etc [7]. The advantages of these organic liquid electrolytes are (1) they have high conductivity, at the level of 10^{-3}

Scm^{-1} at 30 °C [6, 7]; (2) they can remain in good contact with the electrodes [8]. However, the organic solvents are potentially unstable to lithium metal. Different organic solvents exhibit different degrees of kinetic instability to the electrodes [2]. Moreover, since all the ions migrate easily in the liquid electrolytes, electrochemical side reactions may occur. Other problems are: leakage of the liquid electrolytes, freezing at lower temperatures and ignition at higher temperatures [9].

1.4   Solid State Electrolytes

Compared to liquid electrolytes, solid state electrolytes have several advantages: no leakage, less extent of side reaction, longer life time due to little self-discharge, versatile construction and miniaturization of the all-solid-state batteries. A solid state electrolyte may be a fast ionic conductor, where one ionic species migrates through the rigid network with higher mobility than the rest of the species [9]. Types of solid state electrolytes include crystals, glasses and polymers. They are briefly reviewed here.

1.4.1 Crystalline Electrolytes

In crystalline solids, ions or molecules migrate through the rigid matrix by isolated hopping between adjacent sites. The sites could be vacancies or interstitials. Crystalline solids can be classified into two types [10]. One is the "molten sublattice type", where the number of available sites is more than the number of ions. One example is α-AgI where Ag$^+$ ions migrate between empty interstitial sites among the rigid anion sublattice. The other is "point defect type", where the sites are Frenkel or Schottky defects. The defects are thermally generated. The number of vacancies or interstitials can also be increased by doping with heterovalent ions [4, 11].

The ionic mobility μ_i and ionic diffusion coefficient D are related by the Nernst-Einstein relationship :

$\mu = qD/RT$

Equation 1.3

In a crystalline solid, the ionic diffusion coefficient is given as [12]

$$D = \gamma(1-c)a^2 v f \exp\left(-\frac{\Delta G}{RT}\right)$$

Equation 1.4

where c is the degree of occupation of N equivalent lattice site per unit volume, "a" is the jump distance, v is the lattice vibration frequency, γ is a geometrical factor, f is correlation factor and ΔG is the free energy. According to Equation 1.1, Equation 1.3 and Equation 1.4, the conductivity is given as [12]

$$\sigma = \frac{Nq^2\gamma c(1-c)a^2 v f \exp(-\frac{\Delta G}{RT})}{RT}$$

Equation 1.5

where the charge carrier concentration is $n_i = Nc$. According to Equation 1.5, the conductivity in crystalline electrolytes obeys an Arrhenius behavior.

Strategies to achieve high conductivity involve increasing the number of charge carriers or decreasing the energy barrier to diffusion. A larger number of charge carriers can be achieved either by choosing crystal structures which have intrinsically a large amount of available sites for the charge carriers to jump into or by doping with alien ions to extrinsically increase the number of defects. The energy barrier for ionic diffusion is related to the size of the ions and the size of the migration tunnel. The ions can migrate through a size-matched migration tunnel with a lower energy barrier. In addition, as most of the materials studied are polycrystalline, the effects of grain boundaries on the conductivity should be considered, because the migration through the tunnel terminates at the grain boundaries. Some examples of fast Li^+ ion conductors are:

1. Li_3N. Li^+ ions migrate anisotropically through two-dimensional layers in a single crystal. Isotropic conductivity is obtained in polycrystalline materials [9].

2. Lithium-substituted Na superionic conductors (NASICONs) $LiM_2(PO_4)_3$ (M(IV)=Ge, Ti, Hf, Zr). NASICON-type materials have three-dimensional tunnels for the migration of Li^+ ions. Highest conductivity is obtained for M=Ti, as the size of the tunnel is the most suitable for the migration of Li^+ ions. Partly substituting Ti^{4+} with Al^{3+} or doping with a lithium salt such as Li_2O and Li_3PO_4 helps to improve total conductivity by reducing grain boundary resistances [9].

3. Perovskite type ABO_3. Perovskite type materials are in the form of $A^+B^{5+}O_3$, $A^{2+}B^{4+}O_3$ and $A^{3+}B^{3+}O_3$. For some perovskites in the forms of $A_{2/3}BO_3$ and $A_{1/3}BO_3$, such as $Ln_{2/3}TiO_3$ (Ln=La, Nd, Sm, Gd, Ho, Yb) and $Ln_{1/3}NbO_3$ (Ln=La, Ce, Pr, Nd), cations are deficient at A-sites, so some of the A-sites are vacant. If monovalent cations such as Li^+ are introduced, the monovalent cations may migrate between the vacant A-sites with high mobility [13, 14]. The radius of the larger ion on A-site is a crucial factor in the lattice size which determines the Li^+ ionic mobility and thus bulk conductivity. A bulk conductivity of about 10^{-3} Scm^{-1} was obtained for $La_{2/3-x}Li_{3x}TiO_3$ when x=0.1 [13].

4. Li superionic conductors (LISICONs). One example is based on γ_{II}-Li_3PO_4 type materials. γ_{II}-Li_3PO_4 has closely packed orthorhombic structure. When a penta-valent P^{5+} ion is partially substituted by a Si^{4+} ion and a Li^+ ion, this Li^+ ion can not occupy the cation sits. As a result, the doped Li^+ ions migrate through interstitial sites between the MO_4 tetrahedrons [9] [4]. The γ_{II}-Li_3PO_4 type materials are $Li_{3+x}A_{1-x}B_xO_4$ (A=P, V, As; B=Si, Ge, Ti). The lattice size and conductivity increase with the radii of the A^{5+} and B^{4+} ions. Another example of LISICONs is based on γ-Li_2ZnGeO_4 where a Zn^{2+} ion is partially substituted by two Li^+ ions. The formula is given as $Li_{2+2x}Zn_{1-x}GeO_4$. The excess of Li^+ ions occupy interstitial sites, which link to form conduction pathways [4].

1.4.2 Glassy Electrolytes

Glassy electrolytes contain three basic components: (1) a network former, such as SiO_2, P_2O_5, B_2O_3, GeS_2, P_2S_5, B_2S_3, etc. These covalent oxides or sulphides form macromolecular chains by linking through oxygen or sulphur bridges. (2) a network modifier based on oxides or sulphides, such as Ag_2O, Li_2O, Ag_2S, Li_2S, etc. These oxides

or sulphides break the oxygen or sulphur bridges of the macromolecules and lead to shorter network chains. (3) ionic salts, such as halide salts or sulphates, which work as doped salts to increase conductivity [15]. The conductivity is sensitive to the proportions of the three constituents. A conductivity of 1.5×10^{-3} Scm^{-1} was obtained for the $0.63Li_2S-0.36SiS_2-0.01Li_3PO_4$ at room temperature [9].

A two-step displacement mechanism has been proposed for conduction. In step one, a cation leaves its normal site and moves into a neighboring "interstitial site". A defect analogous to a Frenkel defect is formed. In step two, the defect migrates in the electric field. It has been found that the conductivity obeys an Arrhenius behavior below T_g and a Vogel-Tammann-Fulcher (VTF) law above T_g. The VTF equation is written as [15]:

$$\sigma = \sigma_0 \exp\left[-\frac{B}{R(T-T_0)}\right]$$

Equation 1.6

where B is a constant and T_0 is related to T_g. The VTF equation is normally used for those amorphous systems where free volume is involved [16]. In free volume theory, any diffusing species is encaged by surrounding atoms in a cell with the volume of V. V is temperature dependent. Above a critical temperature T_0 (the volume of the cell is V_0 at T_0), "the excess volume of V_f ($V_f=V-V_0$) is considered as free, that is redistribution around its mean value $<V_f>$ without any enthalpic contribution" [15]. It has been suggested that the migration of the defects requires a local deformation of the macromolecular chain which involves a local free volume above T_g [15].

The strategies used to improve room temperature conductivity of glassy electrolytes are: (1) diminishing the coupling of mobile cations to the network; (2) depressing the glass transition temperature [16].

Both crystalline electrolytes and glassy electrolytes can achieve high Li$^+$ ionic conductivity. The disadvantage is that these two categories of electrolytes are brittle and can not accommodate the volume change occurring during the charge and discharge cycling, which could lead to loss of contact at the electrode/electrolyte interface.

- 7 -

1.4.3 Polymer Electrolytes

Polymer electrolytes, due to their good mechanical flexibility, overcome the electrode/electrolyte interfacial contacting problem. In addition, the good mechanical flexibility allows polymer electrolytes to be shaped as a thin film with large surface area, which has low resistance and may thus provide high power density [8]. Processing and manufacture with polymer electrolytes are straightforward. Miniaturized batteries are also possible [17].

Solid Polymer Electrolytes

Solid polymer electrolytes (SPEs) are solid solutions of alkali metal salts (such as lithium salts) in polymers [18]. The most studied polymer is polyethylene oxide (PEO), which provides electrolytes with relatively good conductivity and chemical stability [17].

It has been suggested that the transport of the cations is associated with the segmental motion of the polymer chain in the amorphous phase. In the case of lithium salts, Li^+ ions are complexed to the polymer chain through the Li-O interactions. Below the glass transition temperature T_g, the conductivity is very small. Near T_g, the segmental motion of the polymer chain starts to become active. The segmental motion of the polymer chain assists the transport of Li^+ ions between the complexation sites. In a way similar to the deformation of the macromolecules in glasses, the local segmental motion of the polymer chain involves free volume [19]. The temperature dependence of conductivity for the polymers also obeys the VTF equation above T_g, as given in Equation 1.6.

One of the strategies to improve the conductivity is to increase the charge carrier number. The charge carrier number can be increased either by increasing the lithium salt concentration or by increasing the degree of dissociation of the salt. The effect of the lithium salt concentration on conductivity is complex. On one hand, the number of ions increases with the salt concentration. On the other hand, T_g increases with the concentration of the lithium salt, which indicates that the mobility of polymer chain decreases. The degree of salt dissociation also decreases with increasing salt concentration [18]. Therefore, the effect of lithium salt concentration on conductivity is the result of

these competitive factors. Dissociation of the salt involves breaking the cation-anion interaction of the salt and the dissolution of the ions in the polymer. A salt with low lattice energy and a host polymer with high dielectric constant favor the dissociation [17, 18].

Another strategy to improve the conductivity is to improve the mobility of the Li^+ ions. Since the transport of Li^+ ions is mediated by the segmental motion of the polymer in the amorphous phase above T_g, the conductivity can be increased either by increasing the amount of amorphous phase or by decreasing T_g [16, 19].

The methods used to decrease T_g are (1) using a low molecular weight plasticizer, such as propylene carbonate (PC) or ethylene carbonate (EC). The plasticizers insert between the polymer molecules, decrease the interaction between the polymer chains and thus improve chain mobility [18]; (2) copolymerization. Some of the copolymerization methods are combining dimethylsiloxane (DMS) units and short PEO chains to form linear copolymer or attaching PEO short chain to a polymer backbone to form comb-branched polymer [18].

The methods used to increase the amorphous state are: (1) using host polymers other than PEO, such as polypropylene oxide (PPO), methoxy linked PEO (PMEO), polyethylene glycols (PEGs), etc [17, 19]. (2) crosslinking, as a limited degree of crosslink decreases the crystallinity of the polymers. However, T_g increases with the crosslink density. Crosslinking also restricts the segmental motion of the host chain [18].

The disadvantage of SPEs is that the value of t_{Li^+} is low. For example, t_{Li^+} for $(PEO)_9LiCF_3SO_3$ and $(PEO)_8LiClO_4$ are 0.5 and 0.3 respectively [8].

Polyelectrolytes

In order to improve the t_{Li}^+, anion groups are covalently attached to the polymer repeat unit and the only charge carrier is Li^+ ions [20, 21]. These polymers are called polyelectrolytes (or single ion conductors) [18]. However, the conductivity is not satisfactory, as the cations and the anions can not be completely dissociated. The mechanical flexibility may also be reduced [20].

Gel SPEs

In the polymer-lithium salt-plasticizer system, when the amount of plasticizer is about 80 wt%, a gel electrolyte is formed [18]. Conductivity of 10^{-3} Scm^{-1} at room temperature can be achieved. However, the chemical stability to the electrodes is limited, as a large amount of organic solvent is introduced. Gel electrolytes are much more difficult to shape into thin films than SPEs [18].

In summary, high Li^+ ionic conductivity can be obtained in crystalline and glassy electrolytes which unfortunately are brittle. Polymer electrolytes have the mechanical flexibility to form good interfacial contacts with electrodes, but the conductivity is limited and the t_{Li^+} is low.

1.5 Plastic crystals

Plastic crystals have been of interest recently as potential solid state electrolyte materials due to their good mechanical flexibility and relatively high conductivity [22]. In this section, the basic thermodynamic and kinetic properties will be reviewed first. Conduction mechanism and mechanical properties will then be emphasized for the purpose of developing solid state electrolytes.

1.5.1 Characteristics of Plastic Crystals

Plastic crystals are compounds where the molecules or ions have rotational disorder while the centers of their masses occupy ordered sites in the crystalline lattice structure [23-25]. At low temperature, the compounds are "normal crystals", where molecules or ions have complete order, including both the rotational order and positional order. As temperature increases, the molecules or ions go through one or more phase transitions into plastic crystal phase(s) where the molecules rotate from one orientation to another while their centers of mass remain the same to maintain the lattice structure. Therefore the plastic crystalline phases have rotational disorder while keeping the positional order [24, 26]. The plastic crystal phase is also called "rotator phase" due to the characteristic rotational motion. When the temperature reaches the melting point, the molecules or ions obtain the

- 10 -

energy to break the ordered lattice arrangement and start to possess translational mobility. In the molten state, the molecules or ions have both rotational and positional disorder [24, 26]. The plastic crystal phase is a mesophase between the "normal" crystalline phase and liquid phase [27].

The rotational motions of molecules have been known since the 1930's [28, 29]. In 1961, the first review about plastic crystals was presented by Timmermans [23]. In that review, the characteristics of plastic crystals were summarized. Structurally, the molecules or ions of plastic crystals are usually "globular" shaped, either symmetrical around their centres or giving a sphere by rotation. A decrease in the globularity results in reducing the rotational motion to a less extent or a disappearance of the plastic crystalline phase. Thermodynamically, most of the plastic crystals have one or more endothermic solid-solid phase transition(s)*. The energy absorbed helps the molecules to break their interlocking with the neighboring molecules and initiates the rotational motion. The fusion entropy is smaller than non-plastic crystals, normally less than 20 $JK^{-1}mol^{-1}$. A low fusion entropy less than 20 $JK^{-1}mol^{-1}$ has been known as "Timmermans' criterion for plastic crystal". A low fusion entropy reflects the higher entropy possessed in the plastic crystal phase. Besides these, plastic crystals show some abnormalities compared to "normal" crystals as summarized below:

(1) The melting point of a plastic crystal is relatively higher than that of the non-plastic crystalline isomer [23]. The higher melting point allows the molecules or ions to possess rotational freedom before the crystal lattice collapses at the melting point [24, 32]. For example, tetra-methylmethane exhibits a plastic crystal phase below the melting point at

---

* There are exceptions where some materials enter their plastic crystal phases without discernible endothermal phase transition. One example is benzene. The orientations of benzene are energetically equivalent. The onset of the molecular rotation does not involve a change in the energy [30, 31]. Another example is inert gases such as neon, argon, krypton and xenon. These atoms are perfectly spherical and the rotation is energetically indiscernible. They pass through their plastic crystal phase and acquire plasticity without phase transitions as warmed to their melting points [24].

–16 °C whilst n-pentane shows no plastic crystal phase below the melting point at –141°C [23].

(2) The symmetry of the crystalline lattice structure becomes higher from low to higher-temperature plastic crystal phase(s). For a number of plastic crystals, a cubic lattice structure has been observed in their highest-temperature plastic crystal phase [23]. The symmetry of the lattice structure is related to the symmetry of the rotational motion [33]. From low to high temperature, rotations normally develop from internal rotation with low energy barrier to external rotation and finally to isotropic rotation with higher energy barrier. An isotropic rotation usually accompanies a cubic lattice structure. For example, $(CH_3)_3NC_2H_5I$ goes through three disordered phases below its melting point. As temperature increases, the lattice structure transforms from an orthorhombic structure in phase III to tetragonal in phase II and turns into NaCl-type cubic in phase I [#]. In phase III, the CH_3 groups rotate about their C_3 axis and the $(CH_3)_3N$ group rotates about the C_3' axis passing through the N atom. In phase II, the cation does quasi-isotropic rotation. In phase I, the cation does isotropic rotation [34].

(3) Physically, the materials in their plastic crystal phases are soft and waxy. For example, perfluorocyclohexane flows slowly under its own weight [24]. Plastic crystals show higher plasticity and are easier to deform compared to their corresponding non-plastic crystal phases.

(4) Plastic crystals have relatively high saturated vapour pressures. Some plastic crystals could even sublime under ordinary pressure. For example, small pieces of camphor could disappear at room temperature [24].

(5) Plastic crystals exhibit less volume expansion upon melting than normal crystals [35]. The onset of rotational motion requires the molecules to move apart to reduce the steric

---

[#] In this chapter and hereafter, the highest temperature solid phase is denoted as phase I. Subsequent lower temperature phase(s) are denoted as phase II, III, etc.

- 12 -

hindrance and to gain enough space for rotation [36]. Therefore, a solid-solid phase transition normally accompanies the volume expansion. As a result, less volume expansion is required when the plastic crystal phase enters the molten state.

(6) "Diffusion may be the sine qua non of plastic state" [24]. Translational motion has been detected in a large number of the molecular plastic crystals [37-39], inorganic ionic plastic crystals such as MNO_2 (M=K, Rb, Cs, Tl, Ti, NH_4) [40-51] and organic ammonium salts [34, 52-59].

(7) Plastic crystal phases exhibit "abnormalities" in their heat capacities and dielectric constants. For some materials, the heat capacity decreases when temperature increases in plastic crystal phase. The tendency is opposite in "normal" phases. The dielectric constant in plastic crystal phase is almost continuous with that in liquid phase, but shows discontinuity with lower temperature non-plastic crystal phase [23].

1.5.2 Rotation and Orientation

The rotational motions include internal rotation and external rotation [60]. Internal rotation indicates the rotation of a segment of a molecule (such as CH_3 or OH groups) or the inversion of a ring molecule. Internal rotation results in conformational disorder. Crystals possessing only conformational disorder are called candis crystals [27]. As to external rotation, the whole molecule is involved in the rotation. Plastic crystals could have both external rotation and internal rotation. Internal rotation normally appears at lower temperature than external molecular rotation [60-62].

The rotational motion discussed above may indicate different rotational mechanisms, rotational disorder and orientational disorder [33]. Rotational disorder indicates continuous rotation about one or more molecular axes. Orientational disorder indicates discrete rotation about one or more molecular axes, thus the atoms in a molecule may relocate among a limited number of positions related by rotational symmetry operators. One example is $N(CH_3)_4IO_4$, as shown in Figure 1.2. The $N(CH_3)_4^+$ cation is ordered while three O atoms in the IO_4^- anion relocate among 8 orientations about one of the I-O bonds. Through the x-ray diffraction refinement, 24 positions rather than a continuous distribution

- 13 -

orbit have been found for the three O atoms [63]. The orientations could be energetically equivalent as is the case for the IO_4^- in $N(CH_3)_4IO_4$ [63] or energetically inequivalent as is the case for NO_2^- anion in KNO_2 where the 180° flipping of NO_2^- takes place in an asymmetric double minimum potential well in low temperature phase [64]. The orientational disorder may be the precursor to a full rotational motion [33]. However, the boundary between rotational disorder and orientational disorder has not been well defined so far. It is possible that an orientational disorder could be detected as rotational disorder by an experimental technique with a slower time scale than the reorientation rate. The fast reorientation rate could be in the range of $10^9 - 10^{11}$ s^{-1}. A slower reorientation could occur by $10^{-3} - 10^7$ s^{-1} [31].
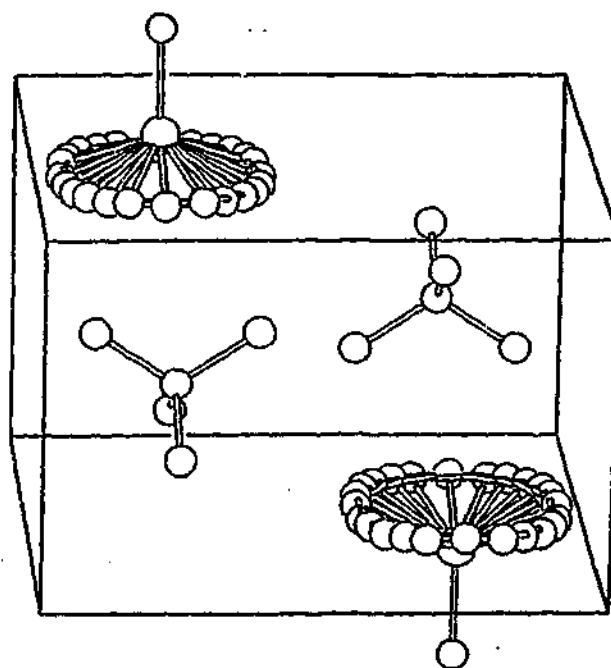
Figure 1.2 Packing of the ordered $N(CH_3)_4^+$ cations and the 4-fold disordered IO_4^- anions in the unit cell of $N(CH_3)_4IO_4$ [63].

Several models of reorientational motions have been summarized by Brot et al. [31]. Among them, free rotation is a primitive model [28]. In a free rotation model, the rotational hindrance is ignored and the correlation time of rotation is of the order of $(I/kT)^{1/2}$ (I is the moment of inertia of the rotating molecule) [31]. However, free rotation is not likely in nature by considering the fact that the intermolecular distance is smaller

- 14 -

than the molecular diameter [65]. Molecular motion is always correlated with the motion of neighboring molecules.

Site model is one of the most possible models [31]. In the site model, the potential wells are fixed according to the symmetry of both the molecules and crystalline lattice. The molecules are supposed to be trapped in potential wells and perform angular oscillations or librations within the well most of the time. The time taken to jump into other wells is much shorter than the dwell time. The jumping time correlation functions are exponentials or sums of exponentials if all the potential barriers have the same height. Otherwise, the correlation time will be a discrete or continuous distribution [31]. Group theoretical methods can be used to calcul. · he evolution of populations in each well and the time correlation function [31]. The libration rate within each well can be detected by far IR absorption and neutron inelastic scattering [31]. The jumping rate can be obtained by neutron quasi-elastic scattering, NMR, etc [66].

Other rotational models include collision-interrupted rotation model and classical rotational diffusion model, both of which are unlikely or unproved [31].

1.5.3 Entropy of Phase Transition

Kabo et al. have studied the factors contributing to the entropy changes at phase transitions (ΔS_{tr}) by investigating the thermodynamic properties of a number of cage hydrocarbons, cyclohexane, cyclopentane and their derivatives. For cyclohexane, cyclopentane and their derivatives, only internal rotation (segmental rotation or ring inversion) is involved in the low temperature phase [60-62]. For the cage hydrocarbons, only the external reorientations are possible [67]. Kabo et al. have proposed that [61, 67, 68]:

$$\Delta S_{tr} = \Delta_V S + \Delta_{vib} S + \Delta_h S + \Delta_{int} S + \Delta_{inv} S + \Delta_{orien} S$$

Equation 1.7

where $\Delta_V S$ is the contribution from volume change corresponding to the changes in crystal structure and molecular packing; $\Delta_{vib} S$ is related to the changes in molecular vibration frequency; $\Delta_h S$ is the contribution from the changes in defects; $\Delta_{int} S$ is the contribution

- 15 -

from internal rotation due to the rotation of small groups such as $-CH_3$, $-OH$, etc; $\Delta_{inv}S$ is the contribution from the ring inversion; $\Delta_{orient}S$ is the contribution from external molecular rotation and $\Delta_{translation}S$ is the contribution from molecular diffusion. According to Equation 1.7, the transformation of lattice structure, molecular vibration, molecular rotation and molecular diffusion all contribute to the entropy changes at solid-solid phase transitions.

$\Delta_{int}S$ can be calculated by molecular mechanism methods. The potential energy changes due to the rotation of the small groups such as OH and CH_3 in cyclohexane and cyclopentane have been reported [60, 62]. The contribution from inversion $\Delta_{inv}S$ can also be calculated by proposing a pseudorotational moment of inertia I. The energy level can be calculated by solving a Schrodinger equation. This method has been compared to the experimental entropies of cyclopentane and its derivatives [69].

$\Delta_{orient}S$ is calculated based on the Guthrie-McCullough model [70]

$$\Delta_{orient}S = R\ln(N_1/N_2)$$

Equation 1.8

where N_1 and N_2 are the number of orientations statistically taken up in the higher and lower temperature phases, respectively. The number of possible orientations depends on the symmetric elements of both the lattice structure and the molecules. The energetically favored orientations are those where the symmetric elements of molecules are aligned with the symmetric elements of the lattice and those where the steric interactions with neighboring molecules are low enough [70]. Webb et al. have constructed a model to calculate the total number of orientations for those systems where neighboring orientational motions are correlated and orientations in some directions are forbidden [71].

Equation 1.8 has been widely accepted, modified and developed [44]. This equation has further been modified by Kabo et al. [62, 67]. In their theory, molecules in the plastic crystal state undergo rotation from one orientation to another having local minima of energy. The lowest-energy orientation is the one the molecules take in their rigid state, defined as "basic orientation". The energy of the basic orientation is H_{bas}. All the other

orientations have higher energy than H_{bas}. The mean energy of these higher energy states is H_{plast}. The entropy change and heat capacity change due to the external orientation can be described as [62, 67, 68]

$$\Delta S_{orient} = -R \sum_{i=1}^{n} x_i \ln x_i$$

Equation 1.9

$$\Delta Cp_{orient} = \frac{1}{RT^2} \sum_{i=1}^{n} x_i \sum_{j>i}^{n} x_j (\Delta H_i)^2$$

Equation 1.10

where x_i and x_j are the mole fractions of molecules taking up the orientations i and j, respectively; n is the number of orientations. $\Delta H_i = H_{plast,i} - H_{basic}$. n_{orient} and ΔH_{orient} can in turn be obtained by measuring ΔS_{orient} and ΔCp [67, 72].

Kabo's results show that $\Delta_{orient}S > \Delta_{int}S$ [68]. The potential barriers for internal rotations are lower than those for external rotations, which explains why internal rotations normally occur at lower temperature than overall rotation.

1.5.4 Prediction of Plastic Crystals

Timmermans' criterion for plastic crystals that the fusion entropy is less than 20 $JK^{-1}mol^{-1}$ has been widely accepted and used to predict plastic crystals. However, there are a number of plastic crystals which do not obey this criterion. Timmermans' criterion has been doubted [65]. From a thermodynamic point of view, a low fusion entropy only indicates a small energy difference between the liquid and solid state. It is not an absolute measure of degree of disorder in solid state. Materials which are highly ordered in their liquid state could also have fusion entropy less than 20 $JK^{-1}mol^{-1}$ [65]. Therefore, a more reliable criterion for plastic crystals has been of interest.

Postel and Riess' Theory

Postel and Riess have suggested that the existence of a plastic crystalline phase depends on intermolecular steric hindrance [65]. Only when the molecular interlocking is sufficiently weak, is the motion of neighboring molecules not impeded. The degree of molecular interlocking is expressed by parameter R [65],

$$R = \frac{d_m}{D_M} = \frac{\text{minimum distance between molecular centers}}{\text{maximum diameter of the molecule}}$$

Equation 1.11

By comparing the values of R for a number of materials, Postel and Riess have found that plastic crystals have R>0.81 while those with R less than 0.81 are not plastic crystals [65]. Therefore, R can be used as the criterion of plastic crystal.

Pople and Karasz's Theory

Pople and Karasz have provided a theory for quantitative predictions of orientational transitions in the solid or liquid states [36]. The theory is based on the Lennard-Jones and Devonshire's theory of melting where only the positional order is considered [73]. Taking orientational order into account, Pople and Karasz's theory introduces a parameter υ [36]:

$$\nu = \frac{z'W'}{zW}$$

Equation 1.12

where z'W' is the energy required for one molecule to turn from one orientation to another and zW is the energy required to move from one position to another. The energy barrier to reorientation is related to the steric hindrance of rotation. ν is the ratio of the energy barriers for rotational disorder and positional disorder. When $\nu<0.325$, the system loses the orientational order at lower temperature than it loses the positional order and is predicted to be a plastic crystal. In Pople and Karasz's theory, the entropy change and volume change at melting for plastic crystals are smaller than non-plastic crystals. These differences arise

- 18 -

from the increased volume and increased entropy in the solid phase due to the rotational motion, which are in agreement with most experimental data [36]. This model is well fitted by the experimental results of inert gas. It can also be used to predict normal crystals (with the orientational order and positional order [26]) and liquid crystals (where the positional order is lost at lower temperature than the orientational order [26]) [36]. The limitation of Pople and Karasz's theory is that only two orientations are considered. As a result, molecules with more than two orientations do not fit into this model [70].

Amzel and Becka's Theory

Based on Pople and Karasz's theory, Amzel and Becka have introduced another parameter N, the number of molecular orientations [35]. N can be defined by considering the symmetric elements of the molecules and the crystal lattice structure [70]. From Amzel and Becka's theory, quantitative prediction of the existence and thermodynamic properties of plastic crystals can be made. Some conclusions from the theory are summarized as follows [35]:

1. The critical value v, which is the criterion to judge the existence of plastic crystal, is N dependent. The critical value v increases with the value of N. For example, the value of v is 0.325 when N=2. The value shifts to 0.50 when N=60. Therefore, the key factors determining the existence and the thermodynamic properties of plastic crystals are the number of orientations N and the energy barriers to reorientation and translation.

2. All of the solid-solid phase transitions are of first order when N>2. The solid-solid phase transitions are of second order when N=2 and $v<0.17$.

3. The solid-solid phase transition and melting temperatures as well as their corresponding entropy changes and relative volume changes can be predicted by considering N and v. Briefly, both the relative volume changes and entropy changes at solid-solid phase transition and melting for plastic crystals are smaller than the changes at melting for non-plastic crystals. For plastic crystals, the relative volume changes at solid-solid transitions could be larger than that at melting. The relative volume change and entropy change at solid-solid phase transitions increase with v whilst both the changes at melting decrease

with v. The volume changes at both solid-solid phase transitions and melting are N independent except for large N. The entropy changes nevertheless exhibit obvious N dependence. The entropy change of solid-solid phase transition, ΔS_{tr}, increases with N. The entropy change of melting, ΔS_m, becomes smaller when N increases. The dependence of ΔS_m on N is less than that of ΔS_{tr}.

4. The equilibrium pressures for solid-solid transition and melting can also be predicted. Under the premise that v is pressure independent, it is possible that some materials are not plastic crystals above their critical pressures, but could become plastic crystals when the pressure is lower than the critical values. This has recently been confirmed by the pressure experiments on chloroadamantane [74].

Amzel and Becka's theory was correlated better with experimental results than Pople and Karasz's theory [70]. The theory can also be used for predicting the thermodynamic properties of normal crystals and liquid crystals. The disadvantage of Amzel and Becka's theory is that even though the models can be tested by experimental results indirectly, it is impossible to obtain v directly from experiments or by theoretical calculation.

Smith's Theory

In order to overcome the disadvantage of Amzel and Becka's theory, Smith has made a modification of Equation 1.12 by introducing a parameter Γ analogous to v [38],

$$\Gamma = \frac{E_R}{E_D}$$

Equation 1.13

where E_R and E_D are the energy barriers for general molecular orientation and self-diffusion, respectively. E_R and E_D can be obtained as the activation energies of orientation and diffusion from experiments [39]. According to the values of E_R and E_D obtained from NMR experiments for a number of materials, Smith has made the suggestion that the material is a plastic crystal if $\Gamma < 1.04$ [26, 38]. However, the effect of the number of

orientations seems to be ignored in Equation 1.13. Smith's criterion has not been widely adopted so far.

Other Theories

Efforts in the prediction of plastic crystal behavior include theoretical calculations. For example, Præstgaard and Perram et al. have recently provided a model which can calculate the second-order phase transition temperatures for elliptical molecules by knowing the lattice constant [75].

1.5.5 Glassy Crystal

Glassy Crystal State

Plastic crystals could show complicated metastable phases. One of the most interesting metastable phases of plastic crystals is the glassy crystal state [76-78]. "Glassy crystal" has been first reported by Seki et al. [79]. They have observed a glass transition in cooling cyclohexanol from plastic crystal phase I. Glass transitions have also been found in a number of plastic crystals. They are cyclohexane [80], cyanocyclohexane[75], cyclohexanol [83] [84] [85] [86] [87-92], cycloheptane [93], cycloheptanol [94], 1,3,5-cycloheptatriene [95], cyclooctane [96], cyclooctanol [97, 98] pentachloro-toluene [66], 1-chloro-1-methylcyclopentane[61], 2,3-dimethylbutane [99], adamantane [100], cyanoadamantane [101, 102] [102-104] [105] [106] [107] [74, 108-121], chloroadamantane [74, 122-125], fluoroadamantane [126], ortho-carborane [127], meta-carborane [128], p-chloronitrobenzene [129], fullerenes [130] [131], solid nitrogen [132], ethanol [133-137], methanol [138], propanol [139, 140], etc.

When a plastic crystal phase is cooled at a relatively fast rate, the disordered orientation could be trapped while the original crystalline lattice structure remains. When warmed up, it exhibits glass transition(s) when the trapped static reorientational motion starts to become dynamic. This frozen state is called "glassy crystal" or "orientational glass" [141, 142]. Glassy crystals show static orientational disorder and positional order. This is in contrast to ordinary glasses, known as "structural glass" [142], which show both orientational

disorder and positional disorder. Angell has suggested that glassy crystals be termed as "orientationally disordered (OD) glasses" and structural glasses as "center-of-mass disordered (CMD) glasses" [25]. The degrees of positional freedom and orientational freedom for plastic crystal, glassy crystal and structural crystal are demonstrated in Figure 1.3.

Energetically, glassy crystals can be described as the molecules trapped in different potential wells corresponding to different static orientations which are separated by high potential barriers. For a highly symmetric molecule such as benzene, since the different orientations are energetically equivalent, the static orientationally disordered state can not be energetically distinguished from the fully orientationally ordered state [137]. Nevertheless, for less symmetric molecules, the statically disordered orientations the molecules take are energetically inequivalent [143]. Extra configurational entropy is required to maintain the static orientational disorder as compared to fully orientationally ordered crystal states. The glassy crystals are therefore generally metastable phases [144].

The glass transition which involves the transformation between the static orientational disorder and dynamic reorientational motion is called the "orientational glass transition" [141, 145]. This is in contrast to the positional disorder involved glass transition called "structural glass transition" [141, 145]. The orientational glass transition is similar in shape to a structural glass transition. In some cases, the orientational glass transition from the glassy state to plastic crystal phase occurs at the same temperature as the structural glass transition when a "normal" glass state transforms into supercooled liquid, as observed in ethanol [133]. The similarity has been explained by the correspondence of the reorientational motions in the plastic crystal state and supercooled liquid of ethanol [137]. Cyanoadamantane also shows resemblance in the orientational relaxation in its plastic crystal state and supercooled liquid state as demonstrated by a stochastic model [146].

Strong and Fragile Theory

Angell has established a theory which can be applied to all materials exhibiting a glass transition [16, 25, 148, 149]. Plastic crystals, due to the existence of orientational glass transitions, are unified with liquids, polymers and glasses under this theory. [25, 137, 150].
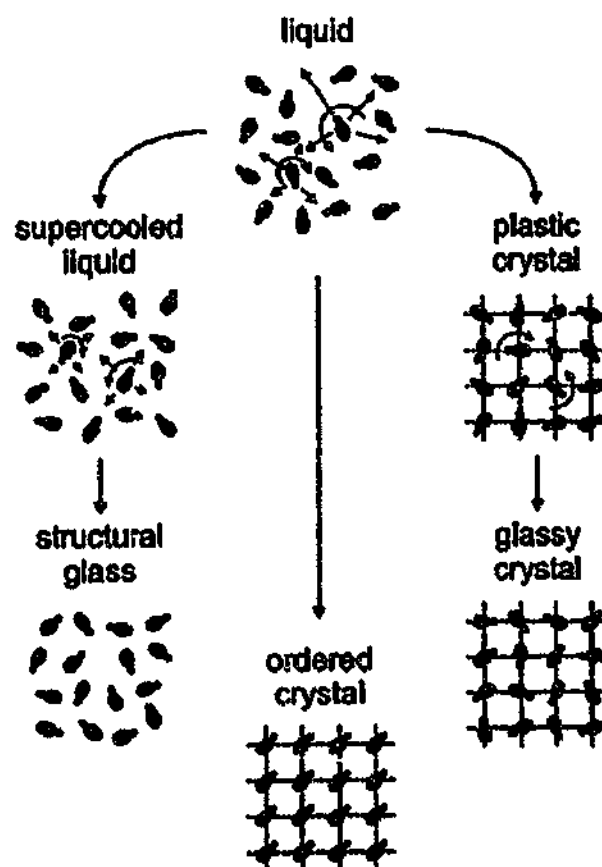
Figure 1.3 Schematic representation of liquid, supercooled liquid, plastic crystal, orientationally ordered crystal, structure glass and glassy crystal [147].

Briefly, Angell's theory can be described as follows. Materials exhibiting a glass transition can be classified as fragile or strong [25, 148]. "Strong" means a higher resistance to structural change while "fragile" means more flexibility in the structural change. Fragility is represented by a parameter m which can be obtained by plotting the correlation time τ as a function of T_g/T [25, 137]:

$$m = \frac{d\log(\tau)}{d(T_g/T)}\bigg|_{T=T_g}$$

Equation 1.14

The smaller the m value, the stronger the material. The thermodynamic and relaxational characteristics of strong plastic crystals are consistent with those of strong liquids and glasses in: smaller heat capacity jump at T_g; smaller temperature dependence of

- 23 -

configurational entropy; a temperature dependence closer to Arrhenius behavior; an exponential relaxation and the relaxation more close to Debye behavior [148]. The "strong" or "fragile" behavior has been explained by topology of potential energy hypersurfaces. The correlation time is presented as [25]:

$$\tau = \tau_o \exp\left(\frac{a\Delta\mu T_o}{K(T-T_o)}\right)$$

Equation 1.15

where τ is the relaxation time; T_o is the configurational ground state temperature; K indicates the number of minima on the potential energy surface; $\Delta\mu$ indicates the barrier heights separating the minima and "a" is a constant. Whether a system is strong or fragile depends on the density of accessible states. The more densely these potential minima are packed (corresponding to a larger value of K) or the more shallow the potential minima is (a smaller value of $\Delta\mu$), the more fragile the system is [137].

Plastic crystals are normally ranked as intermediate or strong [147, 151]. Strong plastic crystals are found for those materials with planar molecular structure, such as thiophene, $TINO_2$ and pentachloronitrobenzene [25, 147]. Plastic crystals cyanoadamantane and ortho-carborane have been found to be strong whilst isocyanocyclohexane, cyclohexanol and cyclooctanol have been found between fragile and strong [150]. The fragility depends on the number of orientations. Cyanoadamantane has six orientations in the plastic crystal state. Isocyanocyclohexane and cyclohexanol have more possible orientations and therefore are more fragile [150].

The fragilities of the plastic crystal state and supercooled liquid of ethanol have also been compared. Although the motional mechanisms in these two states are similar, the plastic crystal state was found stronger than the supercooled liquid. It can be explained by fewer accessible configurations in the plastic crystal phase than in the supercooled liquid [137].

1.5.6 Defects in Plastic Crystals

Defects in Crystals

An ideal crystal contains undistributed periodic structural elements of crystal lattice. However, real crystals contain imperfections, known as defects, in their lattice arrangements. Defects can be point defects, such as vacancies and interstitials, or extended defects, such as vacancy clusters, dislocations and grain boundaries [152]. In a well annealed crystal, which is regarded as the equilibrium state, the only defects are thermally generated vacancies and interstitials. Vacancies are more energetically favorable than interstitials in pure materials, as interstitials require higher formation energy than vacancies. For a less well annealed sample, more defects appear than in its equilibrium state. Crystal growth, thermal shock and mechanical handling may generate line imperfections such as dislocations and grain boundaries, known as pipes, within the solids. These defects can diminish gradually during the annealing process when the crystal returns to its equilibrium state [153].

At the equilibrium state, the number of vacancies present is a function of temperature, given by [153]

$$N_v = N_o \exp\left(-\frac{E_a}{RT}\right)$$

Equation 1.16

where N_v and N_o are the numbers of vacancies and molecules, respectively. E_a is the activation energy for vacancy formation.

Vacancies are always in motion due to the thermal vibration of the crystal lattice [152]. Vacancy diffusion is composed of vacancy formation and migration. According to random walk theory, the vacancy diffusion coefficient D_v is given as [152]:

$$D_v = \gamma a^2 \nu f \exp\left(\frac{S_v + S_m}{R}\right)\exp\left(-\frac{(E_v + E_m)}{RT}\right)$$

Equation 1.17

where γ is a geometrical factor, "a" is the jump distance; ν is attempt jump frequency; f is the correlation factor; S_v and S_m are the vacancy formation and migration entropies, respectively; E_v and E_m are the enthalpics of vacancy formation and migration, respectively. The relationship between E_v and S_v, for both van der Waals bonded crystals and metals, has been found to be [154]

$$\frac{E_v}{T_m} - AS_v = B$$

Equation 1.18

where T_m is the melting point; A and B are constants.

Equation 1.17 can be written as

$$D_v = D_0 \exp\left(-\frac{E_d}{RT}\right)$$

Equation 1.19

where E_d is the activation energy of vacancy diffusion and $E_d = E_v + E_m$; D_0 contains the contribution from the vacancy diffusion entropy S_d, where $S_d = S_v + S_m$. Equation 1.19 indicates that vacancy diffusion obeys Arrhenius behavior. Ed and S_d have also been found to be related by [154]

$$\frac{E_d}{T_m} - A'S_d = B'$$

Equation 1.20

where A' and B' are constants. For metals, E_d is estimated to be $134T_m$ Jmol^{-1} [38]. Sherwood et al. have suggested that the vacancy formation energy E_v is close to the lattice

- 26 -

energy Ls for most solids [153, 155]. The lattice vacancy migration energy E_m is of the same order of magnitude as E_v, and E_d is therefore roughly 2Ls [156, 157].

In crystals, the diffusion of charge carriers is closely associated with the diffusion of the defects. As the probability for a jump of a charge carrier is proportional to the probability of finding a vacancy in the adjacent sites, the diffusion coefficient of a charge carrier D_c is related to the diffusion coefficient of a vacancy D_v by [152]:

$$D_c = D_v N_v$$

Equation 1.21

where N_v is the mole fraction of vacancies. The full form of D_c is expressed as Equation 1.4.

Vacancy diffusion is also related to pressure by [153]

$$\left[\frac{\partial(\ln D)}{\partial P} \right]_T = -\frac{V^+}{RT}$$

Equation 1.22

where P is the pressure and V^+ is the activation volume.

Defects also appear in plastic crystals [153]. Compared to normal crystals, defects in plastic crystals exhibit some abnormal characteristics due to the molecular rotational behavior and the different thermodynamic properties.

Interstitials in Plastic Crystals

On one hand, the formation enthalpy of interstitials E_v is less in plastic crystals than in normal crystals. The reason is that, in order to undergo the molecular rotation, plastic crystals are generally less densely packed compared to normal crystals. Therefore, less energy is required to have a molecule in an interstitial site. On the other hand, since the interstitial molecules could hinder the rotational motion of neighboring molecules, a

- 27 -

negative contribution to the interstitial formation entropy is expected for plastic crystals [154].

Vacancies in Plastic Crystals

Vacancies are an important characteristic of the plastic crystalline state. Smith has suggested that a larger numbers of vacancies appear in plastic crystals [24, 38]. It has also been found that the vacancy concentration at the melting point is in the range of 0.1 mol%-2 mol% for a number of plastic crystals studied [37] whilst it is about 0.01 mol% for normal crystals [158].

Some plastic crystals exhibit vacancy formation energy E_v close to their lattice energy Ls, regardless of the values of their fusion energy ΔS_f. Examples are adamantane (ΔS_f=2.5R) [159], hexamethyl ethane (ΔS_f=2.4R) [154], and d1 camphene (ΔS_f=1.2R) [160], as studied by positron annihilation lifetime spectroscopy (PALS), specific heat measurement and density measurement respectively [37]. Lattice energy Ls for these plastic crystals does not show much difference from that of non-plastic crystals. The vacancy formation energy E_v for these plastic crystals therefore cannot be distinguished from that of normal crystals [37].

For some plastic crystals, E_v has been determined not equal to Ls and the ratio of E_v/Ls increases with fusion entropy ΔS_f [154]. This discrepancy in some cases was explained by the measurement technique error. For example, in PALS measurements, the o-Ps could be trapped in a loosely bound lattice rather than in the lattice vacancies [157]. The smaller E_v could also result from a special vacancy formation mechanism. One example is succinonitrile. The results from NMR, creep and radiotracer experiments all give the same result that $E_d = 0.8Ls$ [37]. According to $E_d = E_v + E_m$, $E_v < 0.8Ls$. The small E_v is due to the fact that succinonitrile is present in two isomeric forms, 20% in the trans and 80% in the gauche configuration. These two isomeric forms are of different sizes. As a result, the 20% trans isomer is regarded as an impurity and causes extrinsic vacancies. The vacancy formation energy E_v is therefore negligible [161].

The discrepancy between E_v and Ls has also been explained thermodynamically by Baughman et al.. The relationship between E_v and Ls for van der Waals bonded solids is given as [154]

$$E_v = L_s - \sum_{n \geq 3}(n-2)E_n + E_0 + 2RT$$

Equation 1.23

where $\sum(n-2)E_n$ is the contribution from n-body potential energy to cohesive energy; E_0 is zero-point energy of the lattice. The many body contribution, expressed as the term 2 in Equation 1.23, accounts for a smaller E_v than Ls [154].

Vacancy formation entropy S_v of plastic crystals is higher than that of normal crystals and metals. The vacancy formation leads to less hindered rotational motion for the molecules neighboring the vacancy and thus increases the entropy. The molecular rotational contribution to vacancy formation entropy is $3ZR \log\left(\frac{Z}{Z-1}\right)^{1/2}$, where Z and Z-1 are the coordination numbers of the molecules in perfect lattice and neighboring a vacancy, respectively [154].

Vacancies in plastic crystals seem to be more mobile than in normal crystals. The vacancy diffusion coefficient at the melting point is in the range of 10^{-14}-10^{-12} m^2s^{-1} for the plastic crystals investigated, more than two orders of magnitude higher than non-plastic crystals. The high diffusion coefficient was thought to result from the relatively high vacancy formation entropy S_V. According to Equation 1.17 and Equation 1.19, D_0 contains the contribution from S_V. A higher vacancy formation entropy S_V thus contributes to a higher D_0 [158]. The more mobile vacancy could also be attributed to a lower vacancy diffusion enthalpy E_d. E_d was found to be in the range of 0.8-2.3Ls from NMR diffusion measurements or in the range of 1.4-2.4Ls according to radiotracer data for plastic crystals while E_d was found to be greater than 2.0Ls for normal crystals [155].

Vacancies in turn enhance the rotational motion in plastic crystals. Firstly, the rotational motion is less hindered when neighboring a vacancy. The hindering potential for rotation

is given as $\frac{V_2}{V_1} \propto \frac{Z-1}{Z}$, where V_1 and V_2 are the hindering potentials for rotation in a defect-free lattice and adjacent to a vacancy, respectively. The molecular coordination numbers are Z and $Z-1$, respectively, in these two cases. The hindering potential for rotation is reduced when a molecule is removed from a perfect lattice site to a site neighboring a vacancy. Secondly, the less hindered rotational motion of molecules leads to the increase in rotational entropy [154]. Molecular dynamics simulation demonstrates that both the molecular vibration amplitude and the rotational jump frequency are increased by neighboring vacancies. The ratio of rotational jump time to dwell time is increased as well [162].

1.5.7 Plastic Deformation

Plastic crystals show distinctive plasticity compared to normal crystals and thus are named "plastic" crystals. It has been found that the pressure needed to extrude a number of plastic crystals through a hole is about 2-15 times less than the pressure needed for the same materials in their non-plastic crystalline phases or for some other non-plastic crystals. Some plastic crystals, for example perfluorocyclohexane, are so easy to deform that they can flow under gravity [24].

The typical deformation behavior is shown in Figure 1.4. In the low stress range where the stress and strain are proportional, it is elastic deformation. Elastic deformation occurs by small displacement of atoms and stretching of inter-atomic bonds under stress. The material returns to the original shape when stress is unloaded. Beyond this range, the stress is not proportional to strain. This is plastic deformation. Plastic deformation occurs by breaking original bonds and reforming new bonds, which is permanent and unrecoverable. When the stress exceeds a particular value, failure occurs [163].

Plastic deformation of amorphous materials, such as liquids, glasses and polymers, occurs by viscous flow. Plastic deformation of crystals occurs by different deformation mechanisms, for example slip or creep, in different temperature and stress ranges. Both of these deformation mechanisms are associated with the formation and migration of lattice defects. It is generally believed that the plastic deformation in plastic crystals occurs in the

- 30 -

same way as in normal crystals [163]. However, the special molecular shape, crystal lattice structure, molecular rotational behavior and properties of the defects in plastic crystals account for the facile plastic deformation.
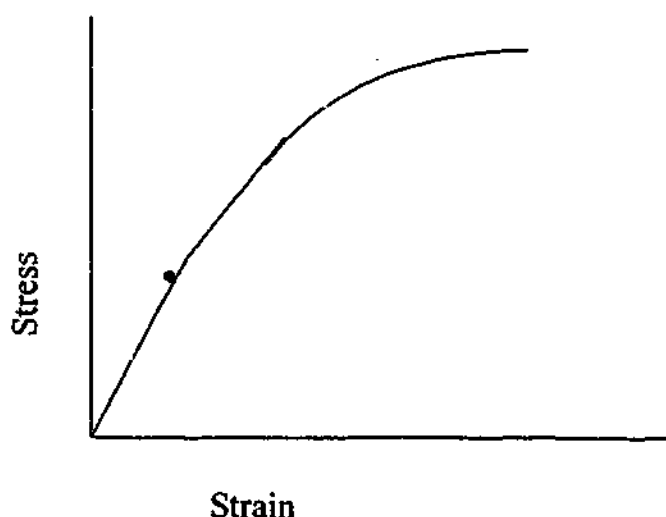
Strain

Figure 1.4. The scheme of a typical stress-strain behavior [163]. The dot indicates the proportional limit.

Plastic Deformation at High Temperature and Low Stress

At high temperature and low stress, plastic deformation occurs by creep [163]. Creep is the permanent deformation under a constant stress. The relationship between the strain rate $\dot{\varepsilon}$ and the applied stress σ is empirically given as [153, 163]

$$\dot{\varepsilon} = A\sigma^n \exp\left(-\frac{E_c}{RT}\right)$$

Equation 1.24

where n and A are constants; E_c is the activation energy of creep. At very high temperature and extremely low stress, the deformation is controlled by the migration of vacancies. Under this condition, n=1 and E_c is the activation energy of vacancy diffusion E_d. Under usual conditions, the creep occurs by dislocation climb. Dislocation climb is demonstrated in Figure 1.5, which involves the diffusion of vacancies through the lattice to accumulate at the dislocation. Therefore the rate of dislocation climb and thus the rate of creep are vacancy self-diffusion controlled. The activation energy of creep E_c is related to the

- 31 -

activation energy of vacancy self–diffusion E_d. n is estimated to be 4.5 and has been measured to be in the range of 4-6 for metals [153]. Since $E_c = E_d$ and according to Equation 1.19, Equation 1.24 can be expressed as [153, 163]

$$\dot{\varepsilon} = A'\sigma^{4.5}D$$

Equation 1.25

Sherwood et al. have studied the creep of a number of plastic crystals. They conclude that dislocation climb is the dominant mechanism for creep in plastic crystals [158]. As suggested in section 1.5.6, E_d of plastic crystals seems to be smaller than that of normal crystals, suggesting easier creep in plastic crystals. It has also been found that plastic crystals with lower fusion entropy exhibit smaller E_d. Therefore, the plastic crystals with a smaller fusion entropy could exhibit higher plasticity [153].
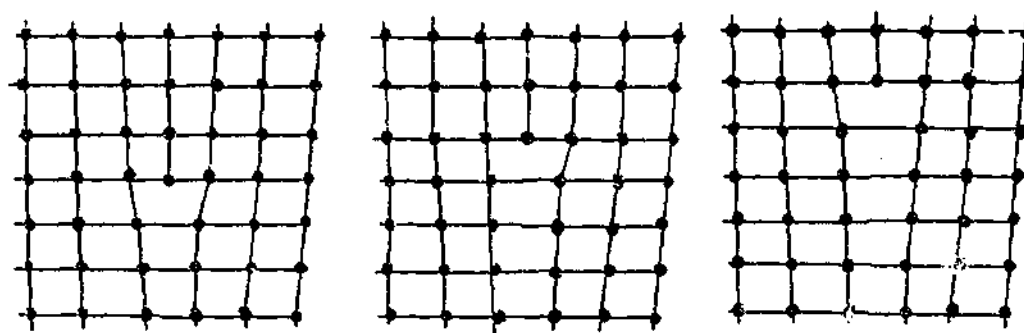
Figure 1.5 The scheme of dislocation climb via the atom-vacancy exchange by solid state diffusion.

Plastic Deformation at Low Temperature and High Stress

At low temperature and high stress, deformation occurs by dislocation slip, which is essentially the migration of dislocations along the specific direction under stress, as shown in Figure 1.6 [163]. It is believed that dislocation slip is the dominant mechanism for plastic crystals as well under this condition. Slip traces have been clearly observed and slip planes well defined in d-camphor and adamantane [164, 165].

- 32 -

Plastic crystals exhibit easier plastic deformation by slip than normal crystals. Small stresses would be adequate to yield slip for plastic crystals [165]. The ease of dislocation slip in plastic crystals can be attributed to a higher number of low energy slip systems compared to normal crystals. Dislocation line energies of plastic crystals (0.38 eV for cyclohexane, 0.6 eV for dl-camphene) are much smaller than those for normal organic crystals (25.7 eV for sulphur, 7.4 eV for hexamethylenetetramine) and even metals (4.6 eV for Ag, 8.1 eV for Fe) [153]. The ease of dislocation slip is also related to the fusion entropy. A lower fusion entropy corresponds to a smaller dislocation line energy. This is evidenced by comparing adamantane ($\Delta S_f = 2.5R$, 4.7 eV) with cyclohexane ($\Delta S_f = 1.0R$, 0.38 eV) and dl-camphene ($\Delta S_f = 1.2R$, 0.6 eV) [153]. It is thought that the low dislocation line energy is related to the symmetry of both the molecules and the lattice structure in plastic crystals. A high symmetry of the molecules and the crystal lattice structure would facilitate the dislocation slip. Molecular interactions and interference would impede the slip for less symmetrical molecules [165].
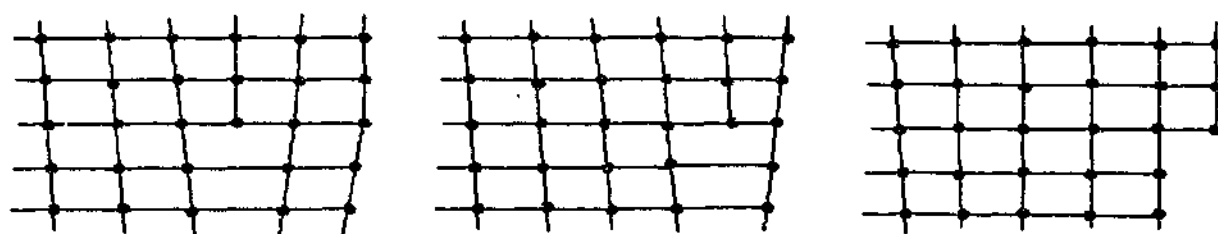
Figure 1.6 The scheme of the movement of edge dislocation.

1.5.8 Conduction Mechanism

Plastic crystals have been of interest as electrolyte materials for the last two decades. As mentioned in section 1.5.1, diffusion has been widely observed in plastic crystals. Plastic crystals also show relatively higher conductivity than normal crystals. For example, in the family of 1-alkyl-2-methyl-pyrrolinium TFSA (MP_xTFSA, x is the number of carbon on the alkyl chain) salts, MP_2TFSA exhibits most solid-solid phase transitions and smallest fusion entropy and is believed to be a plastic crystal. MP_2TFSA displays higher conductivity than all the other salts in the family which have higher fusion entropies and

fewer solid-solid phase transitions [166]. Another example is Li_2SO_4. Li_2SO_4 is a plastic crystal at elevated temperatures. The rotational motion of sulphate groups has been clearly demonstrated by neutron diffraction [167]. Li_2SO_4 has a conductivity of 1 Scm^{-1} at 600 °C. This is in contrast to the related non-plastic crystal Na_2SO_4, which exhibits a conductivity of 7×10^{-4} Scm^{-1} at 550 °C [168].

Angell et al. have suggested the term "plastic crystals fast ion conductor (PLICFICS)" for this new category of electrolyte materials in 1986 [22]. Molecular or ionic transport within plastic crystals is likely to occur by different mechanisms than in normal crystals. The main conduction mechanisms proposed are the "paddle wheel mechanism" and the "percolation mechanism".

In the paddle wheel mechanism, the mobility of some species of molecules or ions is facilitated by the strongly coupled rotational motion of other molecules or ions [12, 168-172]. As mentioned before, molecular motions are correlated with the motions of neighboring molecules because of the insufficient intermolecular distance. As a result, the reorientation of one molecule could contribute to the translation disorder of a neighboring molecule [173]. The rotation-translation correlation has been observed in neopentane by neutron diffraction and is demonstrated by molecular dynamics simulation [173, 174]. When a C-C bond of one molecule points to a neighboring molecule, the latter is pushed away. The latter moves closer when the C-C bond of the former points away from it.

In a percolation mechanism, the mobility of ions is enhanced by "free volume", either by the lattice expansion or by the vacancies created [12, 175-179]. The percolation mechanism works for both rotator phases and non-rotator phases. Since plastic crystals exhibit larger lattice expansion at solid-solid phase transitions and easier vacancy formation and diffusion, the ionic mobility is thus increased.

In the last twenty years, there have been controversies about these conduction mechanisms [168, 176, 178-180]. Lunden and Secco's groups have studied some Li_2SO_4 based salts. Jansen has given a review on the conduction mechanism in 1991, concentrating on inorganic salts [12]. More examples including organic salts will be reviewed here. The materials reviewed are not necessarily limited to Li^+ ion conductors.

Li₂SO4

Li_2SO_4 was once the center of the conduction mechanism controversy [168, 171, 176, 180, 181] [179] [178]. It has been one of the most thoroughly studied materials so far. It is generally accepted that Li_2SO_4 is a plastic crystal. Li_2SO_4 exhibits a solid-solid phase transition at 573 °C with enthalpy of 24.8 kJmol^{-1}. The solid-solid phase transition accompanies a volume change of 4.5% ($\Delta V/V$) [182]. The melting point is at 860 °C with fusion enthalpy of 9.0 kJmol^{-1} [168]. The crystal lattice structure is monoclinic in phase II (space group $P2_1/a$). It is face-centred cubic (FCC) with space group Fm3m in phase I. The sulphate groups occupy the origin position (0, 0, 0). 90% of the Li^+ cations occupy the

tetrahedral sites $\pm\left(\dfrac{1}{4},\dfrac{1}{4},\dfrac{1}{4}\right)$ while the octahedral sites $\left(\dfrac{1}{2},\dfrac{1}{2},\dfrac{1}{2}\right)$ are vacant. The

remaining 10% of the Li^+ are distributed on the shell surrounding the sulphate ions [183]. Raman spectroscopy and neutron diffraction reveal that the sulphate anions perform rotational motion in phase I [167, 184]. Ionic conductivity as high as 1 Scm^{-1} was obtained at 600 °C, which can be ascribed to the high mobility of Li^+ [185]. For normal conducting solid electrolytes, the ratio of the number of the available lattice sites to the number of charge carriers should be at least 3. This ratio is only 1.5 for Li^+ ions in Li_2SO_4 [186]. Therefore, the motion of Li^+ ions could involve a special conduction mechanism.

The motion of Li^+ ions has been investigated by a number of techniques. An electromigration experiment suggested that ^6Li migrates faster than ^7Li in Li_2SO_4 [187, 188]. Because the jumping frequency for spontaneous jumping is inversely proportion to the square root of the mass, this has been used to suggest that the transport of Li^+ ions involves spontaneous jumping [168]. The possible jumping pathways include:

(1) jumping from one tetrahedral site to another tetrahedral site through the octahedral site; This model is not supported by the fact that the octahedral sites are vacant.

(2) jumping between two adjacent tetrahedral sites directly; This model is not likely, as this jumping model indicates a jump distance of 3.5 Å, whilst the jump distance obtained from Raman spectroscopy and neutron scattering studies is 3.7 Å, which is significantly greater [189] [167].

(3) jumping from the tetrahedral site into the spherical shell surrounding the sulphate groups and then jumping into one of the adjacent tetrahedral sites. This jumping model is well supported by the following facts. Firstly, molecular dynamic simulation suggests a curved pathway for Li^+ ions [190]. Secondly, the jump distance for this curved pathway is 3.7 Å, in agreement with the results from Raman spectroscopy and neutron scattering [189] [167].

10% of the Li^+ ions surrounding the shell of the sulphates groups appear to be closely coupled with the sulphate groups. Firstly, the closest distance between Li^+ ions and the oxygen atoms on the sulphate groups is 1.57 Å, less than the radial sum 1.90 Å of Li^+ ion and O atom. Neutron diffraction indicates that the nuclear density of the sulphate group is distorted, which could be attributed to the overlap of O nuclei and Li nuclei [183]. Secondly, the transport of Li^+ ions is strongly correlated to the rotational motion of the sulphate groups. The Li^+ ion jump frequency between the tetrahedral sites as calculated from the conductivity data is 2×10^{11} s^{-1} [191]. This is of the same order of magnitude as the rotational time, 2 ps, of sulphate ions obtained from neutron diffraction, Raman spectroscopy and computer-simulation [167, 184, 191, 192].

The transport of Li^+ cation can thus be inferred as: Li^+ ion jumps spontaneously from a tetrahedral site to the sphere of a sulphate group by attaching to an oxygen atom; It is then pushed by the rotating sulphate group to a new environment and jumps to a new tetrahedral site [172]. This transport model suggests that the rotational motion of the sulphate anions plays an important role in facilitating the Li^+ cation diffusion. The conduction occurs by a paddle wheel mechanism.

The paddle wheel mechanism has been further tested by introducing WO_4^{2-} anions or Mg^{2+} cations into Li_2SO_4. WO_4^{2-} is bigger and has a lower rotational frequency, which should result in a decrease in conductivity if a paddle wheel mechanism is effective. It was observed that the conductivity is decreased by doping with less than 5 mol% Li_2WO_4 [193]. Doping with Mg^{2+} creates vacancies on the Li^+ sublattice. If the percolation mechanism applies, the conductivity would be increased by introducing Mg^{2+} ions. The conductivity was found to be independent of the doped Mg^{2+} concentration, which indicates that the

vacancies do not play an important role in the conduction mechanism [194]. Both results support the paddle wheel mechanism[168, 170] [180].

Secco proposed that the percolation mechanism accounts for the high conductivity observed in Li_2SO_4. His main pieces of evidence are: (1) the conductivity jump is correlated with a volume expansion $\Delta V/V$ at the solid-solid transition temperature, which indicates an effect of "free volume" on conductivity [176]; (2) the conductivity decreases when pressure increases [191]. This could be explained by the reduced lattice "free volume" at high pressure restricting the mobility of Li^+ ions [176]; (3) the conductivity increases with the radii of guest ions introduced, such as Na^+, Rb^+ and Ag^+. The explanation is that the introduction of the larger guest ions leads to the lattice expansion in the absence of vacancies, which supports the percolation mechanism [176]. Secco also admitted that the instantaneous orientations of the sulphate groups could play a role to ease the passage of the cation through the bottleneck separating two available sites [179].

The systems of Li_2SO_4-Li_2WO_4 and Li_2SO_4-Li_3PO_4 have been studied in order to understand the conduction mechanism. Secco observed that the conductivity in phase I becomes higher when Li_2SO_4 is doped with 5 mol% and 10 mol% Li_2WO_4 [179]. However, this can not be powerful evidence against the paddle wheel mechanism. The Li_2SO_4-Li_2WO_4 phase diagram shows that the solubility of Li_2WO_4 in Li_2SO_4 is less than 5 mol% [195], meaning that the 5 mol% and 10 mol% compositions are in a two-phase region in phase I. The higher conductivity could therefore be attributed to the liquid phase or the "non-homogeneities" within the samples [170]. In the Li_2SO_4-Li_3PO_4 system, conductivity is decreased by doping with Li_3PO_4 in phase I [196]. However, this system seems to be an inappropriate example to test the conduction mechanism. On one hand, if the paddle wheel mechanism applies, replacing SO_4^{2-} groups with the bigger PO_4^{3-} anions possessing lower rotational frequency would lead to the decrease in conductivity. This explanation supports the paddle wheel mechanism [196, 197]. On the other hand, the decrease in conductivity could also be explained in favor of "free volume" mechanism, as more interstitial Li^+ ions are created to maintain the electroneutrality in the absence of the SO_4^{2-} vacancies. The interstitial Li^+ ions increase the packing density, decrease the free volume and thus lead to the drop in conductivity [177].

LiAgSO$_4$, LiNaSO$_4$, Li$_4$Zn(SO$_4$)$_3$

LiAgSO$_4$, LiNaSO$_4$, Li$_4$Zn(SO$_4$)$_3$ are plastic crystals. All of them show solid-solid phase transition and small fusion entropy [168]. Sulphate ion reorientation occurs in phase I [170, 186]. Li$_4$Zn(SO4)$_3$ is non-cubic in phase I, whilst LiAgSO$_4$ and LiNaSO$_4$ are body-centered cubic in phase I. In LiAgSO$_4$, Ag$^+$ ions occupy the octahedral site $\left(0,\frac{1}{2},\frac{1}{2}\right)$ and Li$^+$ ions occupy the tetrahedral sites $\left(\frac{1}{4},0,\frac{1}{2}\right)$. Li$^+$ and Ag$^+$ have equal diffusion coefficients. The activation energies for sulphate rotation and cation diffusion are 0.72 eV and 0.52 eV respectively [184]. In LiNaSO$_4$, neutron powder diffraction studies indicate that all the Na$^+$ ions are in the octahedral sites while molecular dynamics simulation gives that 10% Na$^+$ ions are in the octahedral sites, 41% in the tetrahedral sites and 49% in other sites [186].

Conductivities approaching 1 Scm^{-1} were observed for all three compounds at 550 °C (in phase I) [168]. Molecular dynamics simulations have shown that, similar to Li$_2$SO$_4$, the cations bond to the oxygen atoms of the neighboring sulphate groups. The rotational motion of the sulphate groups plays an essential role in the cationic transport. The high conductivity is ascribed to a paddle-wheel mechanism [186]. The paddle wheel mechanism is also operative for doped guest cations in the three compounds [186].

In contrast, Na$_2$SO$_4$ displays very different properties from those of Li$_2$SO$_4$, LiAgSO$_4$, LiNaSO$_4$ and Li$_4$Zn(SO$_4$)$_3$. Na$_2$SO$_4$ was proved not a plastic crystal. Although it exhibits a solid-solid phase transition at 247 °C, no sulphate rotation was observed. It is hexagonal at the high temperature solid phase. The conductivity is 7×10^{-4} Scm^{-1} at 550 °C, more than three orders of magnitude lower than that of Li$_2$SO$_4$ [168]. The conduction mechanism seems to be different from that of Li$_2$SO$_4$, LiAgSO$_4$, LiNaSO$_4$ and Li$_4$Zn(SO$_4$)$_3$. The activation energies of the latter four in their plastic crystal phases are about 0.4 eV while it is 0.5-1.7 eV for the Na$_2$SO$_4$ in the hexagonal phase. The radii of the doped mono and divalent cations have small influence on the conductivity for Li$_2$SO$_4$, LiAgSO$_4$, LiNaSO$_4$ and Li$_4$Zn(SO$_4$)$_3$ while the radii of the doped cations have greater influence on the

conductivity for Na_2SO_4 [186]. This comparison seems to indicate the effect of anionic rotation on the conductivity and favors the paddle wheel mechanism in Li_2SO_4, $LiAgSO_4$, $LiNaSO_4$ and $Li_4Zn(SO_4)_3$

Na_3PO_4

Na_3PO_4 was shown in several studies to be a plastic crystal [198-201]. It displays a solid-solid phase transition at 325 °C and final melting at 1300 °C. It is a tetragonal lattice structure in phase II. In phase I, the tetrahedral PO_4^{3-} anions form a FCC lattice where the Na^+ ions occupy all the tetrahedral and octahedral sites [12]. The solid-solid phase transition accompanies a jump in conductivity and a decrease in the activation energy for conductivity [12].

PO_4^{3-} groups involve rotational motion in two processes. The strong coupling of PO_4^{3-} anions and Na^+ cations occurs in both processes [200]. In process 1, PO_4^{3-} anions rotate about one of the four C_3 axes on a picosecond timescale. In this process, oxygen atoms and Na^+ ions, as probed by quasielastic neutron scattering and high frequency conductivity respectively, display comparable localized diffusion coefficients [199] [202, 203]; [198]. Process 2 involves the reorientation of the C_3 axes of PO_4^{3-} groups among six possible orientations parallel to the cubic axes, in the nanosecond regime. This process is triggered and accelerated in phase I and is superimposed on process 1 [204]. ^{23}Na NMR is influenced by a non-averaged anisotropic contribution which could be assigned to the interaction with the PO_4^{3-} anion. ^{17}O, ^{31}P and ^{23}Na spin-lattice relaxations all gave the same activation energy and pre-exponential factor in process 2, providing further evidence that Na^+ ions are strongly coupled with the rotational motion of the PO_4^{3-} groups. This strongly suggests correlated anion-cation motion, supporting the paddle-wheel mechanism [201].

The conducting process can be inferred as the following:

(1) The process is initiated by the attachment of a Na^+ cation to a PO_4^{3-} anion.

(2) The Na^+ ion leaves its original site by the rotation of PO_4^{3-} group about the C_3 axis.

- 39 -

(3) In the new environment, the Na^+ ion forms a strong attachment to another oxygen atom it encounters and triggers the reorientation of the C_3 axis.

The rotational motion of the PO_4^{3-} groups about the C_3 axis and the reorientation of the C_3 axis help to transport Na^+ ions through the lattice [201].

It is worth noting that the vacancy conduction mechanism also plays a minor role in the overall conduction, due to impurities. It is difficult to obtain Na_3PO_4 in a perfectly pure form. As mentioned before, all tetrahedral and octahedral sites are occupied by Na^+ ions. The Na^+ ions at the octahedral sites are surrounded by eight further Na^+ ions. This closely packed Na^+ ion sublattice favors the incorporation of impurities to loosen the packing on the cation sublattice [12]. As a result, an extra motion occurs for Na^+ ions. This motion is assigned to the translational motion of Na^+ ions by vacancy mechanism. Na^+ cations and PO_4^{3-} anions exhibit the same activation energy in this process according to ^{31}P and ^{23}Na NMR [201]. These results indicate that Na^+ ions are still coupled with the rotational motion of PO_4^{3-} groups during the transport among the vacancies.

Na_3PO_4-Na_2SO_4

The coupling between the vacancy hopping mechanism and the rotation enhanced hopping mechanism has been studied by doping Na_2SO_4 into Na_3PO_4. The effects of doping SO_4^{2-} into Na_3PO_4 are anticipated to be: (1) more vacancies are created on Na^+ ion sites; (2) the lattice constant of Na_3PO_4 does not change substantially at dopant level; (3) the effect of paddle wheel mechanism would be enhanced, as the smaller SO_4^{2-} groups have larger rotational frequency. It has been found that the conductivity increases with the dopant level of Na_2SO_4. The activation energy becomes temperature dependent as compared to the Arrhenius behavior for pure Na_3PO_4 in both phase I and phase II [12].

^{31}P and ^{23}Na NMR studies suggest that the motions of Na^+ cations and PO_4^{3-} anions involve two processes [204]. In process 1, the translational motion of Na^+ ions and the rotational motion of PO_4^{3-} are correlated. This process is independent of the concentration of Na_2SO_4. Process 2 is probably a vacancy hopping mechanism for Na^+ ions. This process is almost absent in pure Na_3PO_4, but becomes more important with increasing

concentration of Na_2SO_4. The effect of Na_2SO_4 concentration supports the vacancy hopping mechanism, as more vacancies are created by doping with Na_2SO_4 [204]. The vacancy hopping mechanism and rotation enhanced cationic motion coexist in the Na_3PO_4-Na_2SO_4 system. These two processes seem to be correlated to each other. Both of the processes display similar activation energy in the Na_2SO_4 concentration range of up to 25 mol%. The correlation time and relaxation strength of the two processes become increasingly similar as the vacancy concentration increases. These results indicate that the transport of Na^+ ions among the vacancies is associated with the rotational motion of PO_4^{3-} groups. In conclusion, a paddle-wheel mechanism is strongly suggested in the Na_3PO_4-Na_2SO_4 system [204].

Na_3PO_4-Na_3AlF_6

The effects of doping the larger AlF_6^{3-} anions into Na_3PO_4 are anticipated to be: (1) the transport volume will be increased; (2) the "paddle wheel" effect will be decreased, as the bigger AlF_6^{3-} groups are less rotationally active; (3) the changes in defects are limited, as the doped isovalent AlF_6^{3-} anions are not expected to create more vacancies or interstitials. The defects due to heterogeneity could also be ignored, because Na_3PO_4 and Na_3AlF_6 are completely miscible above 640 °C [12]. The ionic conductivity and transport volume seem to show some connection. Both the conductivity and the transport volume are increased by doping with AlF_6^{3-} anions up to 20 mol%. Beyond this point, the transport volume and the conductivity both decrease with doping [12]. The results indicate that a percolation mechanism seems to apply in the AlF_6^{3-} doped Na_3PO_4.

$XONa_3$ ($X=NO_2^-$, CN^-, Br^-)

Na_3NO_3 is not simply the ortho salt of Na^+ with NO_3^-, but actually oxide nitrite with the formulation of $(NO_2)ONa_3$. $(NO_2)ONa_3$ goes through three solid-solid phase transitions. The crystal lattice structure is body centred cubic (BCC). The NO_2^- groups possess orientational freedom. Na_3OBr and Na_3OCN have similar lattice structure to that of $(NO_2)ONa_3$. Both also exhibit solid-solid phase transitions. The CN^- groups in Na_3OCN display orientational disorder. Na_3OCN and Na_3NO_3, both of which possess anionic rotational freedom, display higher conductivity than Na_3OBr. Although more details about

- 41 -

the transport mechanism are yet to be explored, this comparison indicates the effect of the anionic rotation on conductivity [12, 172]

MNO$_2$ (M=Cs, Tl, K, Rb)

These nitrites all display plastic crystal phases. They exhibit one or more solid-solid phase transitions. The crystal structures are CsCl type cubic for CsNO$_2$ and TlNO$_2$ and NaCl type cubic for KNO$_2$ and RbNO$_2$. NO$_2^-$ anions perform 180° flipping in low temperature phases. In phase I, NO$_2^-$ anions are detected to participate in isotropic rotation and self-diffusion. The activation energies for the anionic motion in the phase I are listed in Table 1.1.

The data in Table 1.1 indicate that: (1) The activation energies for anionic isotropic rotation are very similar for the four species. (2) The activation energies for conductivity are significantly different from those for the anionic rotation, indicating that the anionic rotational motion is not a dominant contributor to the conductivity. (3) The contribution from cationic diffusion to conductivity can not be ignored. Cationic diffusional motion has been observed by NMR studies in KNO$_2$ and TlNO$_2$ [50, 205, 206]. In TlNO$_2$, the activation energy for cationic diffusion (48 kJmol^{-1}) is very close to that for conductivity (47 kJmol^{-1}), indicating that Tl$^+$ is the main charge carrier [205, 207]. (4) The jumping pathway and the size of the pathway opening are the main factors determining the energy barrier to diffusion. The activation energies of diffusion for CsNO$_2$, TlNO$_2$ and KNO$_2$ are all about 47 kJmol^{-1} except that of RbNO$_2$. The difference is explained by the diffusional process. For CsNO$_2$ and TlNO$_2$, the lattice structures are both CsCl type. The ion can jump by a distance of the cell constant to the nearest vacancy site by one step, as shown in Figure 1.7 (b); Whilst for NaCl type KNO$_2$ and RbNO$_2$, the ion jumps by two successive hopping through an opening surrounded by three nearest opposite ions to a nearby vacancy, shown in Figure 1.7 (a) [56]. The smaller opening for a relatively bigger Rb$^+$ ion accounts for the higher activation energy observed in RbNO$_2$ [49].

The Cs, K or Rb NMR and N NMR studies seem to indicate the cation-anion correlation in both the rotational motion and diffusional motion. It is very possible that the cations could be attached to the oxygen atoms by van der Waals forces. It is confirmed by neutron

diffraction study that the cation and the oxygen atom are actually in contact [208]. However, how the cation and the anion are correlated in the diffusional motion, and the contributions from the cationic and anionic diffusion to conductivity are not quite clear.

Table 1.1 Activation energies of isotropic rotation and self diffusion for NO_2^- in phase I obtained by NMR and the activation energy for conductivity. [a] Obtained from ^{14}N or ^{15}N NMR. [b] obtained from ^{133}Cs, ^{85}Rb, ^{87}Rb, ^{39}K or ^{205}Tl NMR.

Compound	E_a/ kJ mol^{-1}			Reference
	Isotropic Rotation	Self-diffusion	Conductivity	
$CsNO_2$	9.0[a], 9.0[b]	33[a], 47[b]	50, 74	[56]
$TlNO_2$	13.5[a]	47[b]	47	[50, 207]
KNO_2	10[a], 12[b]	48[b], 43[b]	100	[206]
RbNO2	6.2[a], 8.5[b]	110[a], 140[b], 75[b]	100	[49]

Organic Molecular Plastic Crystals

Significant molecular diffusion has been observed using a number of experimental techniques in the organic solids benzene, thiophene, 1,4-Dioxane, cyclohexane, succinonitrile, pivalic acid, cyclohexanol and etc in their plastic crystal phases [37, 209-212]. The diffusion in these molecular plastic crystals is suggested to occur by the molecules migrating through extended defects, most likely grain boundaries, during the premelting [209, 210]. This is "pipe diffusion".

Pipe diffusion is generally more rapid than lattice diffusion. The diffusion coefficient of pipe diffusion is orders of magnitude higher than that of lattice diffusion. The activation

energy of pipe diffusion is smaller than that of lattice diffusion. Pipe diffusion is more competitive than lattice diffusion at lower temperatures when extended defects exist [153]. The facile pipe diffusion observed in these plastic crystal materials is attributed to the low energy requirement to create vacancies and defects on the crystal interface. The interfacial disordering results in premelting behavior in some cases 35 °C below the melting point, and also provides an effective pathway for molecular diffusion [209].

In addition to pipe diffusion, mono-vacancy migration may also occur in some plastic crystals with smaller fusion entropies (1.3±0.4R), such as cyclohexane, succinonitrile and pivalic acid [209]. There seems no direct connection between the rotational motion and the diffusional motion. For example, the correlation times of molecular rotation and hopping are 2.3×10^{-12} s and 2.6×10^{-7} s respectively at 0 °C for cyclohexane. The activation energies of molecular rotation and diffusion are 21.3 kJmol^{-1} and 57.0 kJmol^{-1} respectively for succinonitrile [213]. In contrast, mono-vacancy diffusion is less important in benzene, thiophene and 1,4-Dioxane which have higher fusion entropies (5R). Both the diffusion coefficients of lattice diffusion and pipe diffusion in benzene, thiophene and 1,4-Dioxane (10^{-17} m^{2}s^{-1} for lattice diffusion, 10^{-13} m^{2}s^{-1} for pipe diffusion at melting point) are orders of magnitude lower than the values for plastic crystals with lower fusion entropy (10^{-13} m^{2}s^{-1} for lattice diffusion and 10^{-8} m^{2}s^{-1} for pipe diffusion) [209].

In all, molecular diffusion is directly related to defects in these molecular plastic crystals. Although the diffusion does not contribute to the conductivity, the discussions about the diffusion mechanism are still presented here to give some insight into ionic diffusion. More studies on the diffusion of molecular plastic crystals have been reviewed by Chezeau et al. [11].

Ammonium Salts

The rotational motion of cations in certain ammonium salts has been known for decades [28]. Ammonium salts with highly symmetric anions, such as NH$_4$NO$_3$ [214, 215], NH$_4$PF$_6$ [216], (NH$_4$)$_2$BeF$_4$ [217] and NH$_4$HF$_2$ [218], are known to possess rotational freedom for both the NH$_4^+$ cation and the anions.

A series of alkyl substituted ammonium salts have been investigated. The degree of the alkyl substitution ranges from 1 to 4. The alkyl chain length varies from one carbon to ten carbons. Salts with a nitrogen-containing ring within the cations, such as piperidinium [52, 54], pyrrolidinium [55] and pyrrolinium [166] have recently been studied. The anions are Br^- [58], I^-, ClO_4^- [219, 220], IO_4^- [63], NO_3^- [220, 221], SCN^- [222], PF_6^- [54, 55], SbF_6^- [223], BF_4^-[224] [57], $TFSA^-$ [166], MX_n^- (M, divalent metal and X, halogen) [225] and so on.

Most of the ammonium salts studied are believed to be plastic crystals. They generally exhibit one or more solid-solid phase transitions. A cubic or a tetragonal lattice structure is normally found in phase I. Rotational motion of the cations starts to occur in the low temperature phases. The rotational motions at low temperature are normally internal rotations with low energy requirement, such as the C_3 rotation of the CH_3 groups on the alkyl chains or the C_3 rotation of the NH_3 groups [219, 226, 227]. As temperature increases, the whole cation becomes involved in the rotational motion. Isotropic rotation has been suggested for a number of cations in phase I, for example, the small $CH_3NH_3^+$ [58, 227], and the relatively bulky $(CH_3)_4N^+$ [222], $(CH_3)_3NCH_2CH_3^+$ [53], pyrrolidinium [55] and piperidinium [52, 54]. When one or two long alky chains are attached to the N atom, as in for instance the $C_nH_{2n+1}NH_3^+$ (n=3 – 10) [59, 228-230] and the $(C_nH_{2n+1})_2NH_2^+$ (n=2 – 4) [231], isotropic rotation is restricted. Instead, the cation rotates about its long axis.

In addition to the rotational motion, most of the cations participate in diffusional motion in the high temperature phases. The long, rod shaped $C_nH_{2n+1}NH_3^+$ and the $(C_nH_{2n+1})_2NH_2^+$ are suggested to perform two-dimensional diffusion in the plane perpendicular to the rotational axis [59, 228-231]. Three-dimensional self-diffusion is suggested for the cations with short alkyl groups, such as $CH_3NH_3^+$ [58, 227], $(CH_3)_4N^+$ [222], pyrrolidinium [55] and piperidinium [52, 54]. Some of the high symmetric anions, for example ClO_4^- [52, 232], BF_4^- [57], PF_6^- [53-55] and NO_3^- [52, 53], also perform rotational motion. In some samples, anionic diffusion has also been detected for PF_6^- [54, 55], BF_4^- [57] and Cl^- [59, 230]. The activation energies and correlation times of ionic rotation and diffusion for some of the ammonium salts reported in the literature are listed in Table AP- 2 in Appendix B.

It is found that the energy barrier to cation diffusion does not depend strongly on the species of the anions. One example is CH_3NH_3X (where X= I^-, Br^-, ClO_4^-, NO_3^-). The activation energy for cation diffusion is in the range of 30 – 50 $kJmol^{-1}$ regardless of the anion species. The exception is $(CH_3NH_3)_2SO_4$, where the activation energy for cation diffusion is 76 $kJmol^{-1}$. The relatively higher energy barrier for cation diffusion in this case is attributed to the divalent anion [227]. The $CH_3NH_3^+$ cations have similar jump rate (about 10^{-8} s) at the melting point for all these salts (ref. as in Table AP- 2 in Appendix B). Other examples are pyrrolidiniumX and piperidiniumX (where $X=PF_6^-$ and BF_4^-). The activation energy of diffusion is about 60 $kJmol^{-1}$ for piperidinium [52, 54], and about 46 $kJmol^{-1}$ for pyrrolidinium regardless of the anions [55]. In addition, it seems that the diffusional motion of the cations is not strongly correlated to the rotational motion of the anions. These results indicate that the paddle wheel mechanism is not the main conduction mechanism for these ammonium salts. This is reasonable since the relatively big cations will not be easily attached to or be transported by the rotating anions.

The lattice volume does not play an important role in the conduction mechanism for the ammonium salts. For instance, an increase in conductivity was observed at the phase III to II transition in NH_4NO_3 accompanying a decrease in the lattice volume [214].

Ikeda and Ishida et al. have suggested that cations diffuse by jumping into nearby vacancies [55, 58, 230]. The cationic size is an important factor determining the diffusional energy barrier, as shown by:

(1) As the sizes of cations become more bulky from $(CH_3)_2NH_2ClO_4$ to $(CH_3)_3NHClO_4$ to $(CH_3)_3NCH_2CH_3ClO_4$, the activation energies for cation diffusion increase from 37.6 $kJmol^{-1}$ to 57.9 $kJmol^{-1}$ to 60.0 $kJmol^{-1}$ [53, 226, 233].

(2) The activation energies of cationic diffusion for $CH_3NH_3NO_3$ and $CH_3ND_3NO_3$ are the same, 29 $kJmol^{-1}$, indicating that the energy barrier for diffusion mainly depends on the ionic size and shape, not the mass [221].

(3) Ono et al. have compared the activation energies for a number of the CsCl type ammonium salts having various sized cations. They found that the activation energy for

diffusion increases with the ionic size and lattice size, further suggesting that ionic size is an important factor in the ionic diffusion [55].

The effects of the cationic size on the cationic diffusion are further evidenced by a series of salts with rod shaped cations. In the $C_nH_{2n+1}NH_3Cl$ (n=3-10) family, all the salts have tetragonal lattice structure with a lamellar-type double-layered structure. The axis of the rod like cation is along one of the unit cell axes. The rod like cations perform 1D rotation about the cationic long axis (also parallel to one of the unit cell axes). The cations perform the two-dimensional diffusion in the lamellar plane perpendicular to the rotational axis. The activation energies of cationic rotation are nearly the same, 5-6 kJmol^{-1}, for all the members, regardless of the cationic size. In contrast, the activation energy for cationic diffusion exhibits strong cationic size dependence, increasing with the length of the cation [59, 228-230].

The system of $(C_nH_{2n+1})_2NH_2Br$ (n=2-4) exhibits similar properties. A tetragonal lattice structure has been detected for all these three salts. The cations perform the uni-axial rotation along the cationic long axis (parallel to one of the unit cell axes). The activation energy for cationic rotation is in a narrow range of 12-18 kJmol^{-1}. The cationic diffusion occurs in the 2D plane perpendicular to the cationic long axis. The activation energy for cationic diffusion increases with the length of the alkyl chain, implying that the energy barrier to cationic diffusion depends on the ionic size [231].

In addition to the ionic size, the size of the opening (the bottleneck in the pathway of diffusion formed by nearby ions) is also an important factor determining the energy barrier to diffusion. The effect of opening size is demonstrated by comparing $CH_3NH_3NO_3$ and NH_4NO_3. Both of the salts form CsCl type cubic lattice structures in phase I. The cations jump to the nearest vacant site by passing through an opening surrounded by four anions, as shown in Figure 1.7 (b). The length of the minor axis of the ellipsoid of $CH_3NH_3^+$ is close to the diameter of the NH_4^+ ions, meaning that the same area of opening is needed for the cation to pass through. However, since the lattice constant is bigger for $CH_3NH_3NO_3$, the opening in $CH_3NH_3NO_3$ is bigger than in NH_4NO_3. As a result, the energy barrier for cationic diffusion in NH_4NO_3 (51 kJmol^{-1}) is much higher than in $CH_3NH_3NO_3$ (29 kJmol$^-$

[1]) [221]. The opening theory was also applied to explain the high energy barrier for the diffusion of NH_4^+ in NH_4Cl [234]. In the NaCl-type NH_4Cl, the NH_4^+ ions jump to a nearby vacancy by two successive hops through an opening with a diameter of 1.71 Å, as shown in Figure 1.7 (a) [234]. Whilst the diameter of the opening for NH_4^+ in the CsCl type NH_4NO_3 is calculated to be 3.58 Å by taking 4.40 Å for the cell constant and 1.32 Å for the radius of NO_3^- [214]. The smaller opening in NH_4Cl accounts for a higher activation energy (120 kJmol^{-1}) for the NH_4^+ diffusion.
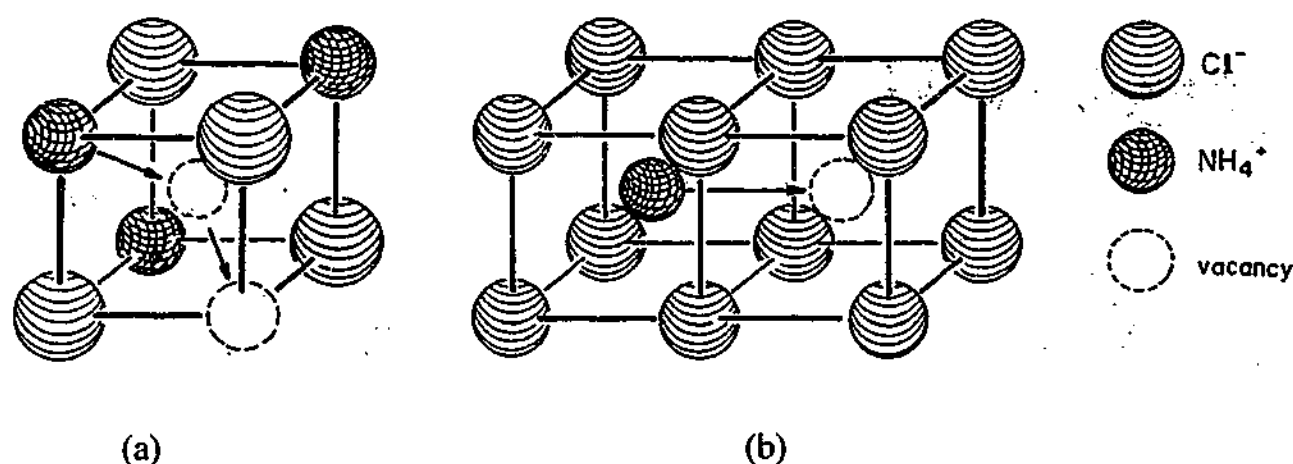

(a)   (b)

Figure 1.7 The scheme of the self-diffusion pathway in (a) NaCl-type crystal and (b) CsCl-type crystal, as demonstrated in NH₄Cl Phase I and Phase II, respectively [234].

It has also been suggested that there seems a correlation between the diffusional motion of the cations and anions. In the $C_nH_{2n+1}NH_3Cl$ system, the activation energy of conductivity is between the values of the activation energies for cationic and anionic diffusion, implying that the diffusional motion of both cations and anions contribute to the conductivity. According to the lamellar-type double-layered structure, the jump distance for Cl⁻ anion is the cell constant "a", nearly the same for the whole system of salts. However, the activation energy for the Cl⁻ anionic jumping still exhibits a dependence on the length of the carbon chain on the cation, implying that the diffusions of the cations and the anions are correlated [230].

The correlation between the cationic diffusion and anionic diffusion could be explained by a Schottky-type lattice defects mechanism. When a cationic lattice defect diffuses, it is accompanied by the diffusion of an anionic defect to remain the neutrality [59, 230].

Moreover, by comparing the activation energies of the cations and the anions for $C_4H_8NH_2PF_6$, $C_5H_{10}NH_2PF_6$ and $(CH_3)_3NC_2H_5PF_6$, it was found that although the activation energies for the cationic and the anionic diffusion are different, the activation energies for the anionic diffusion also show lattice size dependence, similar to that of the cations. Ono et al. suggested that the diffusions of cation and anion are correlated in some way, probably by a vacancy pair and/or a Schottky defects mechanism [55].

It is also interesting that the correlation times of diffusion at the melting point for both the cations and the anions are found to be in the range of $10^{-7} \sim 10^{-8}$ s, as shown in Table AP- 2 in Appendix B. It has been suggested that the jumping rate in this range can be regarded as a crucial point to trigger the melting [54, 55].

In conclusion, a vacancy mechanism is suggested for ionic diffusion in the ammonium salts. The size of the diffusional ions and the size of the opening are important factors determining the energy barrier for ionic diffusion. The correlation between the cationic diffusion - anionic rotation is not strongly suggested by the experimental data obtained so far. The correlation between the cationic diffusion and anionic diffusion is nevertheless well supported. The ionic diffusion in the ammonium salts is suggested to occur by a vacancy pair and/or a Schottky defects mechanism. However, there lacks direct evidence from the studies on defects to support this suggestion. The vacancies and the defects in the ammonium salts need to be explored.

Summary

The conduction mechanism of plastic crystals could be complicated. First of all, the effects of rotational motion and "free volume" on conductivity are hard to separate. The rotational motion is normally accompanied by an increase in lattice volume and the creation of defects in the plastic crystal phase. Other factors, such as the charge carrier concentration and various defects, will also influence the diffusional motion in plastic crystals. Secondly, even if the rotational motion of some ions are involved in the transport of other ions (as revealed in Li_2SO_4 and Na_3PO_4), the role of the rotating ions is difficult to define. The rotational motion could actively assist the translational motion (paddle wheel or cog-wheel mechanism), or merely be a passive response to the translational motion (revolving door

mechanism), or facilitate the passage of diffusing ions in a random and uncoupled way [12]. Thirdly, the transport mechanism may not merely be the rotation-assisted procedure, but could be the combination of several processes and mechanisms, as suggested in Na_3PO_4 [12].

1.6 Background and aim of this study

In this study, N, N-methyl alkyl substituted pyrrolidinium bis(trifluoromethanesulfonyl)amide (P1xTFSA, x is the number of carbons on the alkyl group) salts are studied for the purpose of developing highly conductive solid state electrolyte materials for lithium batteries. The alkyl group in this study is methyl or ethyl (x=1 or 2). On the bases of the studies on the pure P1xTFSA salts, lithium bis(trifluoromethanesulfonyl)amide (LiTFSA) salt is added as a dopant in order to improve conductivity and to achieve a Li^+ ion conductor.

1.6.1 Background

The ionic structures of the $P1x^+$ cations and TFSA⁻ anions are shown in Figure 1.8. Both the $P11^+$ and $P12^+$ are not highly symmetric ions. $P11^+$ is mirror symmetric. When $x \geq 2$, $P1x^+$ does not seem to have any symmetric elements. It is difficult to predict that the N,N-methyl alkyl pyrrolidinium based salts are plastic crystals only from the symmetry of the $P1x^+$ cations. However, a number of N,N-methyl, alkyl pyrrolidinium based organic salts have recently been investigated in our group. It has been found that although the anions range from TFSA⁻, BF_4^-, PF_6^-, OH⁻ to I⁻, most of the salts with short alkyl groups show plastic crystal behavior [32, 33, 235-240]. Therefore, it is interesting to investigate the plastic crystal behavior of these pyrrolidinium salts.

As to the TFSA⁻ anions, the anion lies on a two-fold axis centred on N, which implies that the anion could have some rotational freedom. Another important characteristic is that TFSA⁻ anions provide great dissociation ability. The reason is that the charge on the anion is delocalized among the sulfur, nitrogen and oxygen atoms, as the CF_3 group has strong

electron-withdrawing power to help the charge delocalisation [241]. This characteristic is used to form molten salts with depressed melting point [242].

The lithium salts mostly used in lithium batteries are: $LiClO_4$, $LiPF_6$, $LiBF_4$, $LiAsF_6$ and $LiOSO_2CF_3$. Each of the salts has its disadvantages. $LiClO_4$ can induce explosions under some conditions. $LiPF_6$ and $LiBF_4$ have poor chemical and thermal stability. $LiAsF_6$ degrades into toxic products. $LiOSO_2CF_3$ is relatively more stable and safer, but is corrosive to Al current collectors at high potentials [243]. LiTFSA salt has superiority to these lithium salts in that LiTFSA shows good chemical stability and safety [243]. LiTFSA has become one of the most favored salts for lithium battery research in recently years. LiTFSA doped PEO exhibits low crystallinity, low T_g and conductivity of 10^{-6} Scm^{-1} at 25°C. LiTFSA containing organic solvents exhibit good conductivity at the level of 10^{-2} Scm^{-1} at room temperature [7]. Therefore, LiTFSA is chosen in this study as the doping lithium salt. Another consideration of using LiTFSA is that only Li^+ ions are introduced into the parent P1xTFSA matrix, as P1xTFSA and LiTFSA have the same anions.
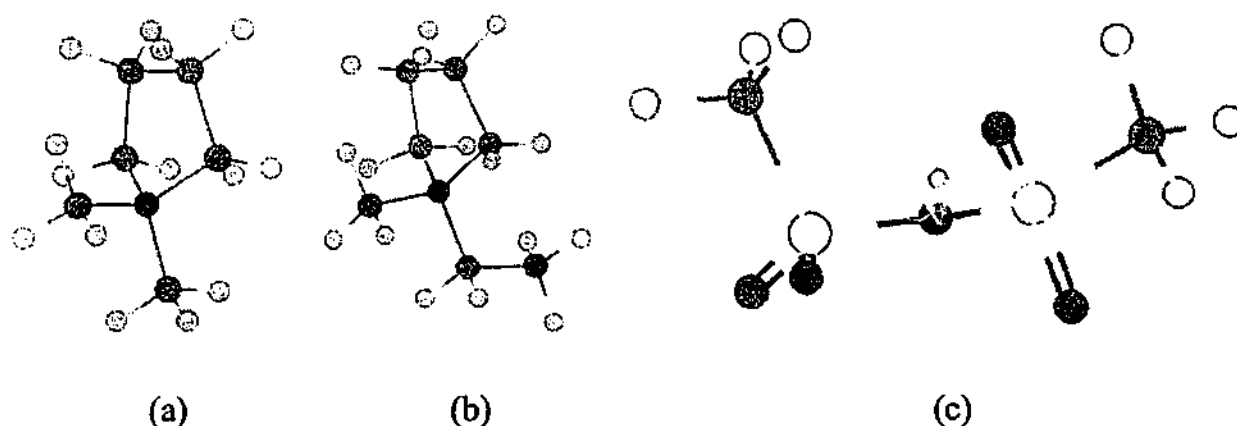

(a)   (b)   (c)

Figure 1.8 The ionic structures of (a) N,N-methyl methyl pyrrolidinium cation (P11$^+$), (b) N,N-methyl ethyl pyrrolidinium cation (P12$^+$) and (c) bis(trifluoromethanesulfonyl)amide anion (TFSA$^-$).

1.6.2 Aim

Central to this study is the understanding of ionic motions, including rotation and diffusion, in the salts P11TFSA and P12TFSA. The diffusional motion is particularly of interest for developing ionic conductors. The studies on the ionic motions involve not only the

macroscopic thermal behaviors and mechanical properties, but also essentially the microscopic properties, such as the crystal lattice structure and defects. More specifically, the aims of this study are:

(1) To provide further evidence of the plastic crystal behaviors of the P1xTFSA salts, via studies of the thermal properties, microstructures, and ionic rotational motions. The techniques of differential scanning calorimetry (DSC), powder x-ray diffraction (XRD) and nuclear magnetic resonance (NMR) will be used for these studies.

(2) To investigate the mechanical properties and the conduction mechanism. Mechanical properties will be tested by mechanical thermal analysis (MTA). Conductivity measurements will be carried out by AC impedance spectroscopy. NMR and analyses of the conductivity data will be applied to study the ionic diffusional motion, the contributions from the charge carriers' mobility and concentration to conductivity. Defects will be studied by positron annihilation lifetime spectroscopy (PALS) and scanning electron microscopy (SEM), which will provide insight into both the conduction mechanism and mechanical properties.

(3) To improve the conductivity by doping with LiTFSA salt. Plastic crystal behaviors of the LiTFSA salt doped systems will be studied. This involves study of the phase diagrams for the LiTFSA-P11TFSA and LiTFSA-P12TFSA binary systems. The influence of doping with LiTFSA salt on the ionic rotational and diffusional motion will be investigated by NMR. Analyses of the diffusional motion for the three ions, Li^+, $P1x^+$ and $TFSA^-$, will be carried out to understand the conduction mechanism for the LiTFSA doped systems.

1.6.3 Outline

The arrangement of this thesis is:

In chapter 2, the experimental procedures will be described in detail. The theoretical background of some of the experimental techniques used will be introduced. These experimental techniques introduced are either very important in this study or newly employed in this group. The routine techniques generally used in this group have been

previously reviewed by other group members and therefore will not be introduced in detail here.

The study of the pure N, N-methyl ethyl pyrrolidinium bis(trifluoromethanesulfonyl)amide (P12TFSA) will be presented in chapter 3.

Chapter 4 will present the study of the pure N, N-methyl methyl pyrrolidinium bis(trifluoromethanesulfonyl)amide (P11TFSA). P11TFSA is to be compared with P12TFSA in the conclusion section in this chapter.

The study of the lithium bis(trifluoromethanesulfonyl)amide doped N, N-methyl ethyl pyrrolidinium bis(trifluoromethanesulfonyl)amide (LiTFSA-P12TFSA) will be presented in chapter 5.

The study of the lithium bis(trifluoromethanesulfonyl)amide doped N, N-methyl methyl pyrrolidinium bis(trifluoromethanesulfonyl)amide (LiTFSA-P11TFSA) will be presented in chapter 6. The two binary systems of LiTFSA-P12TFSA and LiTFSA-P11TFSA are compared in the conclusion section in this chapter.

The overall conclusion of all these studies will be presented in chapter 7. Chapter 7 also includes some suggestions for the future work on this project.

Chapter 2   Experimental Theory and Method

This chapter provides some of the background theories appropriate to the measurements and studies frequently used in this work. Nuclear magnetic resonance spectroscopy, dielectric responses, conductivity and positron annihilation lifetime spectroscopy techniques are introduced in some detail.

2.1   Nuclear Magnetic Resonance Spectroscopy (NMR)

NMR is one of the most widely used techniques for studies of plastic crystals. The main advantages of NMR are:

(1) The motions which the molecules or the ions take can be determined by measuring the second moment, as the value of second moment is greatly influenced by the molecular motion.

(2) The activation energy and correlation time of the motion can be obtained from relaxation measurement as a function of temperature.

(3) The motion of each ion or each part of the molecule can be studied individually by the measurements of different nuclei. For example, the motions of the cations and the anions in pyrrolidinium hexafluorophosphate can be explored by ^1H and ^{19}F NMR respectively [55]. This is important in identifying the contribution of each ion to the overall conductivity.

The introduction of NMR in this section concentrates on solid state NMR, the second moment and relaxation mechanisms as well as their measurements. The NMR theory in this section is based on a number of references [30, 244-250]. They are not quoted hereafter.

2.1.1 Basic Concept

A nucleus of spin I has a magnetic moment μ

- 54 -

$$\mu = \gamma\hbar I$$

Equation 2.1

where I is the spin quantum number; $\hbar = h/2\pi$ (h is Planck's constant); γ is the magnetogyric ratio, a constant for a given nucleus. In the absence of magnetic field, the magnetic moments are randomly oriented. When a magnetic field $\mathbf{B_0}$ is applied, the nuclei adopt particular orientations and precess about the direction of the magnetic field at angular frequency

$$\omega_L = \gamma B_0$$

Equation 2.2

ω_L is known as the Larmor frequency. Each orientation corresponds to an energy level. There are $2I+1$ energy levels involved, each represented by m_i, where m_i is the magnetic quantum number. For nuclei with spin I, there are $2I+1$ values of m_i, ranging from I, I-1, ..., -I+1, -I. The energy levels are equally separated by

$$\Delta E = \gamma\hbar B_o$$

Equation 2.3

The interaction between the magnetic moment and magnetic field, causing the energy level splitting, is known as the Zeeman Interaction. At equilibrium state, the distribution of spins among the energy levels is given by a Boltzmann function,

$$\frac{N_b}{N_a} = \exp(-\frac{\Delta E}{kT})$$

Equation 2.4

where N_a and N_b are the population of the lower and higher energy levels respectively; ΔE is the energy difference between the energy levels; k is the Boltzmann constant and T is temperature. The Boltzmann function is simplified as

- 55 -

$$\frac{N_b}{N_a} \approx 1 - \frac{\Delta E}{kT}$$

Equation 2.5

It implies a slight excess of population in the lower energy level where nuclei are aligned in the direction of B_0. As a result, there is a net macroscopic magnetization M_0 in the direction of the applied magnetic field under the equilibrium state, as showed in Figure 2.1 (a). NMR theory studies the behavior of the net magnetization rather than a single nuclear moment.

The above concepts are introduced in a static laboratory frame, defined by a coordinate system (x, y, z). The applied magnetic field B_0 is in the z direction. The macroscopic magnetization precesses around the z axis at the Larmor frequency ω_L. In order to simplify the treatment of the magnetization motion, a rotating frame is introduced, which is given by another coordinate system (x', y', z'). The z' axis is in the same direction as z. The x'-y' plane is rotating about z' at the Larmor frequency with respect to the x-y plane. The precessing magnetization appears stationary in the rotating frame.

When a magnetic field B_1 generated by a radio frequency (RF) pulse is rotating at ω_L in the x-y plane, it appears stationary in the direction of the x' axis. If B_1 obeys the resonance condition:

$$\nu = \frac{\gamma B_0}{2\pi}$$

Equation 2.6

spins are excited to the higher energy level. The change in the population distribution alters the net magnetization. M_0 appears to precess about the x' axis at a speed γB_1, as shown in Figure 2.1 (b). In a time t, the angle through which M precesses is

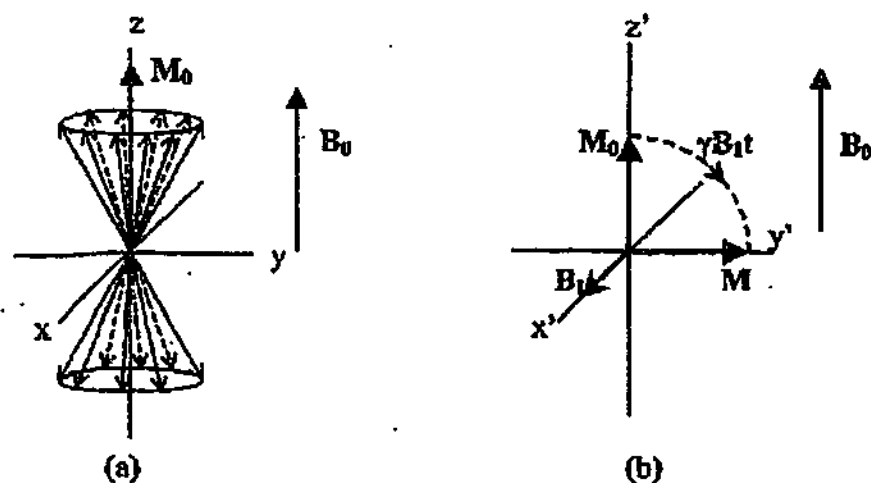$$\theta = \gamma B_1 t$$

Equation 2.7

Figure 2.1 (a) Precession of an ensemble of identical magnetic moments of nuclei with $I = \frac{1}{2}$ and the equilibrium net macroscopic magnetization M_0 in the direction of B_0 (z axis) (b) Precession of M about B_1 in the rotating frame by 90° [245].

Immediately after RF field B_1 is turned off, the magnetization precesses freely at the Larmor frequency in the laboratory frame with a decay rate. When a receiver coil is placed in the x-y plane, the decaying magnetization will induce an RF current in the coil and thus be recorded. The signal induced in the coil is called free induction decay (FID), recorded as magnetization or current as a function of time. The FID can also be represented as a single line at frequency ω_L in the frequency domain by Fourier transform.

In a real material, since the nuclei interact with each other and thus experience different local magnetic fields, the NMR spectrum does not simply show a single line at ω_L, but a response with a band of frequency distribution

NMR spectroscopy provides information about these interactions and local environments of the nuclei. The interactions include the dipole-dipole interaction among spins, the quadrupolar interaction with electric field gradients, the shielding interaction with electrons and the scalar J or indirect coupling of two or more nuclei. One or more of these may dominate the others. The first three are dominant in this study and are emphasized here.

2.1.2 Dipole-Dipole Interaction

A magnetic moment μ_j of spin I at point r interacts with the dipolar field produced by other spins S_k (S_k is a spin quantum number). The dipolar field at point r is given by

$$B(r) = \sum_k \left[-\frac{\mu_k}{|r - r_k|^3} + \frac{3\mu_k(r - r_k)}{|r - r_k|^5}(r - r_k) \right]$$

Equation 2.8

where $\mu_k = \gamma_k h S_k / 2\pi$. Because of the "many body" nature of the spin interaction, the corresponding peaks may overlap, be degenerated and produce a band of absorption, which is difficult to associate with a particular transition. However it is possible to obtain information about the average dipolar interaction from a band of frequencies by the Van Vleck method of moments [251].

The nth moment M_n of $F(\omega)$ is given by

$$M_n = \int_0^\infty (\omega - \omega_L)^n F(\omega) d\omega$$

Equation 2.9

where ω_L is the center of the resonance line and $F(\omega)$ is the normalized shape function. $F(\omega)$ could be a Gaussian curve which is normally observed in solid materials and is described by the normalized function

$$F(\omega) = \frac{1}{\sqrt{2\pi M_2}} \exp\left[-\frac{(\omega - \omega_L)^2}{2M_2} \right]$$

Equation 2.10

where M_2 is the second moment. The full width at half magnitude (FWHM) $\Delta\omega$ can be calculated to be

$$\Delta\omega = 2.36\sqrt{M_2}$$

Equation 2.11

$F(\omega)$ could also be the Lorentzian shape, which normally occurs in solutions and is described by normalized function

$$F(\omega) = \frac{\Delta\omega}{2\pi} \frac{1}{\left(\frac{\Delta\omega}{2}\right)^2 + (\omega - \omega_L)^2}$$

Equation 2.12

M_2 is no longer defined in this case. A trial model is to assume that the curve is described as Equation 2.12 in the interval $\left|\omega - \omega_L\right| \leq \beta$ and zero when $\left|\omega - \omega_L\right| > \beta$, where $\beta \gg \frac{\Delta\omega}{2}$. M_2 is given as

$$M_2 = \frac{\Delta\omega\beta}{\pi}$$

Equation 2.13

For a single crystal, the second moment M_2 due to the interactions between like spins I is given by

$$M_2{}^{II} = \left(\frac{\mu_0}{4\pi}\right)^2 \frac{3}{4} \gamma^4 \hbar^2 I(I+1) \frac{1}{n} \sum_{j,k} \frac{\left(1 - 3\cos^2\theta_{jk}\right)^2}{r_{jk}{}^6}$$

Equation 2.14

where μ_0 is the permeability of a vacuum; θ_{jk} is the orientation of the vector r_{jk} from j to k with respect to the direction of the applied static magnetic field B_0; n is the number of magnetic nuclei in the system over which the sum is taken. For a powder sample where the

crystallites are randomly oriented, $(1-3\cos^2\theta_{jk})^2$ is averaged over all directions. M_2 is given as

$$M_2{}^{II} = \left(\frac{\mu_o}{4\pi}\right)^2 \frac{3}{5}\gamma^4\hbar^2 I(I+1)\frac{1}{n}\sum_{j,k} r_{jk}^{-6}$$

Equation 2.15

For single crystals, the second moment due to the interactions between unlike spins I and S is given by

$$M_2{}^{IS} = \left(\frac{\mu_o}{4\pi}\right)^2 \frac{1}{3}\gamma_I{}^2\gamma_S{}^2\hbar^2 S(S+1)\frac{1}{n}\sum_{j,k}\frac{\left(1-3\cos^2\theta_{jk}\right)^2}{r_{jk}{}^6} \qquad .$$

Equation 2.16

When the spins are randomly oriented in powder samples,

$$M_2{}^{IS} = \left(\frac{\mu_o}{4\pi}\right)^2 \frac{4}{15}\gamma_I{}^2\gamma_S{}^2\hbar^2 S(S+1)\frac{1}{n}\sum_{j,k} r_{jk}^{-6}$$

Equation 2.17

In solids containing two dipole-dipole coupled species I and S, the second moment of spin I has contribution from both I-I and I-S interactions. M_2 is written as:

$$M_2{}^I = M_2{}^{II} + M_2{}^{IS}$$

Equation 2.18

When molecular motions occur, the term of $(1-3\cos^2\theta_{jk})^2$ can be partly or completely averaged out. The second moment is often composed of two parts, the intramolecular contribution from the dipole-dipole interactions within the molecules and the intermolecular contribution from the interactions with surrounding molecules. When the molecules have rotational motion, part or all of the M_2 from intramolecular interaction is

averaged out. If translational motion occurs, part or all of the intermolecular interaction is averaged out. Figure 2.2 shows that when thermally activated motion occurs in a solid sample, M_2 experiences motional narrowing from the "rigid lattice" value to the "motionally averaged" value.

In the transition region,

$$M_2{}^{expt} = \bar{M}_2 + \left(M_2 - \bar{M}_2 \right) \frac{2}{\pi} \tan^{-1} \left(\alpha M_2{}^{1/2} \tau \right)$$

Equation 2.19

where $M_2{}^{expt}$ is the second moment in transition region; M_2 and $\bar{M}_2$ are the rigid lattice second moment and the averaged second moment respectively; τ is the correlation time and α is in the range of 1 to 10. According to Equation 2.11 and Equation 2.19, τ can be obtained by [38]

$$\frac{1}{\tau} = \frac{\alpha \Delta v}{\tan \left[\dfrac{\pi}{2} \left(\dfrac{\Delta v^2 - \bar{\Delta v}^2}{\Delta v_r{}^2 - \bar{\Delta v}^2} \right) \right]}$$

Equation 2.20

where Δv is the FWHM in the transition region; Δv_r and $\bar{\Delta v}$ are the FWHMs before and after transition respectively.

In all, the narrowing of second moment indicates the onset of molecular motion. For materials where the distances between the dipole-dipole interacting nuclei are known, the second moments in their rigid lattice states and in the motion-involved states can be calculated. By comparing the calculated value and the experimental value, the motion the molecules taking can be inferred. In turn, the nuclear distances can be inferred from the experimental values. In addition, Equation 2.20 provides a method to obtain the correlation

time, although the correlation time obtained from M_2 is less accurate than the value obtained from relaxation measurement [38].
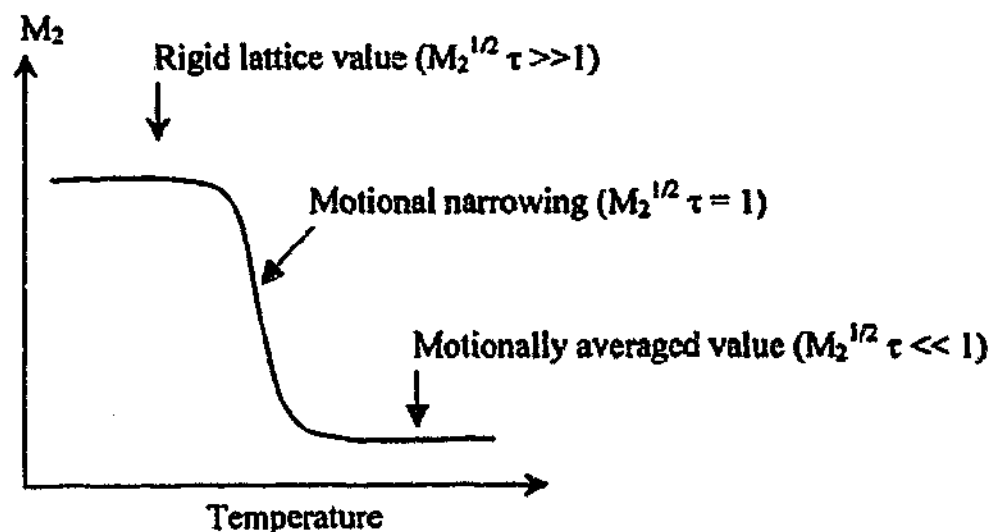

Figure 2.2 Second moment as function of temperature in a solid in the presence of molecular motion [244].

2.1.3 Quadrupolar Interaction

All nuclei with $I > \frac{1}{2}$ have an ellipsoidal distribution of charge and an electric quadrupole moment eQ. eQ has a particular value for a given nucleus. In a molecule, an electric field gradient at a nucleus may exist due to asymmetry in the local charge distribution. The shape and direction of the electric field is described by a tensor V, which is represented by a diagonal matrix composed of three principle elements Vxx, Vyy, Vzz in the order $|Vzz| \geq |Vyy| \geq |Vxx|$. The asymmetry parameter η is

$$\eta = \frac{Vxx - Vyy}{Vzz}$$

Equation 2.21

For an axial symmetric electric field gradient, $\eta = 0$.

The interaction of the quadrupolar moment with the electric field gradient is known as quadrupolar interaction. The first order quadrupolar interaction causes a quadrupolar shift

ω_Q on the base of the Larmor frequency ω_L for the transition from energy level m_i to m_i-1. When $\eta = 0$, ω_Q is given as:

$$\omega_Q = \left(-\frac{3e^2qQ}{4\hbar}\right)\left(3\cos^2\theta - 1\right)\frac{\left(m_i - \frac{1}{2}\right)}{I(2I-1)}$$

Equation 2.22

where eq is the electric field gradient, $eq = V_{zz} = \dfrac{\partial^2 V}{\partial z^2}$; $\dfrac{e^2qQ}{\hbar}$ is the nuclear quadrupole coupling constant (QCC); θ is the angle between the electric field gradient and applied magnetic field. It is averaged out for a powder sample. Quadrupolar interaction can not be observed in isotropic materials such as solutions, where the electric field gradient is averaged to zero.

For a nucleus with $I = 3/2$ (eg. ^{7}Li), the energy level splitting and NMR spectra are shown in Figure 2.3.

2.1.4 Shielding Interaction

For nuclei located in different electronic environments, the interaction with surrounding electrons leads to a change in the local magnetic field. The effective local magnetic field at a nucleus is

$B_{eff}=B_o(1-\sigma)$

Equation 2.23

where σ is the shielding tensor, depending on the electronic structure. In powder samples, the shielding tensor is a diagonal matrix. Three principal elements σ_{xx}, σ_{yy} and σ_{zz} describe the principal values of the electronic cloud. For an axially symmetric chemical shift tensor, $\sigma_{xx}=\sigma_{yy}=\sigma\perp$, $\sigma zz=\sigma//$. For nonaxially symmetric tensor, $\sigma_{xx} \neq \sigma_{yy} \neq \sigma_{zz}$. The spectrum is broad and asymmetric. In liquids, the rapid reorientation of molecules averages all the

electronic cloud orientations. Only an isotropic value $\bar{\sigma}$ is observed. The resonances are sharp and symmetric.

$$\bar{\sigma} = \frac{\sigma xx + \sigma yy + \sigma zz}{3}$$
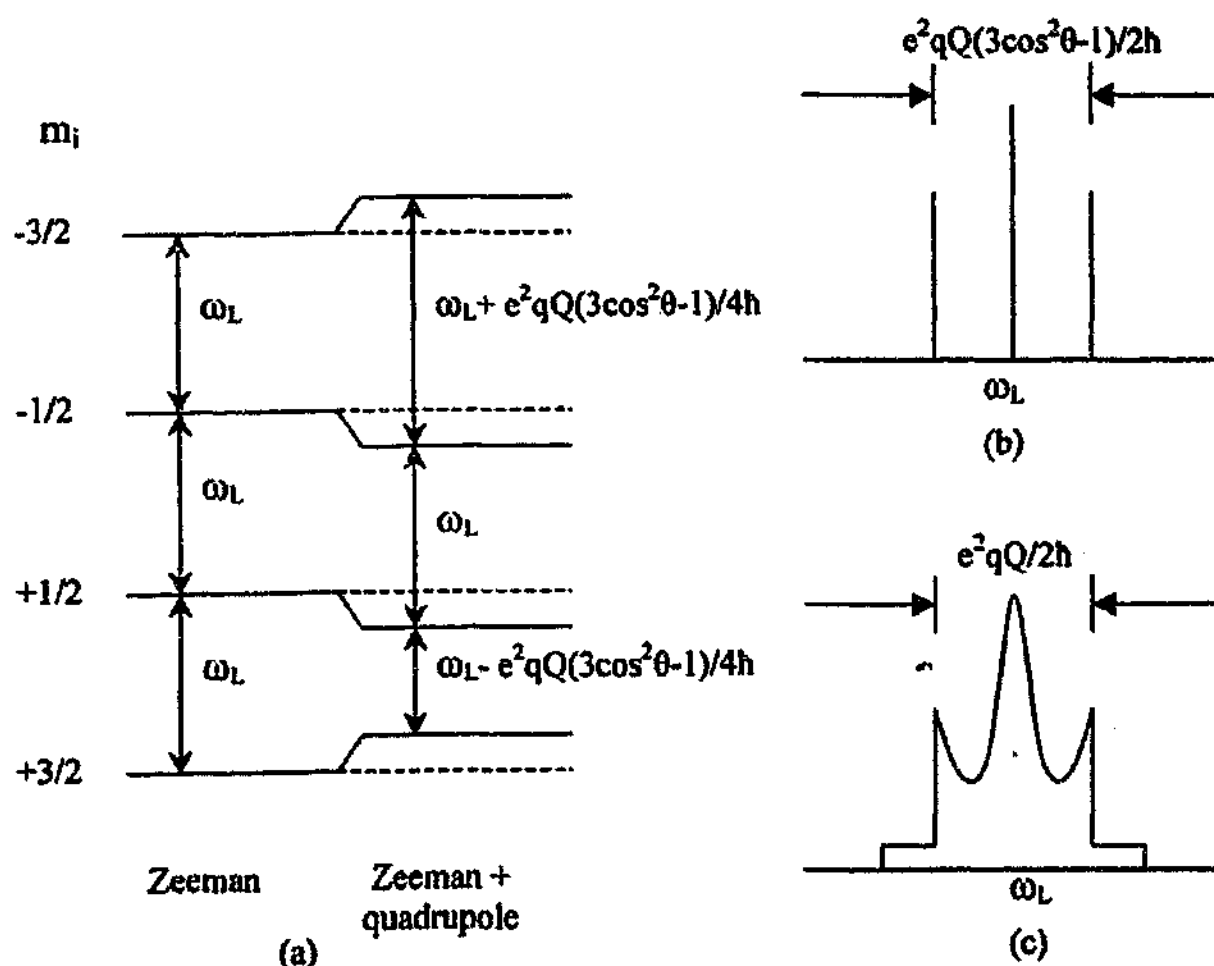
Equation 2.24

Figure 2.3 (a) Energy level splitting with quadrupolar shifts for I = 3/2. (b) Single crystal spectra. (c) Powder spectra.

2.1.5 Relaxation

As mentioned above, in the equilibrium state, there is a magnetization M_0 in the z direction and zero net magnetization in the x-y plane. When an appropriate radio frequency pulse is applied, the nuclei are perturbed from equilibrium. Once the perturbing pulse is removed,

the nuclear spin system returns to its original equilibrium condition. This process is called relaxation. Normally two relaxation measurements, spin-lattice relaxation and spin-spin relaxation, are widely used in NMR.

Spin-Lattice Relaxation

After a pulse has been applied at the x' axis to swing the magnetization 180° into the $-z'$ direction, M_z relaxes toward its equilibrium value by decaying to zero and then building up to M_0 with a time constant T_1. This is called spin-lattice relaxation. Since the inverted magnetization has higher energy than the equilibrium state, the return to equilibrium involves the exchange of energy with the surroundings. The spin-lattice relaxation is carried out using a 180°_x - τ -90°_x pulse sequence as shown in Figure 2.4 (A). The relaxation of M_z as function of τ is show in Figure 2.4 (C). The relationship is given by

$$M_z = M_o\left[1 - 2\exp\left(-\frac{\tau}{T_1}\right)\right]$$

Equation 2.25

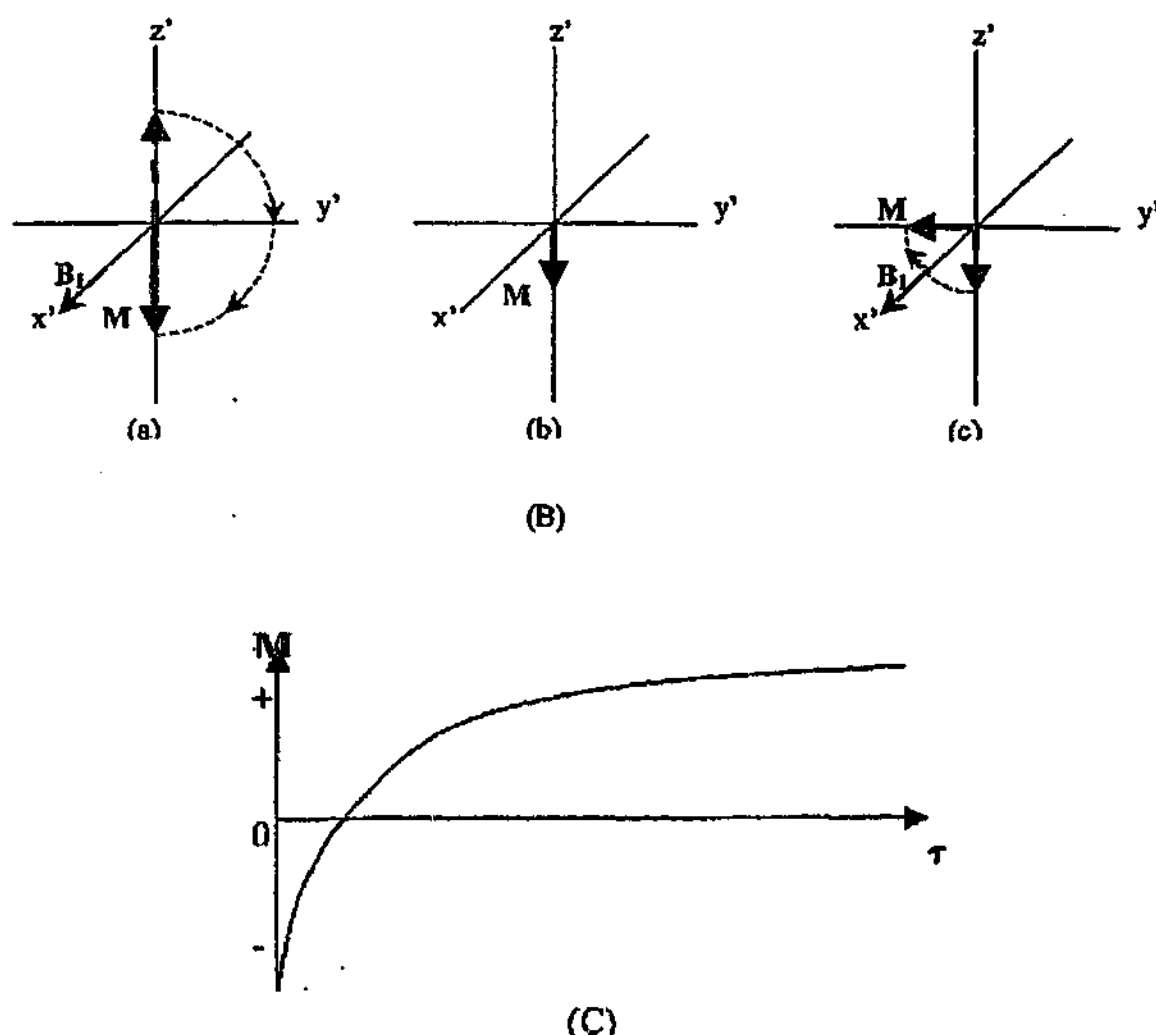By fitting the experimental values of M_z and τ to Equation 2.25, T_1 can be obtained.

(A)
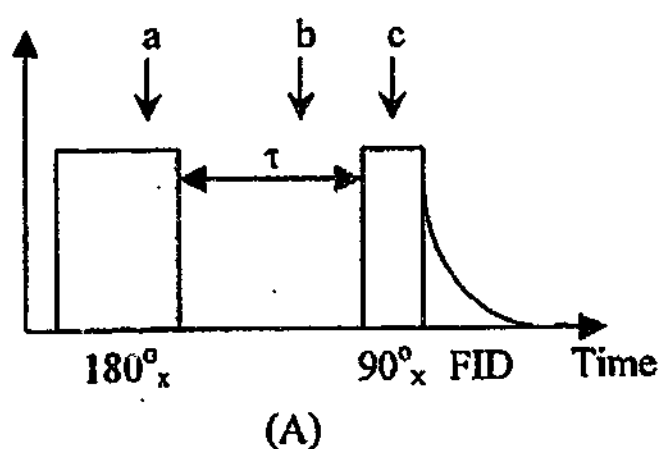
Figure 2.4 (A) A $180°_x - \tau - 90°_x$ pulse sequence. (B) (a) M is inverted to the $-z'$ direction by a $180°_x$ pulse. (b) M relaxes in the z' direction after a $180°$ pulse. (c) After time τ, M is rotated to the y' (or $-y'$) axis by a $90°_x$ pulse and the FID is recorded. (C) The amplitude of M as a function of τ. [245]

Spin-Spin Relaxation

If a $90°$ RF pulse is used to swing the magnetization into the x-y plane, M_z returns from zero to M_0 by spin-lattice relaxation. In the x-y plane, the transverse magnetization rotates at the Larmor frequency. Since each of the nuclei experiences a slightly different local magnetic field because of the inhomogeneity of the sample, their magnetizations precess at slightly different frequencies, which causes the overall magnetization in the x-y plane to decay gradually to zero, the equilibrium state. This decay process is called spin-spin

- 66 -

relaxation, characterized by time T_2. The process is related to the distribution of nuclear frequencies, and involves no energy change.

The spin-spin relaxation measurement is normally carried out by a $90°_x - \tau - 180°_x$ sequence with the FID observed at 2τ, as shown in Figure 2.5 (A). Since each M_i decays during time 2τ because of spin-spin relaxation, the refocused signal obtained at 2τ decays, as shown in Figure 2.5 (C). M as a function of 2τ is given as

$$M(2\tau) = M_0 \exp\left(-\frac{2\tau}{T_2}\right)$$

Equation 2.26

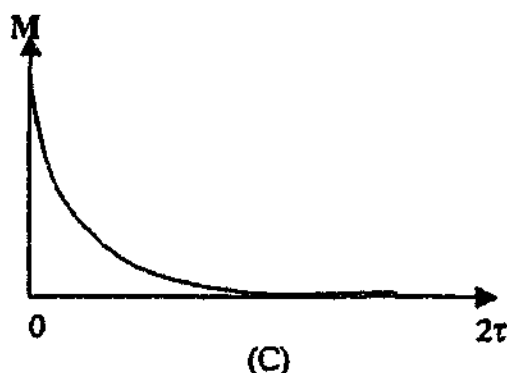By fitting the experimental values M and 2τ to Equation 2.26, T_2 can be obtained.

(A)

(B)

(C)
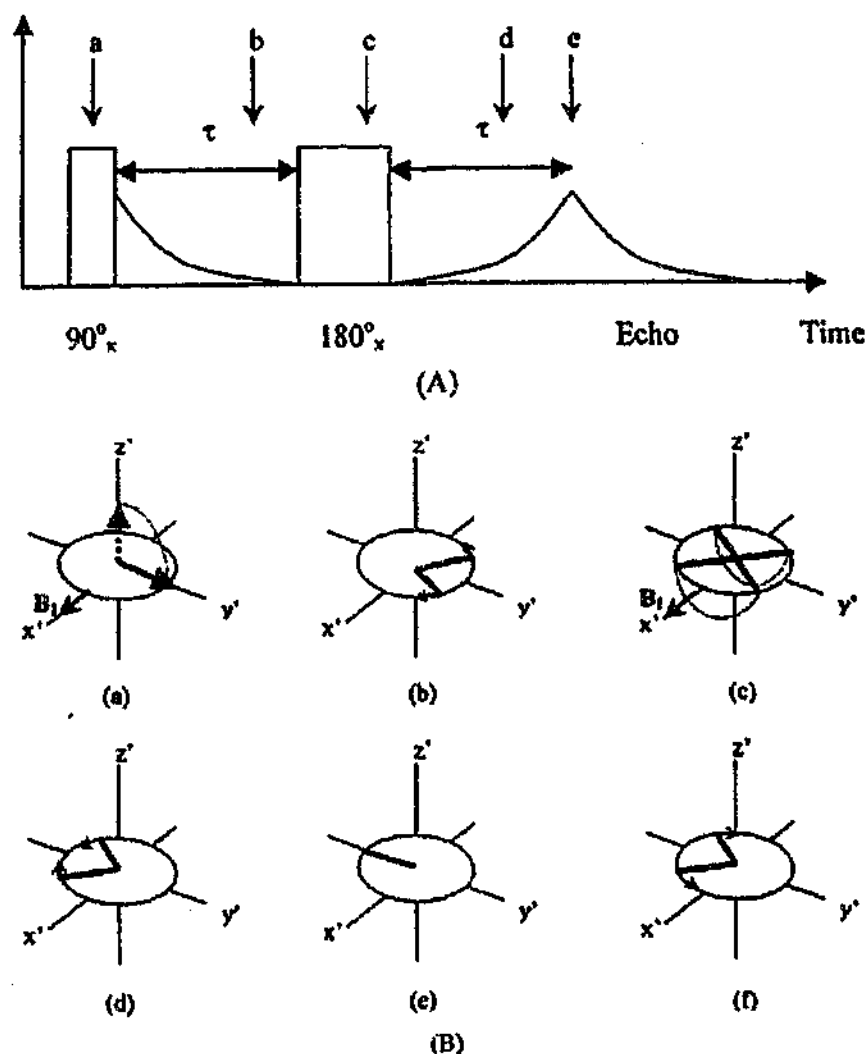
Figure 2.5 (A) A $90°_x - \tau -180°_x$ pulse sequence. (B) Hahn spin-echo experiment. (a) A $90°$ pulse causes M to tip to the y' axis. (b) The macroscopic magnetizations M_i in different parts of the sample dephase. Some precess faster and some precess slower than the rotating rate of the rotating frame. (c) A $180°$ pulse causes all M_i to rotate $180°$ about the x' axis. (d) M_i rephases. (e) All M_i refocus along the $-y'$ axis at 2τ. (f) M_i dephase again. (C) Intensity of FID as a function of 2τ [245].

Dipolar Relaxation Mechanism

For intramolecular dipole-dipole interactions between like nuclei, the T_1 and T_2 are given as

$$\frac{1}{T_1} = \left(\frac{\mu_o}{4\pi}\right)^2 \frac{2\gamma^4\hbar^2 I(I+1)}{5r^6}\{J(\omega_L) + 4J(2\omega_L)\}$$

Equation 2.27

$$\frac{1}{T_2} = \left(\frac{\mu_o}{4\pi}\right)^2 \frac{\gamma^4\hbar^2 I(I+1)}{5r^6}\{3J(0) + 5J(\omega_L) + 2J(2\omega_L)\}$$

Equation 2.28

where $J(\omega)$ are spectral density functions. For molecules reorientated between equivalent orientations or isotropic small-step rotational diffusion,

- 68 -

$$J(\omega) = \frac{\tau}{1 + \omega^2 \tau^2}$$

Equation 2.29

where τ is the correlation time, the time it takes to lose all the memory of its previous behavior. It is a temperature dependent parameter,

$$\tau = \tau_0 \exp(\frac{E_a}{RT})$$

Equation 2.30

The calculation of relaxation due to intermolecular dipole-dipole interactions is far more complicated. It can be simply given as

$$\left(\frac{1}{T_1}\right)_{obs} = C'\left(\frac{\tau}{1 + \omega_L^2 \tau^2} + \frac{4\tau}{1 + 4\omega_L^2 \tau^2}\right)$$

Equation 2.31

$C' > \frac{2}{3} M_{2,intra}$ indicates significant contribution from intermolecular interaction.

When the relaxation mechanism involves the dipole-dipole interactions between unlike nuclei I and S,

$$\frac{1}{T_1} = 2\left(\frac{\mu_o}{4\pi}\right)^2 \frac{\gamma_I^2 \gamma_S^2 \hbar^2 S(S+1)}{15r^6} \{J(\omega_I - \omega_S) + 3J(\omega_I) + 6J(\omega_I + \omega_S)\}$$

Equation 2.32

$$\frac{1}{T_2} = \left(\frac{\mu_o}{4\pi}\right)^2 \frac{\gamma_I^2 \gamma_S^2 \hbar S(S+1)}{15r^6} \{J(0) + J(\omega_I - \omega_S) + 3J(\omega_I) + 6J(\omega_S) + 6J(\omega_I + \omega_S)\}$$

Equation 2.33

where I represents the observed nuclei.

T_2 is related to Lorentzian linewidth Δv by

$$\Delta v = \frac{1}{\pi T_2}$$

Equation 2.34

If the magnetic field is not perfectly homogeneous, the linewidth is broadened to be

$$\Delta v_{obs} = \frac{1}{\pi T_2 *} = \frac{1}{\pi T_2} + \frac{\gamma \Delta B_0}{2\pi}$$

Equation 2.35

ΔB_0 is the inhomogeneity of the magnetic field.

Quadrupolar Relaxation Mechanism

When quadrupolar interaction dominates,

$$\frac{1}{T_1} = \frac{3}{40} \frac{2I+3}{I^2(2I-1)} \left(1 + \frac{\eta^2}{3}\right) \left(\frac{e^2 q Q}{\hbar}\right)^2 \{J(\omega_L) + 4J(2\omega_L)\}$$

Equation 2.36

Since $2I+1$ energy levels exist, different relaxation processes may occur at different energy levels, thus more than one T_1 may be obtained.

In conclusion, the NMR relaxation measurements provide more accurate methods to obtain the correlation time. The activation energy can be calculated by fitting the correlation times as a function of temperature.

2.2 Dielectric Response

Dielectric study has been used as a powerful method to investigate the rotational motion of plastic crystals [41, 45, 51, 64, 84, 105, 137, 144, 147, 252-257]. Restricted dielectric responses are obtained for molecules with frozen rotation. When dipolar molecules possess rotational freedom, they contribute to the dielectric response in the alternating electric field in both liquid and solid states. It has been found that some plastic crystals display dielectric constant values comparable to those of liquids [258].

2.2.1 Basic Concept

When an alternating electric field $E(\omega)$ is applied to a capacitor filled with a dielectric medium, the charges induced at the electrodes will be [259]:

$$Q = Q_0 + Q_m = D(\omega)$$

Equation 2.37

where D is dielectric induction; Q_0 is the charge induced in absence of any material medium; Q_m is the charge induced by the polarization of the material medium.

$$Q_0 = \varepsilon_0 E(\omega)$$

Equation 2.38

$$D(\omega) = \varepsilon_0 [1 + \chi^*(\omega)] E(\omega) = \varepsilon_0 \varepsilon^*_r(\omega) E(\omega) = \varepsilon^*(\omega) E(\omega)$$

Equation 2.39

where the asterix represents a complex quantity; ε_0 is the dielectric permittivity of free space, 8.854×10^{-12} Fm^{-1}; $\varepsilon^*(\omega)$ is the dielectric permittivity, $\varepsilon^*_r(\omega)$ is the relative dielectric permittivity or dielectric constant; $\chi^*(\omega)$ is the dielectric susceptibility, defining the polarization response of the material medium. $\chi^*(\omega)$ may also be written as [259]

$$\chi^*(\omega) = \chi'(\omega) - i\chi''(\omega)$$

Equation 2.40

The imaginary part $\chi''(\omega)$ is defined as dielectric loss.

For any material medium, several polarization mechanisms contribute to the dielectric response. Each mechanism is characterized by its special frequency. The overall dielectric response is shown as [259]

$$\varepsilon^*(\omega) = \varepsilon_0 \left[1 + \sum_a \chi^*(\omega) \right]$$

Equation 2.41

where "a" represents different polarization mechanisms.

2.2.2 Instantaneous Polarization

Among the mechanisms, the electronic polarization and ionic polarization are instantaneous high frequency responses, coming from the relative displacement of valence shell electrons with regards to the atomic nuclei and the relative displacements of positive and negative ions, with the response time of the order of 10^{-15}s and 10^{-13}s respectively [259]. Equation 2.41 can be written as [259]

$$\varepsilon^*(\omega) = \varepsilon_\infty + \varepsilon_0 \sum_{a \geq a_i} \left[\chi'_a(\omega) - i\chi''_a(\omega) \right]$$

Equation 2.42

where ε_∞ is the polarization response. These polarization responses are temperature insensitive and effective for all lower frequency responses [259].

2.2.3 Dipolar Response

Another contribution to the dielectric constant is the response of molecular dipole moments to the alternating electric field [259]. The classic dipole response is a Debye model, which

assumes a set of identical uncorrelated molecular dipoles free to rotate in a viscous medium. The susceptibility is given as [259]

$$\chi^*(\omega) = \chi(0)(\frac{1}{1+\omega^2\tau^2} - i\frac{\omega\tau}{1+\omega^2\tau^2})$$

Equation 2.43

where τ is the Debye relaxation time and is temperature dependent.

$$\tau(T) = \frac{1}{\omega_P} = \tau_0 \exp(\frac{W}{RT})$$

Equation 2.44

where ω_P is the loss peak frequency; W is the activation energy. The susceptibility of a Debye model is shown in Figure 2.6, which shows a symmetric dielectric loss on $\log\omega$ scale with a width at half height (λ_D) of 1.144 decades [259].
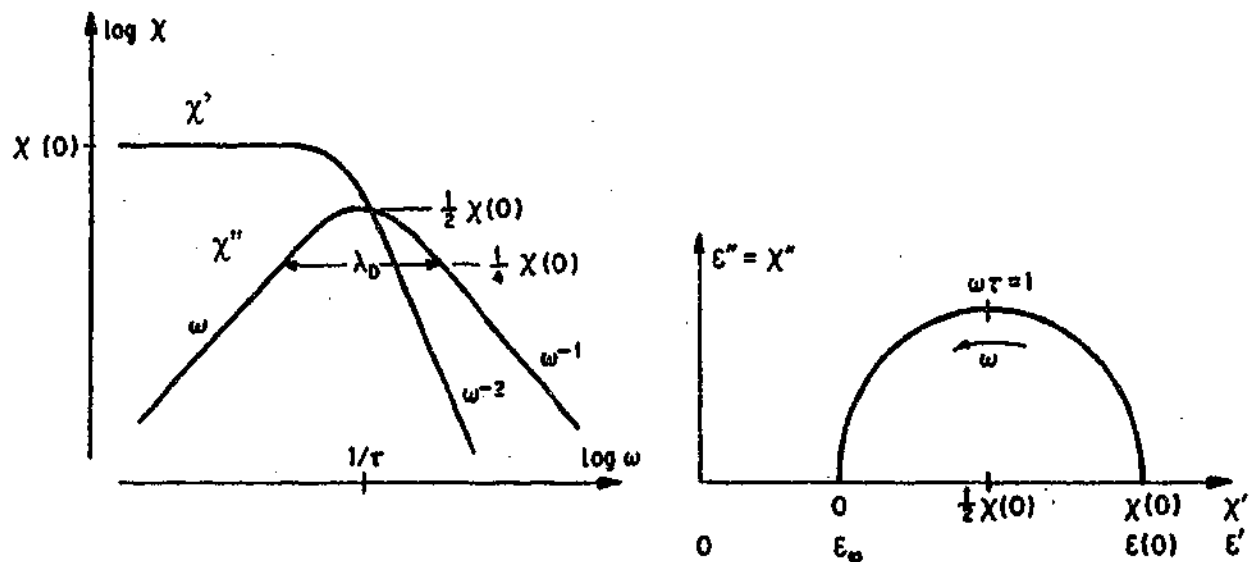

Figure 2.6 The Debye response. The left diagram indicates the frequency dependence of χ' and χ''. The right diagram shows the corresponding complex χ^* and complex ε^*. [259]

However, Debye response is found in rare cases, as many-body interactions are ignored in this model. The Debye model has been modified to give a Cole-Cole response (Equation 2.45) or a Davidson-Cole response (Equation 2.46) for real materials [259].

- 73 -

$$\chi^*(\omega) = \frac{\chi(0)}{1 + (i\omega\tau)^{1-k}}$$

Equation 2.45

$$\chi^*(\omega) = \frac{\chi(0)}{(1 + i\omega\tau)^{1-n}}$$

Equation 2.46

The corresponding susceptibility responses are shown in Figure 2.7 and Figure 2.8. A Cole-Cole response shows a symmetric but slightly broadened loss peak. This response is found in ferroelectrics [259]. A Cole-Davidson response shows an asymmetric loss peak on $\log\omega$ with broader width. Glasses, polymers and glassy crystals normally display Cole-Davidson responses, in the forms of α peaks or β peaks. α peaks are normally found above T_g. The peak frequency does not obey Arrhenius behavior. β peaks normally occur below T_g. Compared to α peaks, β peaks are broader and obey Arrhenius behavior [259]. The high frequency limit of both the Cole-Cole response and the Cole-Davidson response is of the form [259]:

$$\chi(\omega) \propto \left[\sin\left(\frac{n\pi}{2}\right) - i\cos\left(\frac{n\pi}{2}\right) \right] \omega^{n-1} \qquad n<1$$
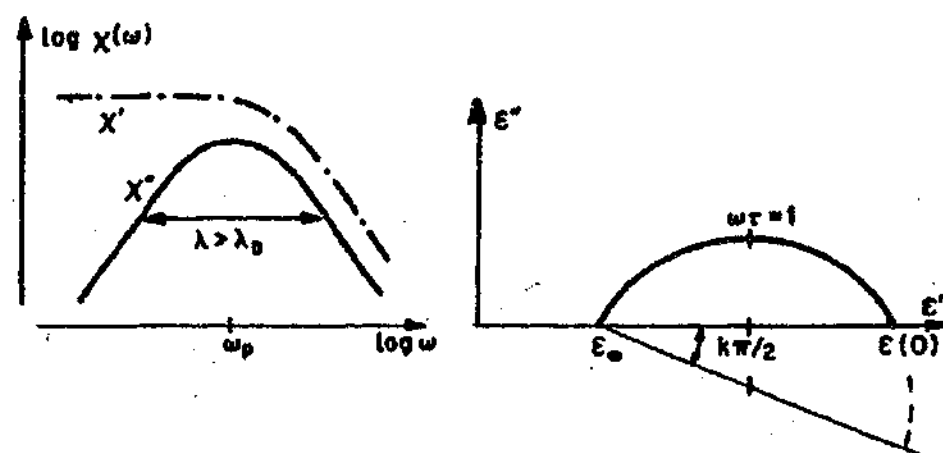
Equation 2.47

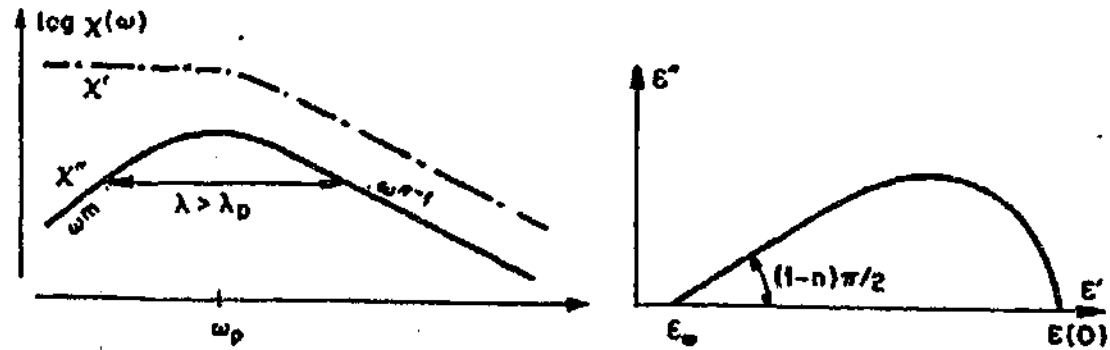**Figure 2.7 The Cole-Cole response [259].**

Figure 2.8 The Cole-Davidson response [259].

2.2.4 Charge Carrier's Response

The dielectric response is dominated by contribution from DC conductivity rather than dipole response, if mobile charge carriers, for example ions, electrons or polarons, present. The dielectric loss does not show a peak, but dispersions as a function of frequency obeying power law. It can be expressed as [259]

$$\chi''(\omega) \propto (\frac{\omega}{\omega_P})^{n_1 - 1} + (\frac{\omega}{\omega_P})^{n_2 - 1} \qquad n<1$$

Equation 2.48

where ω_P is the ion hopping rate. n is slightly temperature dependent and is normally in the range of 0.6-0.95. It is related to the degree of correlation between hopping ions [260]. When the dielectric response is dominated by the contribution from the lattice or matrix, n is close to unity. This normally occurs at low temperature or relatively high frequency and shows a frequency independent loss. The scheme of the corresponding susceptibility response is shown in Figure 2.9.

2.2.5 Universal Dielectric Response

Both Equation 2.47 and Equation 2.48 obey

$$\chi''(\omega) \propto \omega^{n-1} \qquad n<1$$

Equation 2.49

- 75 -

And

$$\frac{\chi''(\omega)}{\chi'(\omega)} = \cot(\frac{n\pi}{2})$$

Equation 2.50

Equation 2.49 and Equation 2.50 are the universal dielectric response, suitable for all structure forms, chemical bonds, polarizing species and different geometrical configurations [259, 261].
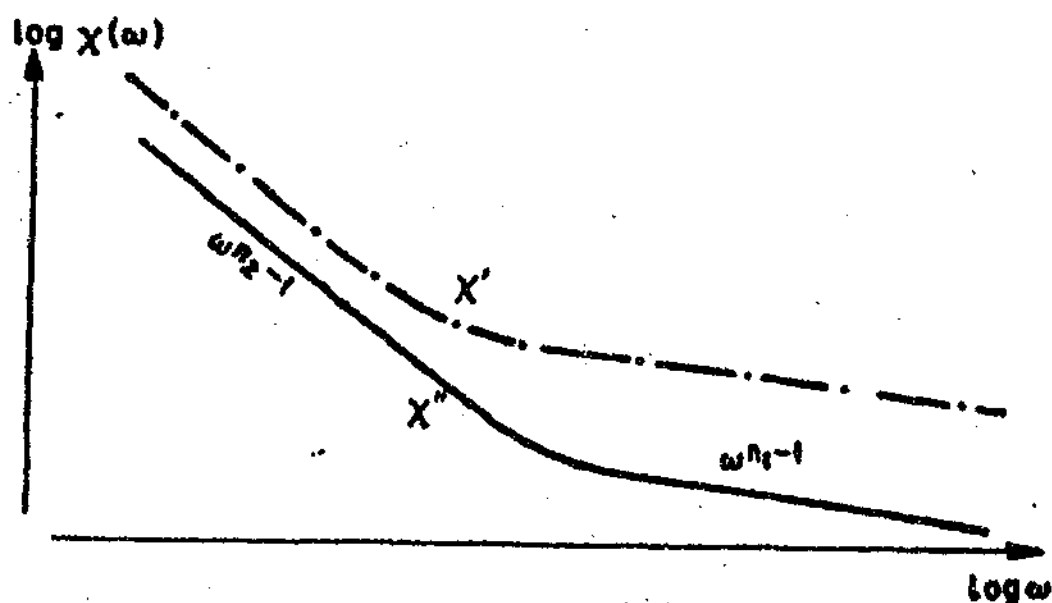

Figure 2.9   The scheme of the dielectric response for the systems where the dominant contribution to polarization comes from hopping charge carriers [259].

2.3   AC Conductivity

AC conductivity has employed in the studies of plastic crystals [262, 263]. In conducting solids, dielectric loss is related to AC conductivity $\sigma(\omega)$ by [264]

$$\chi''(\omega) \equiv \frac{\sigma(\omega)}{\varepsilon_0 \omega}$$

Equation 2.51

According to Equation 2.48 and Equation 2.51, $\sigma(\omega)$ is written as [264],

$$\sigma(\omega) = K\omega_p^{1-n_1}\omega^{n_1} + K\omega_p^{1-n_2}\omega^{n_2}$$

Equation 2.52

AC conductivity shows continuously increased conductivity as a power of frequency with the exponents of n_1 and n_2 in two frequency regions, respectively. High frequency power-law dispersion is essentially the dipolar response while low frequency dispersion is the respon of the translational motion of ions. The low frequency dispersion is related to the presence of impurities or crystal lattice imperfections or restricted ionic motion in one or two dimensions [264]. In the absence of imperfection or the ionic motion restriction, $n_1=0$. Equation 2.52 is then written as [264]

$$\sigma(\omega) = K\omega_p + K\omega_p^{1-n}\omega^n = \sigma(0) + A\omega^n$$

Equation 2.53

where $\sigma(0)$ is the DC conductivity. AC conductivity shows a frequency-independent plateau at low frequency dominated by DC conductivity and obeys the power law in the high frequency region [259]. DC conductivity is determined by the most restricted transport of charge carriers between the two electrodes while AC conductivity includes the easier local movement of charges.

The power law frequency dependence of the AC conductivity has been interpreted by different mechanisms which were reviewed by Vaysleyb et al. [254]. Among the theories, random free-energy barrier model and jump relaxation model propose the close relationship between DC conductivity and AC conductivity. In the latter model, the ion moves into an adjacent site which is less potentially favorable than the original site and tends to return to the original site. The new environment performs relaxation to accommodate the hopping ion. An unsuccessful accommodation results in forward-backward jumping and contributes to the AC response. The time constant of the relaxation process is roughly equal to the successful hopping. 1-n indicates the energy difference

between the two sites. n is proposed to increase as the temperature decreases or the Coulombic interaction decreases.

2.4 DC Conductivity

Based on the random walk theory, DC conductivity of a crystalline ionic conductor is given as [265]:

$$\sigma(0) = K\omega_P = \frac{Nq^2a^2\gamma c(1-c)\omega_P}{RT}$$

Equation 2.54

where γ is a geometrical factor; "a" is the jumping distance and "q" is the ionic charge; "c" is the concentration of mobile ions on N equivalent lattice sites per unit volume,

$$c = c_e \exp\left(-\frac{E_c}{RT}\right)$$

Equation 2.55

where c_e is the effective infinite temperature charge carrier concentration. Concentration c may or may not depend on temperature. E_c is the activation energy of creation of mobile charge carriers for the former case.

Hopping rate is thermally activated and is given by [265]:

$$\omega_P = \omega_o \exp\left(-\frac{\Delta G_a}{RT}\right) = \omega_o \exp\left(\frac{\Delta S_a}{R}\right)\exp\left(-\frac{E_a}{R}\right) = \omega_e \exp\left(-\frac{E_a}{R}\right)$$

Equation 2.56

where ΔG_a, ΔS_a and E_a are the free energy, entropy and activation energy of the hopping process, respectively; ω_o is the vibrational frequency of the ions; ω_e is the effective attempt frequency.

The contributions of jump frequency and the number of charge carriers to conductivity can be separated [260, 264, 265]. According to Equation 2.53, $\sigma(0)$, n and A can be obtained by fitting the AC conductivity. The jump frequency can then be obtained by

$$\omega_P = \left(\frac{\sigma(0)}{A}\right)^{\frac{1}{n}}$$

Equation 2.57

Combining Equation 2.54 and Equation 2.57, the contribution from the charge carrier number can be estimated.

Recently, Vaysleyb et al. have suggested that Equation 2.53 should be in the form of [266]

$$\sigma(\omega) = \sigma(0) + A\omega_n = K\omega_m + K\omega_m\omega_r^{-n}\omega^n$$

Equation 2.58

where ω_m is the ionic hopping frequency, ω_r is related to AC relaxation time. ω_m and ω_r are different conceptions. Only when $\omega_m = \omega_r$, the AC conductivity is in the form of Equation 2.53 and the frequency obtained from Equation 2.57 is the ionic hopping frequency. Otherwise, the frequency obtained from Equation 2.57 is ω_r rather than the ionic hopping rate ω_m.

2.5 Equivalent circuit

When an alternating voltage is applied to a cell consisting of an electrolyte between blocking electrodes, the alternating current measured is composed of the contributions from the localized dipolar response and polarization response of the electrolyte, the ionic transport through the electrolyte (DC conductivity) and the electrolyte/electrode interface response. An ideal equivalent circuit is represented in Figure 2.10. The corresponding Cole-Cole impedance plot is a standard semicircle with a vertical spike [17].
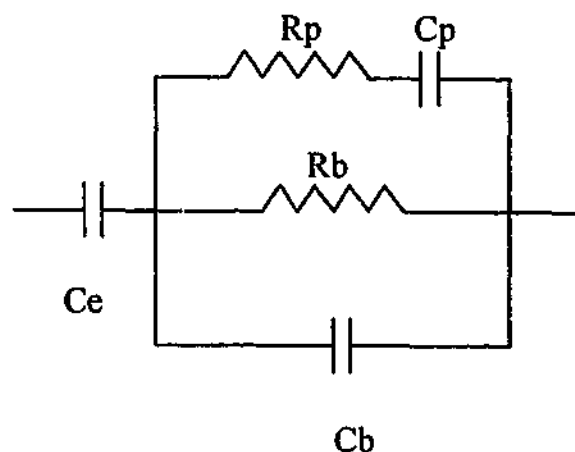
Figure 2.10 Equivalent circuit of ideal cell. Ce represents electrode capacitance. Cb represents electrolyte capacitance. Rb indicates electrolyte resistance. Cp and Rp represent dipolar and polarization responses.

In real experiment, the equivalent circuit could be more complicated due to the possibilities of non-blocking electrodes, adsorption occurring on the electrodes, the interfacial layer formed between the electrolyte and the electrode, inhomogeneous electrolyte which is composed of different microscopic regions and grain boundaries, several dielectric relaxation processes and the distribution of the dielectric relaxation time [17]. All these result in a distorted and tilted Cole-Cole impedance plot. The equivalent circuit of each of these un-ideal states has been reviewed [267]. The effects of a series of inhomogeneous polymer - ceramic composite electrolytes have been studied [268].

2.6 Positron Annihilation Lifetime Spectroscopy (PALS)

Vacancy diffusion has been studied by radiotracer technique [269, 270], isotope-effect method [271-273], positron annihilation techniques [157, 274, 275], NMR [276-278], molecular dynamics simulation [279] and plastic deformation [158]. Among these techniques, positron annihilation lifetime spectroscopy (PALS) is a very useful tool for studying defects. It can provide information about the size and concentration of defects.

- 80 -

2.6.1 Basic Concept

Theoretically, when energetic positrons are injected into a condensed medium from a radio source, they are slowed to their thermal velocities in a short time scale of 1 ps by inelastic scattering with the atoms of the medium. A positron and an electron with an anti-parallel spin undergo annihilation by the emission of two γ-quanta of 0.51 MeV energy at 180° to each other. When the annihilation particles have parallel spins, three-photon emission is allowed. Since a positron is repelled by the surrounding atoms, it may be trapped in defects where the electron densities are low. This results in a longer lifetime compared to the bulk value. By measuring the lifetime and the fraction of the trapped positrons, the information about the size and concentration of the defects can be obtained [275].

A fraction of the injected positrons could also form a positron-electron bound state, named positronium (Ps) before annihilation under the condition:

EB>EA+PA

Equation 2.59

where EB is the positronium binding energy; EA and PA are the affinities to the molecules of the medium for the electron and the positron, respectively. The defects or the loosening of the microstructure help to reduce the interaction between Ps and the surrounding molecules, increasing the positronium binding energy and initiating the positronium formation [275].

Positronium exists in two states: the short-lived para state p-Ps (spin anti-parallel) and the long-lived ortho state o-Ps (spin parallel). A free p-Ps decays by 2γ annihilation with a lifetime of 0.125 ns and is not an effective probe of microstructure. A free o-Ps undergoes 3γ annihilation with lifetime of 140 ns. The theoretical ratio of the numbers of o-Ps to p-Ps is 3:1 [275]. Since the lifetime of a p-Ps is too short on the time scale of an instrument, o-Ps is normally used as a probe in the study.

In condensed materials, the annihilation of o-Ps could occur by overlap of the wave function of the positron in the o-Ps with the wave function of the electron having opposite

spin in the medium with emission of two γ-quanta. This is known as "pick off" annihilation, which dominates the decay of the o-Ps and reduces the o-Ps lifetime to 1-10 ns. In analogy to the annihilation of positrons, the o-Ps lifetime is related to the surrounding electron density and therefore provides information about the defects and structure of the medium [275].

2.6.2 Measurement of Positron Lifetime

The radioactive isotope ^{22}Na is used as the low energy positron source. ^{22}Na decays to the excited state of ^{22}Ne with the emission of a positron. After 3 ps, the excited state of ^{22}Ne becomes de-excited with the emission of a 1.28 MeV photon. The emission of the positron and the 1.28MeV photon can be seen as occurring simultaneously on the time scale of the experiment. The positron then annihilates with the emission of 0.51 MeV photon. The time interval between the detection of the 1.28 MeV photon and the 0.51 MeV photon is the positron lifetime.

The time interval can be recorded by a multi-channel analyzer. The channel number is proportional to the lifetime [37]. Assuming spherical potential wells with the radius of Ro corresponding to vacancies with the radius of R, the average vacancy radius R (Å) can be estimated from the lifetime τ (ns) by [274, 280]:

$$2\left[1 - \frac{R}{Ro} + \frac{1}{2\pi}\sin(\frac{2R\pi}{Ro})\right] = \frac{1}{\tau}$$

Equation 2.60

where Ro= R+1.66 Å. The volume of this vacancy is estimated to be [280]:

$V(\tau)=4\pi R^3/3$

Equation 2.61

The number in each channel is the number of the positrons which have lived for a certain time [37]. As mentioned above, the positrons decay at different rates due to different

annihilation mechanisms. Therefore the measured signal is composed of several components:

$$I(t) = \sum_i^n I_i \exp(-\lambda_i t)$$

Equation 2.62

where I_i represents the number of positrons annihilating at the rate of λ_i. λ is related to the lifetime τ by

$\lambda_i = 1/\tau_i$

Equation 2.63

For plastic crystals, three components are normally expected [37, 157, 275]. They are the responses of p-Ps, free positron and o-Ps, respectively. O-Ps give the long lifetime response. The long lifetime response could be deconvoluted into two components, corresponding to the bulk o-Ps and the defect trapped o-Ps respectively. The characteristic lifetimes for these components are [275]:

p-Ps	$\tau_1 = 0.125$ ns
Free positron	$\tau_2 = 0.3\text{-}0.4$ ns
o-Ps pick off (bulk)	$\tau_3 = 1\text{-}1.8$ ns
o-Ps pick off (defect)	$\tau_4 = 1\text{-}3$ ns

2.6.3 Trapping Model

The trapping model was developed from the model for trapped positrons in the defects in metals [281]. This model has been applied to plastic crystals [37, 275]. Trapping model assumes that the positroniums can either annihilate in the bulk state or transfer from the

- 83 -

bulk state to the trapped state and then annihilate. The lifetimes and intensities of the positroniums in these two states are given as [37, 275]:

$$\tau_b = \frac{1}{\lambda_b + K}$$

Equation 2.64

$$\tau_t = \frac{1}{\lambda_t}$$

Equation 2.65

$$I_b = I_{o-Ps} \frac{\lambda_b - \lambda_t}{\lambda_b - \lambda_t + K}$$

Equation 2.66

$$I_t = I_{o-Ps} \frac{K}{\lambda_b - \lambda_t + K}$$

Equation 2.67

where λ, τ and I are annihilation rate, lifetime and intensity, respectively. Subscripts "b" and "t" represent the bulk state and the trapped state respectively. K is the trapping rate. K is related to defects by [37, 275]

$$K = \mu_v C_v$$

Equation 2.68

where μ_v is the specific trapping rate, assumed to be a temperature and vacancy independent constant. C_v is the defect concentration. When the vacancies are the dominant defects [153],

$$C_v = C_o \exp(-\frac{E_v}{RT})$$

Equation 2.69

- 84 -

where E_v is the activation energy of vacancy formation. According to Equation 2.67, Equation 2.68 and Equation 2.69, I_t is proportional to the vacancy concentration. By determining I_t as a function of temperature, E_v can be obtained. A relative fraction of the free-volume (Fr) can also estimated by knowing the average volume of vacancies $V(\tau)$ and the intensity I. A semiempirical equation is given as [280]:

$$Fr = V(\tau)I = 4\pi R^3 I/3$$

Equation 2.70

2.7 Vacancy Measurement by Density and Heat Capacity

When the crystal lattice structure of a material is known, the density in its perfectly defect-free condition (ρ_x, known as the x-ray density) can be calculated. However, when defects are present, the real density (ρ, known as bulk density) deviates from the x-ray density ρ_x. Vacancies result in a smaller bulk density value than x-ray density while interstitials result in a larger bulk density [160]. The defect concentration can thus be estimated by comparing the difference between the bulk density and the x-ray density [160]:

$$C_v = \left| \frac{\rho_x - \rho}{\rho_x} \right|$$

Equation 2.71

where C_v is the vacancy concentration when the value of $(\rho_x - \rho)/\rho_x$ is positive or the interstitial concentration when the value of $(\rho_x - \rho)/\rho_x$ is negative; ρ_x and ρ are the x-ray density and bulk density, respectively.

Vacancies and interstitials both make positive contribution to the heat capacity. The defect formation energy can be obtained from heat capacity by [154]

$$Cp - Cp_0 = \frac{n_v E_v^2}{RT^2}$$

Equation 2.72

where Cp and Cp$_0$ are the specific heats of the real sample and the defect-free sample, respectively; n$_v$ is the number of vacancies or interstitials; E$_v$ is the vacancy formation energy. Cp$_0$ can be obtained either by extrapolating the Cp at low temperature when the defect-free condition is assumed to high temperature or by calculating the contribution from lattice vibration and molecular rotation [154].

2.8   Experimental Method

2.8.1   Sample Preparation

The synthesis of N, N-methyl, alkyl pyrrolidinium bis(trifluoromethanesulfonyl)amide (P1xTFSA) is summarized in the following scheme:
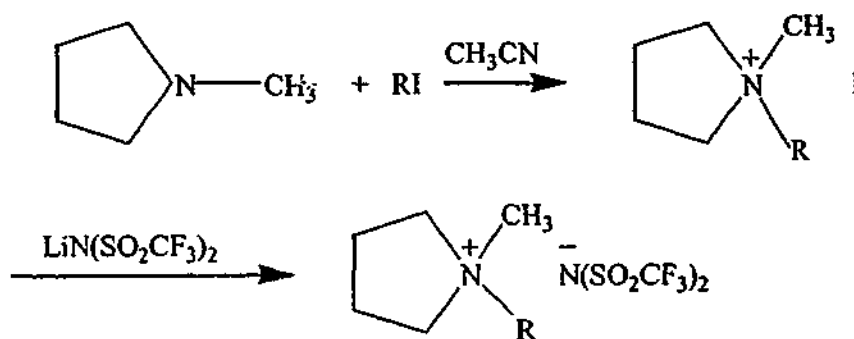
P1xI

10 g methyl pyrrolidine (Aldrich Chemical Co., Inc) was mixed with about 20 g CH$_3$CN in a three neck flask. The mixture was stirred in an ice bath. Slight excess of ethyl iodide or methyl iodide (Aldrich) was added at 10 ml per 10 minutes. Reactions were carried out by stirring in the ice bath for about 20 hours. CH$_3$CN was then removed by rotating evaporation. A pale yellow powder was obtained. The powder was washed with hexane, then filtered and stored under vacuum. The yielding was >90%.

P1xTFSA

The dry P1xI powder was mixed with a slight excess of lithium bis(trifluoromethane sulfonyl)amide (LiTFSA) (3M Specialty Chemicals Division, USA) in distilled water and was stirred for about 2 hours. White precipitate was obtained. The precipitate was

collected by filtering and washed with distilled water. It was filtered again and dried under vacuum for at least three days before experiments. The yielding was >90%.

P1xTFSA-LiTFSA

A chosen amount (between 0.5 and 50 mol%) of LiTFSA was mixed with P1xTFSA to obtain a series of P1xTFSA-LiTFSA mixtures (all compositions are expressed as mol%). The mixtures were stirred at 100 °C (for P12TFSA-LiTFSA) or 140 °C (for P11TFSA-LiTFSA) for two hours. Clear liquids were observed for all the samples. The mixtures were then allowed to cool to room temperature. The samples had the appearance of a waxy solid. All the samples were dried under vacuum at room temperature for at least three days before experiments.

2.8.2 Differential Scanning Calorimetry (DSC)

The thermal properties were studied using a Perkin-Elmer Model 7 Differential Scanning Calorimeter. About 10 mg samples were sealed in aluminum pans and were heated at a rate of 20 °Cmin⁻¹. The thermal behaviors from –120 °C to 250 °C were obtained by measuring the samples over three smaller temperature ranges, from –120 °C to 20 °C, from –50 °C to 50 °C and from 20 °C to 250 °C. The temperature was calibrated using cyclohexane (solid-solid transition temperature -87.06 °C, m.p. 6.54 °C), decane (m.p. – 29.66 °C), p-nitrotoluene (m.p. 51.64 °C) and indium (m.p. 156.60 °C).

The solid phase right below the melting point is represented as phase I. The solid phase at lower temperature is represented as phase II, and so on.

2.8.3 Conductivity and Dielectric Measurements

Conductance measurements were carried out in locally designed multi-sample conductance cells. The details of the cell were given in a thesis from the same group and are summarized here [282]. The cell body was made from a block of aluminum. Cylindrical sample compartments with highly polished stainless steel walls were machined in the aluminum block. The scheme of the conductance cell is shown in Figure 2.11. The inner and outer stainless steel walls serve as two blocking electrodes. The inner diameter of the

cylindrical compartment is 9.6 mm. The thickness and the length of the cell are 0.2 mm and about 24.4 mm, respectively.
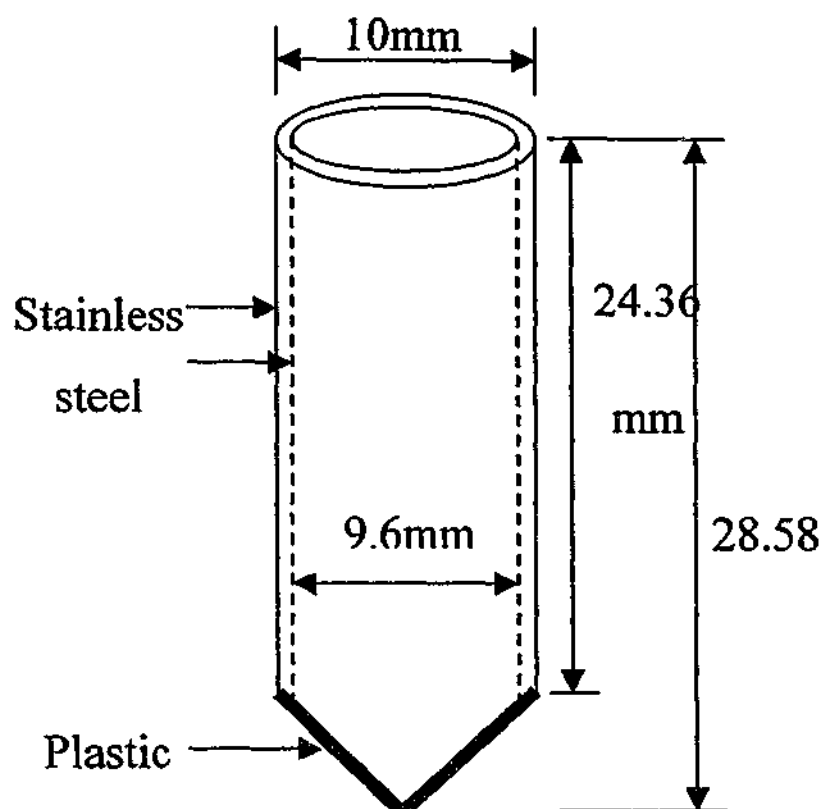

Figure 2.11 The scheme of the conductance cell.

The temperature was measured by a type-T thermocouple probe located in the aluminum block close to the sample compartment. During the measurement, the cell was cooled using liquid nitrogen and heated by a heater located within the aluminum block under the control of a Shimaden Digital FP21 Temperature controller. The temperature was ramped up at a steady rate of 0.2 °Cmin^{-1} in all the temperature dependence experiments.

The cell constant, b, of each compartment was obtained by determining the capacitance of the empty cell as function of frequency before and after each sample measurement. Cell constants were calculated via:

$b = \varepsilon_0/C_0$

Equation 2.73

where ε_0 is the permittivity of free space and C_0 is the empty cell capacitance. The cell constants measured were about 0.0025 cm^{-1}, which coincides with the value of 2.67×10^{-3} cm^{-1} calculated from the cell dimensions.

Conductivity was obtained by measuring the admittance Y* (Y, θ) in the frequency range from 20 Hz to 1 MHz using a HP 4284A Impedance Meter. The impedance Z* and dielectric constant ε_r* were derived from Y* by

$$Y^* = \frac{1}{Z^*} = j\omega C_0 \varepsilon_r{}^*$$

Equation 2.74

where C_0 is the vacuum capacitance of a cell and ω is the frequency. The Cole-Cole plots of the impedance data were relatively classic semicircles with electrode spikes in most cases. The real axis touchdown point in the Cole-Cole plot was taken as the resistance. The reliability of the real axis value of the touchdown point as the resistance was tested by fitting the data with the LEVM Complex Nonlinear Least Squares (CNLS) Immittance Fitting Program [283]. A simple equivalent circuit, as shown in Figure 2.12 was used in the fitting.

Two examples of the fitted Cole-Cole plots at two different temperatures are shown in Figure 2.13. The fitted parameters and the Z' values of the touchdown points are listed in Table 2.1. The resistances obtained from the touchdown points and from the curve fitting are 5.7×10^5 Ω and 5.1×10^5 Ω respectively at -38 °C or 3.9×10^4 Ω and 3.3×10^4 Ω respectively at 53 °C. The values obtained from the touchdown points are very close to the values obtained from the curve fitting, indicating the reliability of using the Z' values of the touchdown points. Therefore, the Z' value of the touchdown point was used as the resistance in this study. The resistances were then converted to conductivities using the cell constant values.
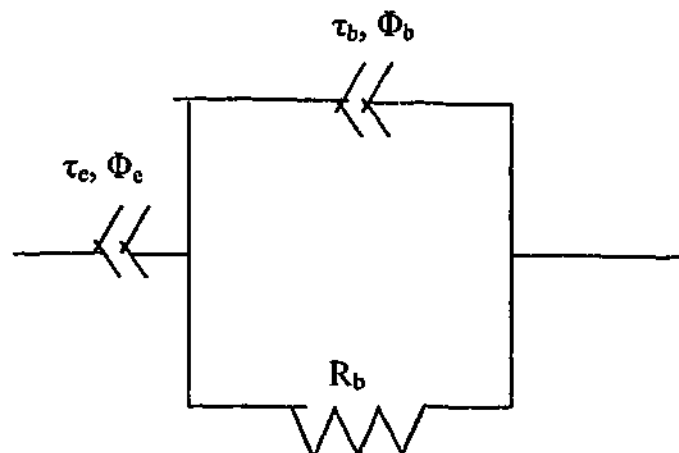
Figure 2.12 The scheme of the equivalent circuit. << is the constant phase element (CPE), represented by parameters τ and Φ. τ is a frequency-dependent capacitance. Φ is a measure of the frequency dependence. When $\Phi=1$, CPE acts like a pure capacitor. The CPE produces an impedance having a constant phase angle $(\pi/2)^*\Phi$ in the complex plane [283]. τ_e and Φ_e are the parameters characterizing the CPE representing the electrodes. τ_b and Φ_b are the parameters characterizing the CPE representing the electrolyte. R_b is the resistance of the electrolyte.
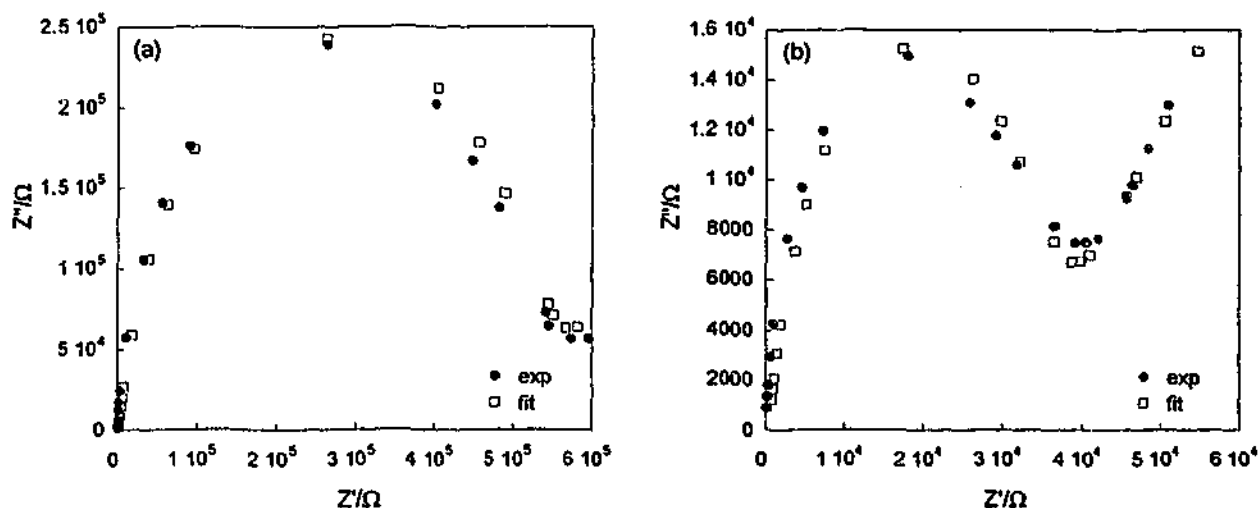

Figure 2.13 The experimental data (the circles) and the fitted data (the squares) of the Cole-Cole impedance plots for P12TFSA at (a) –38 °C and (b) 53 °C.

- 90 -

Table 2.1 The values of fitted parameters and the Z' values of the touchdown points in Figure 2.13.

Parameters	-38 °C		53 °C	
	Curve Fitting	Z' (touchdown)	Curve Fitting	Z' (touchdown)
τ_c (F)	1.4×10^{-6} ($\pm 17.8\%$)		4.6×10^{-6} ($\pm 13.7\%$)	
Φ_c	0.38 ($\pm 14.4\%$)		0.38 ($\pm 9.3\%$)	
R_b (Ω)	5.1×10^5 ($\pm 3.0\%$)	5.7×10^5	3.3×10^4 ($\pm 6.2\%$)	3.9×10^4
τ_b (F)	2.9×10^{-10} ($\pm 13.8\%$)		8.9×10^{-10} ($\pm 46.5\%$)	
Φ_b	0.94 ($\pm 1.8\%$)		0.89 ($\pm 4.6\%$)	

2.8.4 Nuclear Magnetic Resonance Spectroscopy (NMR)

^{7}Li NMR was performed on a Bruker AM-300 pulse NMR spectrometer operating at a Larmor frequency of 116.6 MHz. The 90° and 180° pulse lengths were 5.3 μs and 10.6 μs respectively. The 90°-τ-180° and the 90°-τ-90° pulse sequences were both used for the linewidth measurements. The τ was 20 μs in all cases. Both pulse sequences gave similar central peak responses although the 90°-τ-90° pulse sequences also clearly showed the quadrupolar peaks at low temperatures. Only the central transition is considered in this work. A 180°-τ-90° pulse sequence was employed for the spin-lattice relaxation measurements. A 90°-τ-180° pulse sequence was used for the spin-spin relaxation experiments. The range of τ for the relaxation measurements varied according to the values of T_1 and T_2 at different temperatures. Relaxation delays varied from 50 s at about − 100 °C to 5 s at 100 °C, dependent on T_1. Spectra were typically accumulated for 16 scans at −100 °C and 4 scans at 100 °C.

^{1}H NMR experiments were carried out on a Bruker AM-300 pulse NMR spectrometer at 300 MHz. The 90° and 180° pulse lengths were 9.0 μs and 18.0 μs respectively. The 90°-τ-180° pulse sequence was used for the linewidth measurement. The length of τ was 50 μs. The 90°-τ-180° and 180°-τ-90° pulse sequences were used for the spin-spin relaxation and

spin-lattice relaxation measurements respectively. The ranges of τ in these relaxation experiments varied from temperature to temperature. The relaxation delays were also temperature dependent (actually T_1 dependent), about 10 s at $-100\ ^{\circ}C$ and 5 s at $100\ ^{\circ}C$. The number of scans varied from 16 at $-100\ ^{\circ}C$ to 4 at $100\ ^{\circ}C$.

^{19}F NMR was conducted on a Varian Unity Plux 300 NMR spectrometer by magic angle supersonic spinning solid NMR probe DSI-V139 (Doty Scientific Inc, U. S. A.) operating at 282.2 MHz. Signals were acquired 10 µs after a single pulse 2.6 µs in length (90°) and accumulated for 16 scans. The relaxation delay was 10 s in all cases. There was interference from F in the Teflon in the probe on the ^{19}F NMR spectra. The interference was present as a peak at about -7 kHz in the spectra. As the signals from the samples all appeared in the higher field, the inference from the background could be carefully eliminated during the analyses.

All the samples were sealed in glass tubes about 2 cm long and 5 mm in diameter under dry condition. The temperature was controlled by balancing the heating rate and the flow rate of gas from liquid nitrogen or air. Methanol and 1, 2-ethanediol were used to calibrate the thermocouples below and above room temperature respectively. The real temperature was calculated from the chemical shift difference between the OH proton and the protons on the CH_3 or CH_2 group [284]. A peak simulation program package (Mac FID) was used to analyze the data.

2.8.5 Mechanical Thermal Analysis (MTA)

MTA was conducted on Perkin Elmer Dynamic Mechanical Analyzer DMA 7 and Thermal Analysis Controller TAC 7/DX. A Pyris Manager Program was used to control the experiments and analyze the data. Indium (m.p. 156.6 $^{\circ}C$) and octane (m.p. -56.76 $^{\circ}C$) were used for temperature calibration. The samples P12TFSA and P11TFSA were first heated in aluminum pans (0219-0041, Perkin Elmer) until melting. The samples were then naturally cooled down to room temperature. Each sample was about 6mm in diameter and 1mm in thickness. All the samples were prepared in dry condition at least two days before the experiments. During the experiments, the samples were held on a flat plate. The force

was pressed on the samples through a probe. The area of the probe tip is 0.78 mm^2. The MTA measurements were carried out in the isothermal state and by ramping the temperature.

Ramping temperature

P11TFSA was cooled at −100 °C for 10 minutes by liquid nitrogen and was heated to 130 °C at a heating rate of 5 °Cmin^{-1}. The static force was 10 mN. The dynamic force was 1 mN with frequency of 1.0 Hz. P12TFSA was cooled at −120 °C for 10 minutes and then was heated to 90 °C at a rate of 5 °Cmin^{-1}. The static force was 5 mN. The dynamic force was 2 mN with frequency of 1.0 Hz.

Isothermal experiment

The samples were held at a constant temperature for at least 15 minutes before the isothermal experiments. The force changed from 1 mN to 2000 mN at the rate of 50 mNmin^{-1}.

2.8.6 Positron Annihilation Lifetime Spectroscopy (PALS)

The experiemtns were performed with an automated EG&G Ortec fast-fast coincidence system. Two identical samples were placed on either side of a ^{22}NaCl/mylar source and the sample-source sandwich was placed in a dry nitrogen atmosphere inside a temperature-controlled chamber. Only the component of the orthoPositronium pickoff annihilation characteristics (τ_3, I_3) were measured. A source correction was used based on the oPs source component for control samples of annealed aluminum. Data points represent the average of one to five spectra.

2.8.7 Scanning Electron Microscopy (SEM)

Ambient temperature scanning electron microscopy was performed on the as-grown P12TFSA or P11TFSA powder with a Philips XL30 Field Emission Gun (FEG) SEM. Samples were transferred into the microscope observation chamber through a Polaron LT7400 cryoprep stage and placed under a vacuum of at least 3.7×10^{-6} mbar. The complete

dryness of the samples meant that sublimation under high vacuum was not a problem. Images were acquired with a secondary detector to reveal detailed surface topography. A low accelerating voltage of 2.0 kV was used to minimize sample charging and damage. Gold sputtering was not required as evidenced by the adequate spatial resolution attained.

2.8.8 Density Measurement

The densities of P12TFSA and P11TFSA powders were measured by Accupyc 1330 Pycnometer at room temperature. Before measuring the samples, the pycnometer was calibrated with a ball whose weight and volume are known. During the experiment, about 1.5 g of the powder samples were put in a metal cup in the pycnometer chamber. Nitrogen was purged into and then released from the chamber. The pressures were read when stable states were reached after purging or releasing the nitrogen. The sample volumes can then be calculated. Each sample was measured 15 times. The samples were accurately weighed before and after the volume measurements.

Chapter 3   N-methyl-N-ethylpyrrolidinium bis(trifluoromethanesulfonyl)amide Salt

3.1   Introduction

Several families of salts, based on: N-alkyl-N-methylpyrrolidinium (P1x)* [32, 235], 1-alkyl-2-methylpyrrolinium (MPx)* [166] and N-alkyl-N-methylimidazolium (Im1x)* [285] cations, have been synthesized in our group. The anions used are bis(trifluoromethanesulfonyl)amide (TFSA$^-$) [32, 235], BF$_4^-$ [239, 286], PF$_6^-$ [238], OH$^-$ [166, 236, 237], dicyanamide (DCA) and halide ions[33, 238].   Some of the salts are molten at room temperature. Highest conductivity has been found to be 2×10^{-3} Scm^{-1} at 25 °C [235].

A number of these salts exhibit plastic crystal behaviors: they are waxy, with one or more solid-solid phase transitions and low fusion entropy. The plastic crystal phases normally exhibit significant conductivity. For example, MP2TFSA has the richest solid-solid phase transitions and lowest fusion entropy in the MPxTFSA family. It exhibits conductivity of 10^{-4} Scm^{-1} at 25 °C in the solid state, higher than the rest of MPxTFSA salts [166]. In contrast, P15TFSA and P16TFSA salts exhibit high fusion entropy and lack of solid-solid phase transitions. These two salts have significantly lower conductivity values in the solid state than the other P1xTFSA salts which have one or more phase transitions below the melting point and small fusion entropies [32].

Diffusion has been suggested as an important characteristic in plastic crystals [24]. There has been controversy over the diffusion mechanism in plastic crystals: "paddle-wheel" [168, 170-172, 180] or "percolation" [176, 178, 179]. A paddle-wheel mechanism

---

* x indicates the number of carbon on the alkyl chain.

indicates that translational motion is associated with rotational motion. The transport of charge carriers is facilitated by molecular rotation. This mechanism has been found in Li_2SO_4 and Na_3PO_4 [172, 201]. The small cations are attached to the anions by the interaction between Li^+ (or Na^+) and O atoms and are transported by the rotational motion of the anions. However, the way the rotational motion facilitates diffusion is not very clear so far for large sized ionic or molecular plastic crystals in most cases. A percolation mechanism suggests that the diffusion of charge carriers is related to the lattice expansion or defects. Lattice defects have been suggested as an important feature of plastic crystals and account for the mechanical flexibility [153]. Ikeda et al. have observed self diffusion in a large number of ammonium salts [52, 54, 55, 57]. They ascribed the diffusion to Schottky vacancy and /or vacancy-pair mechanisms [55, 58]. However, there are not enough direct evidences from the defect studies for these salts so far.

In this study, the hypothesis that defects are mainly responsible for the ionic transport in P1xTFSA salts will be investigated. This will involve studying the thermal properties, microstructure and mechanical properties of P12TFSA in detail. Lattice vacancy, both in number and size, and ionic motion of P12TFSA are investigated to understand the conduction mechanism. The possible conduction mechanisms include: ions hop between vacancies relatively independently; or ions hop between vacancies in a correlated way such as cation-anion ion pairs; or ions diffuse through extended defects such as grain boundaries. The relationship between rotational motion and ionic long range transport will also be considered.

3.2   Results and Discussion

3.2.1   Thermal Analysis

The DSC traces of P12TFSA are shown in Figure 3.1 (a). An unusually shaped peak is centred around −92 °C. It is followed by a solid-solid transition from phase III to phase II. This phase transition is reproducibly broad on the low temperature side with the peak appearing between 10 °C and 16 °C. Another broad transition from phase II to phase I starts at about 20 °C, reaching a peak at 45 °C. This unusual shape is again reproducible.

Finally, a sharp melting of phase I occurs at 88 °C. The enthalpies and entropies of the transitions are listed in Table 3.1.
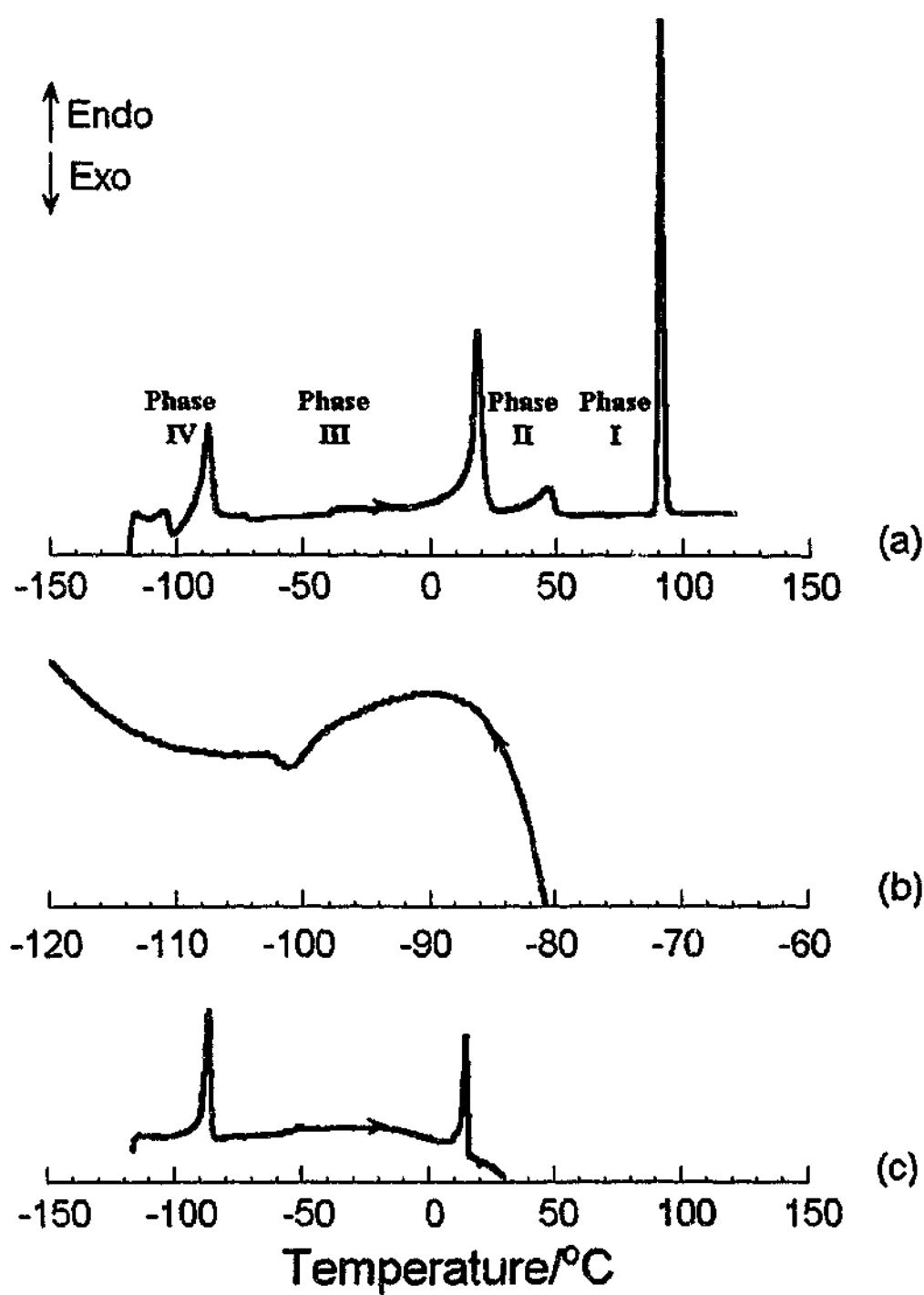

Figure 3.1 DSC traces of P12TFSA. (a) Heat at 20 °Cmin⁻¹ after cooling the sample from room temperature to –120 °C in about 15 minutes. (b) Cool from –60 °C to –120 °C at 1 °C/min. (c) Heat from –120 °C at 20 °Cmin⁻¹ after process b.

Table 3.1. Phase transition temperatures, enthalpies and entropies for P12TFSA. [a] Peak temperature. [b] Onset temperature.

Phase Transition	T/°C ±2 °C	ΔH/kJmol^{-1} ±5%	ΔS/Jmol^{-1}K^{-1} ±5%
IV>>III	-87[a]	1.9	10.3
III>>II	14[a]	1.1	3.8
II>>I	45[a]	1.0	3.0
Melting	88[b]	9.1	25.2

The -92 °C peak has been assumed to involve an orientational glass transition [235]. The peak comprises three transitions merged together: a glass transition at -105 °C, immediately followed by an exothermic transition at -101 °C and then an endothermic transition at -87 °C. This assumption is confirmed in this study by the following experiments. When the sample is cooled slowly from -60 °C to -120 °C at scan rate of 1 °Cmin^{-1}, an exothermic peak appears at -101 °C. When this slowly cooled sample is heated from -120°C, neither the T_g at -105 °C nor the exothermic peak at -101 °C are exhibited, although the -87°C peak remains at the same position with the same enthalpy change. This implies that a "glassy crystal" is formed when the sample is cooled from room temperature to -120 °C at a relatively fast rate as described above. The ions still occupy the phase III (or II) lattice positions while the orientations of phase III (or II) are arrested as a relatively static but disordered state [25, 137, 141]. This is a metastable state. Comparing the enthalpy of the exothermic peak at -101 °C (ΔH=1.2 kJmol^{-1}) to that at 14 °C (ΔH=1.1 kJmol^{-1}) may suggest that the frozen phase could be the trapped phase II. When the temperature increases, the glassy crystal goes through a glass transition at -105

°C and then forms an energetically stable phase IV by an exothermic transition at −101 °C. Phase IV then transforms into phase III at −87°C. If the sample is slowly cooled, phase IV is allowed to form, so no glass transition nor exothermic peak are observed in this case.

The phase transitions at 14 °C and 45 °C are quite broad, in some cases culminating in a sharp completion and thereby a sharp trailing edge of the thermal analysis peak. These are indicative of a progressive onset of the motions involved or a slow transformation rate. These "long tails on the low temperature side of phase transitions" have been observed in other plastic crystals such as a number of methylammonium salts [287-289] where motions could become gradually intensive in a large temperature range below a phase transition [64].

The DSC traces show that P12TFSA transforms from ordered phase into disordered phase through a series of phase transitions in a progressive way. The fusion entropy is 25 Jmol^{-1}K^{-1}, slightly higher than Timmermans' criterion for a plastic crystal, 20 Jmol^{-1}K^{-1} [23]. The sum of the entropy changes of the three phase transitions is 68% of the fusion entropy change.

3.2.2 Scanning Electron Microscopy

The SEM micrographs of P12TFSA are shown in Figure 3.2. Figure 3.2 (a) and (b) show the spherical morphology of P12TFSA. Unlike normal crystals, P12TFSA crystals do not have sharp edges, flat surfaces nor regular shapes. The semi-crystal feature is very similar to that observed in the plastic crystal phases of P1xBF$_4$ (x=1-3) salts [290]. All the spherical powders of P12TFSA and P1xBF$_4$ (x=1-3) salts are in contrast to non-plastic crystal P14BF$_4$ which exhibits regular shapes and flat surfaces [290]. Therefore, the spherical morphology of P12TFSA seems to indicate the plastic crystal phase.

The spherical morphology of the plastic crystals could be the result of plastic deformation. Plastic deformation occurs by crystallographic planes slipping in favorable crystallographic directions, associated with the motion of dislocations [153, 163]. The regular parallel lines shown in Figure 3.2 (c), (d) and (e) are believed to be slip lines which are very similar to the parallel steps observed on the surface of Zinc [163]. The crystallographic plane slip

occurs by the motion of dislocations under mechanical or thermal stress [153, 163]. The mobility of dislocations and thus the occurrence of slip are dependent on the intermolecular bonding interactions [163].

In the case of P12TFSA, the plastic deformation is believed to have occurred when the sample was being dried under vacuum and loaded prior to experiments, with mechanical handling increasing the number of dislocations. The ease of plastic deformation, which is also measured in the probe penetration experiments in section 3.2.3, is thought to result from the low impedance to crystallographic plane slip due to the relatively high crystallographic symmetry [165], as is the case for the plastic deformation of metals [163]. Since the plastic deformation occurs by the motion of dislocations, which are closely associated with the diffusion and congregation of vacancies [153], it is believed that dislocations and vacancies are important lattice defects in P12TFSA. The vacancies are studied by positron annihilation lifetime spectrum and will be discussed in section 3.2.4.

In addition to the vacancies and dislocations, another lattice defect in the form of grain boundary is shown in Figure 3.2 (f). Grain sizes vary markedly but grain boundaries are clearly resolved. Figure 3.2 (g) show a complex array of periodic slip planes appearing as steps at the surface and terminating at grain boundaries which retain their coherency.
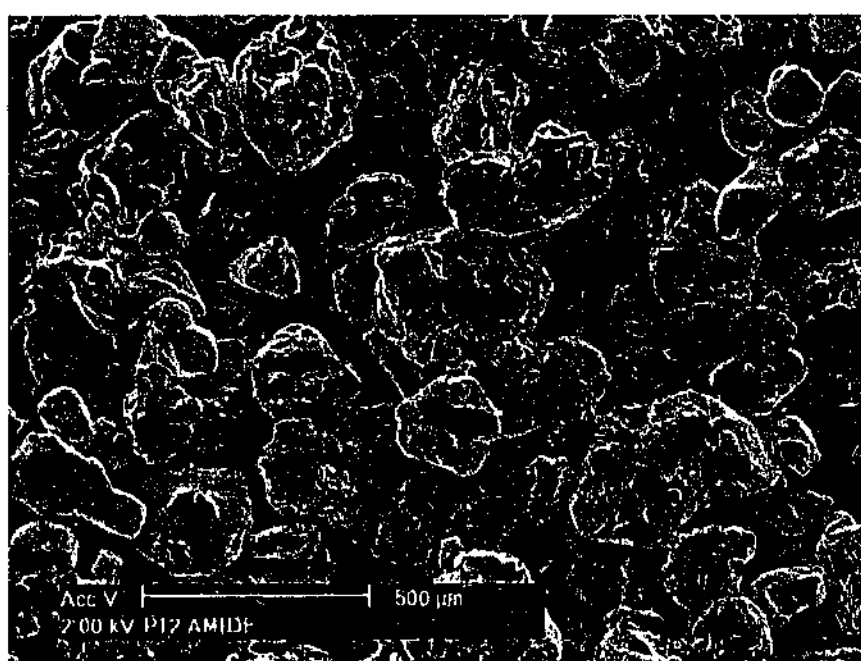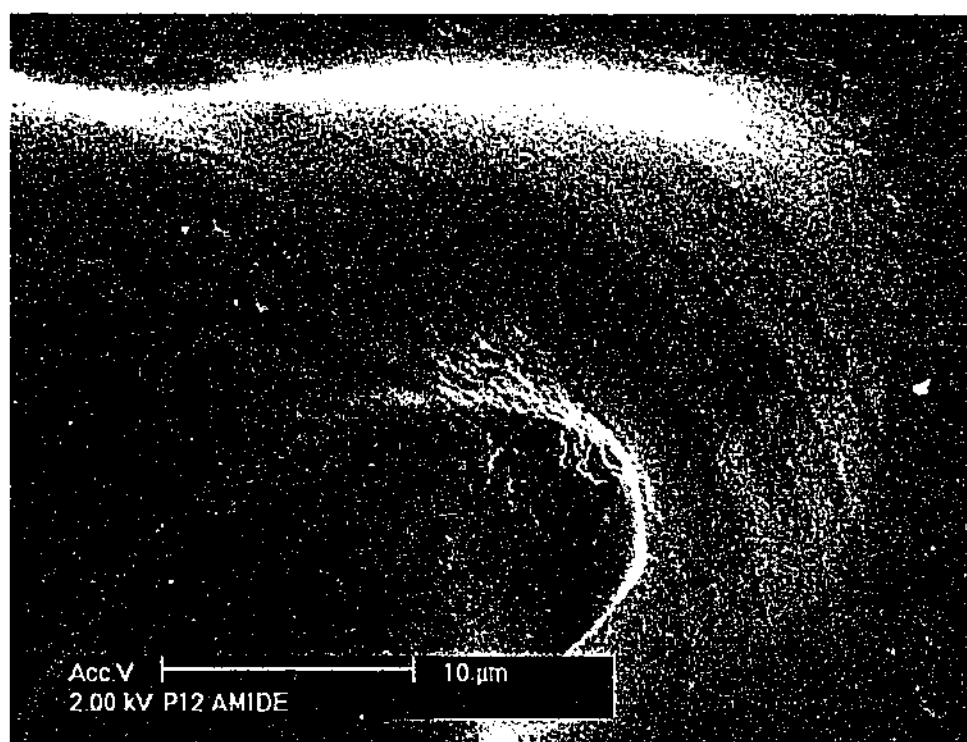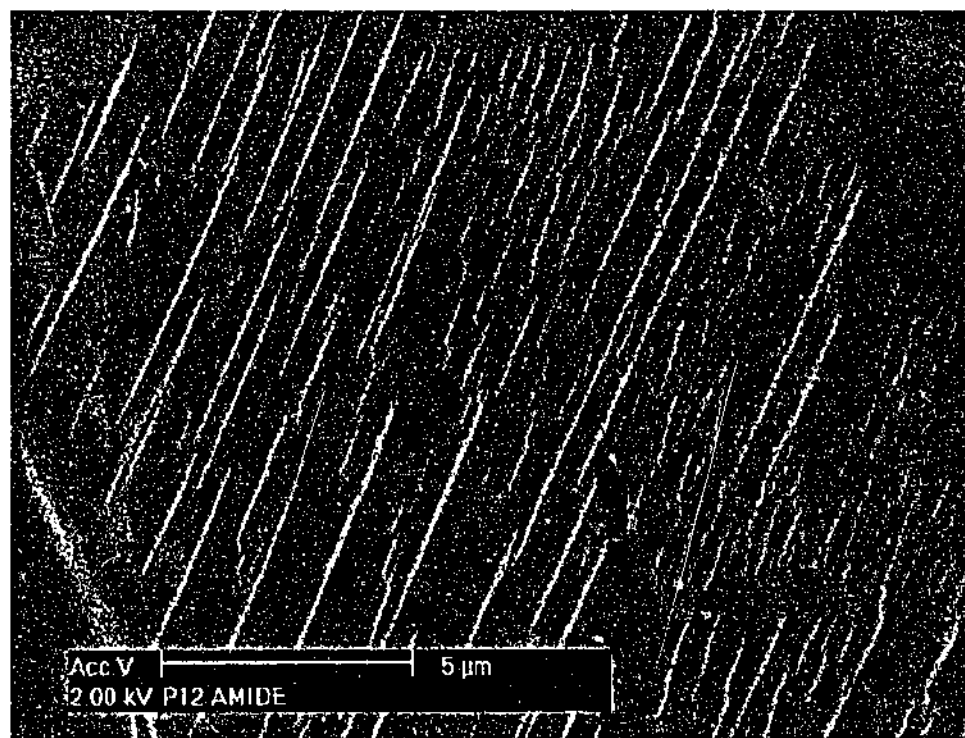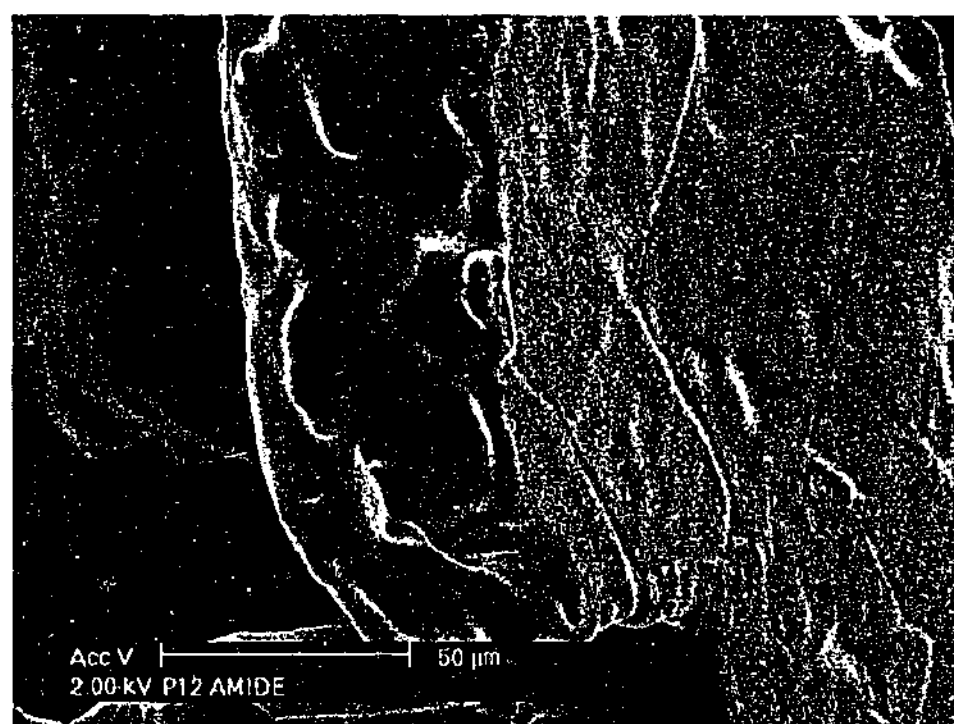

(a)
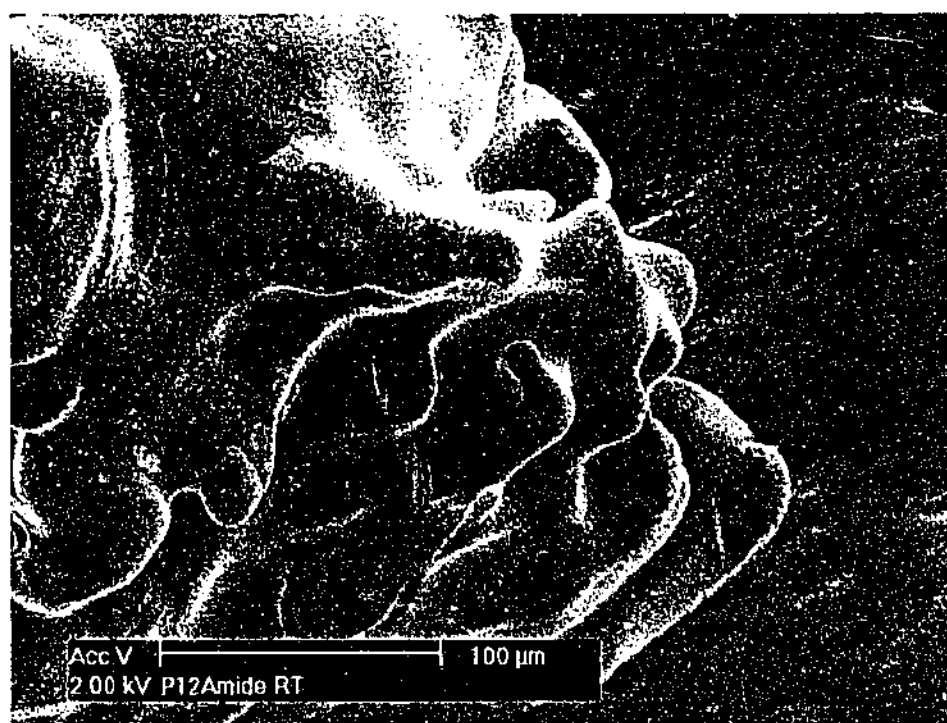
(b)

(c)

(d)

(e)

(f)

(g)

Figure 3.2 SEM of P12TFSA. (a) and (b) show the semi-crystal feature. (c), (d) and (e) show the slip lines on the surface of the crystal. (f) shows the grain boundaries. (g) shows the grain boundaries and the slip steps within one grain.

It is worth noting that the lattice defects, in the form of vacancies, dislocations and grain-boundaries, not only are responsible for the mechanical properties, but also are involved in different ionic diffusion mechanisms and hence affect the conductivity. For example, vacancies are involved in the lattice self diffusion while the dislocations and grain-boundaries could provide highly effective conducting tunnels by pipe diffusion [153, 186].

3.2.3 Mechanical Properties

Isothermal Analysis with Changing Force

The mechanical properties of P12TFSA were tested by applying a gradually increased static force on the sample and measuring the depth of the probe penetration, as shown in Figure 3.3. Elastic deformation, of course, contributes partly to the penetration depth. When the probe was unloaded after the experiment, a dent was observed where the probe was located. Neither fracture nor cracks were visually observed. Therefore the dent indicates the occurrence of plastic deformation.

P12TFSA displays increased plasticity relative to normal ionic crystals. The penetration depth of P12TFSA is about 3% of the sample thickness at $-7\ ^\circ$C and 22% at 78 $^\circ$C without any observation of obvious fracture, while normal crystals fail after only about 0.1% strain [163]. The plastic deformation is associated with the slip of crystallographic planes, essentially the motion of dislocations [153, 163]. The ease of the plastic deformation depends on the mobility of dislocations. For plastic crystals, the high symmetry of both the molecules and the crystalline structure facilitates the slip and enhances the plasticity [165]. Moreover, the motion of dislocations is closely associated with self diffusion of vacancies [153]. Thermodynamically, the high vacancy diffusion entropy of plastic crystals results in a high vacancy diffusion coefficient [154, 158] and thus improves the mobility of dislocations. The mobility of the dislocations also depends on the intermolecular interactions as the diffusion of vacancies involves breaking and forming intermolecular bonds [163]. For P12TFSA, both the cations and anions are relatively large - 3.1 Å and 3.7

Å in radius respectively[i]. The large ionic size combined with delocalized charges on the anions due to the strong electron-withdrawing CF_3 groups results in a weak intermolecular bond and thus facilitates the dislocation motion [241]. The slip traces can be observed by SEM as in section 3.2.2.

The depth of the probe penetration increases with temperature. The penetration depth at 78 °C is 7 times that at –7 °C. It indicates the decrease of hardness and increase of plasticity with temperature, which is also normally the case for metals [163]. The degree of plasticity shows a remarkable increase in phase I compared to in phase II. The increased plasticity is attributed to the increased mobility of dislocations and vacancies in this phase. The increased size and number of vacancies in phase I are also observed with PALS as shown in section 3.2.4. The increased symmetry in lattice structure in the high temperature phase, as is normally the case for plastic crystals, may also assist the slip.

Volumetric Expansion

The P12TFSA volumetric expansion was measured by exerting a small constant static force on the probe, whilst ramping temperature. The result is shown in Figure 3.4. The elevation of the probe position indicates the expansion of the sample. The thermal expansion anomalies correspond well to the phase transition temperatures. Two small contractions are observed at –107 °C and –103 °C. An obvious drop occurs at –87 °C. These three features correspond with the phase transition temperatures from DSC traces: the glass transition of frozen metastable phase II' (-105 °C), transformation of phase II'→IV (-101 °C) and phase IV→III transition (-87 °C). In phase III, the volume expands continuously except that a small discontinuity is observed at –8 °C, probably due to the onset of the phase III→II transition. A step occurs at about 14 °C, the phase III→II transition temperature. Another small step is exhibited at about 40 °C, in the broad temperature range of phase II→I transition. In phase I, the expansion coefficient is greater than either in

---

[i] Ionic sizes are estimated by Chem3D software.

phase III or phase II. Substantial volumetric changes occurring at phase transitions have also been reported in some plastic crystals such as ammonium tetrabromoindate salts [225].
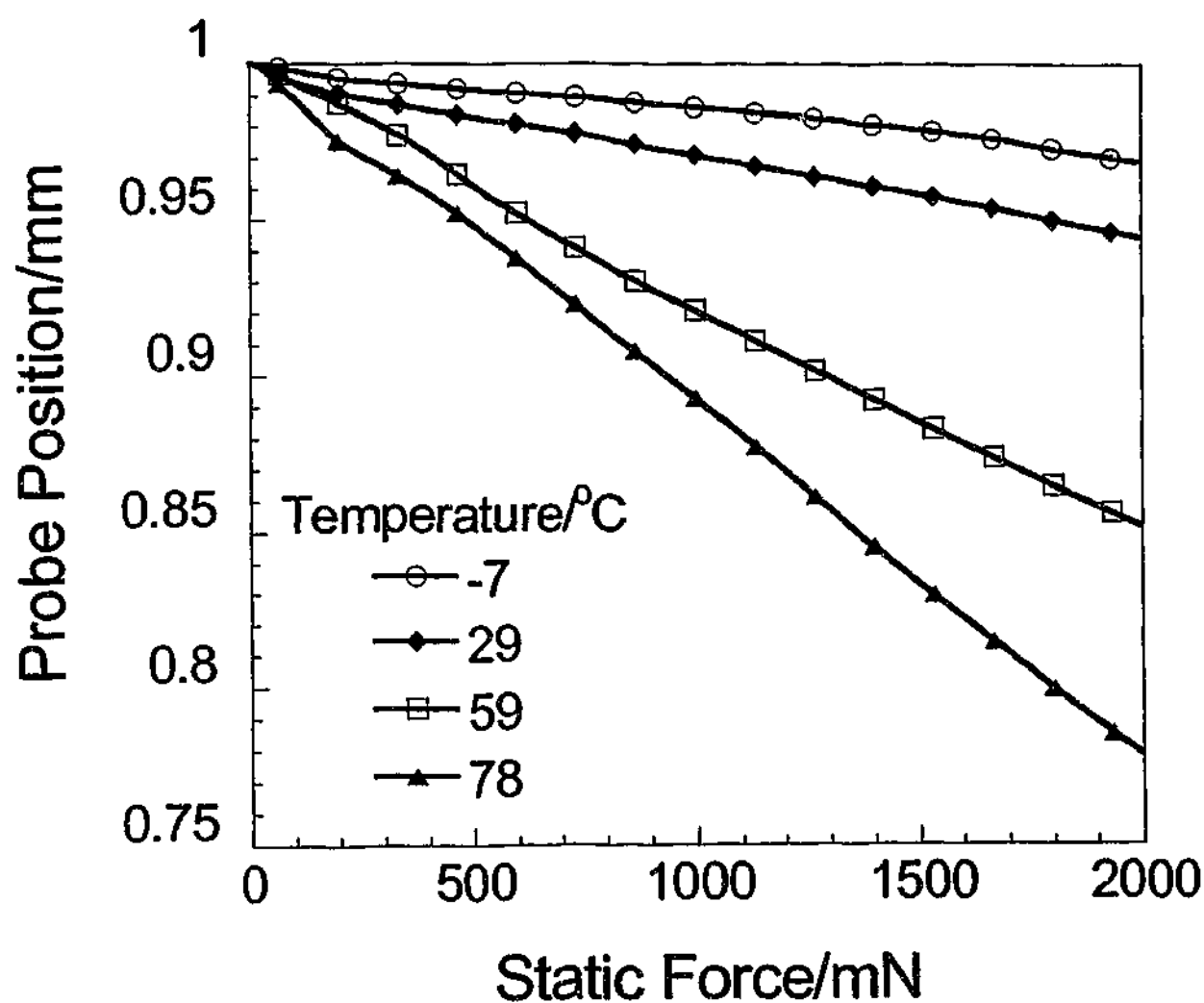

Figure 3.3   Probe position as a function of static force applied to P12TFSA at various temperatures. Static force starts at 1 mN and increases by 50 mNmin⁻¹. The sample is about 1 mm in thickness and 6 mm in diameter. The area of the probe tip is 0.78 mm².
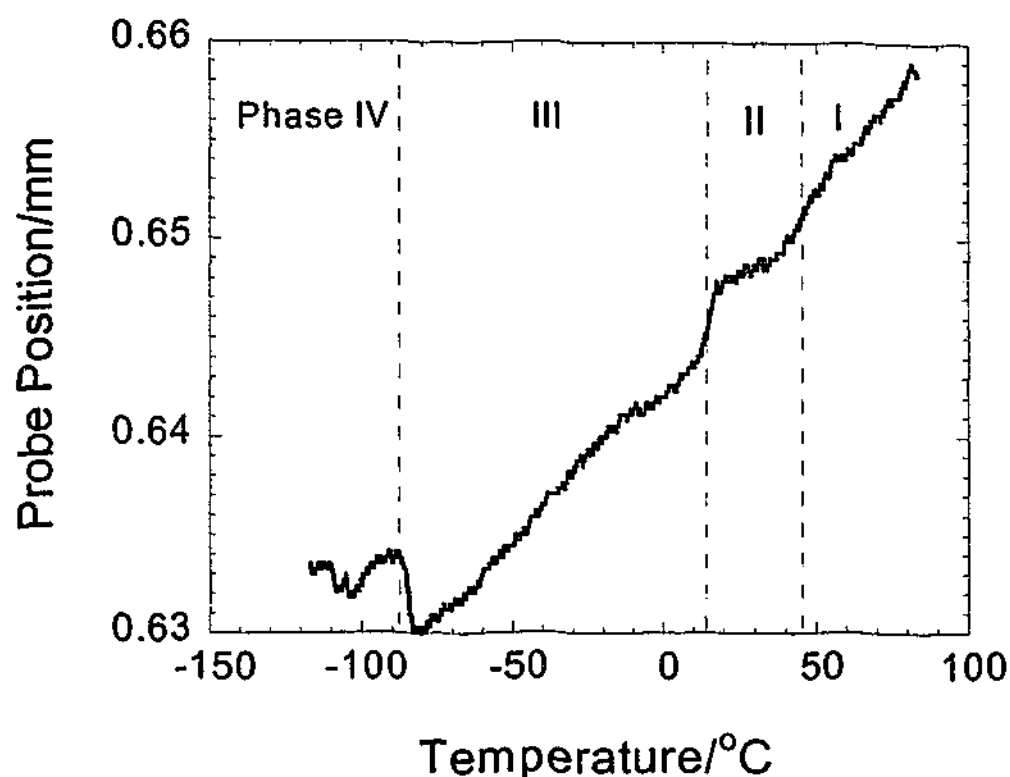
Figure 3.4 Volumetric expansion behavior of P12TFSA. Temperature ramps at 5°Cmin⁻¹. 5 mN Static force and 2 mN dynamic force with frequency 1 Hz are applied. These forces are too small to cause significant sample deformation. The sample is 6 mm in diameter and 1 mm in thickness. The area of the tip of the probe is 0.78 mm².

3.2.4 Positron Annihilation Lifetime Spectroscopy

The component of ortho-Positronium (oPs) pickoff annihilation measurement (τ_3, I_3) was recorded. The results are shown in Figure 3.5. The analyses of τ_3 and I_3 are complicated, as they could be the average result of two oPs states, the oPs in bulk material and the oPs trapped in defects [275]. Since the data precision did not justify a further deconvolution, in this work τ_3 and I_3 were tentatively assigned to the responses of the oPs trapped in the defects. Intensity I_3 is proportional to the vacancy concentration. Lifetime τ_3 is related to the average size of vacancies. The vacancy size calculated from τ_3 by Equation 2.60 is shown in Figure 3.6. The relative fraction of free volume (Fr) obtained from the vacancy number and size, according to Equation 2.61 and Equation 2.70, is shown in Figure 3.7.

- 107 -

Figure 3.5 and Figure 3.6 indicate that the changes of vacancy parameters are closely associated with phase transitions. In phase III, the vacancy size increases steadily, corresponding to thermal expansion and is consistent with volumetric expansion data shown in Figure 3.4. Over the broad phase III → II transition range −5~10 °C, the vacancy number increases substantially, showing stronger effect of temperature than in phase III. The vacancy size increases at the same rate as in phase III, probably still due to the thermal expansion. Both the τ_3 and I_3 show a step around 15 °C, which could be associated with the change of lattice structure. In phase II, both the I_3 and τ_3 increase steadily, but with a steeper slope than in phase III, suggesting a higher vacancy expansion coefficient and the greater ease of formation of new vacancies. A small step is observed in τ_3 at 45 °C, the phase II to I transition. In phase I, the vacancy size continues to expand while the number remains constant until a dramatic drop near the melting point, suggesting that the vacancies expand and congregate to form bigger voids.

The cationic and anionic radii are estimated to be 3.1 Å and 3.7 Å*, respectively. The cationic size roughly matches the vacancy size in phase III. The slight discrepancy could be attributed to the lattice distortion in the vicinity of the vacancy. The vacancy size exhibits a greater expansion coefficient in phases II and I. The reason could be that the temperature has more effect on lattice expansion in the higher temperature phases. It is also possible that larger vacancies become dominant. The vacancy size measured by oPs is the average over the vacancies of different sizes. When larger vacancies are created, PALS would measure a bigger average value. The bigger average vacancy radius could be attributed to the generation of bigger anionic vacancies. Moreover, an anionic vacancy and a cationic vacancy could join into a bigger void. This implies that both the cations and the anions could involve in the diffusional motion.

The overall vacancy volume as indicated by Fr in Figure 3.7 increases steadily in phase III due to the steady increases in both number and size. It increases substantially in phase II with a steeper slope. In phase I, changes in Fr come from increased size of the nearly constant number of vacancies.

---

*Estimation was made by Chem3D software.

As discussed in section 2.6, the intensity I is proportional to the vacancy concentration. The vacancy formation energy E_v can be obtained by determining I as a function of temperature. The E_v was thus estimated by plotting $\ln(I_3)$ vs. $1/T$. Arrhenius behaviors are assumed and thus the slope $= E_v/R$ (R=8.314 $JK^{-1}mol^{-1}$). The results are shown in Table 3.2. The biggest E_v was found in phase II, suggesting higher energy barrier to form a vacancy in this phase. E_v drops significantly in phase I, indicating either much easier vacancy formation in phase I or saturation of vacancies in phase I. E_v's of P12TFSA are relatively small compared to some molecular plastic crystals investigated by Sherwood et al. where the lowest E_v found is about 13 $kJmol^{-1}$ for cyclooctane [37].
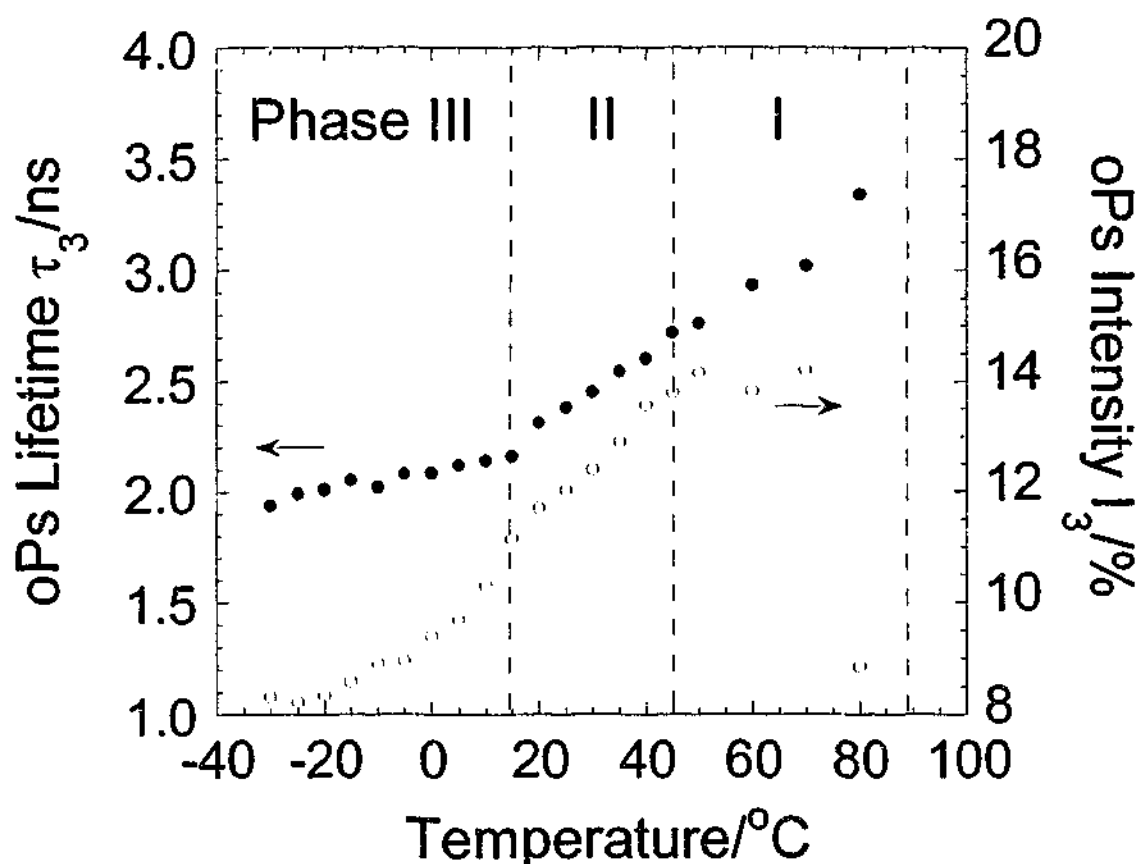

Figure 3.5. The vacancy parameters of P12TFSA as a function of temperature. OPs lifetime τ_3 is related to the vacancy size. OPs intensity is related to vacancy concentration. Dashed lines indicate the phase transition temperatures as observed in DSC. Error range in data is estimated to be of the size of the data point.
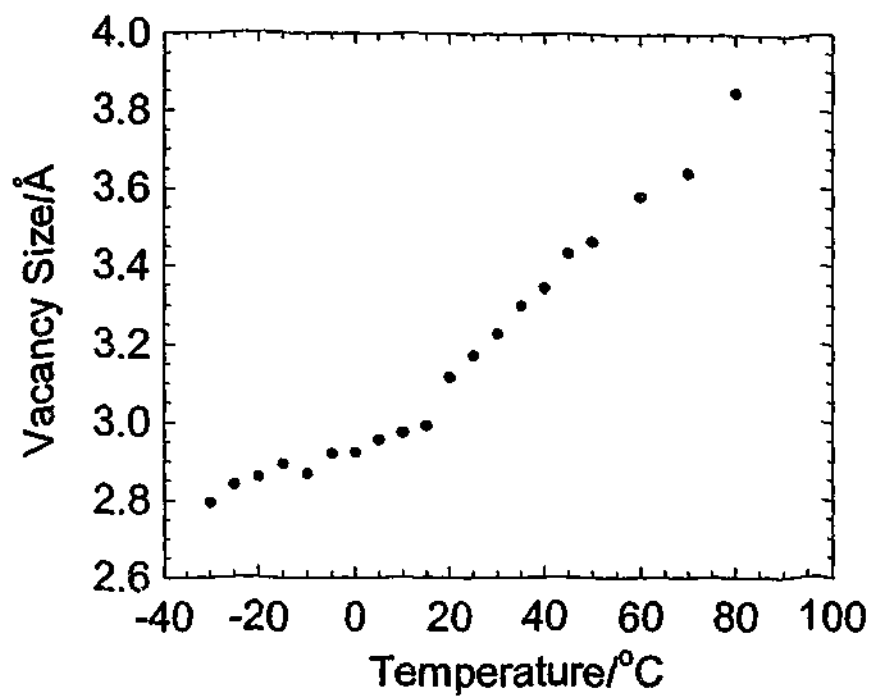
Figure 3.6. The average radius of vacancies in P12TFSA as a function of temperature. The vacancy sizes are calculated from oPs lifetime τ_3 data by Equation 2.60
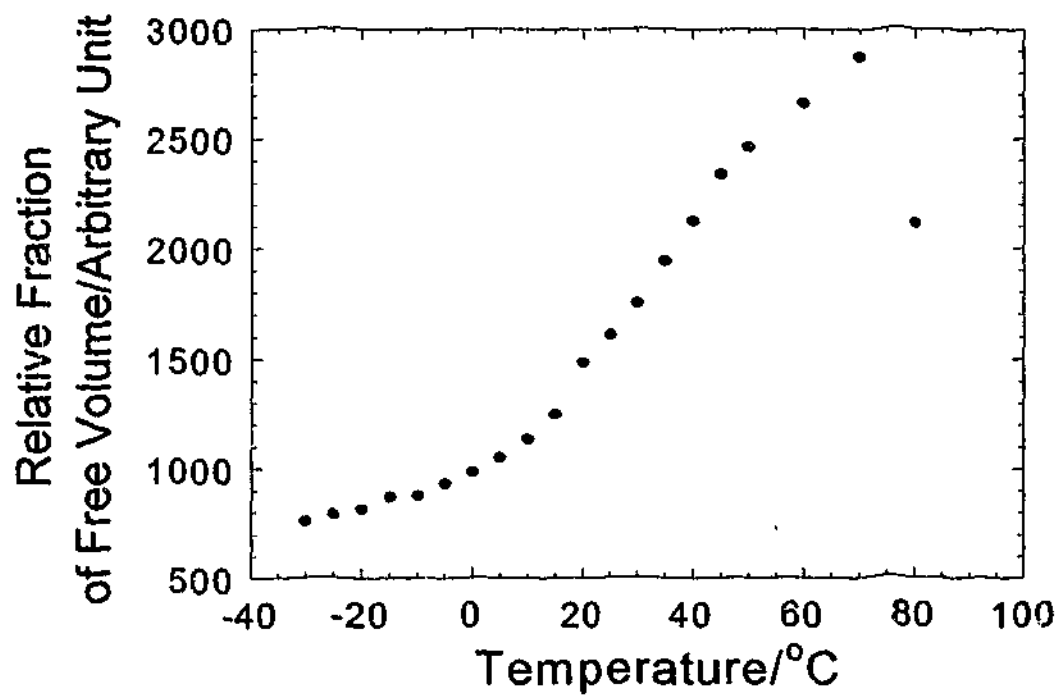

Figure 3.7 The relative overall volume of vacancies in P12TFSA as a function of temperature.

Table 3.2. Vacancy formation energy (E_v) obtained from the slopes by plotting $\ln(I_3)$ vs. 1/T for P12TFSA.

Temperature range/°C	Phase	E_v /kJmol^{-1} ($\pm 2\%$)
-25 ~ -5	III	2.9
-5 ~ 10	Phase transition III>>II	5.7
15~ 45	II	5.5
45~70	I	0.6

3.2.5. Nuclear Magnetic Resonance

^{1}H Linewidth

The temperature dependent ^{1}H NMR spectra are shown in Figure 3.8. Broad peaks are observed at low temperatures. Narrow peaks superimposed on top of the broad ones appear from −20 °C. The intensity of the narrow component increases continuously with temperature while that of the broad part decreases. These "narrow on top of broad" spectra have been observed in a number of plastic crystals, such as benzene, thiophene, 1,4-dioxane and cyclohexanol, where the narrow lines are ascribed to the locally mobile domains due to grain boundaries while the broad lines are attributed to the normal orientationally disordered solid [209, 210, 291]. Some plastic crystals such as cyclohexane and succinonitrile have homogeneous NMR peaks even though premelting occurs. This has been explained by the fact that the orientationally disordered molecules have a similar value of spin-spin relaxation time T_2 to the mobile molecules [209].
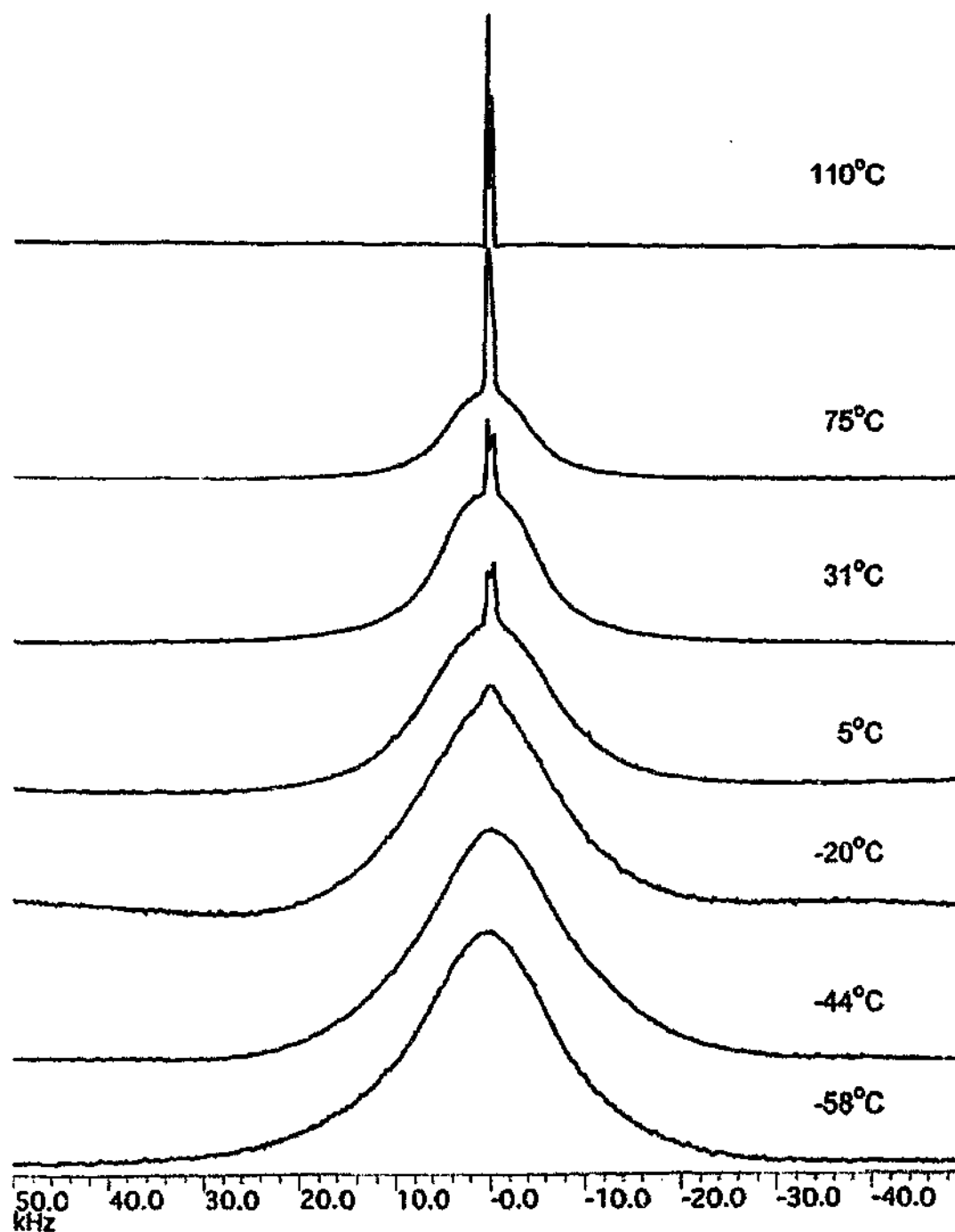
Figure 3.8 ^{1}H NMR spectra for P12TFSA.

In the case of P12TSFA, information about the cationic motions can be obtained by comparing the measured linewidths and the linewidths calculated from second moment. The deconvoluted linewidths are shown in Figure 3.9. The calculated second moments (M_2) and linewidths of P11TFSA in Table 4.3 in section 4.2.5 are used here to assess the

ionic motions in P12TFSA by assuming that P11TFSA and P12TFSA have similar crystal structures[ii]. The calculated linewidths corresponding to CH_3 group rotation only and cationic isotropic motion are 50 kHz and 7 kHz in P11TFSA, respectively.

The measured linewidth of the broad peak is about 20 kHz in phase III, which implies that the cations undergo some motion which is more active than the CH_3 group rotation and less active than isotropic tumbling. Therefore, the cations are thought to undergo anisotropic rotation. Since the energy barrier to CH_3 group C_3 rotation is normally less than that of the rotation of the ion or molecule, the ionic or molecular rotation is generally accompanied by the rotation of CH_3 group [59, 68, 292]. The cation in P12TFSA anisotropically rotates about some axis of the ring while the CH_3 group rotates about the C_3 axis. Line narrowing occurs in the range from −10 to 45 °C, where lattice structure goes through a transformation according to DSC, volumetric expansion and PALS results. Linewidth is reduced to 11 kHz in phase I. These results indicate that cationic motion transforms from one anisotropic rotation to another, or that additional anisotropic motion is superimposed during the lattice structure change. The anisotropic rotation could be ring inversion or flipping, but has not been identified in detail at this point.

The two narrow peaks represent protons of different chemical shifts. The linewidths of both peaks are much less than 7 kHz (7kHz is the calculated value of cationic isotropic rotation according to Table 4.3). The Linewidth decreases further from about 1 kHz in phase III to about 500 Hz in phase II and I. These narrow linewidths indicate that diffusion motion must be taking place to further narrow the line. Since the energy barrier to diffusion motion is normally higher than that of rotation, diffusion is normally accompanied by isotropic rotation [68]. Hence on the basis of the observation of the

---

[ii] The linewidth calculation of P12TFSA is difficult as the atomic positions in P12TFSA crystal lattice are not well defined at this stage due to the difficulty in obtaining a single crystal. A full set of linewidth calculation was possible on P11TFSA because a crystal structure exists for this compound. The P11TFSA linewidth calculation is discussed in detail in the next chapter.

narrow lines, it appears that detectable cationic diffusion superimposed on isotropic rotation occurs from –20 °C.

Theoretically, the linewidth of diffusing molecules is zero, because both intra- and inter-molecular dipolar interactions are averaged out [249]. The residual linewidth of the diffusing cations observed here could result from: (1) Cations may experience inhomogeneous environments because of the distribution of defects such as vacancies; (2) The inter-ionic dipole-dipole interactions may not be totally averaged out due to the existence of a large number of non-diffusing ions, as discussed below; (3) Each peak observed here could be composed of more than one narrower component of different chemical shift. The linewidth is nevertheless still valuable in the interpretation of the diffusion motion.

The linewidth decreases further above the melting point. This could be attributed to a different diffusion mechanism in the molten state. Further averaging of inter-ionic dipole-dipole interactions or a more homogenous environment could also explain the narrowing.
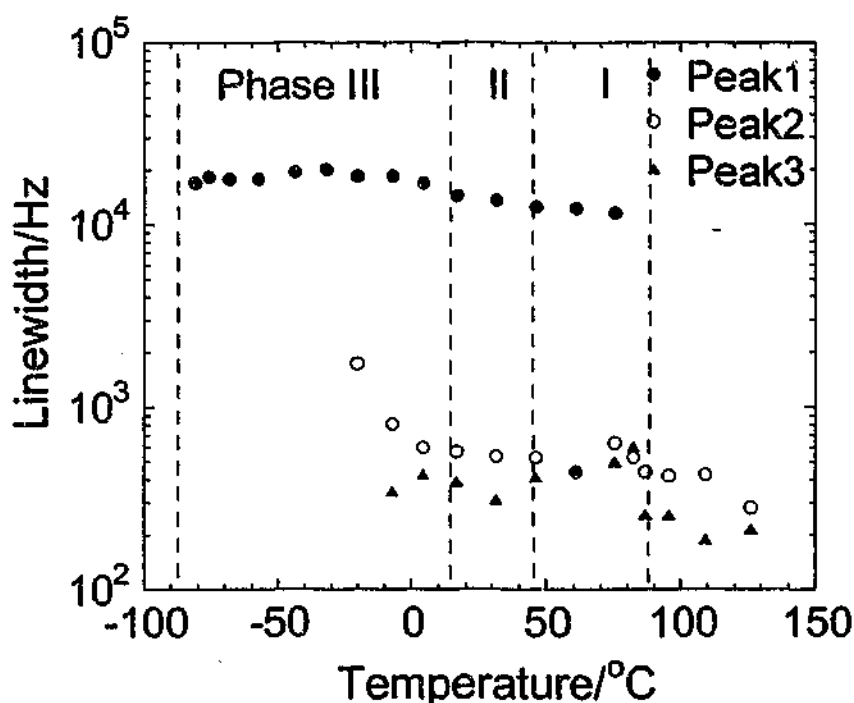

Figure 3.9 ^{1}H NMR Linewidth for P12TFSA as a function of temperature. Dashed lines indicate phase transition temperatures.

The fractions of the broad and narrow components, as shown in Figure 3.10, indicate the fractions of the non-diffusing and diffusing cations. More than 90% of the cations maintain their positional order up to 75 °C. About 1% of the cations are detected diffusing in phase III. The diffusing population increases dramatically in phase I, from about 2.5% to nearly 100% at the melting point. The effect of temperature on the diffusing population varies obviously in different phases, suggesting different energy barriers to create mobile cations in each phase.
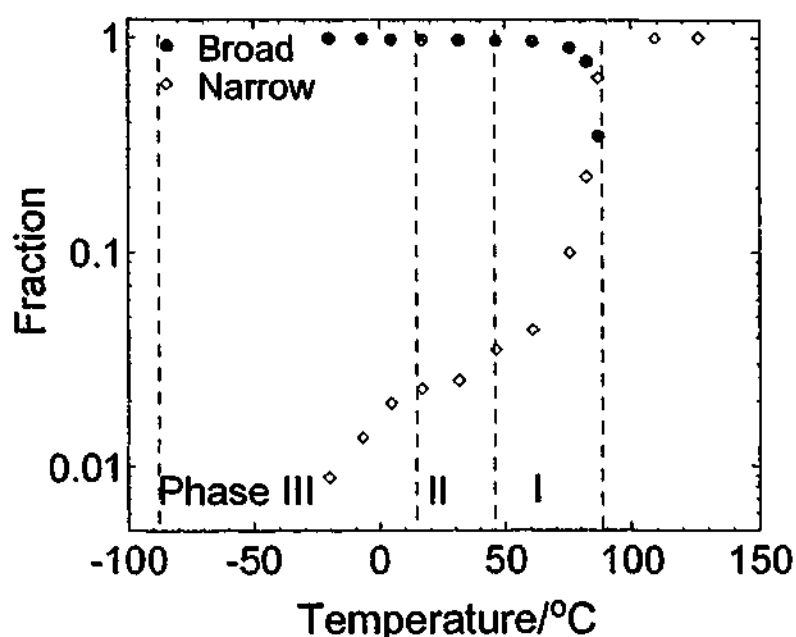

Figure 3.10 The fraction of the broad and narrow components in the ^1H NMR as a function of temperature for P12TFSA. "Broad" is the fraction of broad peak area in the whole peak area. "Narrow" is the fraction of the mobile component (ie. the fraction of the area sum of the two narrow lines).

^{1}H NMR Relaxation

NMR relaxation measurements can provide information about the activation energies and frequencies of the ionic motions. However, in the case of P12TFSA, the interpretation of T_1 and T_2 is complicated by considering the following factors. Firstly, the ions could participate in more than one type of motion. For example, positionally ordered cations could undergo the rotation of the ring in addition to the rotation of the CH_3 group. The translating cations could also undergo isotropic rotation. As a result, the relaxation

- 115 -

mechanism could be composed of several components corresponding to different motions. Secondly, different motions could exhibit different correlation times and activation energies. The correlation time and activation energy of each motion are probably different in different phases. Thirdly, DSC and PALS indicate that the crystal structure and vacancies go through gradual changes over broad temperature ranges. Therefore it is very possible that the activation energy and correlation time for one motion are temperature dependent even in one single phase. The complicated motions make the relaxation analyses difficult.

In the following analyses, the one broad and two narrow components are analyzed separately. The three magnetizations were curve fitted as a function of τ [iii] to determine the T_1s and T_2s. In each fitting, more than one T_1 could be obtained. There are several possible explanations for this. Firstly, the existence of several distinct motions within each ion could result in more than one distinguishable T_1. The magnitude of each T_1 component should be temperature dependent in this case. Secondly, spin exchange between ^1H and ^{19}F could also result in more than one T_1 values. For some ammonium ionic plastic crystals containing F atoms in the anions such as PF_6^- and BF_4^-, SbF_6^-, HF_2^-, BeF_4^{2-}, non-exponential behavior of T_1 has been observed in some temperature ranges due to the spin exchange between ^1H and ^{19}F when $1/\tau_F$ or $1/\tau_H$ is comparable to $(\omega_H-\omega_F)$ [54, 55, 57, 216-218, 223, 224].

In this study, the Magnetization M versus τ [iv] curves exhibit good exponential behavior. A single T_1 can be obtained with R>0.98 for each fitting. Use of a double-exponential equation improved the fitting, but the ratio of the two component magnitudes as well as the second T_1 were found to vary randomly with temperature, suggesting that the second exponential term should be attributed to errors. Therefore, a single T_1 was obtained for

---

[iii] τ here is the time interval between 180° and 90° pulses for T_1 measurement or between 90° and 180° pulses for T_2 measurement. τ otherwise unspecified in this section refers to correlation time.

[iv] τ is the time interval between pulses here.

each component. Consequently, three T_1 values and three T_2 Values were obtained for the one broad and two narrow peaks. The relaxation times T_1 and T_2 are shown in Figure 3.11.

Broad peaks correspond to anisotropic rotational motion as discussed in the linewidth analyses. The T_2 of the broad peak obeys the relationship $T_2 = 1/(\pi \Delta v)$, where Δv is the FWHM. The M_2 calculation in Table 4.3 shows that when the motion of the cation is less than isotropic, the M_2 mainly results from intra-ionic ^1H-^1H dipole-dipole interactions. Therefore, only ^1H-^1H interactions are considered in the further analyses. The ^1H-^{19}F dipole-dipole interactions are ignored. The linewidth analyses indicate that the broad peaks represent at least two rotation mechanisms, therefore, the overall T_1 is given by:

$1/T_1{}^H = 1/T_1{}^H{}_{rot1} + 1/T_1{}^H{}_{rot2}$

Equation 3.1

where rot1 and rot2 indicate the two rotation mechanisms, respectively. One of these is probably the CH_3 group C_3 rotation since this is very facile. The other of these is probably an anisotropic rotation of the ring or a rotation of the ethyl group. According to Equation 2.27 and Equation 2.29, Equation 3.1 is written as:

$$\frac{1}{T_1{}^H} = C_1 \left(\frac{\tau_1}{1 + \omega_H{}^2 \tau_1{}^2} + \frac{4\tau_1}{1 + 4\omega_H{}^2 \tau_1{}^2} \right) + C_2 \left(\frac{\tau_2}{1 + \omega_H{}^2 \tau_2{}^2} + \frac{4\tau_2}{1 + 4\omega_H{}^2 \tau_2{}^2} \right)$$

Equation 3.2

where C_i is a constant, ω_H is the angular Larmor frequency of ^1H, which is 1.88×10^9 s^{-1}, and τ_i is the correlation time of rotational motion i. The relationship between τ and activation energy E_a is given as:

$$\tau_i = \tau_{oi} \exp \left(\frac{Ea_i}{RT} \right)$$

Equation 3.3

The curve is fitted by assuming that both of the activation energies of the rotational motions are temperature independent in the temperature range investigated. The calculated

T_1s of the broad component are shown in Figure 3.12. Two sets of C, E_a and τ_0 corresponding to two motional mechanisms are obtained, as shown in Table 3.3.
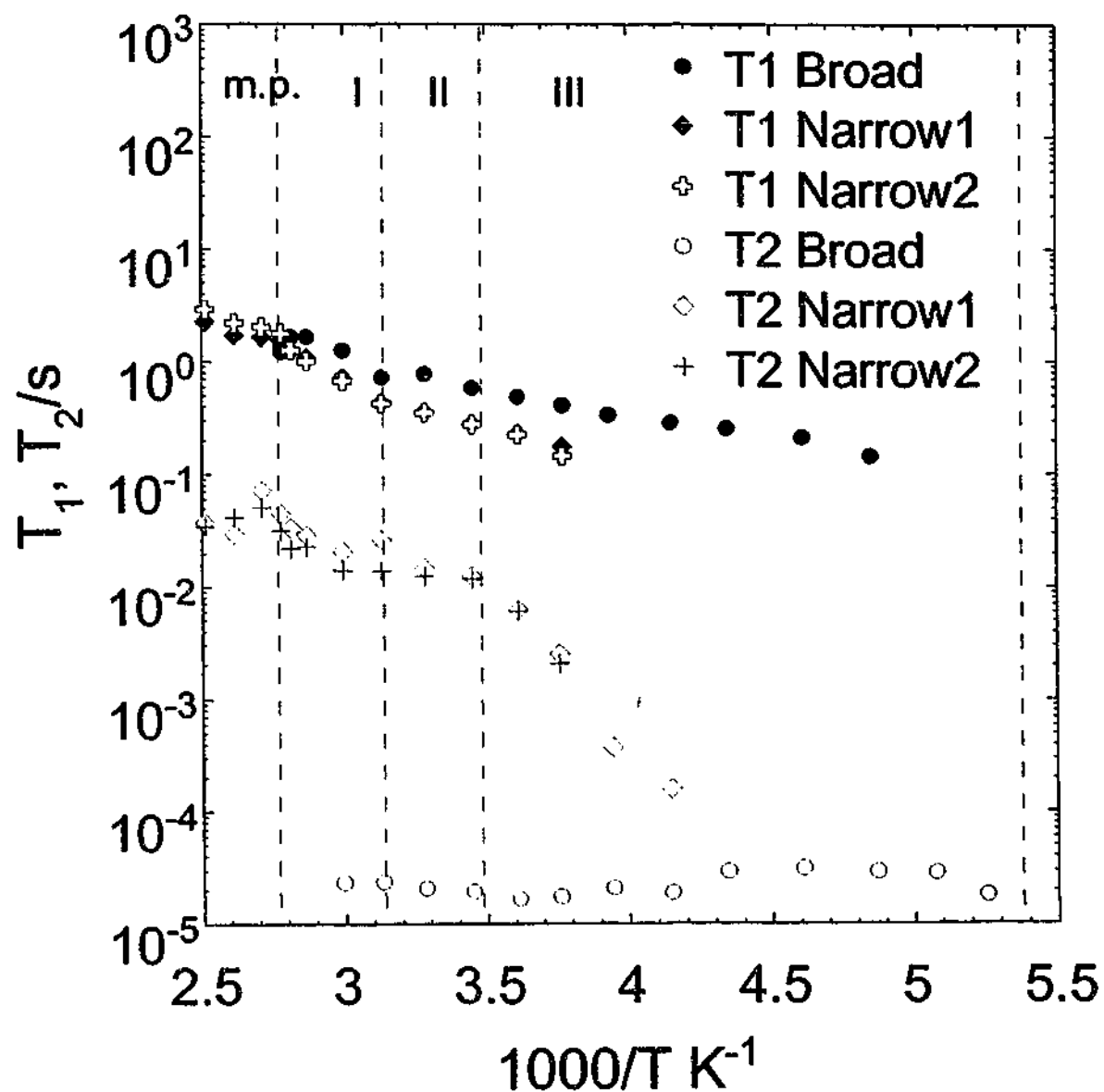

Figure 3.11 Temperature dependence of relaxation times T_1 and T_2 for ^{1}H NMR in P12TFSA.
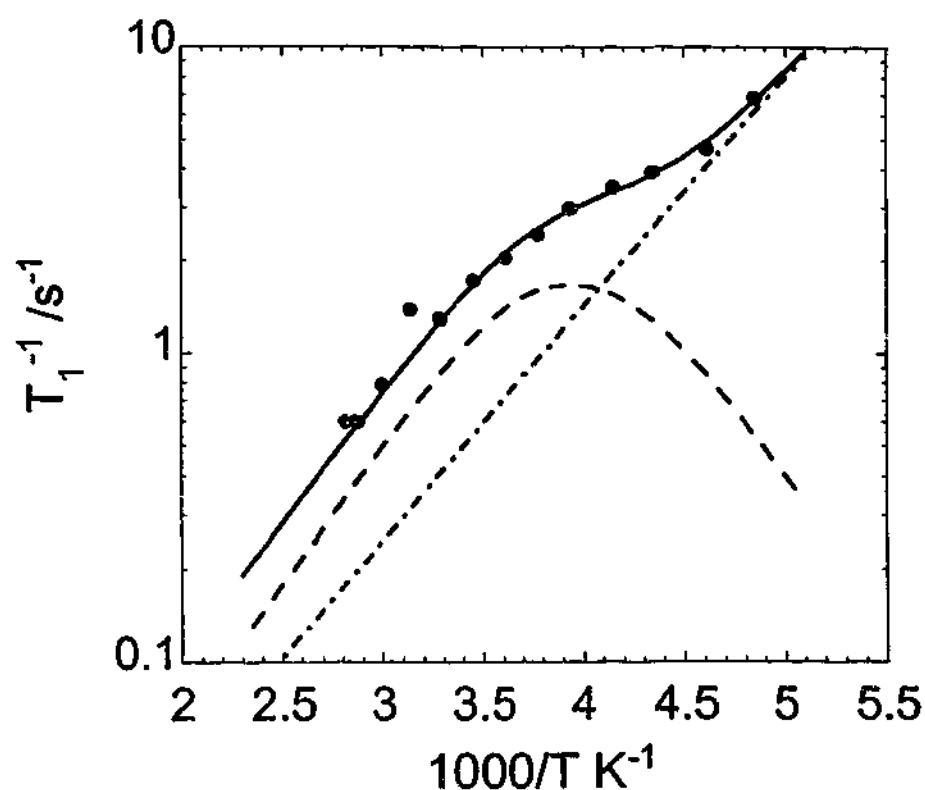
Figure 3.12 Curve fitting of T_1^{-1} of the broad ^1H NMR peak for P12TFSA. The solid circles are the experimental values. The two dashed lines are the calculated values corresponding to two motions. The solid line is the sum of the two calculated values.

The two narrow peaks represent similar relaxation behavior. $1/\pi T_2$ is about two orders of magnitude smaller than the linewidth. The discrepancy is due to the line broadening as discussed in the linewidth analyses. The much narrower linewidths than the isotropic value suggest that the relaxation is dominated by diffusional motion, therefore only a diffusion mechanism is considered. For diffusing cations, inter-ionic ^1H-^1H and ^1H-^{19}F dipole-dipole interactions both play important roles in the relaxation mechanism. Therefore, overall T_1 and T_2 are written as:

$$1/T_1{}^H{}_{dif} = 1/T_1{}^{H-H}{}_{dif} + 1/T_1{}^{H-F}{}_{dif}$$

Equation 3.4

$$1/T_2{}^H{}_{dif} = 1/T_2{}^{H-H}{}_{dif} + 1/T_2{}^{H-F}{}_{dif}$$

Equation 3.5

where superscripts H-H and H-F indicate contributions from ^{1}H-^{1}H and ^{1}H-^{19}F dipole-dipole interactions respectively. Equations for T_1 due to dipole-dipole interactions between like and unlike nuclei are introduced as Equation 2.27 and Equation 2.32 in section 2.1.5. Equation 3.4 can then be written as:

$$\frac{1}{T_1^H} = C_{H-H}\left(\frac{\tau}{1+\omega_H^2\tau^2} + \frac{4\tau}{1+4\omega_H^2\tau^2}\right)$$
$$+ C_{H-F}\left(\frac{\tau}{1+(\omega_H-\omega_F)^2\tau^2} + \frac{3\tau}{1+\omega_H^2\tau^2} + \frac{6\tau}{1+(\omega_H+\omega_F)^2\tau^2}\right)$$

Equation 3.6

where ω_H is 1.884×10^9 s^{-1}, ω_F is 1.772×10^9 s^{-1}. In this measurement, T_1 is on the high temperature side of the minimum over all of the temperature range investigated. Therefore $\omega\tau\ll1$ is assumed in order to simplify the fitting. By comparing Equation 2.15 with Equation 2.27, Equation 2.17 with Equation 2.32, Equation 3.6 can then be written as:

$$\frac{1}{T_1^H} = 10\times\left(\frac{M_2^{H-H}}{3} + \frac{M_2^{H-F}}{2}\right)\tau = C\tau_0\exp\left(\frac{Ea}{RT}\right)$$

Equation 3.7

where M_2^{H-H} and M_2^{H-F} are the reduced second moments due to diffusion. They are 2.3×10^8 and 1.2×10^8 s^{-2} respectively according to Table 4.3. C is calculated to be 1.4×10^9 s^{-2} here. Both T_1 and T_2 show slope discontinuity at phase transitions, indicating different activation energies in different phases. E_a and τ_0 in different phases can then be inferred according to Equation 3.7. The T_1 and T_2 fittings are shown in Figure 3.13. The resultant E_a and τ_0 are shown in Table 3.3. τ at the melting point is calculated to be 5.1×10^{-10} s.

The diffusion coefficient D can be estimated by [153]

$$D = \frac{<r^2>}{6\tau}$$

Equation 3.8

where $\langle r^2 \rangle$ is the mean-square-jump distance and τ is the diffusional correlation time. r is taken as approximately 10 Å being of the order of the unit cell dimension obtained from powder x-ray results in Appendix A. D is calculated to be 3.2×10^{-10} $m^2 s^{-1}$, coinciding approximately with the value of 3×10^{-10} $m^2 s^{-1}$ determined by pulsed field gradient NMR [293]. The consistence of the result by different techniques suggests the reliability of the T_1 measurement and analyses in this study. The results from T_1 measurements provide more information about ionic motion than gradient field NMR techniques by which the diffusion coefficient for $P12^+$ ions was only detectable above 70 °C.
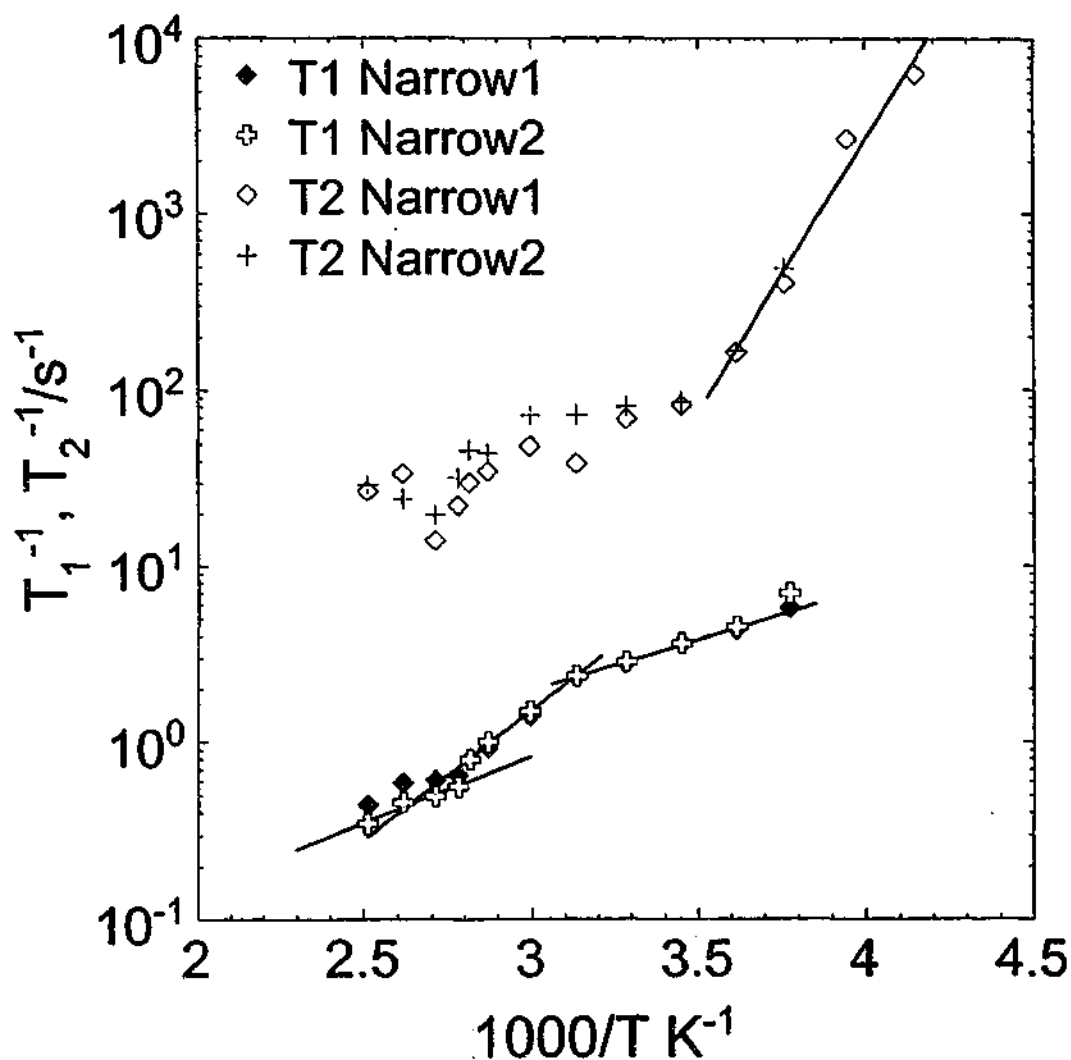

Figure 3.13 Curve fitting of T_1^{-1} and T_2^{-1} of the narrow ^1H NMR for P12TFSA. The solid lines are the calculated values.

The diffusion coefficients of some pyrrolidinium or piperidinium-containing ionic plastic crystals have been reported to be about 10^{-13} m^2s^{-1} [54, 55]. The value of D obtained for P12TFSA by both calculation here and measurement in previous work [293] is about three orders of magnitude higher. The correlation time τ ($=5.1\times10^{-10}$ s) at the melting point of P12TFSA is smaller than the 10^{-7}-10^{-8} s range suggested as the characteristic correlation time for triggering crystal melting [54] [58]. This clearly reflects the rapid diffusional motion which are already present in the phase I of P12TFSA prior to melting.

According to the E_a and τ_o obtained, the correlation times τ for rotational motion I, rotational motion II and diffusion at 30 °C are: 2.1×10^{-12}, 8.36×10^{-11} and 2.1×10^{-9} s respectively.

Table 3.3 Activation energies (E_a), correlation times at the limit of infinite temperature (τ_o) and motional constants (C) evaluated for cationic motion from ^1H NMR relaxation time T_1 and T_2 for P12TFSA.

Motion	Phase	$C/10^8$ s^{-2}	$E_a/kJmol^{-1}$	τ_o/s	Correlation coefficient	Method
Rotation I		390±71	14.5±3.8	$(6.8\pm0.9)\times10^{-15}$		T_1
Rotation II		22±14	17.4±0.7	$(8.6\pm6.7)\times10^{-14}$	0.999	T_1
Diffusion	III	14*	59.6±1.1	$(1.8\pm0.8)\times10^{-20}$	0.978	T_1, T_2
	II	14*	11.0±0.6	$(2.6\pm0.6)\times10^{-11}$	0.997	T_1
	I	14*	28.0±0.5	$(4.5\pm0.9)\times10^{-14}$	0.999	T_1
	molten	14*	14.3±2.2	$(3.4\pm2.8)\times10^{-12}$	0.978	T_1

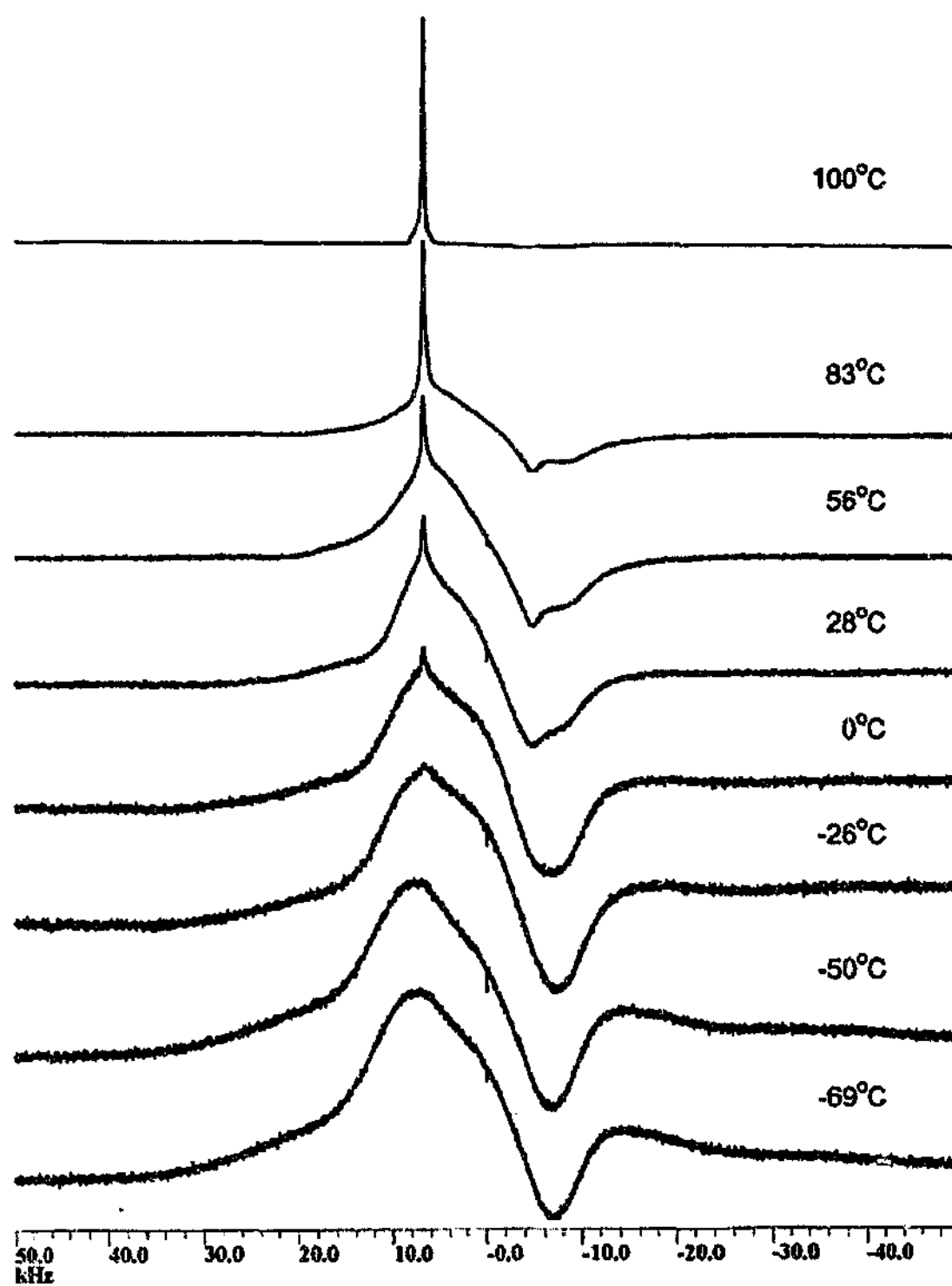*Calculated from second moment.

^{19}F Linewidth

The ^{19}F NMR spectra are shown in Figure 3.14 (a). Broad peaks are observed at low temperature. A narrow line on top of the broad base appears from –25 °C. The amplitude of the narrow peak increases with temperature. The broad bottom can be deconvoluted into three peaks over the entire temperature range investigated, as shown in Figure 3.14 (b). The three peaks are thought to be attributable to ^{19}F of different chemical shifts due to three different sites.

The linewidth and fraction of each component are shown in Figure 3.15 and Figure 3.16. M_2 and corresponding linewidth calculated for ^{19}F of P11TFSA, as shown in Table 4.4, are used here to interpret the motion of the TFSA⁻ anion. The FWHMs in the three states: rigid lattice, CF_3 group rotation and anion isotropic rotation, are calculated to be 22, 14 and 8 kHz respectively.
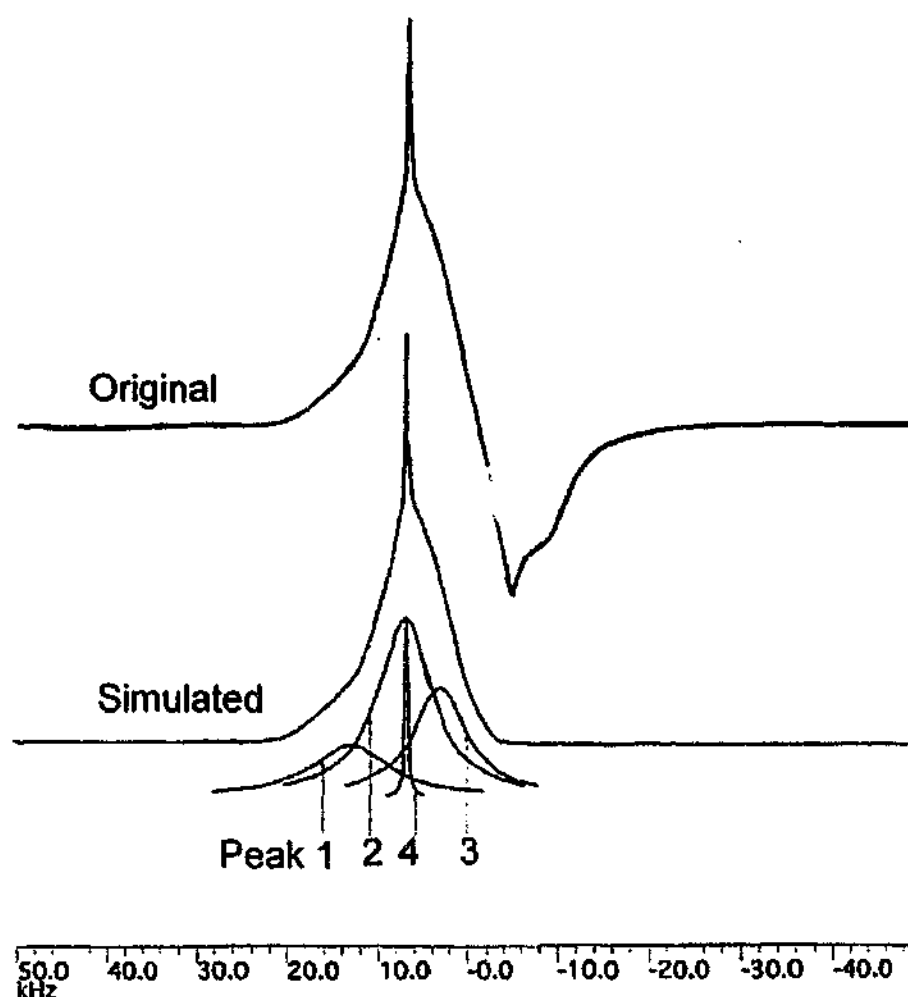
The linewidth of Peak 1 is about 22.2 kHz at –77 °C. It decreases slightly to 20.1 kHz at 8 °C. The linewidth reduces to 11.0 kHz in phase II and then constantly decreases to 8.0 kHz at the melting point. Therefore, corresponding anions are relatively static at low temperature in phase III. These anions undergo an anisotropic rotation superimposed on CF_3 group C_3 rotation in phase II, because the linewidth in this range is right between the values of CF_3 group rotation and isotropic rotation. Isotropic rotation occurs near the melting point.

Peak 2 and peak 3 have similar linewidths in the whole temperature range. The linewidth starts at about 13 kHz at –77 °C. Line narrowing occurs from about 0 °C. It shows a relatively constant linewidth 7.2 kHz in phase II and I. A further narrowing occurs near the melting point. Peak 2 and 3 can be assigned to the anions which undergo CF_3 group rotation in phase III and isotropic rotation in phase II and I.

Peak 4 is much narrower than the isotropic value and can therefore be assigned to the diffusing anions. The linewidth of the first detectable peak 4 is 620 Hz. It is then in the range of 350~400 Hz over all the temperature range in the solid state. The line reduces to 250 Hz above the melting point.

- 123 -

100°C

83°C

56°C

28°C

0°C

-26°C

-50°C

-69°C

50.0 kHz   40.0   30.0   20.0   10.0   -0.0   -10.0   -20.0   -30.0   -40.0

(a)

(b)

Figure 3.14 ^{19}F NMR spectra for P12TFSA. The peak at about -7 kHz comes from background. (a) At various temperatures. (b) The original peak at 56 $^\circ$C and the simulated peak composed of four smaller peaks. The broad bottom can be deconvoluted into peaks 1, 2 and 3. The top narrow line is simulated by peak 4.

The area fractions of peak 2 and peak 3 are relatively constant, about 0.5 and 0.25 respectively. The fraction of peak 1 is about 0.25 in phase III, but decreases in phase II and I. The ratio of the three positionally ordered components is peak1:peak2:peak3 = 1:2:1. Similar to cation diffusion, the fraction of the diffusing anions shows distinctively different temperature dependence in different phases. The number of apparently diffusing anions increases from 2.8% to 100% in phase I.
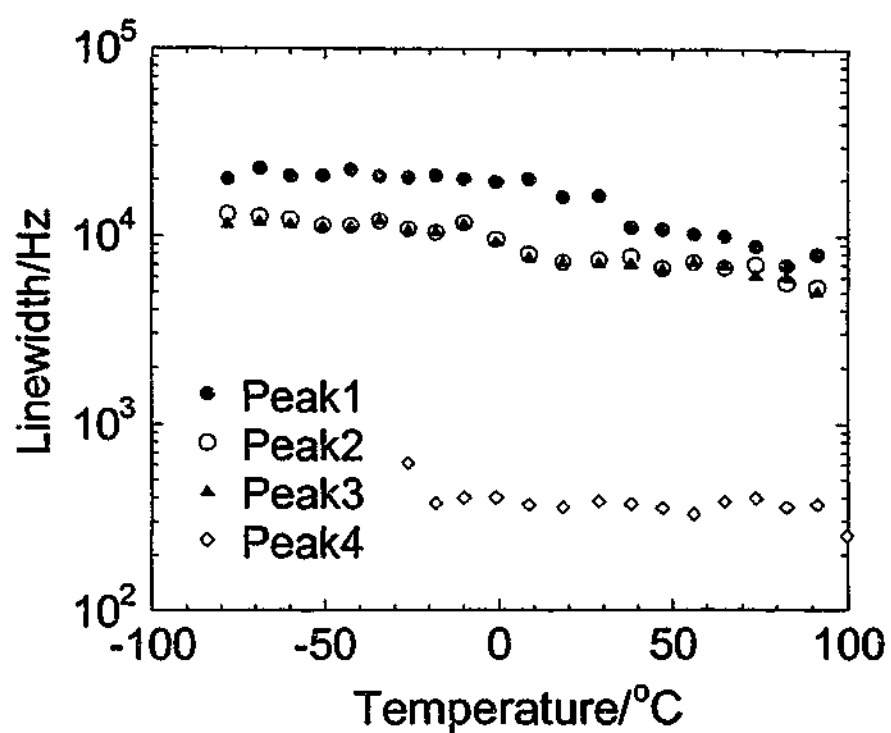
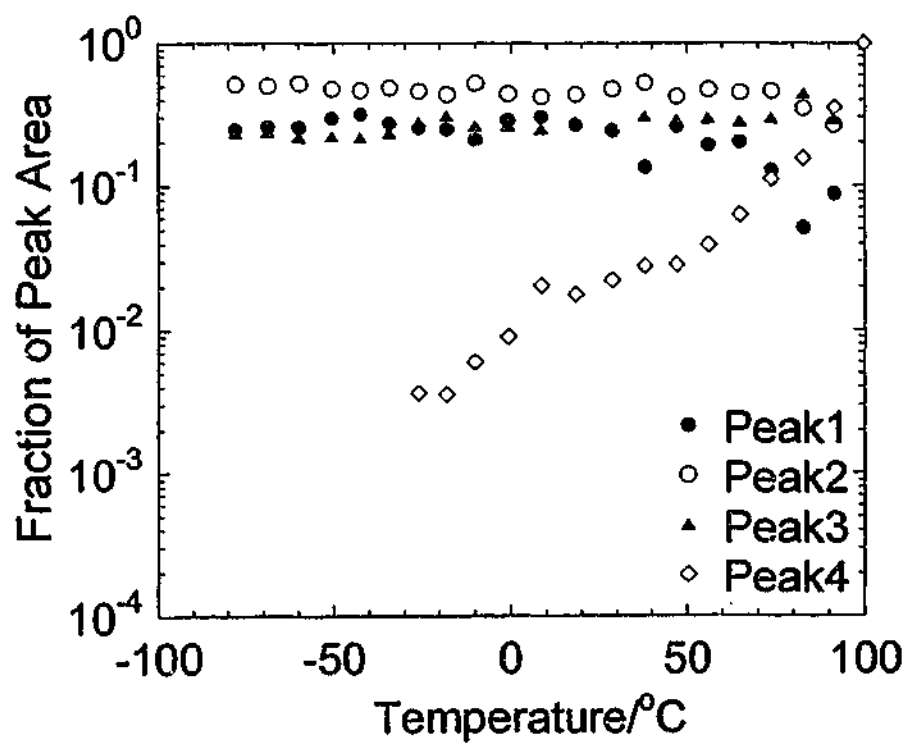**Figure 3.15** ^{19}F NMR Linewidth for P12TFSA as a function of temperature.

Figure 3.16 The area fraction of each component in ^{19}F NMR for P12TFSA as a function of temperature.

The fractions of the cations and anions that are, on average, undergoing translational motion are compared in Figure 3.17. It shows that the numbers of diffusing cations and anions are remarkably comparable, especially in phase II and phase I, probably indicating the association of the cations and anions in some way in the diffusion process.

The association of the cationic and the anionic diffusion is also supported by the diffusion coefficient measurement data [293]. First, the diffusion coefficients of the cations and the anions are very similar near the melting point. Second, the measured conductivity is smaller than the one calculated from the diffusion coefficients of the cations and the anions. The explanation is that the correlated cation-anion diffusion does not contribute to the conductivity.

This correlated cation-anion diffusion has been suggested to occur by an ion-pair mechanism where a cation and an anion are closely associated in the diffusion process [293]. However, the ion-pair mechanism is not supported by comparing the sizes of the ions and vacancies. If the ion-pair mechanism was effective, the cation vacancy and the anion vacancy would exist (or be created) in very close proximity. These correlated vacancies could not be separated as individual vacancy in PALS, but actually as a single evenly shaped empty volume the PALS can detect as a whole. According to the PALS results in section 3.2.4, the vacancy average radius ranges from 2.8-3.9 Å in the temperature range investigated. The average volume of vacancy is about $90 - 240$ Å^3. The radii of cation and anion are estimated to be 3.1 Å and 3.7 Å[v], respectively. The volume of a cation-anion pair is estimated to be 428 Å^3 at room temperature according to the powder X-ray diffraction data in Appendix A[vi]. Each vacancy can accommodate one cation or one anion, but not one ion-pair.

---

[v] Estimation is made using Chem3D, Cambridge Soft Corp..

[vi] Estimation is made assuming that each unit cell contains four cations and four anions, similar to that in P11TFSA.

A more possible explanation is a Schottky vacancy mechanism where a number of vacancies bearing positive or negative charges require the same number of vacancies bearing opposite charges to maintain neutrality. As a result, the same numbers of cations and anions leave their normal lattice positions to diffuse at the same rate. The cationic vacancy and the anionic vacancy are correlated, but not in as close proximity as in an ion-pair mechanism. Each vacancy can be detected in PALS as a mono-vacancy. The Schottky-type defects have been also suggested to be responsible for the translational motion of some ammonium salts and pyrrolidinium hexafluorophosphate, where the activation energies of anion and cation diffusion seem to show some association [55, 58, 230]. Therefore, a Schottky vacancy mechanism seems a plausible explanation of the diffusion mechanism in P12TFSA.
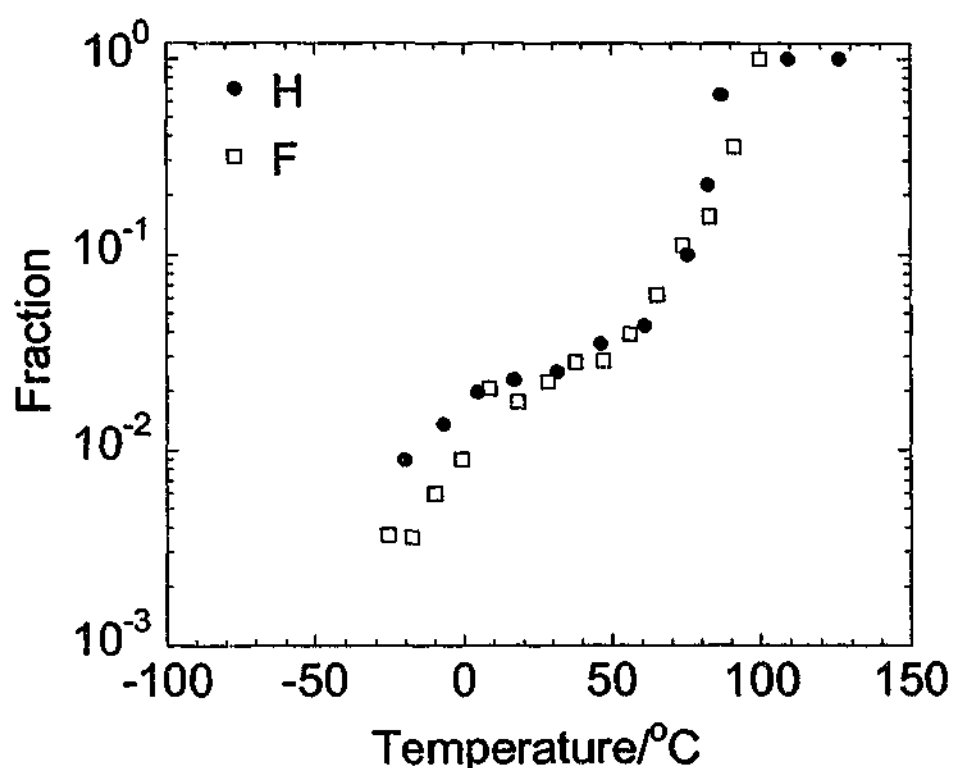

Figure 3.17 The fraction of the narrow components of ^{1}H and ^{19}F NMR as a function of temperature for P12TFSA. The narrow components correspond to diffusing ions.

3.2.6 Dielectric Response

Dipolar Response

The dielectric responses of P12TFSA are shown in Figure 3.18 and Figure 3.19. A broad peak of the imaginary part of dielectric permittivity ε" is observed in the high frequency range below –90.3 °C. The real part of dielectric permittivity ε' is almost independent of frequency at low frequencies, but drops on the high frequency end. These high frequency dielectric responses correspond to a relatively classic dipolar behavior [261], which could be assigned to the response of ionic rotation or the displacement of one ionic sublattice with respect to the opposite ionic one in the AC field. The ionic rotation is more likely at this low temperature, as the activation energy of ionic rotation is lower than that of the sublattice displacement. The rotational motions of both cations and anions are observed in the ^{1}H and ^{19}F NMR as discussed in section 3.2.5. The peak magnitude of the imaginary part, ε", shows a small jump and the peak frequency shifts to higher frequency at –87.7 °C, the phase IV>>III transition. A small step in the magnitude of the real part of dielectric permittivity ε' also occurs at –87.7 °C, suggesting a small change in the ionic rotation mechanism. It is worth noting that the phase below –87.7 °C could be trapped metaphase II' given the relatively fast cooling procedure during the experiment. The metaphase II' is not absolutely static. Some motions are still involved. Large amplitude molecular motions have also been reported in some glassy crystals such as cyclohexanol [141].

These dipolar responses are still observed between –87.7 ~ -57.2 °C with nearly constant magnitude and frequency range. Above –57.2 °C, the dipolar response is not detected in the imaginary part of dielectric permittivity ε" and is not obvious in the real part of dielectric permittivity ε'. There are two possibilities. Firstly, the dipolar response may be "drowned" in another dominant mechanism which will be discussed next. Secondly, a change may occur in the dipolar mechanism, causing the frequency to move out of the experimental frequency range.

Hopping-Charge Response

Above -77.6 °C, both the imaginary part ε" and real part ε' of dielectric permittivity show linear dispersions as a function of log-frequency in the low frequency range, corresponding to a hopping-charge mechanism [259, 261]. The charge hopping response is not obvious below -87.7 °C, which means either the charge hopping frequency is slower than the experimental low frequency limit, 20Hz, or the number of hopping charges is small and negligible compared to the dipolar response. From -77.6 °C to -18.2 °C, ε" displays a single dispersion over the entire frequency range and a gradual increase in the magnitude. In this temperature range, ε' shows a linear dispersion in the low frequency range a id a flat response in the high frequency range, corresponding to the instantaneous polarization ε_∞. The transition frequency shifts to higher frequencies with temperature. Both ε" and ε' do not change much between -18.2 °C and $+20.9$ °C, which covers the phase transition III>>II. Slight increases in the magnitudes of both ε' and ε" are observed in phase II from 20.9 °C to 50.6 °C. In phase I, the magnitudes of ε" and ε' increase steadily and jump dramatically near the melting point. Another unidentified mechanism, as displayed by an additional ε" peak, occurs above the melting point. Unfortunately, some of the ε' values obtained at high frequency and high temperature are negative, probably due to the instrumental limit, and are deleted here. The additional ε" peak may be attributed to the response of the electrode.
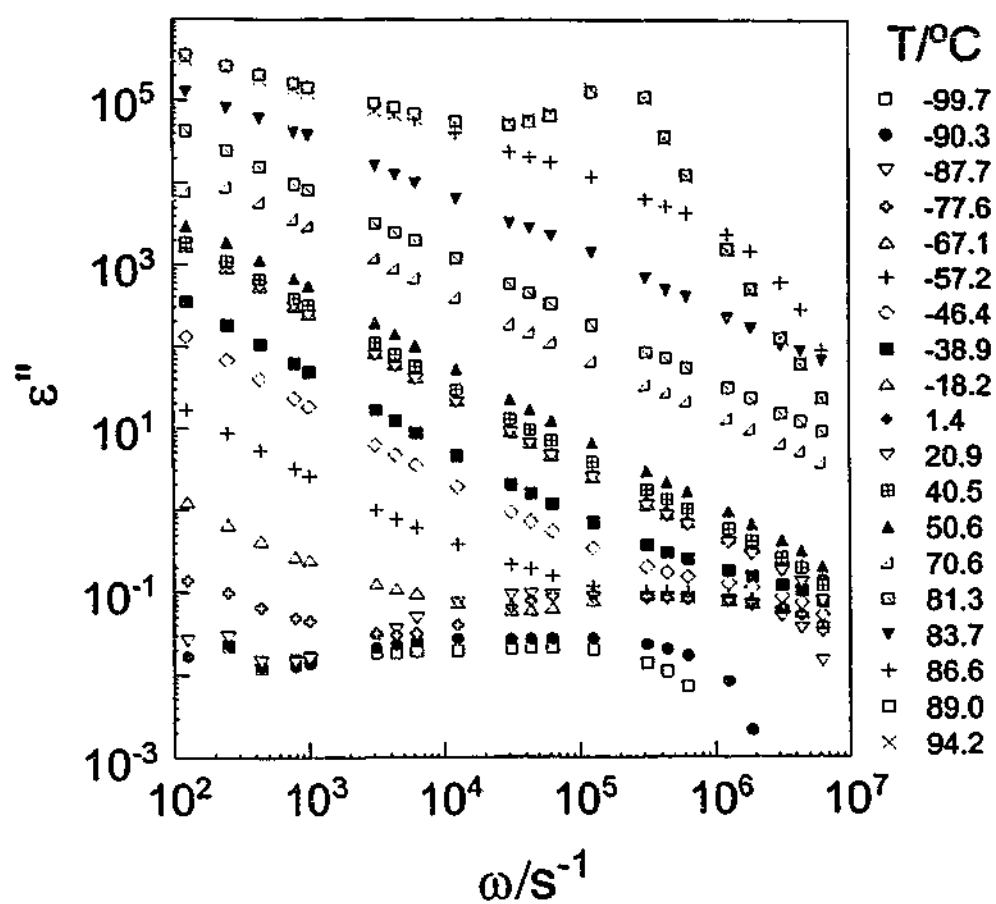
Figure 3.18 Imaginary part of dielectric permittivity of P12TFSA as a function of frequency at various temperatures.
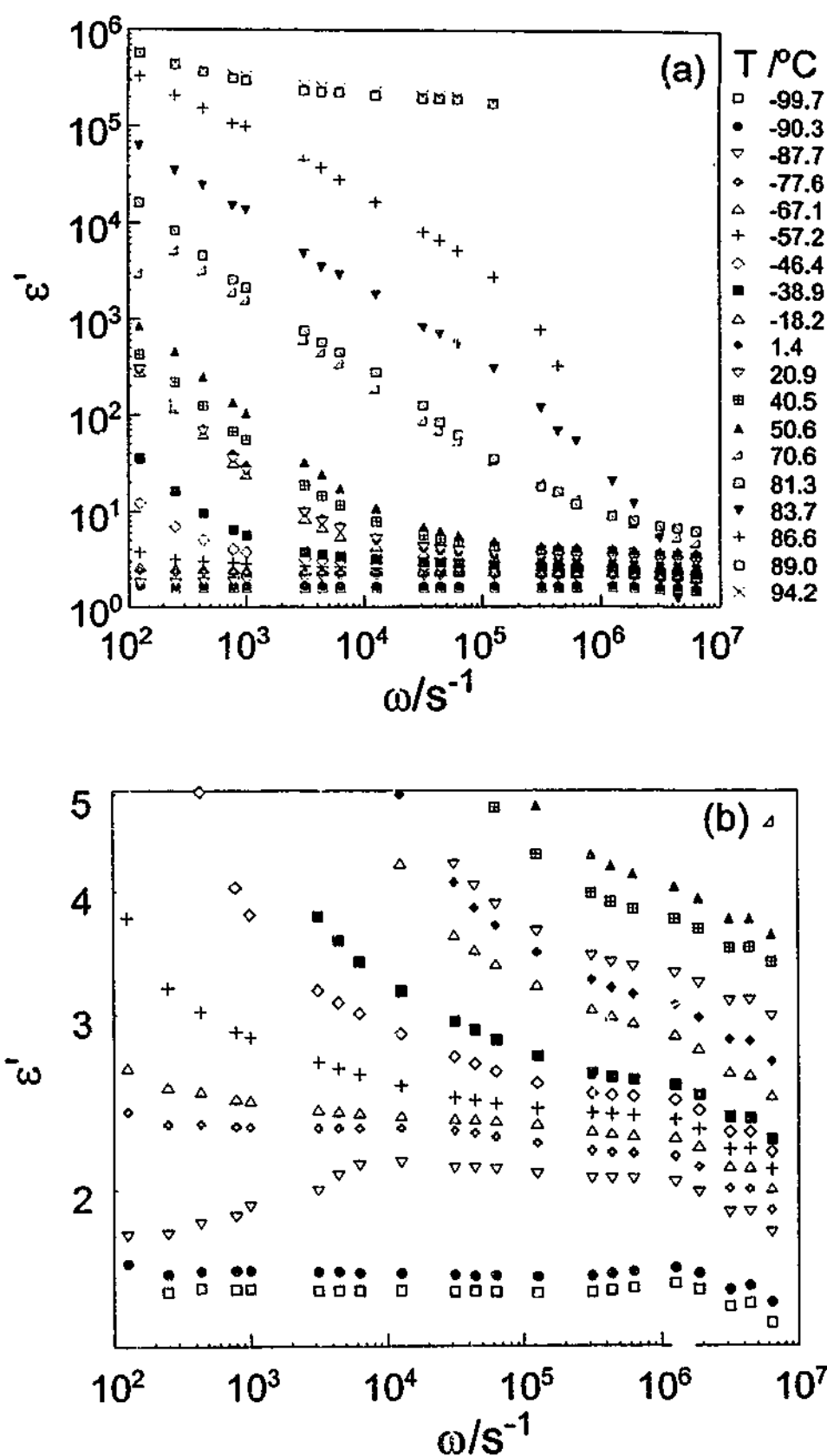
Figure 3.19 Real part of dielectric permittivity of P12TFSA as a function of frequency at various temperatures. (b) shows part of the expanded (a).

3.2.7 AC Conductivity

AC Conductivity vs. Temperature

The charge-hopping and dipolar responses with temperature are also clearly presented in AC conductivity, as shown in Figure 3.20. According to the dielectric studies as discussed above, the effect of dipolar response at 40 Hz is weak. Therefore, 40 Hz AC conductivity is dominated by DC conductivity. This is exhibited in Figure 3.20, which shows that DC conductivity and 40 Hz AC conductivity are very close at low temperatures. The discrepancy at high temperatures is probably caused by electrode polarization. 100 kHz AC conductivity contains contributions from both DC conductivity and dipolar response. The difference between the 40 Hz and 100 kHz conductivities may be assigned to the contribution from dipolar response.

40 Hz conductivity is almost flat at the level of 10^{-12} Scm^{-1} below -87.7 °C. It increases from -87.7 °C to -7 °C by four orders of magnitude, implying the substantial increase of DC conductivity in phase III. 100 kHz conductivity increases with temperature below -87.7 °C and shows a step at -87.7 °C near the phase IV→III transition. It then becomes stable for about 30 °C in phase III and increases with temperature up to -7.0 °C. This may indicate that the rotational motion accounting for the dipolar response already exists below phase III and is intensified at the phase IV>>III transition, probably due to either higher rotational frequency or an increase in the number of ions involved in the rotation. This rotational mechanism should not change much in phase III. The further increase in AC conductivity with temperature is probably attributed to the increased DC conductivity which becomes dominant in this temperature range as discussed in dielectric analysis and reflected by the similar values of 40 Hz and 100 kHz conductivities.

Between -7.0 °C and 45 °C, AC conductivity is relatively flat. Two "bumps" are observed at 16 °C and 30 °C. In phase I, AC conductivity increases rapidly up to the melting point and becomes almost flat above the melting point. It is worth noting that electrode polarization becomes more effective with temperature, which is reflected by a rapid decrease in AC conductivity with decreasing frequency [264]. The electrode polarization

also accounts for lower conductivity values at 40 Hz and 100 kHz than the DC conductivity at high temperatures as shown in Figure 3.20. Therefore, high temperature AC conductivity is not discussed in detail here.

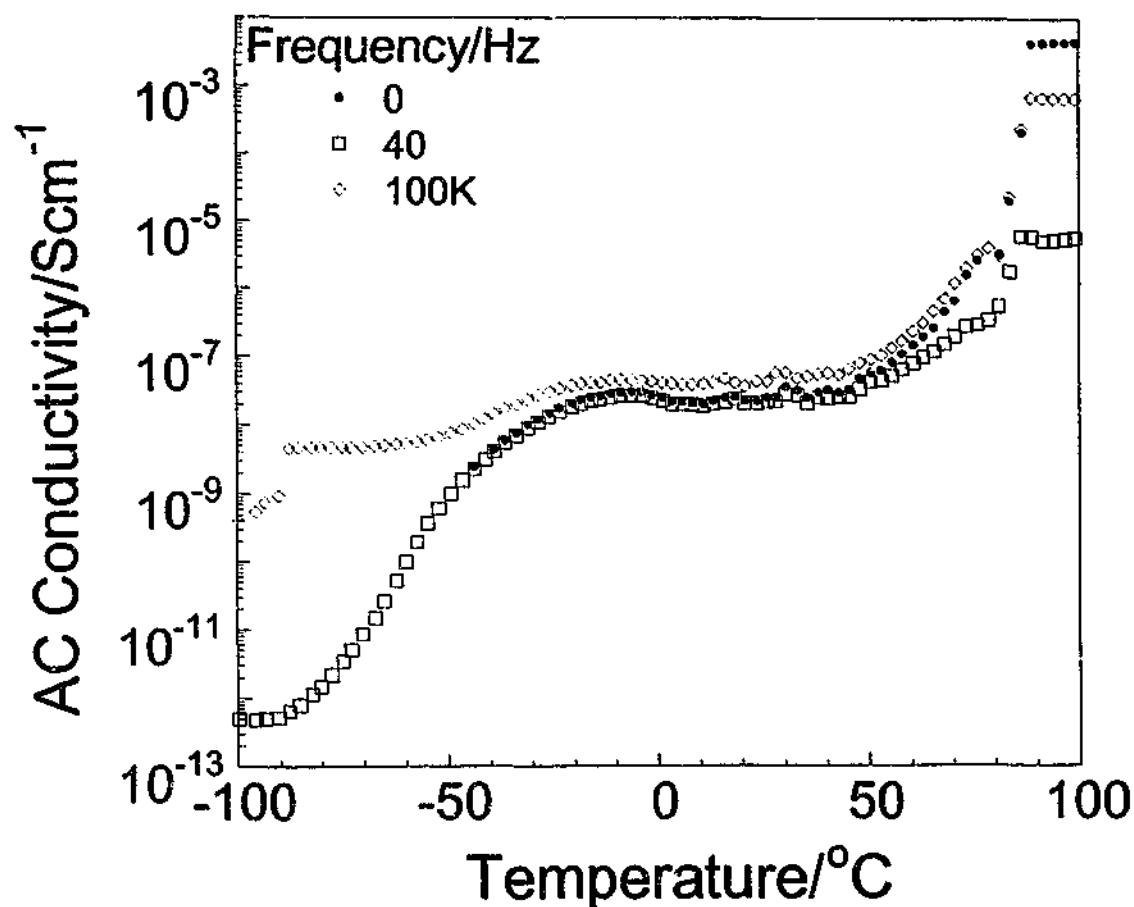**Figure 3.20** AC conductivities at 40 Hz and 100 kHz of P12TFSA as a function of temperature. DC conductivity obtained from Cole-Cole plots is shown here for comparison.

AC Conductivity vs. Frequency

AC conductivity as a function of frequency is first fitted by Equation 3.9 [264], as shown in Figure 3.21.

$$\sigma(\omega) = K\omega_p^{1-n_1}\omega^{n_1} + K\omega_p^{1-n_2}\omega^{n_2}$$

Equation 3.9

where ω_p is the ionic hopping rate and K is related to the concentration of mobile ions. More detailed definitions are given in section 2.3. The first term represents the low frequency dispersion and the second term represents the high frequency dispersion.
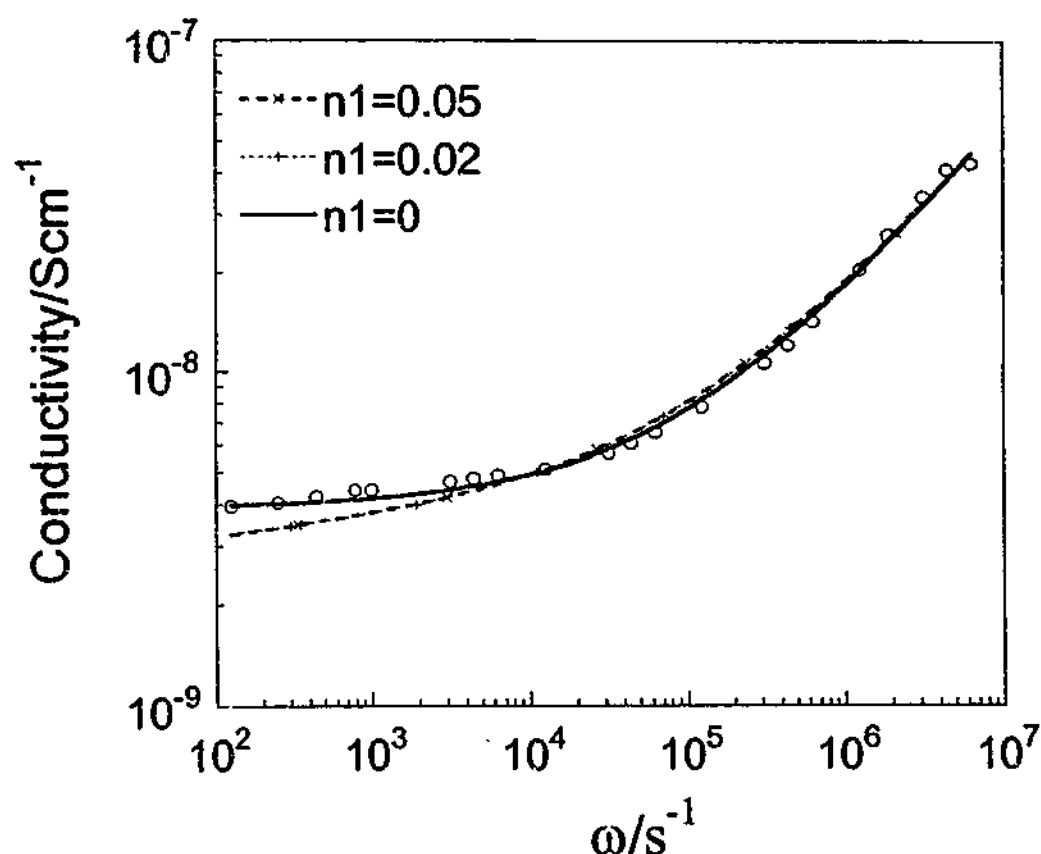
Figure 3.21 Curve fit of AC conductivity of P12TFSA at –38 °C by Equation 3.9. The circles are experimental values. The lines are the values of fits. n_2=0.58 gives the best fit in all the three fits.

The best fit was obtained when n_1=0. Almond et al. suggest that n_1=0 indicates that it is free of lattice crystalline imperfections or ionic motion restriction [264]. Equation 3.10 was used in all subsequent fits.

$$\sigma(\omega) = K\omega_p + K\omega_p^{1-n}\omega^n = \sigma(0) + A\omega^n$$

Equation 3.10

Some of the fitted AC conductivities are shown in Figure 3.22. Below −75 °C, n is close to 0.95. Between −75 °C and 70 °C, n is in the range of 0.5-0.9, values related to a dipolar or ion hopping mechanism [259, 260]. The resultant parameters ω_p and K are shown in Figure 3.23 and Figure 3.24.

The ionic hopping rate ω_P rises by four orders of magnitude from $1.9 \times 10^2 \, s^{-1}$ to $1.4 \times 10^6 \, s^{-1}$ in phase III. It drops slightly as the temperature reaches 14 °C, phase III>>II transition temperature. The hopping rate shows a small step when it enters phase II and remains constant in phase II. The hopping rate rises again in phase I.

KT is related to the number of hopping ions by [265]

$$K = \frac{Ne^2 a^2 \gamma c(1-c)}{RT}$$

Equation 3.11

where γ is a geometrical factor; a is the jumping distance; e is the electric charge and c is the concentration of mobile ions on N equivalent lattice sites per unit volume. The value of KT increases 15 fold from −80 °C to −40 °C and then exhibits a drop. It increases again in phase II and phase I. A substantial jump occurs near the melting point. K ranges from $3 \times 10^{-15} \, Scm^{-1}s$ at −80 °C to $2.2 \times 10^{-13} \, Scm^{-1}s$ at 68 °C, exhibiting less increase as compared with ionic hopping rate ω_p and thus less contribution to DC conductivity. Comparing the value of K to those of fast ionic conductors sodium-β" alumina ($1.5 \times 10^{-12} \, Scm^{-1}s$) and sodium-β alumina ($5 \times 10^{-12} \, Scm^{-1}s$) [264] indicates that the charge carrier number is significantly smaller in P12TFSA.

3.2.8 DC Conductivity

Conductivity vs. Temperature

DC conductivity as a function of temperature is shown in Figure 3.25. In phase III, conductivity increases continuously due to the increases in both ionic hopping rate and charge carrier number. From −60 °C to −10 °C, conductivity increases by nearly two orders

of magnitude. Above –10 °C, only a slight decrease in conductivity is observed. The conductivity is then relatively constant up to 40 °C. Two "bumps" are observed at 16 °C and 30 °C. Above 45 °C, conductivity rises dramatically by nearly five orders of magnitude in phase I and reaches 4×10^{-3} Scm^{-1} at the melting point. In the molten state, the conductivity is nearly constant.

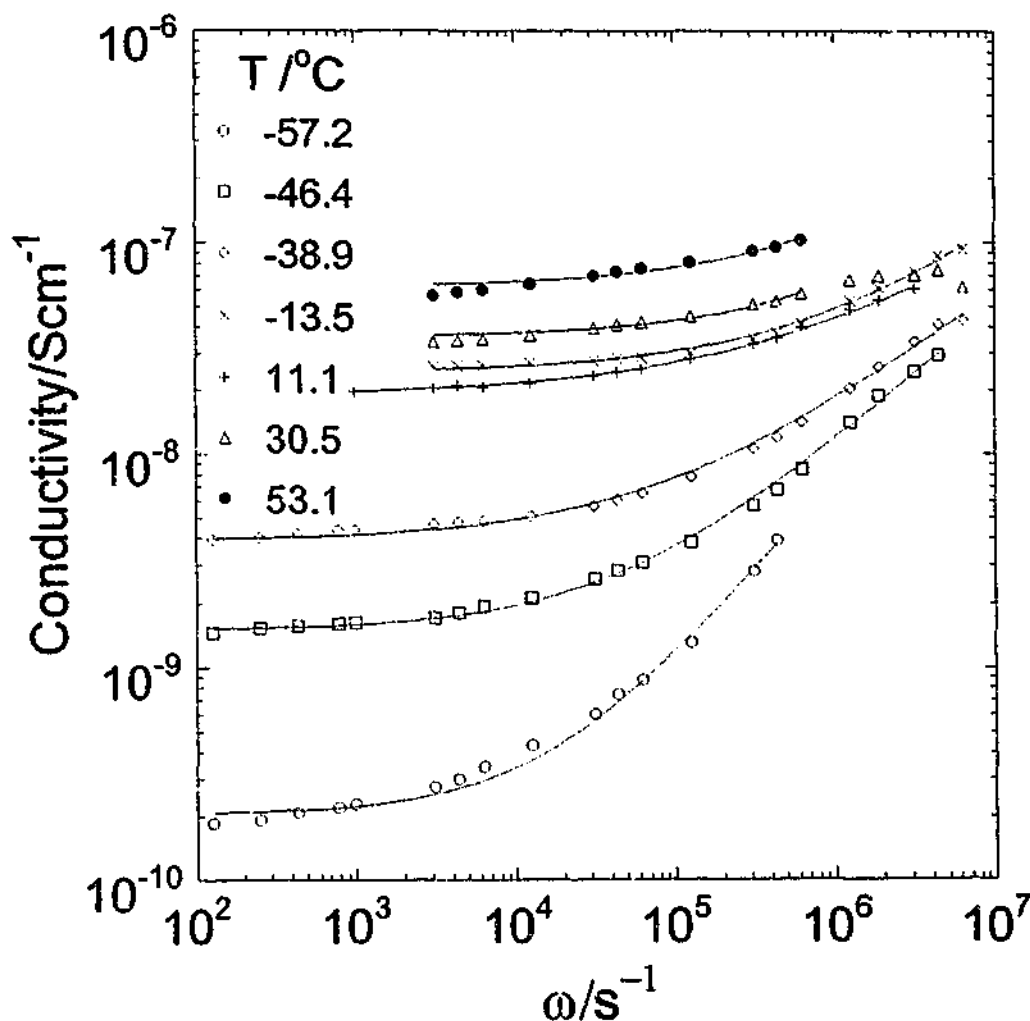Figure 3.22 Fitted AC conductivity as a function of frequency for P12TFSA. Below –50 °C, high frequency points are ignored in the fits due to the dipolar response as discussed in the text. Above –25 °C, some points at low frequency are omitted due to the effect of electrode polarization. The fits are conducted up to 70 °C. Above 70 °C, the fits are not reliable due to the strong interference of electrode polarization.

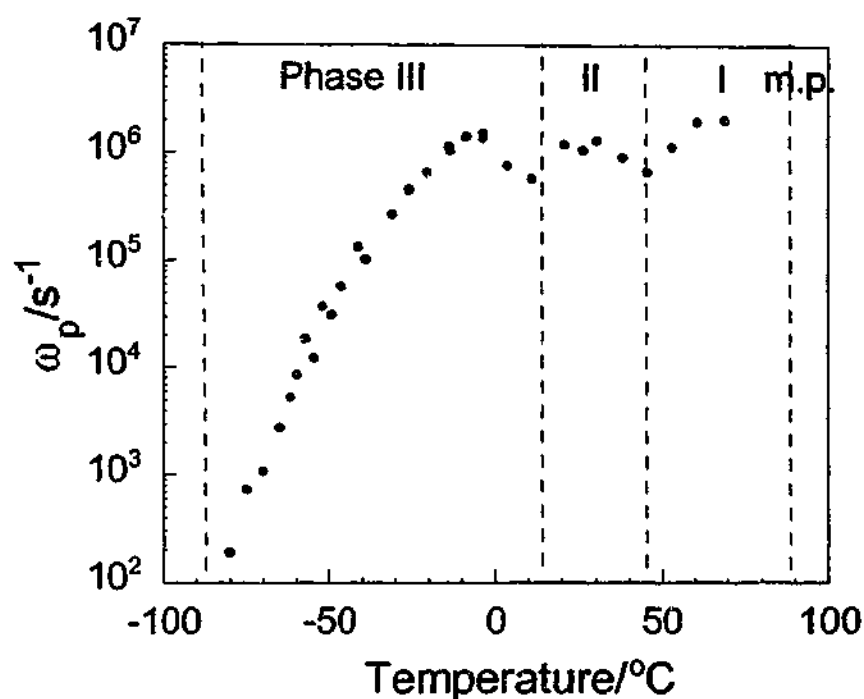**Figure 3.23 Hopping rate of P12TFSA as a function of temperature. ω_P is obtained by fitting AC conductivity to Equation 3.10. Dashed lines mark the phase transition temperatures.**
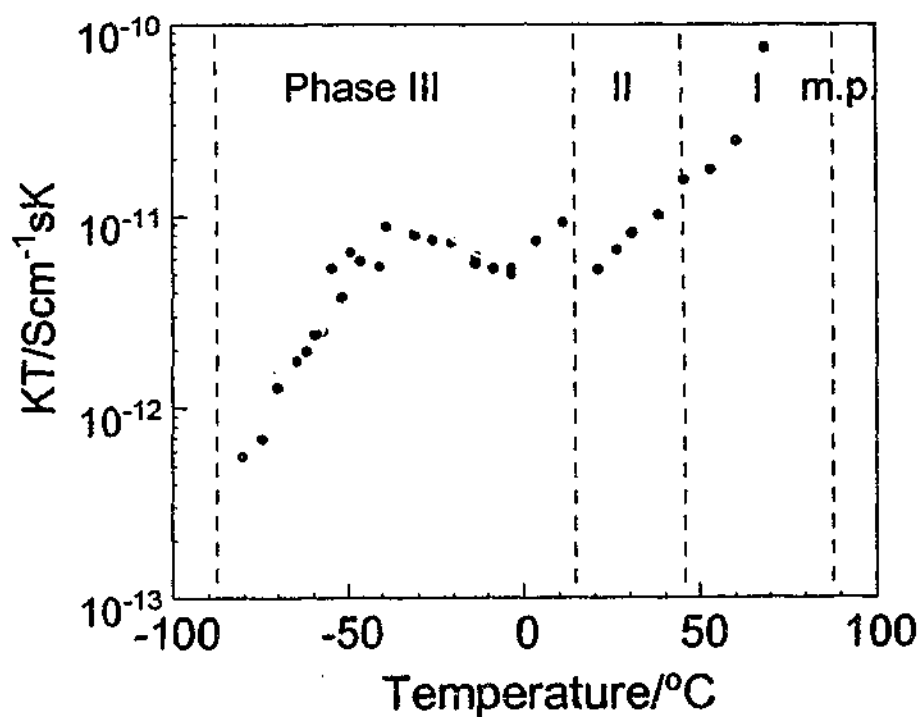

Figure 3.24 KT of P12TFSA as a function of temperature. KT is a function of charge carrier number. K is obtained by fitting AC conductivity to Equation 3.10. Dashed lines mark the phase transition temperatures.

In phase III, the conductivity shows non-Arrhenius behavior. It is possible that the activation energy for ionic hopping rate or the number of hopping ions is temperature dependent. An attempt is made to fit the phase III conductivity to a VTF Equation 3.12, as shown in Figure 3.26.

$$\sigma = \sigma_0 \exp\left(-\frac{E_a}{R(T-T_o)}\right)$$

Equation 3.12

where the E_a is the pseudo activation energy; T_o indicates the configurational ground state temperature. Ea and T_o are related by $D=E_a/RT_o$ by considering the relaxation dynamics, where D is the so-called strength parameter. D^{-1} indicates the fragility [16].

VTF behavior is normally observed in amorphous materials, such as glasses and polymers, where a free volume mechanism is generally established to account for the VTF behavior. VTF behavior has also been found in some plastic crystals, such as Li_2SO_4, $LiNaSO_4$ and $LiAgSO_4$ [186]. Sophisticated studies of Li_2SO_4 have suggested that the conduction mechanism is "paddle-wheel" rather than free volume [172, 180]. The VTF behavior has been suggested to result from, akin to the ionic transport in polymers, the disordered environment of mobile ions [194]. However, pure Na_3PO_4, which is also believed to be a plastic crystal and whose mobile cations are supposed to experience disordered anion environments, displays an Arrhenius behavior [12]. It is more plausible to consider that the different degrees of deviation from the Arrhenius behavior are attributed to the different fragilities of these plastic crystals.

In the case of P12TFSA, best VTF fitting is obtained when T_o=-90 °C. This temperature is very close to the phase IV>>III transition temperature. If free volume concepts are useful here, it could indicate that transport volume only becomes effective from phase III, which could be attributed to the formation of vacancies or the lattice expansion. Indeed, the volume expansion experiment in section 3.2.3 does show a substantial increase in the sample volume in phase III. The pseudo activation energy E_a obtained is 2.4 kJmol^{-1} in phase III. The strength parameter D was calculated to be 1.58. This indicates a relatively fragile material [25]. The relatively high fragility could be explained by the less symmetric

- 139 -

cationic shape and a less symmetric crystal lattice (monoclinic according to appendix A) [147]. A glass transition T_g which is normally expected above T_o is missing in the DSC trace. The possible reason is that, for a high fragility system, T_g/T_o is close to 1 [25]. The glass transition probably occurs immediately following the phase IV>>III transition and is hidden under the phase IV>>III transition peak.

Conductivity vs. Time

The stability of P12TFSA conductivity in phase III (7 °C) and phase I (56 °C) as a function of time is shown in Figure 3.27. At 7 °C, the conductivity drops from 9.2×10^{-9} Scm^{-1} to 6.5×10^{-9} Scm^{-1} in the first 60 hours and then becomes stable. At 56 °C, P12TFSA maintains a constant conductivity for one week. The decrease in conductivity at 7 °C might be attributed to the reduced number of extended defects during the measurement. Extended defects such as dislocations and grain boundaries can be produced by mechanical handling or thermal treatment. They provide effective tunnels for pipe diffusion which are relatively significant at low temperature due to the small activation energy [153]. Pipe diffusion becomes less effective at high temperature, which could account for the relatively constant conductivity at 56 °C.
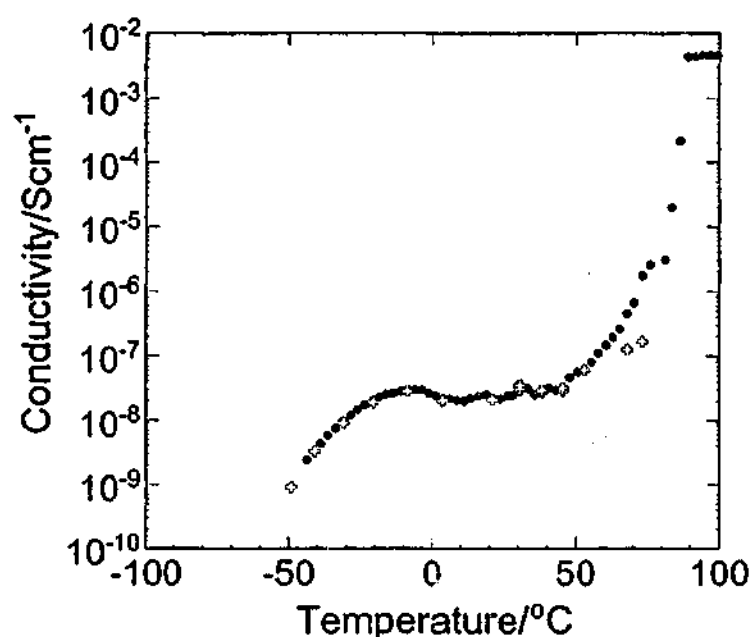
Figure 3.25 DC conductivity for P12TFSA as a function of temperature. Solid circles are the values obtained from Cole-Cole plots. "+" are the values obtained by AC conductivity fitting.
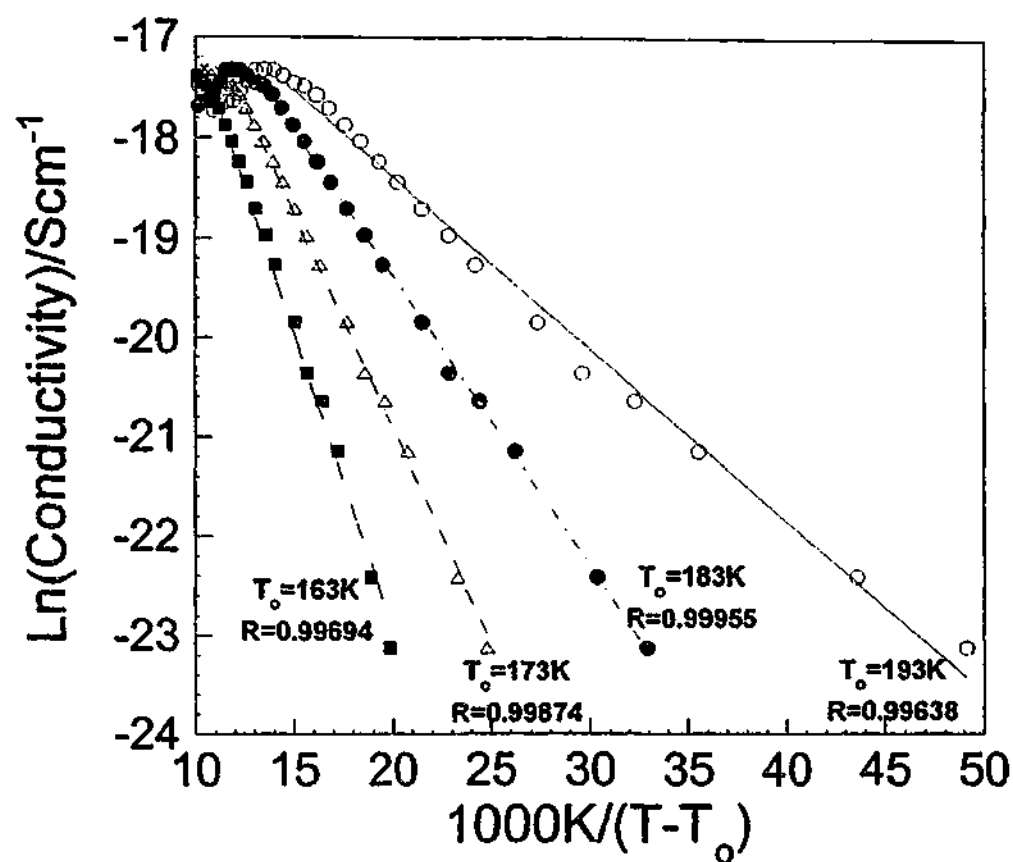
Figure 3.26 VTF fitting of conductivity for P12TFSA in phase III as a function of $T-T_o$. T_o is tested as 163K, 173K, 183K and 193K. R is the correlation coefficient of the curve fit.
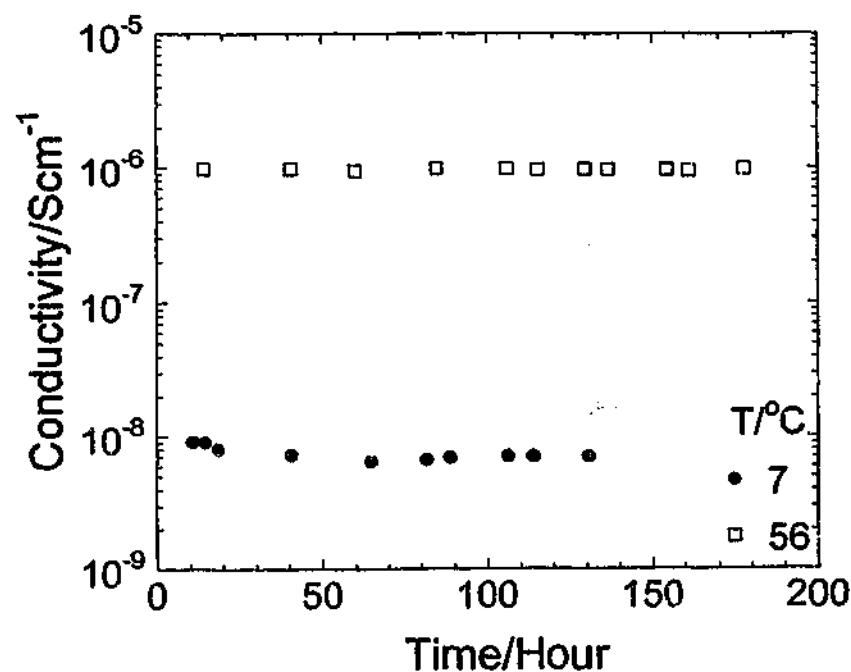

Figure 3.27 Time dependence of conductivity for P12TFSA at 7 °C and 56 °C.

3.3 Conclusions

3.3.1 Microstructure, Ionic Motion and Phase Transitions

The above discussion on the microstructure, ionic motion and conductivity of P12TFSA in different phases may be summarized as follows:

1. Below phase IV>> III (below –87 °C)

The phase below –87.7 °C depends on the cooling rate from room temperature. A slow cooling procedure, for example 1 °Cmin^{-1}, produces stable phase IV whilst relatively fast cooling produces frozen metastable phase II'. The orientational glass transition and the following crystallization to form phase IV involve a lattice contraction according to the volumetric expansion results. The dielectric studies indicate that the metastable phase below –87.7 °C is not static, but is involved in dielectric relaxation. The DC conductivity is almost constant at the level of about 10^{-12} Scm^{-1}.

2. Phase IV>>III (at –87 °C)

This phase transition involves the largest entropy change, 10.3 Jmol^{-1}K^{-1}, among the three solid-solid phase transitions. It is accompanied by a volume contraction. However, the motions are intensified, which results in a step in dielectric magnitude and higher motional frequency.

3. Phase III (-87 °C ~ -10 °C)

The volume expands substantially, accompanied by a jump in the DC conductivity by four orders of magnitude in phase III. Both the number of charge carriers and hopping rate increase dramatically, which account for the rise in the conductivity. However, only a small fraction of ions have translational mobility in this temperature range. At –20 °C, only 0.9% cations and 0.3% anions are detected diffusing by NMR. Most of the ions maintain positional order and undergo rotational motion. The cations execute anisotropic rotation in addition to CH$_3$ group C$_3$ rotation. Anions are in three different sites. More

than 75% of the anions are present in two of the sites and appear to undergo CF_3 rotation. About 25% of the anions in a third site are rigid. The volumetric expansion has little effect on the rotational motion. The rotational motions are relatively stable in this temperature range, reflected by the relatively constant ^1H and ^{19}F NMR linewidths as well as the steady magnitude and frequency of dielectric response.

4. Phase III>>II (-10 °C ~ 16 °C)

Phase III>>II shows a long tail on the low temperature side in the DSC trace, starting at about -10 °C. It is also characterized by a discontinuity in the thermal expansion.

More vacancies are created in the transition while the vacancies expand at the same rate as in phase III, probably due to thermal expansion. Both the size and the number of the vacancies increase by a step at 14 °C, indicating a dramatic lattice structure transformation which corresponds to a peak in the DSC trace. The volume also increases by a step at 14 °C.

In this broad transition temperature range, the rotational motions of both the cations and anions become more active as reflected by the line narrowing in ^1H and ^{19}F NMR. Cations start to develop another anisotropic rotation while 75% of the anions transform to isotropic rotation and the remaining static anions start to rotate. In contrast to the substantial changes in ionic motions and microstructure, the DC conductivity is nearly constant during the transformation, showing a slight drop.

5. Phase II (16 °C ~ 45 °C)

This temperature range covers the phase II>>I transition which appears to have a long tail on the low temperature side. The size and number of vacancies increase steeply whilst the volume expansion shows a lower thermal expansion compared to phase III and phase I. The cations are still developing anisotropic rotation in this phase reflected by the continuing line narrowing. 75% of the anions undergo isotropic motion and the remaining anions perform anisotropic rotation superimposed on the C_3 rotation of the CF_3 groups.

DC conductivity increases slightly due to the increased number of charge carriers, whilst the ionic hopping rate is nearly constant in this temperature range.

6. Phase I (45 °C ~ 88 °C)

Phase II>>I transition is characterized by the increases in vacancy size and volumetric expansion by small steps. In phase I, the vacancies expand continually whilst the number remains constant. The overall vacancy void increases continually, which is also reflected by the increase in sample volume. The plasticity shows a jump in phase I compared to in phase II and III and still increases with temperature.

The positionally ordered cations perform anisotropic rotation while most anions rotate isotropically. The rest of the anions transform from anisotropic to isotropic rotation. All the anions are rotating isotropically at the melting point. The fractions of both cations and anions moving translationally rise from about 2.8% at 40 °C to 100% at 88 °C, which causes the collapse of the crystal lattice and results in the melting. The ionic hopping rate also increases in phase I. The diffusion coefficient of cations reaches 3.2×10^{-10} s^2m^{-1}. The anions display the same level of diffusion coefficient at the melting point [293].

3.3.2 Defects and Conduction

According to the activation energies and correlation times for cationic rotation and diffusion, as shown in Table 3.3, the ionic rotation and diffusion do not display obvious correlations. Defects are more likely to be responsible for the conduction mechanism in P12TFSA.

Defects are important characteristics in P12TFSA. It is inferred from the PALS data that the dominant defects are point defects by comparing the vacancy size (2.8-3.9Å in average radius) and ionic sizes (3.1Å for cation and 3.7Å for anion). The vacancy is of a Schottky type. Extended defects, such as dislocations and grain boundaries, are also clearly observed in SEM. The defects account for the plasticity.

The conduction mechanism seems to be closely associated with transport volume or vacancies. In phase III, the DC conductivity displays VTF behavior with T_o at −90 °C,

coinciding with the phase IV>>III transition temperature where the volumetric expansion occurs. The expanded volume could be attributed to thermal expansion or increased vacancy volume, which provides spaces for more ions to leave their normal lattice positions at higher probability. This is confirmed by the increased number of charge carriers having higher hopping rate. The association of conduction with transport volume is also reflected in phase I where the overall vacancy volume increases and the conductivity rises by four orders of magnitude. Both the number and hopping frequency of diffusing ions show a jump in this phase.

Pipe diffusion due to grain boundaries and dislocations also plays a role in conductivity, especially at low temperature. Annealing diminishes the extended defects and reduces conductivity. The conductivity nevertheless is relatively stable in phase III and I, which indicates the stability of P12TFSA and the potential of practical use as electrolyte materials.

The paddle wheel mechanism seems more suitable for some ionic plastic crystals, such as Li_2SO_4 and Na_3PO_4, composed of small ions which can be attached to the relatively bigger and rotationally disordered opposite ions and be transported [172, 201]. For molecular plastic crystals and ionic plastic crystals composed of comparable sized cations and anions, defects are more significant for the conduction mechanism.

There is a discrepancy between the ionic hopping rate detected by NMR and conductivity. The value is 5×10^8 s^{-1} by NMR and 1×10^6 s^{-1} from AC and DC conductivity at room temperature. This coincides with the observation that the conductivity predicted from the diffusion coefficient obtained by NMR is higher than the measured value [293]. The discrepancy suggests that the ions might undergo short-range translational motion, which can be detected by NMR, but does not contribute to the DC conductivity. The same reason might also account for the discrepancy between the number of charge carriers as reflected by kT obtained from AC and DC conductivity and the fraction of mobile ions obtained from NMR.

Chapter 4 N-methyl-N-methylpyrrolidinium bis(trifluoromethanesulfonyl)amide Salt

4.1 Introduction

A number of organic salts based on ammonium or nitrogen containing ring structured cations have been studied [32, 34, 53, 59, 166, 230, 235, 238, 239]. It has been found that the length of the alkyl substituent influences the properties of the salts. For example, an increase in the alkyl chain length results in depressed melting point in the series of $C_nH_{2n+1}NH_3Cl$ (n=4-10) [59, 230], P1xTFSA [32, 235], P1xBF$_4$ [239] and P1xPF$_6$ [238]. The length of the alkyl substituent also plays an important role in determining the ionic motion and plastic crystal behavior. In the $C_nH_{2n+1}NH_3Cl$ (n=4-10) system, solid-solid phase transitions have been observed in all the family members, implying that they all belong to rotator phases. The cations undergo one dimensional uniaxial rotation along the ionic long axis and two dimensional self-diffusion. The activation energy of rotation is nearly independent on the length of the alkyl chain while that of the self-diffusion increases with the number of carbons [230]. In contrast, in the families of P1xTFSA, P1xBF$_4$, P1xPF$_6$, only the salts with short carbon chains (x≤3) display one or more solid-solid phase transition(s). The salts with longer carbon chain do not exhibit any solid-solid phase transitions, such as P14BF$_4$, P17PF$_6$, P16TFSA and MP4TFSA [32, 166, 238, 239]. The lack of a solid-solid phase transition suggests that the salts do not possess rotational disorder in their solid states, which is attributed to the higher energy barrier to the rotation due to the bulky alkyl substituents [32]. It is interesting to note that when the substituent is ethyl, as in the cases of P12TFSA, P12BF4 and MP2TFSA, the lowest fusion entropy and/or the richest solid-solid phase transitions have been observed [32, 166, 235, 239]. These indicate that the plastic crystal behavior is related to the length of the alkyl substituent.

In this chapter, P11TFSA is studied on the hypothesis that the shorter methyl substituent as compared to the ethyl group in P12TFSA brings about different plastic crystal behavior.

P12TFSA and P11TFSA are compared in order to obtain a better understanding about the relationship between ionic motion, microstructure, mechanical properties and conductivity in the P1xTFSA family.

4.2 Results and Discussion

4.2.1 Thermal Analysis

The DSC thermogram of P11TFSA, as shown in Figure 4.1, exhibits three phase transitions below the melting point. There is a weak endothermic transition peak at -41 °C, which is assigned to the phase IV$\rightarrow$III transition. It is followed by a broad phase transition III$\rightarrow$II, which starts at about -19 °C, reaches a peak at 26 °C and completes at 36 °C. Phase transition II$\rightarrow$I is another broad transition. The onset of this transition is indiscernible. It completes at 81 °C. A sharp peak corresponding to the melting point is observed at 137 °C.

The shape of phase III$\rightarrow$II transition is similar to that of the broad phase transitions in P12TFSA; a long tail on the low temperature side combined with a sharp completion. The phase II$\rightarrow$I transition is characterized by a completion at 81 °C without a distinguishable onset. Akin to P12TFSA, as well as other plastic crystals [64], these broad phase transitions suggest that progressive transformation occurs over a large temperature range in P11TFSA.

The enthalpy and entropy data are shown in Table 4.1. The smaller solid-solid entropy changes and higher fusion entropy of P11TFSA compared to P12TFSA suggest that P11TFSA has less rotational freedom than P12TFSA. The fusion entropy is 51.1 $Jmol^{-1}K^{-1}$, which is much higher than 20 $Jmol^{-1}K^{-1}$, the criterion for the existence of plastic crystal as suggested by Timmermans [23]. The sum of the three phase transition entropies is about 40% of the fusion entropy, which again does not follow Timmermans' theory of a high value of the transition entropy [23].

The violation of Timmermans' theory could be attributed to the following reasons. (1) The rotational motion occurs, but in a restricted way. The occurrence of an internal or anisotropic rotation normally requires less entropy change than an isotropic rotation in the

- 147 -

solid state and thus results in higher fusion entropy at the melting. (2) As suggested previously, fusion entropy equal to or higher than 20 $Jmol^{-1}K^{-1}$ could be a reflection of the fact that Timmermans' observations applied mainly to molecular compounds whereas in the case of ionic plastic crystals, potentially only the cation or the anion possesses rotational degrees of freedom in the plastic phase [235]. Therefore, higher fusion entropy is required to activate the motion of the other ions. This suggestion has been supported by a number of ionic plastic crystals. For example, $[(CH_3)_4N]InBr_4$ possesses both cationic and anionic rotational disorder. It has more solid-solid phase transitions and higher transition entropy than $[(C_2H_5)_4N]InBr_4$ which is composed of ordered $InBr_4^-$ and disordered cations [225]. Another example is the N-Methyl-N-alkylpyrrolidinium hexafluorophosphate family where the symmetrical anion allows both cations and anions to be involved in the rotational disorder. Small fusion entropy of about 20 $Jmol^{-1}K^{-1}$ has been observed for a number of salts in this family [238]. The rotational motion of both the $P11^+$ cations and the $TFSA^-$ anions will be studied and discussed later in this chapter.
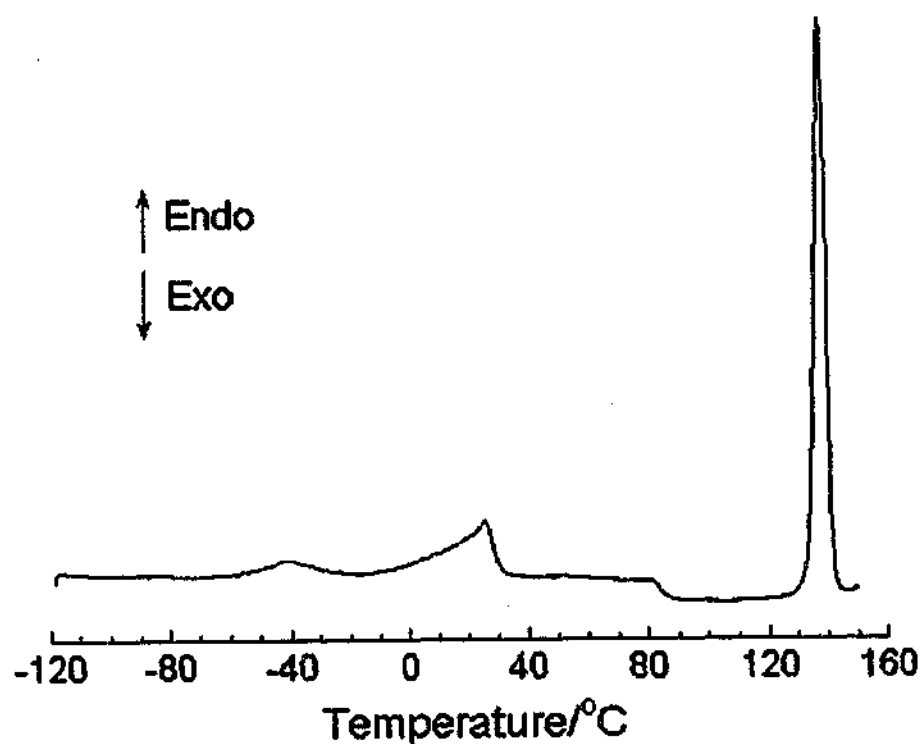

Figure 4.1 DSC trace for P11TFSA.

- 148 -

Table 4.1 Phase transition temperatures, enthalpies and entropies of P11TFSA. [a] Peak temperature. [b] Onset temperature.

Phase Transition	Temperature/°C ±2 °C	$\Delta H/kJmol^{-1}$ ±5%	$\Delta S/Jmol^{-1}K^{-1}$ ±5%
Phase IV>>III	-41^a	1.55	6.7
Phase III>>II	26^a	2.94	9.8
Phase II>>I	81^a	1.27	3.6
Melting Point	137^b	20.95	51.1

4.2.2 Scanning Electron Microscopy

The SEM micrographs of P11TFSA are shown in Figure 4.2. The particle size is smaller than that of P12TFSA due to the synthetic procedure. Similar to the spherical powders of P12TFSA (as in section 3.2.2) and P1xBF$_4$ (x=1-3) salts which are in their plastic crystalline phases [290], P11TFSA powders exhibit spherical morphology, suggestive of the plastic crystalline phase. However, compared to P12TFSA, the spherical powders of P11TFSA show less surface features, more regular shapes and sharper edges. Parallel steps are observed on the surface of the particles. These could be slip lines, evidence of plastic deformation which occurs as a result of sample handling. No obvious, dense slip lines, as observed in P12TFSA, are seen here at the same magnification scale as the SEM of P12TFSA. The possible occurrence of plastic deformation but with a lower number of slip planes probably suggests that the plasticity of P11TFSA is less than P12TFSA.

It has been suggested that the plasticity is related to the fusion entropy [37, 153]. As discussed in section 3.2.1 and 4.2.1, the fusion entropies for P11TFSA and P12TFSA are 51 $Jmol^{-1}K^{-1}$ and 25 $Jmol^{-1}K^{-1}$, respectively. This seems to confirm that lower fusion entropy corresponds to easier plastic deformation.

A mirror feature is observed in Figure 4.2 (c), probably indicative of twins. Twin formation is thought to be the result of anisotropic intermolecular forces and anisotropic molecular shape [294]. Twinning has also been found to be responsible for deformation of some plastic crystals, such as dl-camphor [164]. The mirror feature shown here suggests that plastic deformation of P11TFSA might also be associated with twinning.
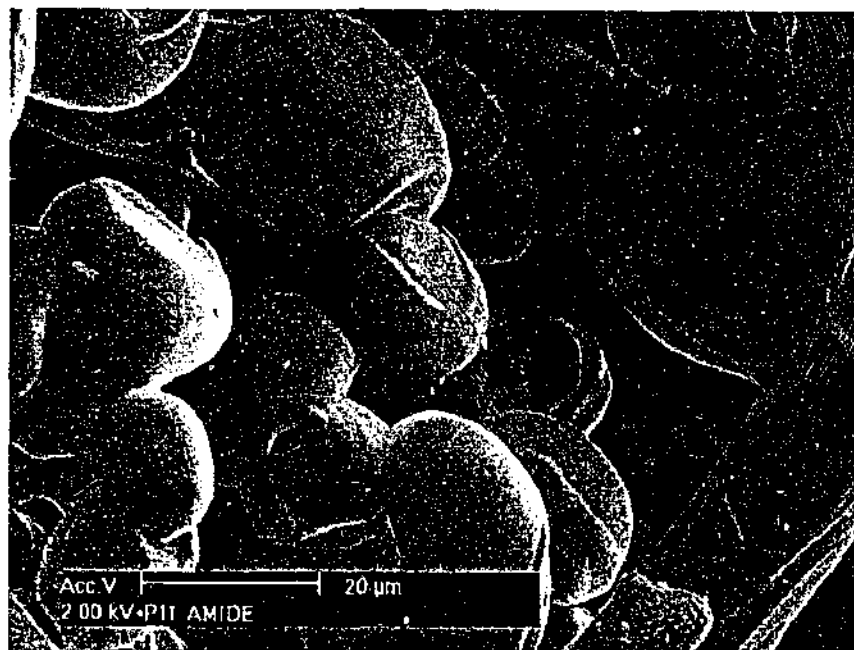
(a)
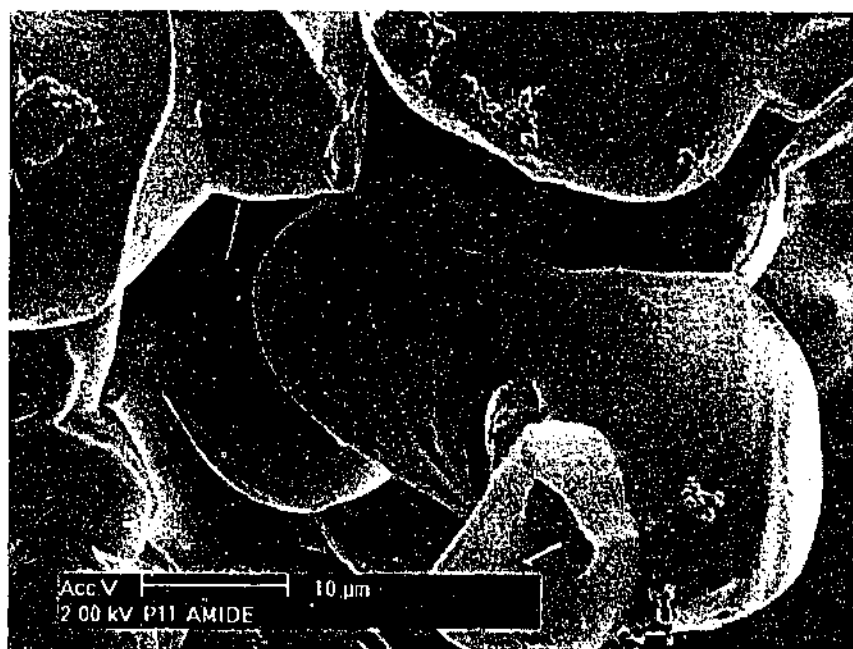
(b)
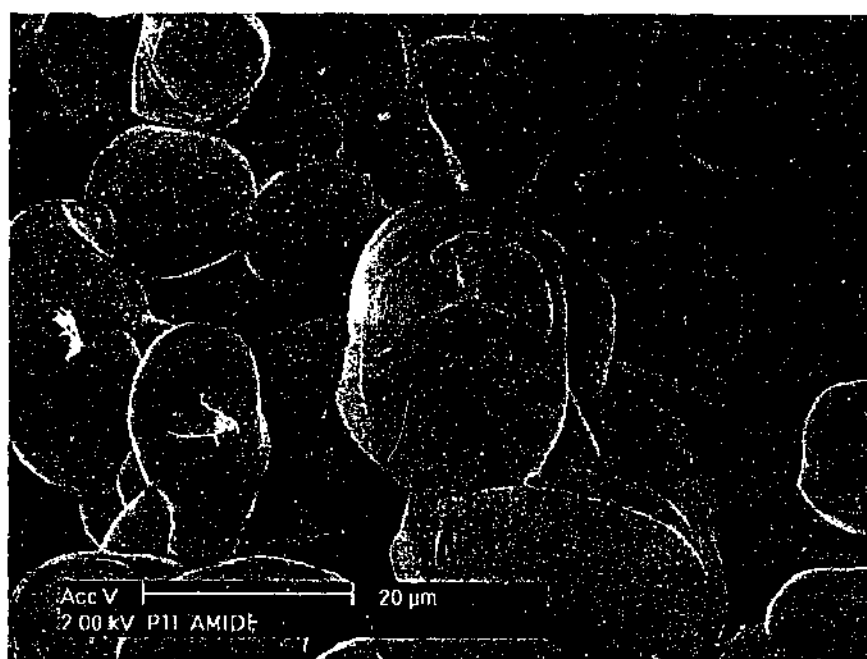
(c)

Figure 4.2 SEM of P11TFSA at room temperature. (a) and (b) show parallel steps. (c) shows mirror features.

4.2.3 Mechanical Properties

Isothermal Analysis with Changing Forces

The deformation of P11TFSA is shown in Figure 4.3. A dent was left on the sample and no obvious fracture or cracks were observed after each experiment, indicating plastic deformation. The penetration depth is about 4% of the sample thickness when 2 N force was applied at −17 °C. Similar to P12TFSA, the penetration depth shows a remarkable increase in phase I compared to phase II and phase III. The depth of probe penetration at 102 °C is about 5 times that at −17 °C. Permanent deformation of P11TFSA without failure indicates better plasticity than normal ionic crystals. Moreover, the plasticity increases with temperature. Relatively easier dislocation motion accounts for the plasticity, as discussed for P12TFSA.
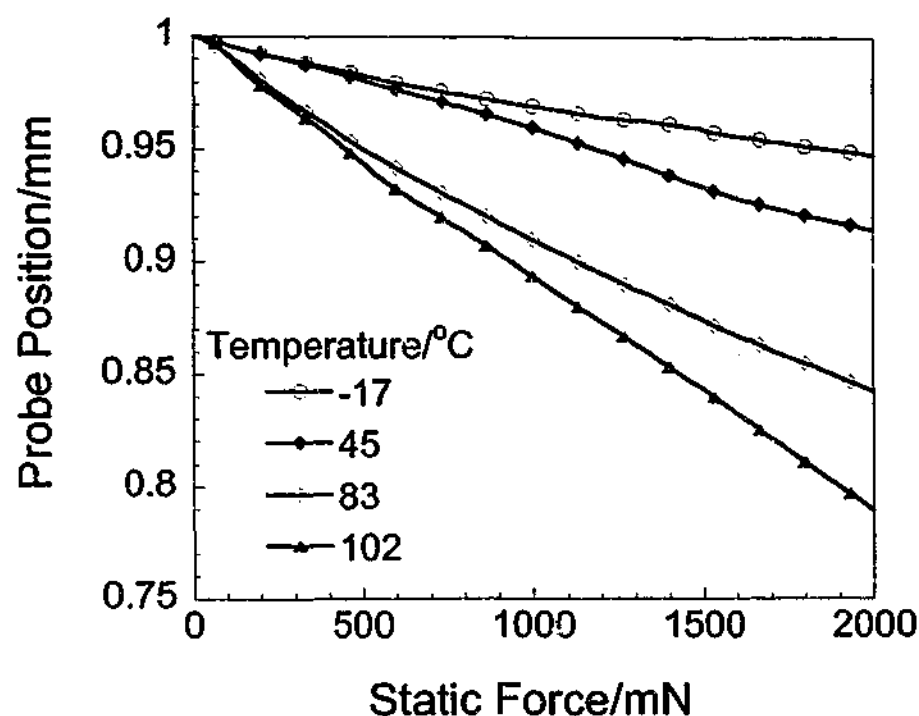
Figure 4.3 Deformation of P11TFSA as a function of static force at various temperatures. Static force starts at 1 mN and increases by 50 mNmin^{-1}. The sample is about 1 mm in thickness and 6 mm in diameter. The area of the probe tip is 0.78 mm^2.

Volumetric Expansion

The volumetric expansion is shown in Figure 4.4. P11TFSA displays less volumetric expansion in phase IV and phase I. The volume expands continuously in phase III and phase II by different expansion coefficients as indicated by the dashed lines. The first process occurs from –40 °C to about –15 °C, in phase III. The second process is in the range of –15 °C to 36 °C, covering the broad phase transition III→II from onset to completion. Process 3 occurs over the whole temperature range of phase II.

Both P12TFSA and P11TFSA volumetric expansion results correspond well to the phase transitions as observed using DSC. Relatively sharp phase transitions, e.g. the phase IV→III and phase III→II transitions of P12TFSA, correspond to discontinuous volume change while broad phase transitions are related to gradual volume expansion.

- 152 -
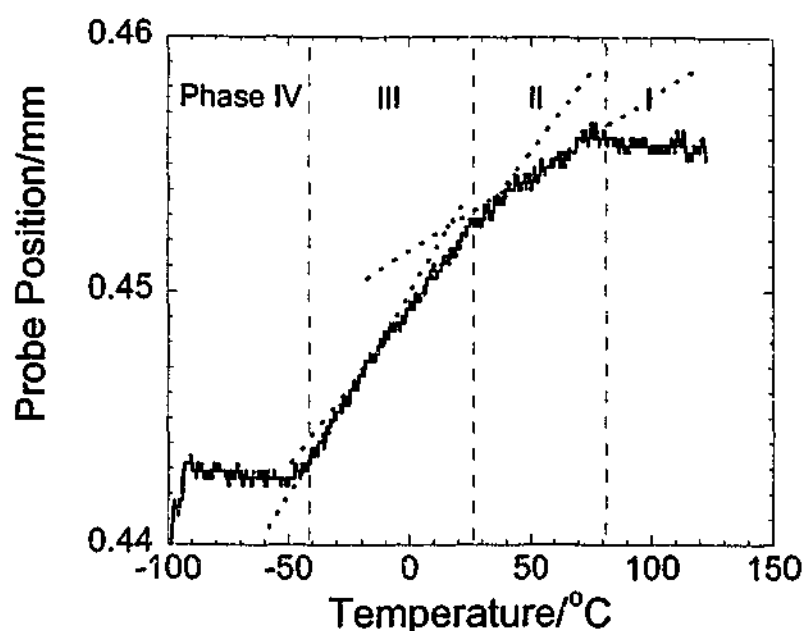
Figure 4.4 Volumetric expansion behavior for P11TFSA. Temperature ramps at 5 °Cmin⁻¹. 10 mN static force and 1 mN dynamic force at 1 Hz are applied. The sample is 6 mm in diameter and 1 mm in thickness. Vertical dashed lines indicate phase transition temperatures. Dotted lines are used to guide eyes of different expansion coefficients. The area of the tip of the probe is 0.78 mm².

4.2.4 Positron Annihilation Lifetime Spectroscopy

The component of ortho-Positronium (oPs) pickoff annihilation measurement (τ_3, I_3) is shown in Figure 4.5. Analogous to the analysis of PALS for P12TFSA in section 3.2.4, τ_3 and I_3 were tentatively assigned as the responses of the oPs trapped in defects. The lifetime τ_3 and the intensity I_3 indicate the vacancy size and number, respectively.

Three cusps in the lifetime τ_3 and the intensity I_3 are observed at (1) −20 to −15 °C, the onset of phase III>>II transition; (2) 0 to 5 °C, which could suggest a sudden change occurring in the broad phase transition process; and (3) at 25 to 30 °C where the peak of phase III>>II appears. The discontinuity indicates that the congregation, separation and redistribution of vacancies occur in the broad phase transition III>>II.

- 153 -

The average vacancy radius is calculated from τ_3 using Equation 2.60. It ranges from 2.1 to 2.7 Å over the temperature range investigated, as shown in Figure 4.6. Accordingly, the average vacancy volume calculated from Equation 2.61 ranges from 40 to 82 Å^3. The vacancy size is smaller than that in P12TFSA. The average vacancy size in P12TFSA is in the range of 2.8-3.9 Å in radius and is big enough to accommodate a P12$^+$ cation or a TFSA$^-$ anion. For P11TFSA, the radii of the P11$^+$ cation and TFSA$^-$ anion are estimated to be 2.7 Å and 3.7 Å, respectively[vii]. The volume of a cation-anion pair is estimated to be 400 Å^3 at 20 °C[viii]. Therefore, the vacancy volume in P11TFSA is big enough to hold a cation, but not to hold an anion or an ion-pair.
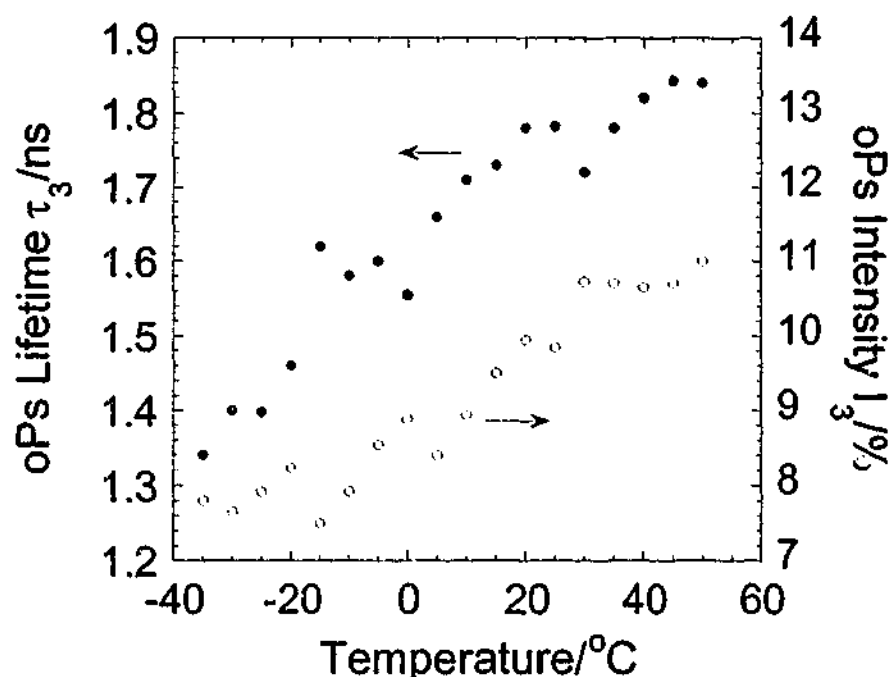
Figure 4.5 Vacancy parameters for P11TFSA as a function of temperature. Lifetime is related to vacancy size. Intensity is related to vacancy concentration.

[vii] Estimated using Chem3D.

[viii] Assuming four cations and four anions in one unit cell and the volume for a unit cell is 1600 Å^3 according to Appendix A.
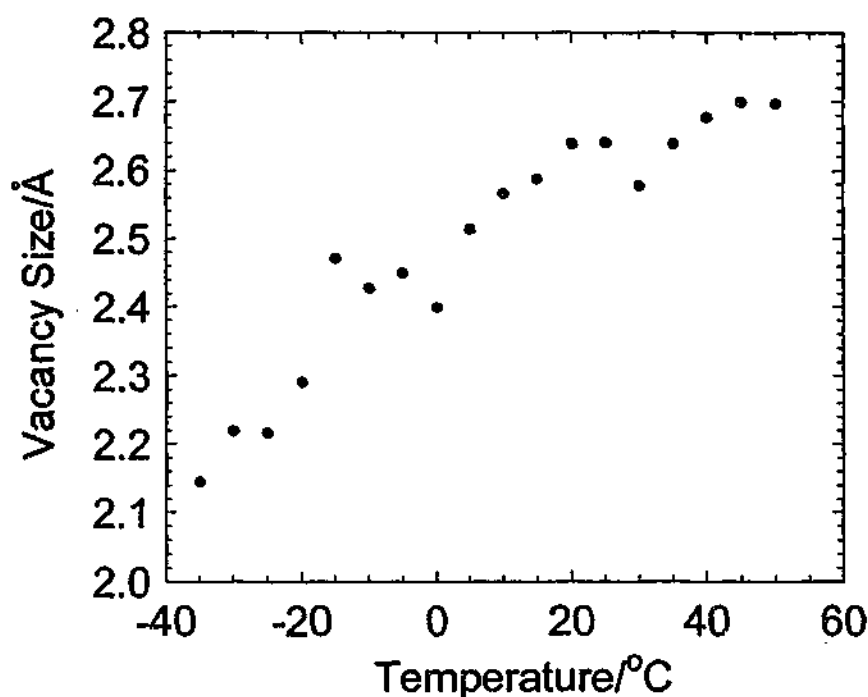
Figure 4.6 Temperature dependence of average vacancy radius for P11TFSA.

Fewer vacancies are created in P11TFSA than in P12TFSA as can be seen by comparing the values of I_3 at the same temperature. I_3 of P11TFSA and P12TFSA are comparable in phase III. At the phase III>>II transition, I_3 is about 11 for P12TFSA at 14 °C and 10 for P11TFSA at 26 °C. I_3 shows a substantial increase for P12TFSA in phase II while it is relatively stable for P11TFSA.

The vacancy concentration, C_v, for P11TFSA at room temperature can be estimated from the density according to [160]:

$$C_v = \frac{\rho_x - \rho}{\rho_x}$$

Equation 4.1

where ρ_x is the density calculated according to lattice structure obtained from powder x-ray result (ref. Appendix A). It is 1.5788 gcm^{-3} at 25 °C. ρ is the density measured at room temperature, 1.5746 gcm^{-3}. The vacancy concentration at room temperature is thus estimated to be 0.27%. Although this estimated value may not represent the equilibrium vacancy concentration as mechanical handling during density measurement could create

- 155 -

more defects, this value roughly reflects the level of vacancy concentration in P11TFSA. For plastic crystals, the vacancy concentration at the melting point typically ranges from 0.1% to 2% [37].

The presence of a larger number of vacancies seems to be one of the characteristics of plastic crystals. The vacancy content N_v is given as [11, 158]

$$N_v = \exp(-\Delta G_v / RT)$$

Equation 4.2

where ΔG_v is the free energy of vacancy formation. In plastic crystals, on one hand, the vacancy reduces the hindering potential of the neighboring molecular rotation, facilitates rotation and results in increased vacancy formation entropy ΔS_V [154]. On the other hand, the occurrence of rotation requires a loosely packed lattice structure and weak bonding, otherwise the rotation is hindered [65]. Therefore, the relatively large intermolecular distance and weak intermolecular interactions result in a smaller vacancy formation enthalpy ΔH_v. The increased ΔS_V and reduced ΔH_v give a more negative ΔG_v and benefit the formation of vacancy in plastic crystals.

The overall vacancy volume is indicated by the relative fraction of free volume (Fr). Fr is calculated from τ_3 and I_3 using Equation 2.61 and Equation 2.70. Fr exhibits a continuous increase with temperature, as shown in Figure 4.7.

The vacancy formation energy E_v is estimated by plotting $\ln(I_3)$ vs. $1/T$, where the slope = E_v/R ($R = 8.314$ JK^{-1}mol^{-1}). The results are shown in Table 4.2. The vacancy formation energies of P12TFSA and P11TFSA are relatively small compared to some molecular plastic crystals investigated by Sherwood et al. where the lowest E_v found was about 13 kJmol^{-1} for cyclooctane [37]. They are nonetheless still comparable to the E_vs of cyclopentane derivatives which were estimated to be 2.5~4.0 kJmol^{-1} [61].
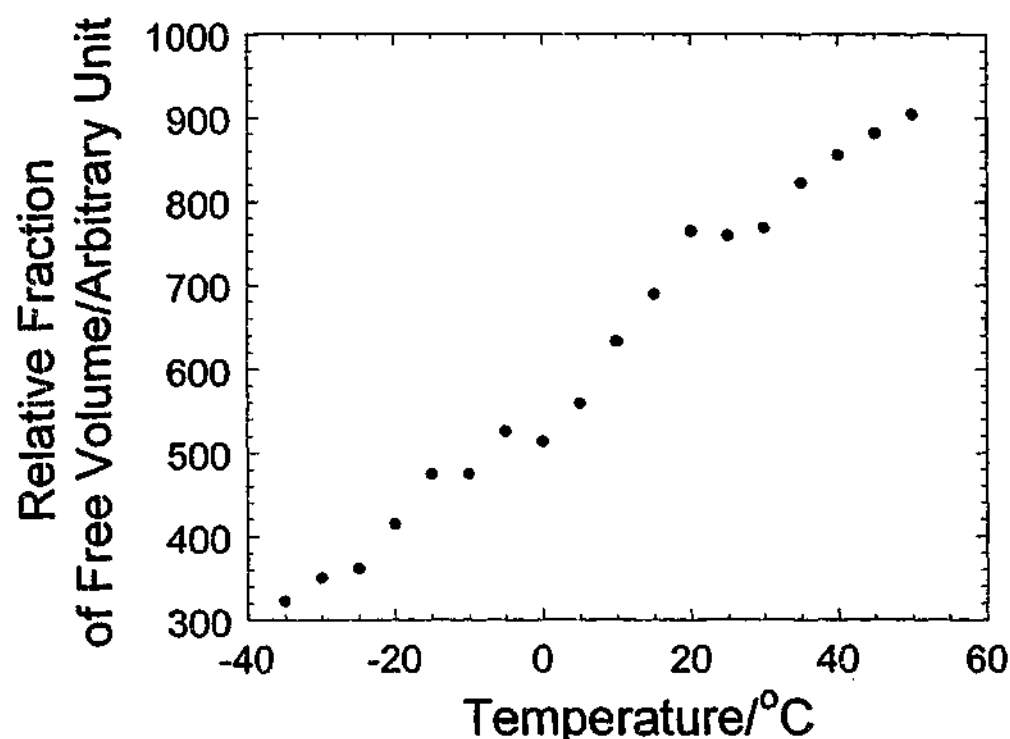
Figure 4.7 Temperature dependence of relative overall volume of vacancies for P11TFSA.

The small vacancy formation energy in P1xTFSA indicates low energy barriers for ions to leave their original lattice positions and form vacancies. It can be explained by the weak ionic bond between cations and anions, which is partly due to the delocalized charges on the anions because of the strong electron-drawing CF_3 groups. Therefore less energy is required to break the intermolecular interactions and to generate vacancies.

Another possibility for the small vacancy formation energy is that the vacancy is associated with conformers. A sample contains an equilibrium concentration of conformers. The transformation between these conformers is regarded as internal rotation. Different conformers in a neighborhood could locally produce free volume, as are the cases for succinonitrile and cyclohexane [275]. The inversion of five-membered rings such as cyclopentane and its derivatives has been seen in molecular mechanics studies [69]. Similarly, for P1xTFSA containing five-membered rings as cations, the inversion of a neighboring ion could produce a vacancy. The formation energy for this inversion created vacancy is low, because the energy barrier of conformer transformation is much less than

- 157 -

that of making "holes" according to molecular mechanics calculations and thermal analyses for cyclopentane and its derivatives [61]. In this case, the internal cation rotation is the source of the vacancy. It is assumed that this "inversion created vacancy" occupies less volume than that of the ion. It is interesting to note that the average vacancy size for P11TFSA at low temperature phases is smaller than the sizes of both cations and anions. This probably supports the notion that the cation ring inversion is related to the vacancies at low temperature. As temperature goes up, the sizes of ions and vacancies start to match, which is probably indicative of "hole" formation.

Table 4.2 Vacancy formation energy (E_v) for P11TFSA obtained by plotting $\ln(I_3)$ vs. $1/T$.

Temperature range /°C	Phase	E_v/kJmol^{-1} (±10%)
-30~ -20	Phase III	3.7
-15 ~ 0	Onset of phase III>>II	6.8
5 ~ 20	Phase III>>II	7.7
20 ~ 50	II	~ 0

4.2.5 Nuclear Magnetic Resonance

Second Moment Calculation

The second moments of ^{1}H and ^{19}F are calculated based on a single crystal structure obtained at $-150\ °C$ [295]. Six elements, S, F, O, N, C, H, are present in P11TFSA. The contribution of each nucleus to the second moment depends on its magnetogyric ratio γ and

natural abundance. ^{1}H and ^{19}F are dominant in the second moment according to their magnetogyric ratios ($\gamma_H = 2.67 \times 10^8$ rads^{-1}T^{-1}, $\gamma_F = 2.52 \times 10^8$ rads^{-1}T^{-1}) and natural abundances (99.98% and 100%, respectively) [247].

For ^{1}H, the second moment is mainly composed of two contributions. One is the ^{1}H-^{1}H dipole-dipole interactions within one cation $M_{2\text{intraH-H}}$ and between neighboring cations $M_{2\text{interH-H}}$. The other is the ^{1}H-^{19}F dipole-dipole interactions between ^{1}H in the cation and ^{19}F in the neighboring anions $M_{2\text{interH-F}}$. $M_{2\text{intraH-H}}$ is composed of $M_{2\text{intraH-H}}^{CH3}$, the contribution from the protons within one methyl group, and $M_{2\text{aH-H}}^{rest}$, the contribution from ^{1}H$_{CH3}$-^{1}H$_{ring}$, ^{1}H$_{CH3}$-^{1}H$_{CH3'}$, and ^{1}H$_{ring}$-^{1}H$_{ring}$. The overall second moment of ^{1}H is written as:

$$M_2^H = M_{2\text{intraH-H}}^{CH3} + M_{2\text{intraH-H}}^{rest} + M_{2\text{interH-H}} + M_{2\text{interH-F}}$$

Equation 4.3

For ^{19}F, the second moment is composed of the ^{19}F-^{19}F dipolar interactions within the anion $M_{2\text{intraF-F}}$ and between the neighboring anions $M_{2\text{interF-F}}$, and the ^{19}F-^{1}H interactions between anion and cation $M_{2\text{interF-H}}$. $M_{2\text{intraF-F}}$ is composed of the contribution from ^{19}F-^{19}F dipolar interactions within one CF$_3$ group, $M_{2\text{intraF-F}}^{CF3}$, and the ^{19}F-^{19}F dipolar interactions between the two CF$_3$ groups $M_{2\text{intraF-F}}^{rest}$. The overall second moment of ^{19}F is written as:

$$M_2^F = M_{2\text{intraF-F}}^{CF3} + M_{2\text{intraF-F}}^{rest} + M_{2\text{interF-F}} + M_{2\text{interF-H}}$$

Equation 4.4

The calculation is carried out by using the following equations according to the equations of second moment between like and unlike nuclei Equation 2.15 and Equation 2.17 in section 2.1.2:

$$M_2^H = \left(\frac{\mu_0}{4\pi}\right)^2 \frac{3}{5} \gamma_H^4 \hbar^2 I_H(I_H+1)\frac{1}{N_H}\sum_{j,k} r_{jk}^{-6} + \left(\frac{\mu_0}{4\pi}\right)^2 \frac{4}{15}\gamma_H^2\gamma_F^2\hbar^2 I_F(I_F+1)\frac{1}{N_H}\sum_{l,m} r_{lm}^{-6}$$

Equation 4.5

- 159 -

$$M_2{}^F = \left(\frac{\mu_o}{4\pi}\right)^2 \frac{3}{5}\gamma_F{}^4\hbar^2 I_F(I_F+1)\frac{1}{N_F}\sum_{j,k}r_{jk}{}^{-6} + \left(\frac{\mu_o}{4\pi}\right)^2 \frac{4}{15}\gamma_H{}^2\gamma_F{}^2\hbar^2 I_H(I_H+1)\frac{1}{N_F}\sum_{l,m}r_{lm}{}^{-6}$$

Equation 4.6

where, the first term is the contribution from ^1H-^1H or ^{19}F-^{19}F dipolar interactions. The second term is the contribution from ^1H-^{19}F dipolar interactions. $\mu_o=4\pi\times10^{-7}$ NA^{-2}, $\gamma_H=2.67\times10^8$ $rads^{-1}T^{-1}$, $\gamma_F=2.52\times10^8$ $rads^{-1}T^{-1}$, $\hbar=1.056\times10^{-34}$ $Jsrad^{-1}$, $N_H=14$, $N_F=6$. Different ionic motions are taken into account in the calculation. The full width at half magnitude (FWHM) is estimated from Equation 2.11, which is written as:

$$\Delta v = \frac{2.36\sqrt{M_2}}{2\pi}$$

Equation 4.7

where Δv is the full frequency width at half magnitude. The M_2 calculation results and corresponding linewidths are shown in Table 4.3 and Table 4.4.

a). Rigid Lattice

It is assumed that the ions are static in the rigid lattice. The calculation of rigid lattice is based on the atomic positions obtained from single crystal x-ray diffraction at -150 °C [295]. There are four ion-pairs in each unit cell. All cations and anions within one unit cell and the surrounding 26 unit cells are considered. The results show that the contribution from the intra-ionic dipole-dipole interactions is dominant in $M_2{}^H$ and important in $M_2{}^F$.

b). Effect of methyl group rotation

When the methyl group rotates rapidly enough about the C_3 symmetry axis, $M_{2intraH\text{-}H}{}^{CH3}$ is reduced to one-quarter of its rigid lattice value [39, 296]. $M_{2intraH\text{-}H}{}^{rest}$, $M_{2interH\text{-}H}$ and $M_{2interH\text{-}F}$ are calculated by assuming that the three protons in the methyl group appear as if they are all located at the center of their rigid lattice positions [39].

c). Effect of trifluoromethyl group rotation

Similar to methyl group rotation, $M_{2intraF\text{-}F}^{CF3}$ is reduced to one-quarter of its rigid lattice value. The three fluorine atoms are assumed to appear as if located at the center of their rigid lattice positions in the calculation.

d). Effect of isotropic reorientation

When cations (or anions) undergo isotropic reorientation, the intra-ionic dipole-dipole interactions are averaged to zero. The second moment comes from the inter-ionic dipolar interactions. Therefore, only the third and forth terms in Equation 4.3 and Equation 4.4 are used in the calculation. All the nuclei are assumed to appear as if concentrated at the centers of mass of the ions [38, 39, 249].

e). Effect of self diffusion

Normally, translational motion is superimposed on the ionic isotropic reorientation. When self-diffusion occurs, the intra-ionic and inter-ionic dipolar interactions are all averaged to zero. Accordingly, the linewidth is reduced to zero. The remaining linewidth results from the inhomogeneity of the magnetic field around the sample.

Possible errors in the calculations are estimated as follows:

a). Lattice expansion

The calculations are based on the crystal structure at −150 °C. By comparison of the lattice parameters obtained from single crystal x-ray diffraction at −150 °C [295] and powder x-ray diffraction at 25 °C in Appendix A and assuming that the ions maintain their relative positions, the lattice expands by 4.8% in the "a" direction and 2.2% in the "c" direction. The lattice expansion slightly increases inter-ionic distances with temperature and reduces the inter-ionic dipolar interaction. Therefore, it has more influence on those motions where inter-ionic dipolar interactions dominate, such as isotropic rotation. Maximum correcting factors of 0.75 for second moment and 0.86 for linewidth are estimated for isotropic rotation. For intra-ionic interaction dominated conditions, such as the rigid state, the effect of lattice expansion can be ignored.

Table 4.3 M_2 calculation and corresponding linewidths of ^1H NMR for P11TFSA.

	M_2^{H-H} /10^8 s^{-2}			M_2^{H-H} /10^8 s^{-2}	M_2^{H-F} /10^8 s^{-2}	M_2^{H} /10^8 s^{-2}	FWHM /kHz
	CH_3	intra-cation^{rest}	cation-cation	all	cation-anion		
Rigid	176.7	130.3	8.7	315.7	3.6	319.3	67.1
CH_3 rotate CF_3 static	44.2	126.1	7.3	177.6	3.5	181.1	50.5
CH_3 static CF_3 rotate	176.7	130.3	8.7	315.7	2.6	318.2	67.0
CH_3 rotate CF_3 rotate	44.2	126.1	7.3	177.6	2.5	180.1	50.4
Cation isotropic CF_3 rotate	0	0	2.3	2.3	1.1	3.4	6.9
CH_3 rotate Anion isotropic	44.2	126.1	7.3	177.6	2.0	179.6	50.3
Cation isotropic Anion isotropic	0	0	2.3	2.29	1.2	3.5	7.0

Table 4.4 M_2 calculation and corresponding linewidths of ^{19}F NMR for P11TFSA.

	$M_2^{F\text{-}F}$ /10^8 s^{-2}			$M_2^{F\text{-}F}$ /10^8 s^{-2}	$M_2^{F\text{-}H}$ /10^8 s^{-2}	M_2^F /10^8 s^{-2}	FWHM /kHz
	CF$_3$	Intra-anion CF$_3$-CF$_3$	anion-anion	all	anion-cation		
Rigid	36.19	0.14	8.00	44.33	8.43	52.76	27.3
CH$_3$ rotate CF$_3$ static	36.19	0.14	7.96	44.30	8.10	52.40	27.2
CH$_3$ static CF$_3$ rotate	9.05	0.15	4.89	14.08	5.98	20.06	16.8
CH$_3$ rotate CF$_3$ rotate	9.05	0.15	4.85	14.05	5.82	19.86	16.7
Cation isotropic CF$_3$ rotate	9.05	0.15	4.87	14.06	2.63	16.69	15.3
CH$_3$ rotate Anion isotropic	0	0	0.71	0.71	4.63	5.34	8.7
Cation isotropic Anion isotropic	0	0	0.71	0.71	2.86	3.57	7.1

b). The number of surrounding ions

As mentioned above, one unit cell and the first surrounding layer of 26 unit cells are considered in the calculation. The rest of the unit cells contribute to the inter-ionic dipolar interaction and have more effect on those motions where the intra-ionic dipolar interactions are averaged out. Taking one of the closest unit cells in the second layer of 98 unit cells into account and assuming all the 98 unit cells have the same effect on the second moment, the differences in linewidth calculated are estimated to be 13.85% for H and 2.38% for F in the isotropic motion.

^{1}H Linewidth

The ^{1}H NMR spectra are shown in Figure 4.8. A broad Gaussian peak is observed at low temperature. As temperature increases, the peak becomes narrower. Only at 10 °C below the melting point does a narrow peak appear on the top of the broad one. The intensity of the narrow peak increases at the expense of the broad one until finally the broad bottom totally disappears above the melting point.

The linewidths and the fraction of the broad and narrow peaks are shown in Figure 4.9 and Figure 4.10. The linewidth of the broad peak is 22.6 kHz in phase III. It decreases to 18 kHz in the broad phase III>>II transition temperature range. Further line narrowing occurs in phase II until the linewidth reaches a relatively constant value of 11.7 kHz in phase I. The broad line is further narrowed to 10.4 kHz 10 °C below the melting point. The whole range of linewidth is smaller than 50 kHz, the value when CH_3 groups rotate according to the M_2 calculated, and broader than the value of 7 kHz when cations are in isotropic rotation. These observations indicate that the cations execute some anisotropic rotation in addition to the CH_3 group rotation in phase III. As temperature increases, another anisotropic rotation is introduced and causes the line narrowing. In phase I, the cations rotate anisotropically. These anisotropic rotations are not identified so far. The possible rotational motions the five-membered ring could undergo include the ring inversion, flipping etc. The linewidth is comparable to that of P12TFSA, from 20 kHz in phase III to 11 kHz in phase I. The similar range of linewidth suggests that the cations could undergo similar rotational motion in P11TFSA and P12TFSA.

The linewidth of the narrow line is in the range of 710–210 Hz, far smaller than the isotropic rotational value of 7 kHz calculated. Therefore it represents the diffusing cations. The linewidth is relatively broad for diffusion. This broadening is attributed to the merging of the peaks of different chemical shifts and/or the inhomogeneity in the sample due to the coexistence of positionally ordered ions, diffusing ions and possible vacancies. In contrast to P12TFSA, only 1% cations are detected diffusing at 10 °C below the melting point. The extensive diffusion occurring only near the melting point indicates a premelting behavior.
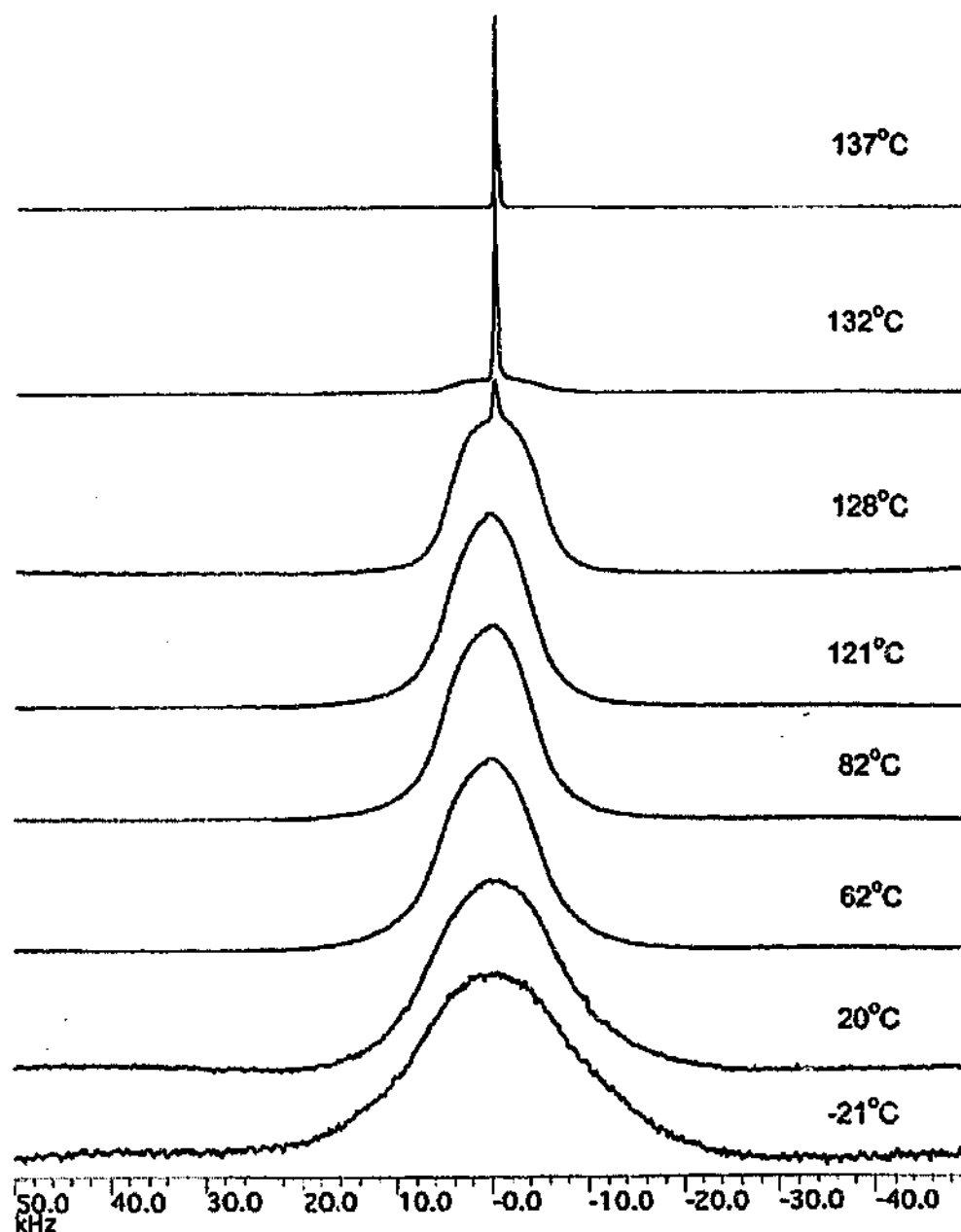
Figure 4.8 ^{1}H NMR spectra for P11TFSA.

- 165 -
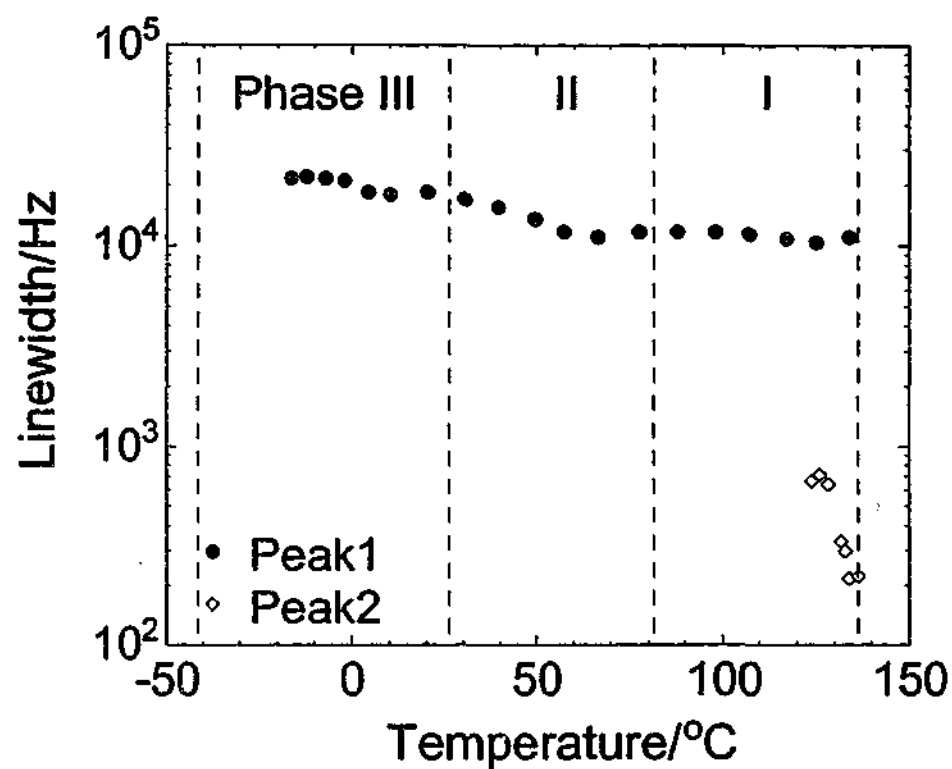
Figure 4.9 Temperature dependence of ^{1}H NMR linewidth for P11TFSA.
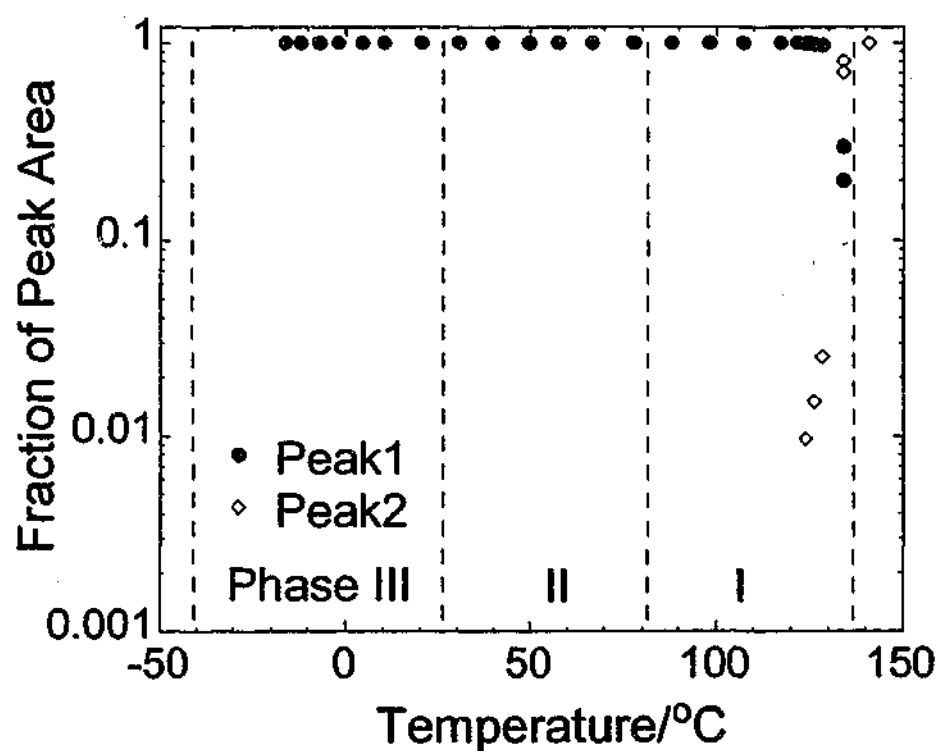
Figure 4.10 The fraction of peak area of ^{1}H NMR for P11TFSA as a function of temperature. Peak1 and peak2 represent the broad and narrow components respectively.

^{19}F Linewidth

The ^{19}F NMR spectra are shown in Figure 4.11. They are fairly broad peaks which can be deconvoluted into three peaks of different chemical shifts, as demonstrated in Figure 4.11 (b), over all of the temperature range. Similar to P12TFSA, the three peaks of different chemical shifts probably correspond to three different fluorine sites.
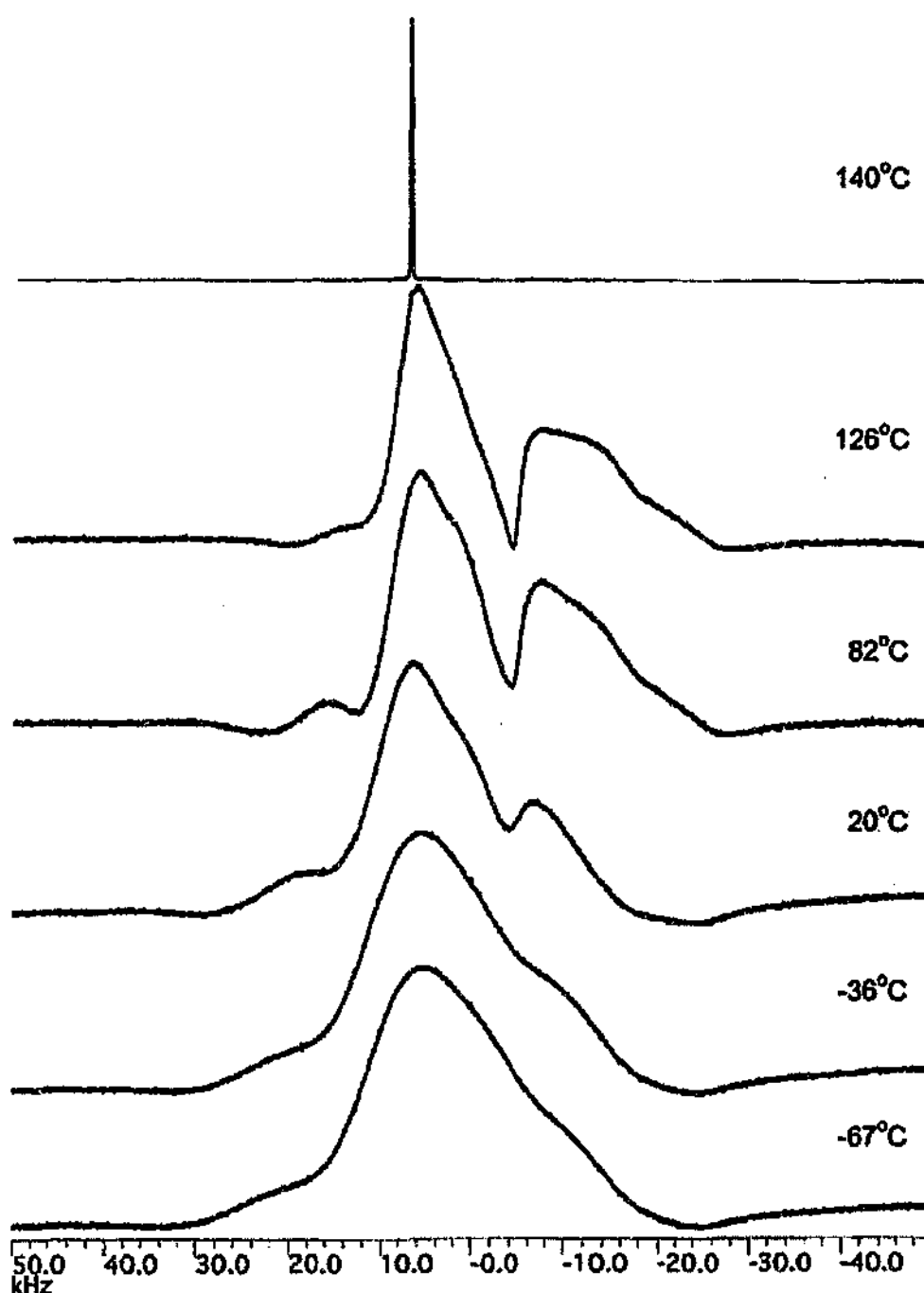
(a)
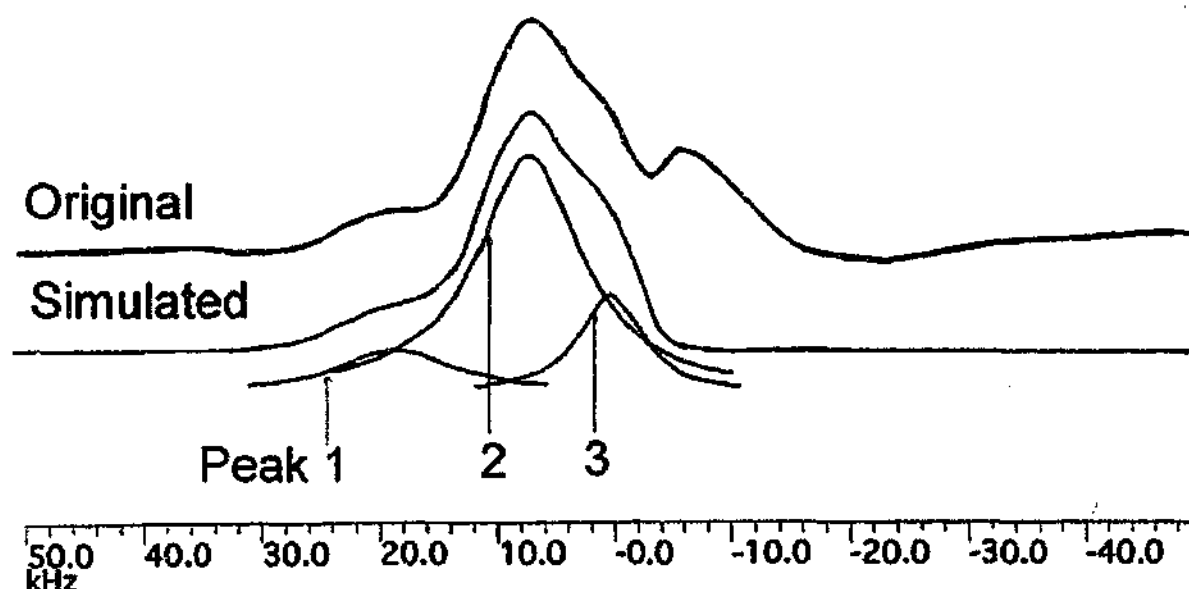
(b)

Figure 4.11 ^{19}F NMR spectra for P11TFSA. The peak at about –7 kHz comes from background. (a) At various temperatures. (b) The original peak at 20 °C and the simulated peak which can be deconvoluted into three smaller peaks.

The linewidth is shown in Figure 4.12. The linewidth of peak 1 is about 15 kHz in phase IV. It reduces to 13 kHz in phase III and about 10 kHz in phase II. The line is narrowed to about 7 kHz in phase I. According to the M_2 calculations, the expected linewidth when only the CF$_3$ groups rotate is about 16 kHz; whilst the linewidth expected if the anions rotate isotropically is about 8 kHz. The anions represented by peak 1 in phase IV are therefore experiencing only CF$_3$ group rotation. Two further anisotropic rotation mechanisms are believed to cause the line narrowing observed in phase III and phase II. In phase I, the anions is undergoing isotropic rotation.

Peak 2 and peak 3 have similar linewidth and variation behavior with temperature, indicating that the anions in the two different sites possess similar motions. The linewidths of both peaks are about 15 kHz in phase IV, decreasing to 13 kHz in phase III. Another narrowing starts at about –10 °C and reaches 8.6 kHz at 28 °C, covering the broad phase III>>II transition range. This narrowing is accompanied by a different volumetric expansion coefficient as shown in section 4.2.3 and coincides with the ^{1}H line narrowing.

- 168 -

These results indicate that the lattice structure and ionic motions of both cations and anions change in this broad transition. A slight narrowing is observed at 50 °C. The peaks are about 7 kHz in phase I. A further narrowing occurs 10 °C below the melting point. Comparing to the linewidths expected from M_2 calculations, the anions represented by peak 2 and peak 3 undergo only CF_3 group rotation in phase IV. Two further anisotropic rotation mechanisms are involved in phase III and phase II, which are believed to cause the line narrowing. In phase I, the anions are undergoing isotropic motion. The line narrowing corresponding well to the phase transition temperatures, especially the phase IV>>III and phase III>>II transitions, indicates that there are motional changes occurring at the phase transitions.

The fraction of each component is shown in Figure 4.13. Below the melting point, peak 1 represents about 8% of the anions. More than 90% of the anions are represented by peak 2 and peak 3. The ratio of the numbers of the anions found in these two different sites is about 3:2.

Similar to ^1H NMR of P11TFSA, a narrow peak of about 200 Hz appears on top of the broad peaks close to melting point. The narrow peak indicates the diffusion of the anions, since the linewidth is much less than the isotropically rotating value of 7 kHz. Only 1% of the anions are detected diffusing 10 °C below the melting point. The amount of diffusing cations and anions are comparable. As suggested above, this diffusion behavior indicates the premelting phenomenon. Premelting is generally believed to be associated with defects which cause the variation of the local effective pressure and alter the melting point of the crystals around the defects. Premelting has been observed in a number of plastic crystals [57, 209, 210, 220, 287, 291]. Extended defects, mainly grain boundaries, are believed to be responsible for diffusion in benzene, thiophene, 1,4-dioxane and cyclohexanol [209, 210, 291]. In the case of P11TFSA, the amounts of the diffusing cations and anions are nearly equal, indicating the correlation between the cations and the anions in the diffusion process. This suggests that, similar to the diffusion behavior in P12TFSA, a Schottky vacancy mechanism could account for the diffusional motion in P11TFSA.
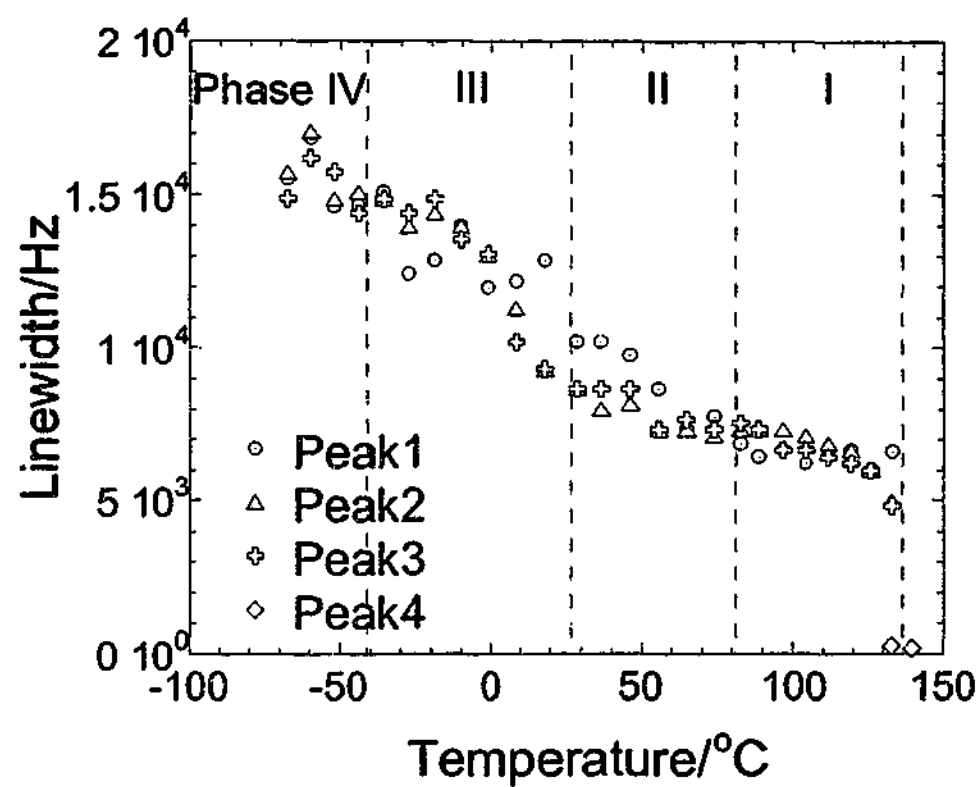
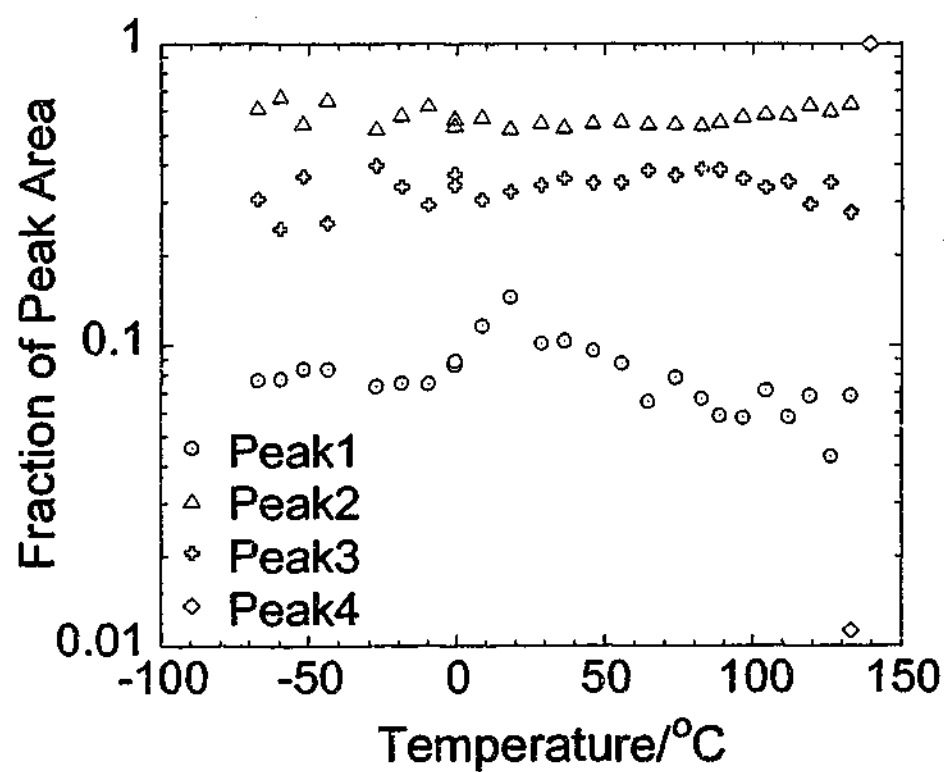Figure 4.12 Temperature dependence of ^{19}F NMR linewidths for P11TFSA.

Figure 4.13 The fraction of peak area of ^{19}F NMR for P11TFSA as a function of temperature.

4.2.6 Dielectric Response

The dielectric responses are shown in Figure 4.14 and Figure 4.15. Low frequency dispersions of both the imaginary and real part of dielectric permittivity obey a power law, implying a charge-hopping model [261] [259]. This indicates that long distance ionic transport occurs at temperatures as low as $-50\ °C$, in phase IV. As temperature increases, the magnitudes of both the imaginary part, $\varepsilon"$, and the real part of dielectric permittivity, ε', increase. The transition frequency of the real part of dielectric permittivity shifts to higher frequency, suggesting an increased ionic hopping rate.

The dielectric responses in high frequency range $(10^6\text{-}10^7\ s^{-1})$ show dipolar response. Peaks in $\varepsilon"$ are observed in the range from $-50\ °C$ to $32\ °C$. The peak frequency slightly shifts positively and the peak magnitude increases slightly with temperature. A substantial increase in the magnitude of the dipolar response is obtained if the contribution from charge-hopping is subtracted from the overall dielectric response. The real part of dielectric permittivity, ε', shows a flat response as a function of frequency when the frequency is higher than the transition value. These relatively constant responses at high frequency correspond to the instantaneous polarization [259]. The values of ε' drop in the frequency range of $10^6\text{-}10^7\ s^{-1}$. These combined with the $\varepsilon"$ peaks are relatively classic dipolar responses. The dipolar responses could come from two sources, the displacement of cations and anions under the AC electric field or the ionic rotation. Considering the fact that this dipolar response is observed as low as $-120\ °C$ which is not shown here, ionic rotation seems more likely due to the lower energy barrier than that of displacement of ions. This assumption is also confirmed by the ^1H and ^{19}F NMR linewidth measurements, which indicate significant rotation behavior in phases IV and III as discussed in section 4.2.5.

Above $42\ °C$, the dipolar response disappears in both the imaginary part and real part of dielectric permittivity, which coincides with the ^1H and ^{19}F NMR line narrowing as shown in section 4.2.5. This indicates the change of rotational mechanism and that the frequency corresponding to the rotational motion shifts out of the experimental frequency range.

Similar to P12TFSA, a plateau appears in the imaginary part of dielectric permittivity above the melting point, which may be attributed to the response of the electrode.
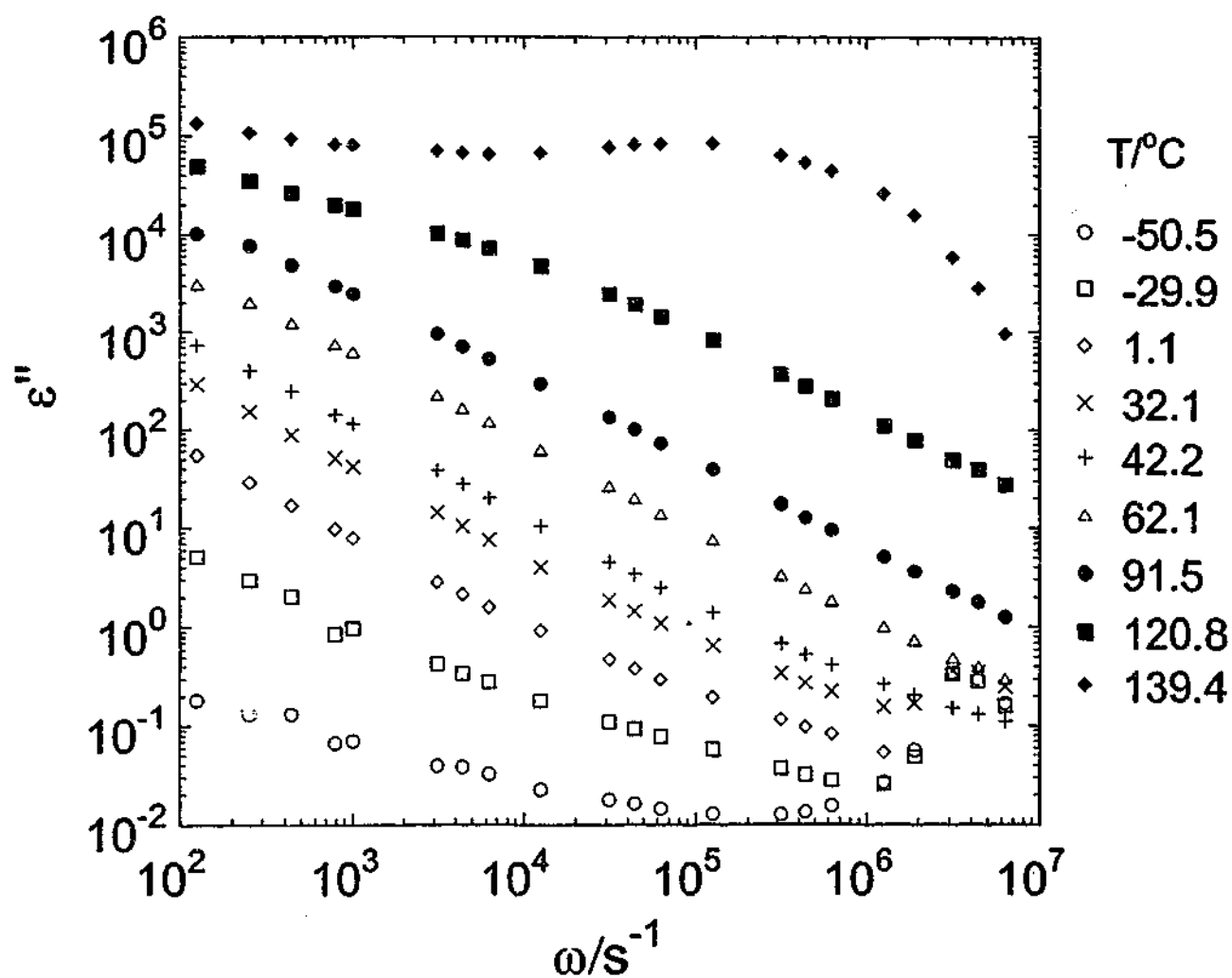

Figure 4.14 Imaginary part of dielectric permittivity of P11TFSA as a function of frequency at various temperatures.
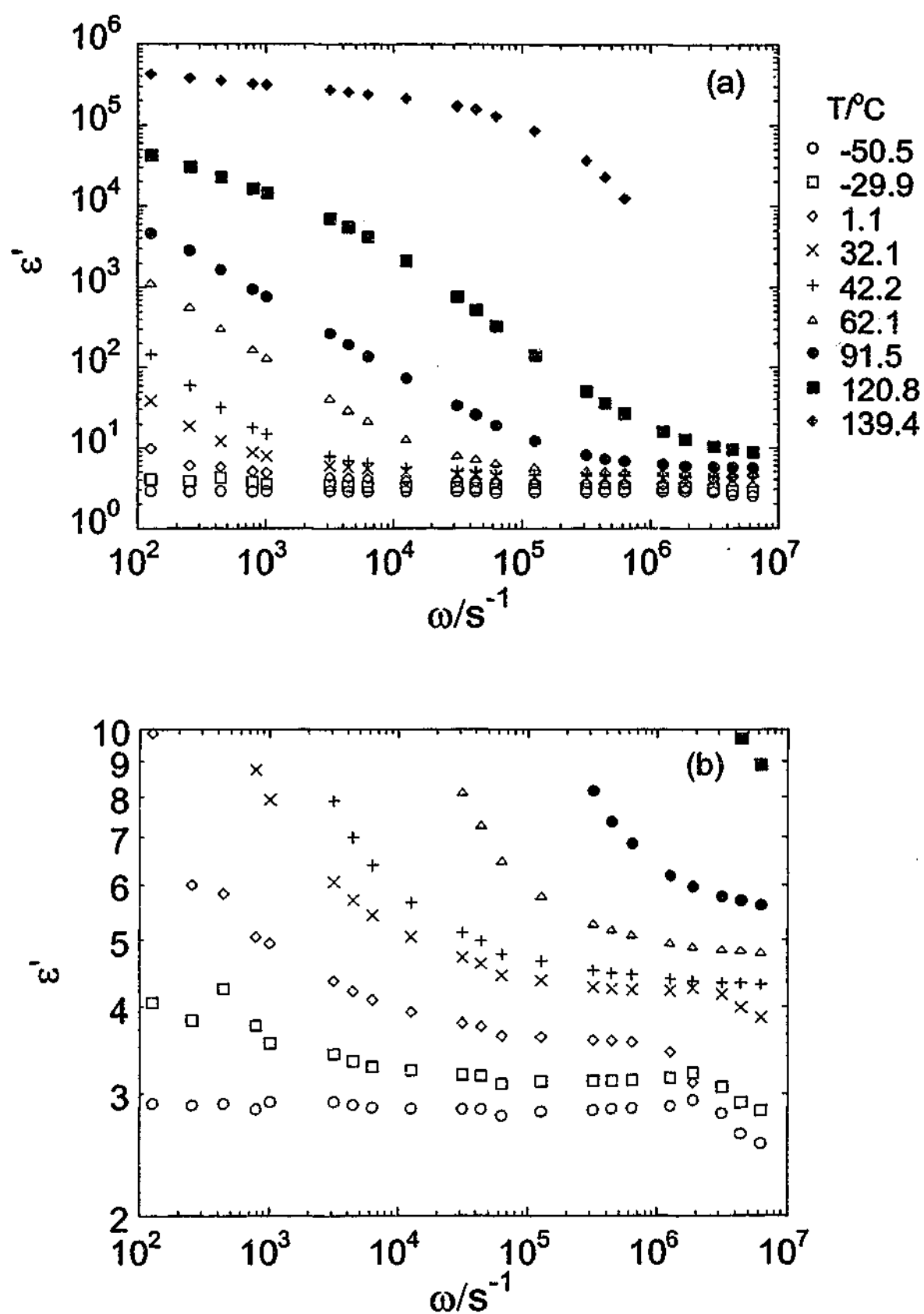
Figure 4.15 Real part of dielectric permittivity of P11TFSA as a function of frequency at various temperatures. (b) is the expanded part of (a).

4.2.7 AC Conductivity and DC Conductivity

The AC conductivity of P11TFSA, as shown in Figure 4.16, exhibits relatively classic dispersions in the low and high frequency ranges. The flat low frequency dispersion is dominated by the DC conductivity while local motion of the ions in the AC electric field contributes in the high frequency range. As temperature increases, the AC conductivity rises and the transition frequency shifts to higher frequency. The AC conductivity is fitted by

$$\sigma(\omega) = K\omega_P + K\omega_P^{1-n}\omega^n = \sigma(0) + A\omega^n$$

Equation 4.4.8

where $\sigma(0)$ is the DC conductivity, ω_p is the hopping rate and K is related to charge carrier number. n is found to be in the range of 0.52-0.76. ω_p and K obtained by curve fitting are shown in Figure 4.17 and Figure 4.18. K is plotted in the form of kT in view of Equation 3.11. ω_P and KT for P12TFSA are also included for comparison.

ω_P exhibits distinctively different thermal activation behavior in different phases, as characterized by different slopes. A substantial increase in ω_P occurs in phase III and phase II while the curve is relatively flat in phase I. It is interesting that a "knee" is observed at about –20 °C, the onset of phase III>>II. ω_P results seem to coincide well with the volume expansion experiment, as discussed above in section 4.2.3. Both show phase-dependent behavior. Both of the slopes are relatively flat in phase I. Compared to P12TFSA, the P11TFSA ionic hopping rate exhibits a wider range of values. In phase III, ω_P of P11TFSA is about two orders of magnitude slower than that of P12TFSA while it is about one order of magnitude faster in phase I.

The number of charge carriers is related to KT by Equation 3.11. Figure 4.18 shows that the charge carrier number increases with temperature by a constant rate in phase III and phase I. It is double at 80 °C compared to –30 °C. A dramatic increase in charge carrier number occurs in phase I. The dramatically increased numbers of diffusing cations and anions near the melting point are also observed in the ^1H and ^{19}F NMR as shown by Figure

4.10 and Figure 4.13. In the range of –30 °C ~ 40 °C, KT of P12TFSA and P11TFSA are comparable. The discrepancy occurs above 40 °C when P12TFSA enters phase I.

The DC conductivity is shown in Figure 4.19. According to the analyses of ω_P and charge carrier number, in phases III and II, the increase in DC conductivity is mainly attributed to the increase in ionic hopping frequency. In phase I, a dramatically increased number of conducting ions mainly account for the increase in conductivity.
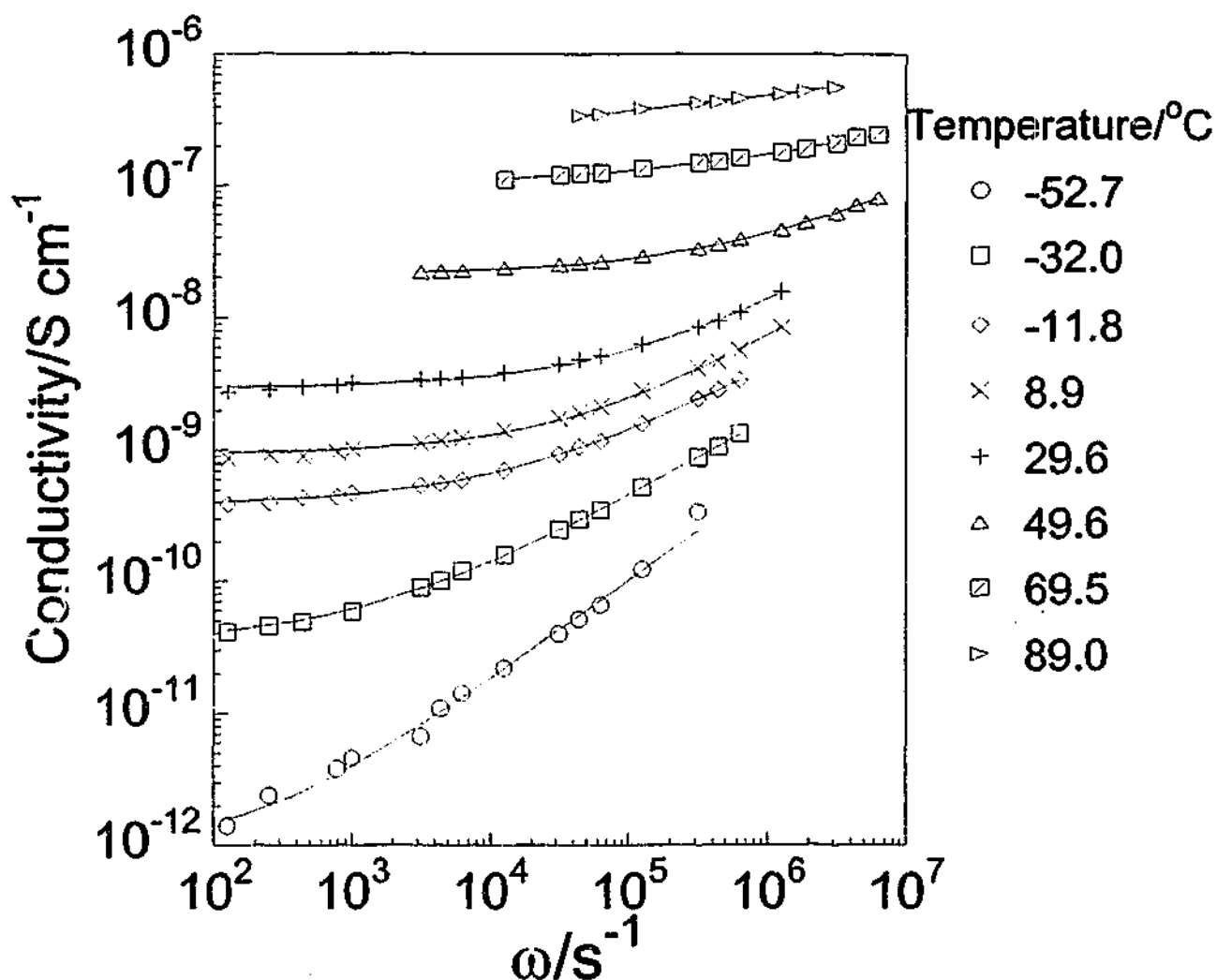
Figure 4.16 AC conductivity of P11TFSA as a function of frequency at various temperatures. The lines are the values calculated using Equation 4.4.8. The data in the frequency range of 10^6-10^7 s^{-1} below 42.2 °C are ignored due to the rotational mechanism as discussed in the section 4.2.6. The low frequency responses at high temperature are omitted as well due to electrode polarization.
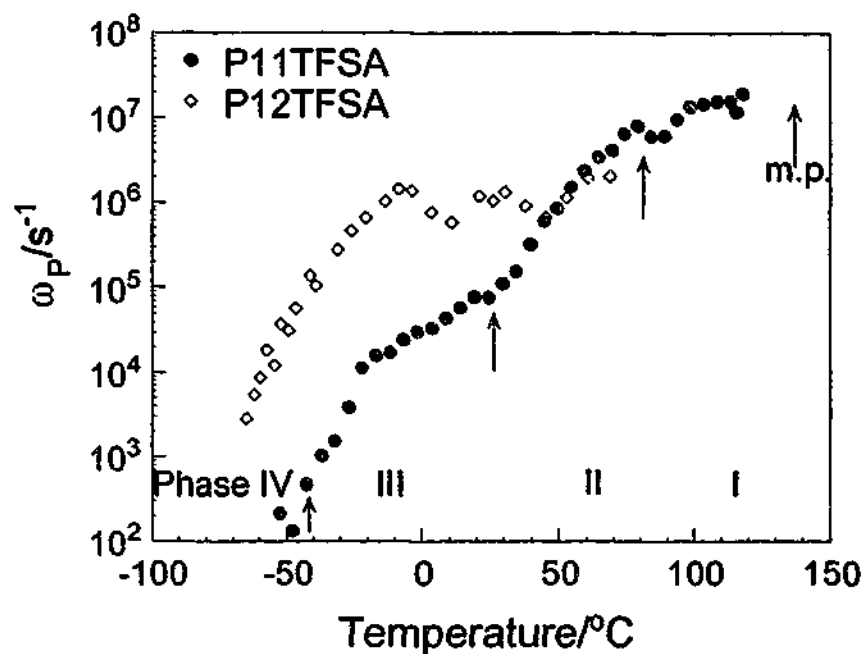
Figure 4.17 Hopping rate ω_P for P11TFSA as a function of temperature. The arrows mark the phase transition temperatures of P11TFSA. Hopping rates for P12TFSA are quoted here as comparison.
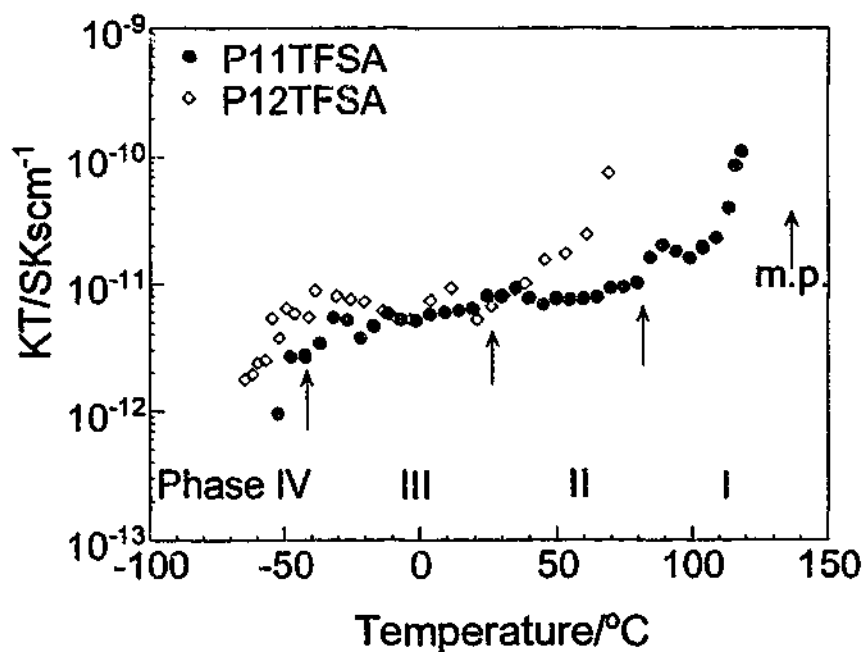
Figure 4.18 KT as a function of temperature. KT is the function of charge carrier number according to Equation 3.11. The values for P11TFSA and P12TFSA are shown here as comparison. The arrows mark the phase transition temperatures of P11TFSA.
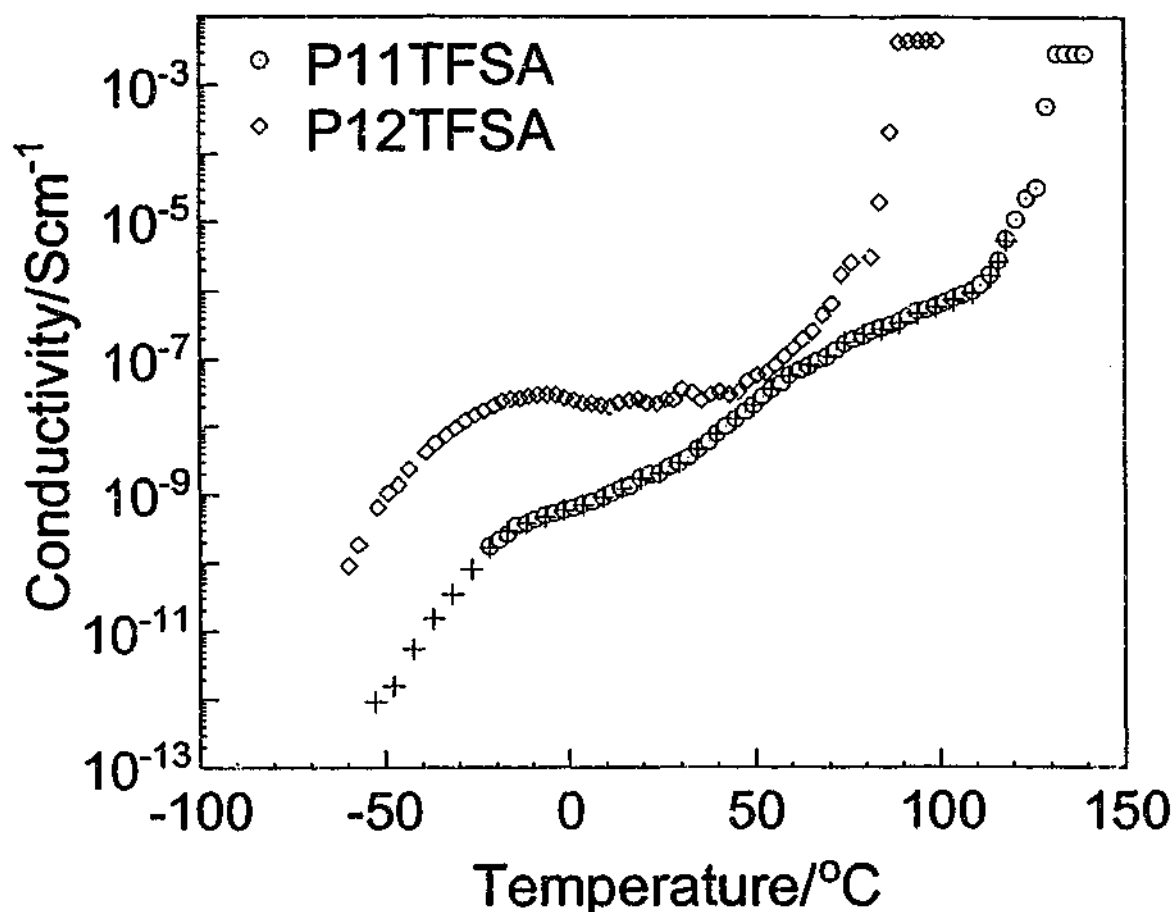
Figure 4.19 DC conductivity for P11TFSA as a function of temperature. The open circles are obtained from Cole-Cole plots. The "+" values are obtained by fitting Equation 4.4.8. The values for P12TFSA are quoted here as comparison.

4.3 Conclusions

4.3.1 Microstructure, Ionic Motion and Phase Transition

P11TFSA goes through three phase transitions below the melting point. Phase III>>II and II>>I transitions cover broad temperature ranges, indicative of the gradual transformation in microstructure and ionic motion rather than sudden changes. The microstructure, ionic motion and conduction are summarized as:

1. Phase IV (below −41 °C)

The volumetric expansion is negligible in phase IV compared to phase III and phase II. Dipolar response as shown in dielectric spectroscopy indicates that rotational motion already exists in phase IV. The anions undergo C_3 rotation of the CF_3 groups according to ^{19}F NMR.

2. Phase III (-41 °C ~ -15 °C)

At -40 °C, the lattice volume begins to expand. The anions start to perform anisotropic rotation as characterized by the line narrowing in ^{19}F NMR. The cations undergo anisotropic rotation in addition to the C_3 rotation of the CH_3 group according to ^1H NMR. The rotational motions are also responsible for the dipolar responses in the high frequency range in the dielectric studies. The number of hopping ions doubles and the ionic hopping rate increases by more than one order of magnitude. The increases in both the number and hopping rate of ions account for the increase of conductivity by nearly two orders of magnitude.

3. Phase III>>II (-15 °C ~ 26 °C)

The phase III>>II transition exhibits the biggest entropy change among the three solid-solid phase transitions. It covers a broad temperature range, starting from -15 °C according to the DSC trace. During the transformation, the volumetric expansion exhibits a different expansion coefficient compared to in phase III. The variation in the size and number of vacancies with temperature shows several cusps while the overall void volume increases steadily, indicative of the redistribution of vacancies by congregation and separation. Both ^1H and ^{19}F NMR show line narrowing, suggesting that more rotational disorder develops in the transformation. The ionic hopping rate increases by about one order of magnitude in this range probably due to a different hopping mechanism as characterized by a different activation energy. The number of charge carriers increases by a factor of 1.5.

4. Phase II (26 °C ~ 81 °C)

The volume expansion displays a different expansion coefficient in phase II. Cations develop further anisotropic rotational motion, as shown by the substantial line narrowing in

^{1}H NMR. ^{19}F linewidth displays a slight drop at 40 °C ~ 50 °C. Anions undergo isotropic rotation above 50 °C. In the range of 40 °C ~ 50 °C, the electric dipolar response due to rotational motion disappears. These minor changes in this temperature range could indicate the onset of the phase II>I transition which is not distinguishable on the DSC trace. The number of charge carriers is nearly constant in phase II while the ionic hopping rate increases by two orders of magnitude, which mainly accounts for the increase of conductivity.

5. Phase I (81 °C ~ 137 °C)

In phase I, the sample volume is relatively constant. The cations rotate anisotropically while anions undergo isotropic rotation. 1% of cations and anions are detected diffusing by NMR at a temperature 10 °C below the melting point. More ions are involved in diffusion in the temperature range up to melting until 100% of cations and anions are detected diffusing at the melting point, which suggests premelting behavior. The amounts of diffusing anions and cations detected in this range are almost the same, which seems to indicate a Schottky vacancy mechanism in the premelting. Correspondingly, the number of charge carriers exhibits a dramatic increase, which is mainly responsible for the increase in conductivity.

4.3.2 Comparison of P11TFSA and P12TFSA

Phase Transitions

A phase transition is associated with an alteration in lattice structure, vacancies and ionic motion, therefore ΔS_{tr} contains contributions from several factors, such as the change of rotational motion, vacancy formation and redistribution, change of lattice structure and volume expansion. Relatively sharp DSC peaks, such as the phase III>>II transition in P12TFSA, correspond to radical lattice structure changes and discontinuous volume expansion or contraction. Broad peaks are attributed to gradual transformations, such as the phase II>>I transitions in P11TFSA and P12TFSA. Both P11TFSA and P12TFSA go through a series of broad phase transitions below their melting points, indicating

- 179 -

progressive transformation from the more ordered phases into disordered phases in both cases.

ΔS_f values for P11TFSA and P12TFSA are relatively larger than Timmermans' criterion. The discrepancy comes from the degree of rotational disorder in the solid state. The degree of rotational disorder is determined by two factors: (1) the number of the ions performing the rotational motion. Timmermans' criterion is mainly based on molecular plastic crystals. For some ionic plastic crystals, where only one of the ions undergo rotational motion in the solid, higher fusion entropy is required to excite rotational motion of the other ion; (2) the degree of disorder of the rotational motion. Isotropic rotation accounts for a lower fusion entropy while the plastic crystals undergoing anisotropic rotation, such as 1,4-dioxane, benzene and thiophene, show relatively higher ΔS_f [209]. As to P11TFSA and P12TFSA, the anisotropically rotating cations plus anions undergoing isotropic motion in phase I probably account for the higher fusion entropy in both cases.

The higher fusion entropy of P11TFSA compared to P12TFSA suggests that P11TFSA has a lower degree of freedom in the solid state than P12TFSA. The discrepancy may be attributed to greater volume expansion, larger number of vacancies of larger size in P12TFSA. More ions having translational disorder in P12TFSA may also account for the difference.

Ionic Motion

The linewidths of ^1H and ^{19}F NMR signals for P11TFSA and P12TFSA are almost in the same range, indicating that the cations and anions in P11TFSA and P12TFSA probably undergo similar rotational motion.

1% of ions are detected diffusing in phase III in P12TFSA while in P11TFSA, 1% of the diffusing ions are only detected at a temperature 10 °C below the melting point.

Both P12TFSA and P11TFSA display substantial increases in DC conductivity in phase III with relatively large E_a. Another dramatic increase in conductivity occurs near the melting point. DC conductivity is determined by two factors, the hopping rate and the number of

charge carriers. According to Figure 4.18, the KT values of P12TFSA and P11TFSA are at the same level in the range −50 ~ 40 °C. According to Equation 3.11, the charge carrier concentrations are nearly the same in P11TFSA and P12TFSA by considering that the values of equivalent lattice sites per unit volume N, jumping distance "a" and geometrical factor γ are similar. The difference in conductivity results from the difference in ionic hopping rate. The hopping rate of P12TFSA is about two orders of magnitude higher than that of P11TFSA in the temperature range −50 ~ 40 °C. The values of KT for P11TFSA and P12TFSA are comparable in this range. In this temperature range, diffusion of cations and anions is detected in P12TFSA by NMR.

Vacancies and conductivity

A comparison of P11TFSA and P12TFSA shows that higher vacancy concentration and larger vacancy size are present in P12TFSA. These are consistent with a larger number of diffusing ions detected by NMR and a higher conductivity observed in the solid state of P12TFSA. This comparison indicates that ionic diffusion in P12TFSA and P11TFSA is closely associated with vacancies. Comparing the ionic sizes and the vacancy size suggests that the cations and the anions diffuse by a mono-vacancy mechanism. The cationic diffusion and the anionic diffusions show some correlation. It is very likely that a Schottky mechanism is responsible for the diffusional motion in both P12TFSA and P11TFSA.

Chapter 5 Lithium Doped N-methyl-N-ethylpyrrolidinium bis(trifluoromethanesulfonyl)amide Salt Mixtures

5.1 Introduction

Chapter 3 discussed the plastic crystalline behavior exhibited by P12TFSA, such as several solid-solid phase transitions and rotational disorder of both cations and anions. The conduction mechanism was found to be associated with vacancies. In this chapter, lithium bis(trifluoromethane sulfonyl)amide salt (LiTFSA) is doped into the P12TFSA salt. The hypothesis is that, since the lithium salt contains the same anion as the parent phase, at dopant levels the solid state mixtures are cation substituted analogues of the pure P12TFSA. The small lithium ions could be very conductive in the P12TFSA network given the high degree of internal mobility possessed by the $P12^+$ cations and $TFSA^-$ anions. P12TFSA-LiTFSA mixtures with compositions ranging from the doped solid solution to a 1:1 mole ratio mixture are studied. Phase behavior and the motions of the three different ionic species are investigated.

5.2 Results and Discussion

5.2.1 Thermal Analysis

DSC

Typical DSC traces are shown in Figure 5.1 for a number of P12TFSA-LiTFSA compositions ranging between 0 to 50.4 mol% LiTFSA. The DSC trace of pure P12TFSA is quoted here for comparison.

When 0.6 – 4.6 mol% LiTFSA is doped into the P12TFSA, all the transitions remain the same shape and at approximately the same temperatures except for a broadened and shifted final melting, indicative of liquidus behavior. These may suggest a LiTFSA solid solution

in the P12TFSA matrix. In most cases, the DSC traces in this composition range show good reproducibility even after different heat treatments, as shown in Figure 5.2. The transition peaks retain almost the same shapes and positions except that the phase III>>II transition and melting point slightly shift to lower temperatures in process b and c.

For compositions beyond 9.3 mol% LiTFSA a further transition occurs at approximately 35 °C (±3 °C). This peak reproducibly appears in all the compositions from 9.3 mol% to 50.4 mol%, suggesting that it may represent a eutectic transition. It should be noted that the DSC traces in these cases are highly dependent on the thermal history of the samples. Metastable behavior can be seen in all the compositions between 9 mol% and 50 mol% LiTFSA if the samples are cooled from above 30 °C relatively quickly. A glass transition is regularly observed and always in the same temperature region, −65 °C (±8 °C). This is usually followed by a devitrification exotherm at −20 °C (±3 °C). The thermal data suggest that the phase changes in these mixed systems are kinetically slow and hence there is a tendency for the sample to become trapped in an amorphous state with subsequent devitrification into metastable phases. This could have significant impact on any devices that contained these materials as electrolytes and for which thermal cycling is likely. However, the observed transitions as represented by the 9.3 mol% LiTFSA sample in Figure 5.1 are reproducible when the samples have been stabilized at room temperature for at least 20 minutes before any measurement.

In the case of the 33 mol% LiTFSA sample the final melting occurs at approximately 35 °C and is quite sharp, indicative of a eutectic transition. To confirm that this is indeed a final melting, the sample has been visually confirmed to be a fluid liquid above 35 °C. These observations, combined with the fact that this peak has the highest molar enthalpy for the 35 °C transition among all the samples investigated, suggest that the eutectic temperature is about 35 °C (±3 °C) and that the eutectic composition is close to 33 mol%.
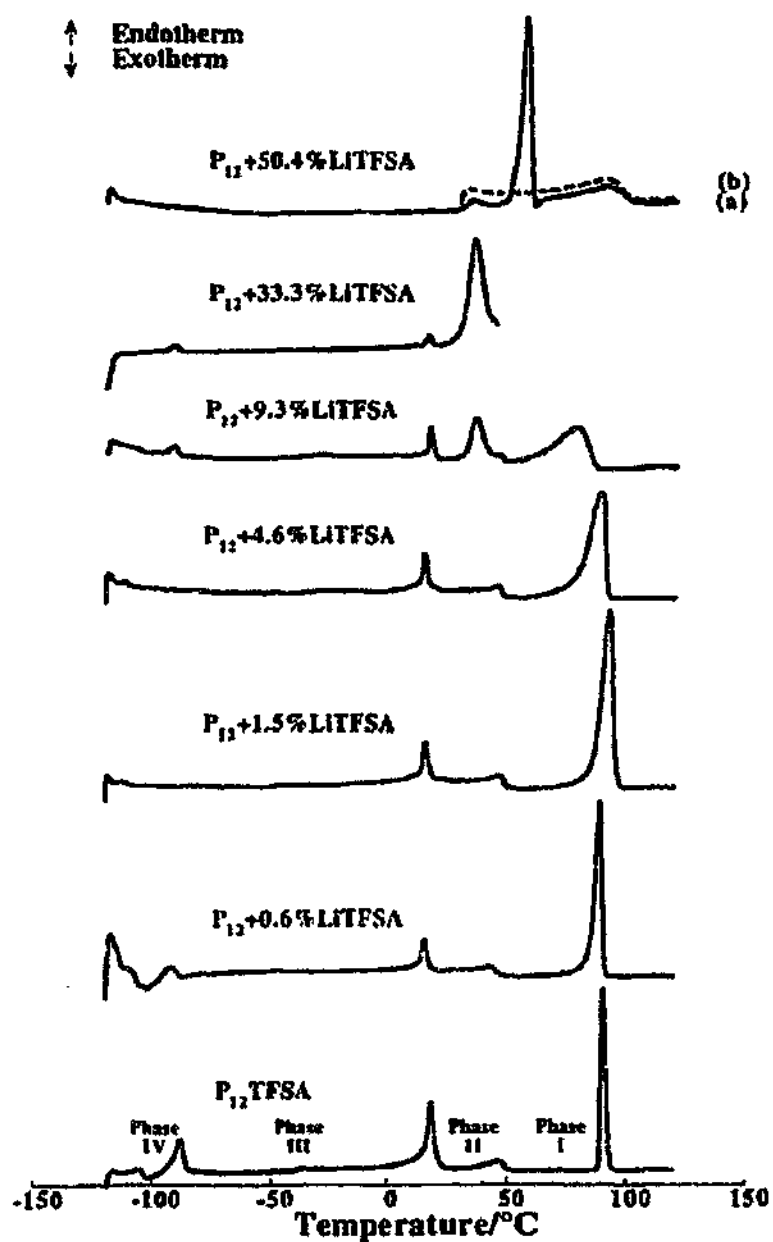
Figure 5.1 DSC traces for P12TFSA-LiTFSA mixtures at compositions indicated. These measurements were usually performed by heating in two different temperature regimes: -120 °C ~ 35 °C and 20 °C ~ 120 °C at 20 °Cmin⁻¹. The cold head experiments were performed after the samples had being cooled from room temperature (23 ± 2 °C) to -120 °C in about 15 minutes. Traces have been scaled for comparison of relative peak area. Phase I to IV are indicated on the diagram.
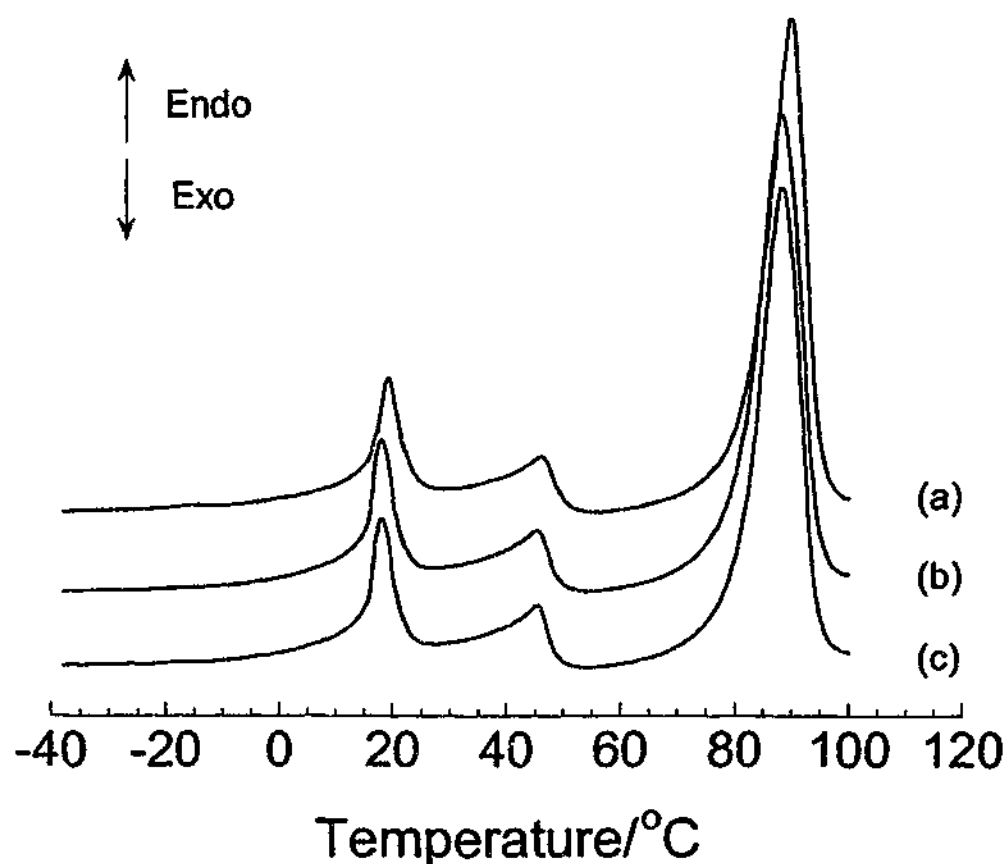
Figure 5.2 DSC traces for 2 mol% LiTFSA in P12TFSA sample. These measurements were performed by heating from –50 °C to 100 °C at 20 °Cmin^{-1} after (a) the sample had been stabilized at 20 °C for 20 minutes. (b) the sample had been melted to 100 °C. (c) the sample had been stabilized at 50 °C for 30 minutes.

When this sample is quenched from the melt, a glass transition is observed at about –60 °C (±3 °C) followed by a devitrification exotherm at –20 °C (±3 °C), as shown in Figure 5.3 (b). The final melting appears at lower temperature 31 °C (±3 °C). It is thought that a glassy liquid is formed by quenching the sample from the melt. The glassy liquid is transformed into a supercooled liquid through the glass transition. The low temperature crystallization process appears to produce a metastable crystal phase with poorer lattice packing and higher free energy than the stable phase. The metastable phase exhibits a lower melting point. A certain amount of stable phase is also present in this thermal process, which accounts for the "shoulder" at about 35 °C on the melting peak. Given the effect of slow diffusion on solid state reaction kinetics, it is not unexpected to observe such a high degree of metastable behavior. When the sample is cooled from the melt to –45 °C

- 185 -

and is stabilized for 15 minutes, the DSC trace shown in Figure 5.3 (c) still exhibits similar metastable behavior.

For the samples of 42 mol%, 46 mol% and 50 mol% LiTFSA, the phase II>>I transition at 45 °C disappears. Instead, a strong peak is observed at 56 °C (± 2 °C). However, the peak is not reproduced on a second run, as indicated by the dotted trace for 50 mol% LiTFSA in Figure 5.1. It is thought that this transition may be associated with the formation of a LiTFSA rich phase which is formed only slowly in the undercooled state.

Although compositions as high as 75 mol% LiTFSA have been investigated, the data are only discussed for samples up to 50 mol% LiTFSA due to the difficulty with reproducibility encountered for the higher compositions.
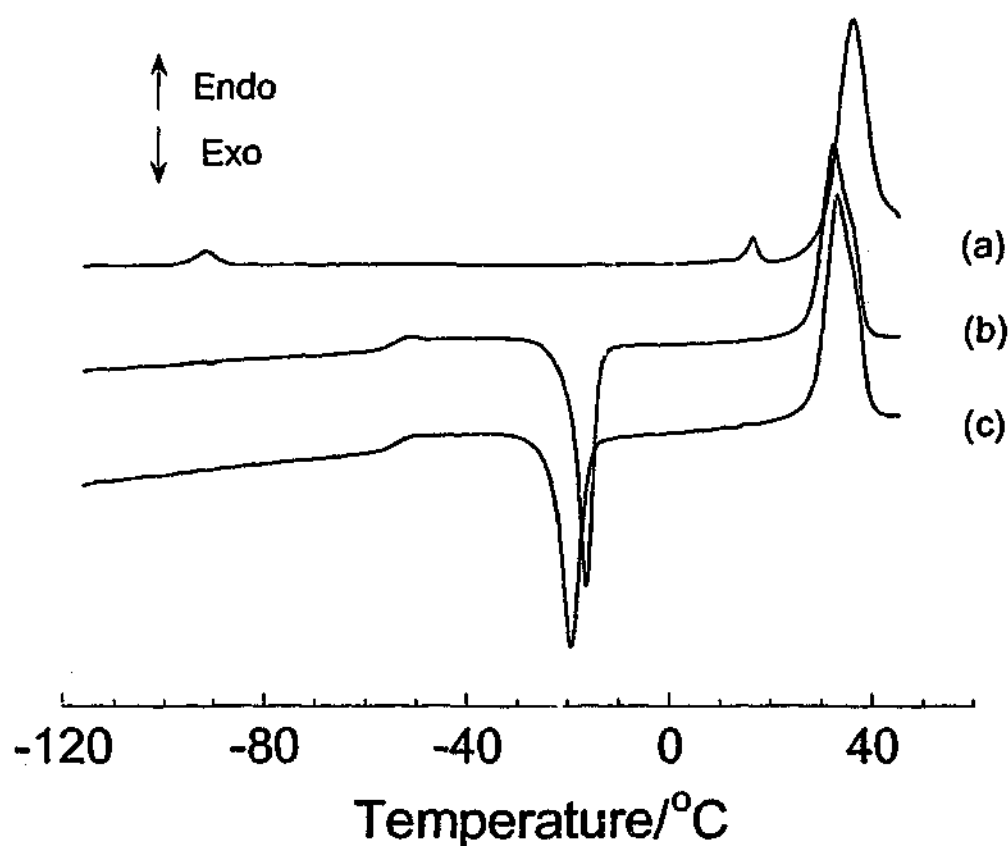
Figure 5.3 DSC traces for 33 mol% LiTFSA in P12TFSA sample during heating from –120 °C to 40 °C at 20 °Cmin⁻¹ after (a) the molten sample had been stabilized at 20 °C for 10 minutes. (b) the molten sample had been cooled to –120 °C. (c) the molten sample had been stabilized at –45 °C for 15 minutes.

Phase Diagram

Figure 5.4 presents a summary of the reproducible phase transitions as measured by DSC. This representation allows the suggestion of possible phase behavior.

The partial phase diagram appears to be a relatively classic binary system, the melting point being depressed by doping with LiTFSA. A eutectic transition occurs at 35 (±3) °C with a eutectic composition of approximately 33 mol% LiTFSA.

A solid solution region is present at the low LiTFSA content edge of the binary, with a maximum solubility of lithium ions in the P12TFSA lattice of between 4.8 and 9.3 mol%. The solubility could be dramatically increased above the phase III>>II transformation at 14 °C. The possible reasons are: (1) The small Li^+ ions could occupy the interstitial sites. Given the relative radii of the cations in this system, 0.6 Å for Li^+ versus approximately 3.1 Å for $P12^+$, this postulate is likely; (2) According to the PALS results for P12TFSA in section 3.2.4, when phase III transforms to phase II, vacancies increase significantly both in size and number. The formation of vacancies could favor the accommodation of the Li^+ ions into vacancies originally occupied by $P12^+$ cations. The latter postulate is more possible, as more energy is required for a Li^+ ion to occupy an interstitial site than to accommodate in a $P12^+$ site.

The other significant feature of the phase diagram is the constancy of the P12TFSA solid-solid phase transitions as a function of composition across the P12TFSA rich region of the diagram, in particular the region of solid solution. This suggests that the solid solutions can be accurately considered to be analogues of the pure P12TFSA phases, exhibiting the same dynamic rotational disorder as the pure plastic crystal phases. Phase IV>>III and III>>II transitions can be observed up to 50 mol%, which can be attributed to the presence of the P12TFSA rich phase in this solid two-phase region, although the other LiTFSA rich phase is unidentified. The phase II>>I transition can be observed up to 26 mol%, which again can be attributed to the presence of the P12TFSA rich solid solution phase in this two-phase region above the eutectic temperature. The other phase is the liquid domain. Phase II>I transition disappears beyond 33 mol%, where a liquid phase and a LiTFSA rich

solid phase coexist. Instead, another transition appears at about 56 °C, which may be attributed to the LiTFSA rich phase.
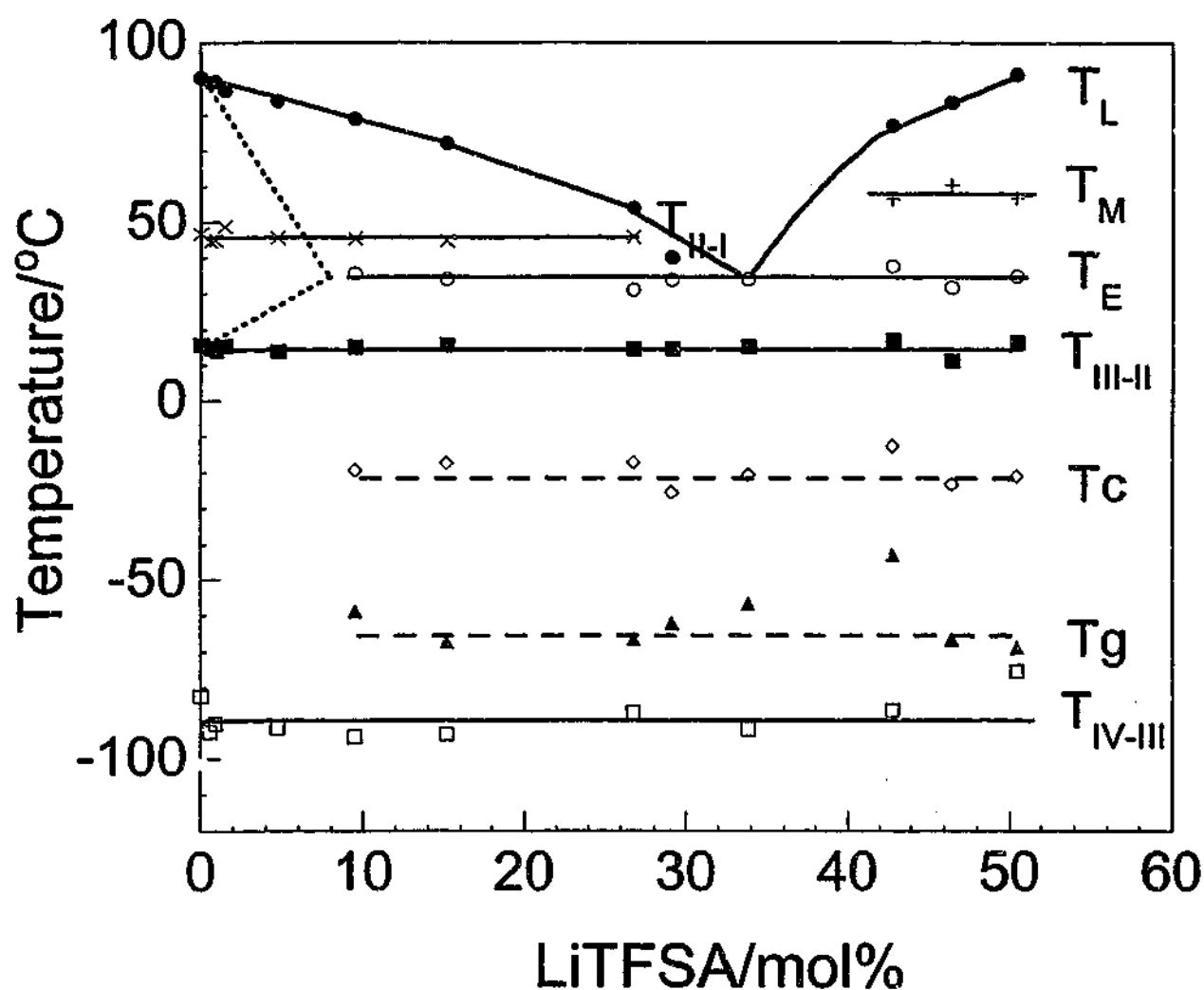
Figure 5.4 Partial phase diagram for P12TFSA-LiTFSA binary, indicating apparently equilibrium solid-solid phase transitions T_{IV-III}, T_{III-II} and T_{II-I}, liquidus temperature T_L, eutectic temperature T_E, glass transition temperature T_g, devitrification temperature T_C and a transition temperature T_M. T_g is the onset temperature. All the rest are peak temperatures. Solid and dashed lines are used to guide the eye, indicating equilibrium and metastable phase transitions, respectively. Dotted lines are tentatively drawn to indicate the solid solution region.

A glass transition and devitrification exotherm are observed for compositions between 9.3 mol% and 50 mol%, which could be attributed to the formation of supercooled liquid domain. These are quite normal for the components close to eutectic composition [297]. Thermodynamically, the free energy and the freezing point of the melt are decreased by mixing with another salt, which less favors nucleation during the cooling process and results in the amorphous state [297]. Kinetically, the diffusion and redistribution rate of P12TFSA and LiTFSA is slow. These are in contrast to the relatively constant solid-solid phase transition temperatures, which indicates that doping with LiTFSA salt alters the plastic crystal phase behavior to a lesser extent.

5.2.2 Conductivity

Conductivity vs. Temperature

Figure 5.5 (a) and (b) present temperature dependent ionic conductivity data for the LiTFSA-P12TFSA system spanning the composition range from the pure P12TFSA up to 50 mol% lithium salt and including a number of compositions in the doped region (up to 4.8 mol% LiTFSA). The Arrhenius format, $\log \sigma$ vs. inverse temperature, is used here in order to readily compare activation energy changes with composition. The observation of significant conductivity in the pure P12TFSA well below the melting point has been discussed in section 3.2.8 and has been associated with the vacancies present in the "plastic crystal" phases of this compound. The rapid increase in the conductivity as a function of temperature by several orders of magnitude from 45 °C up to the melting point can be attributed to an increased diffusion coefficient of the mobile ions and a rapidly increased number of charge carriers.

The samples doped with 0.9 mol% Li^+ show a steady divergence from the P12TFSA curve beginning at –25 °C. By 25 °C the sample reaches 10^{-6} Scm^{-1}, two orders of magnitude higher than the pure P12TFSA phase. This increase must be associated with either a larger number of charge carriers or, more likely, the availability of significantly more mobile ions compared with those in P12TFSA. Above 1.4 mol%, all the curves show obvious "knees" starting from about 14 °C, the phase III>>II transition. Considering the discussion in

- 189 -

section 5.2.1 that the solid solubility of Li^+ in P12TFSA matrix increases above the phase III>>II transition, it is likely that a greater amount of Li^+ ions is incorporated into the P12TFSA, accounting for the increase in conductivity. In the temperature range between 20 to 45 °C, in phase II, the slope $d\ln\sigma/d1/T$ remains nearly constant from 1.4 mol% to 4.8 mol%, suggesting a similar conduction mechanism and energy barrier in this solid solution region. The conductivity at 40 °C increases from 10^{-8} Scm^{-1} to 10^{-4} Scm^{-1} between 0 and 4.8 mol% LiTFSA. Considering the facts that the lithium salt contains the same anion as in the P12TFSA and that the lattice is doped without changing the phase behavior of the parent material, we can make a hypothesis that the motion of Li^+ ions is mainly responsible for the increased conductivity. In phase I, a sudden upturn of the conductivity is seen for all the components between 0 to 4.8 mol% LiTFSA as the liquidus temperature is approached.

For 9.3 ~ 50 mol% samples, all the conductivity curves show a jump in the temperature range of 16 ~ 30 °C. The enhanced conductivities can be attributed to the appearance of the eutectic domain which transforms from solid to liquid in this temperature range. Indeed at these higher concentrations the samples are heterogeneous, with at least part of the sample having melted at the eutectic transition 35 °C. Thus one would expect both a higher mobility and a larger number of the mobile charge carriers as the content of LiTFSA salt is increased towards the eutectic composition at any given temperature below the liquidus, since the volume fraction of the liquid phase increases. The conductivity data indicates that the highest conductivity is achieved at the eutectic composition 33 mol%. It is interesting to note that the conductivity of 33 mol% LiTFSA at 40 °C is about one order of magnitude higher than that of 4.8 mol% whilst it increases by four orders of magnitude from 0 to 4.8 mol%. Above the eutectic composition the conductivity would then decrease as the concentration of LiTFSA increases. In contrast to the sharp increase in conductivity near the melting point observed for the 0 ~ 4.8 mol% compositions, $d\ln\sigma/d(1/T)$ is practically constant below the final liquidus temperature for samples of 9.3 ~ 50 mol% and there is no sharp step in conductivity at the liquidus temperature. This distinctly different behavior provides us with some additional evidence that, for compositions between 0 and approximately 5 mol% LiTFSA, phase I is a doped solid solution phase.
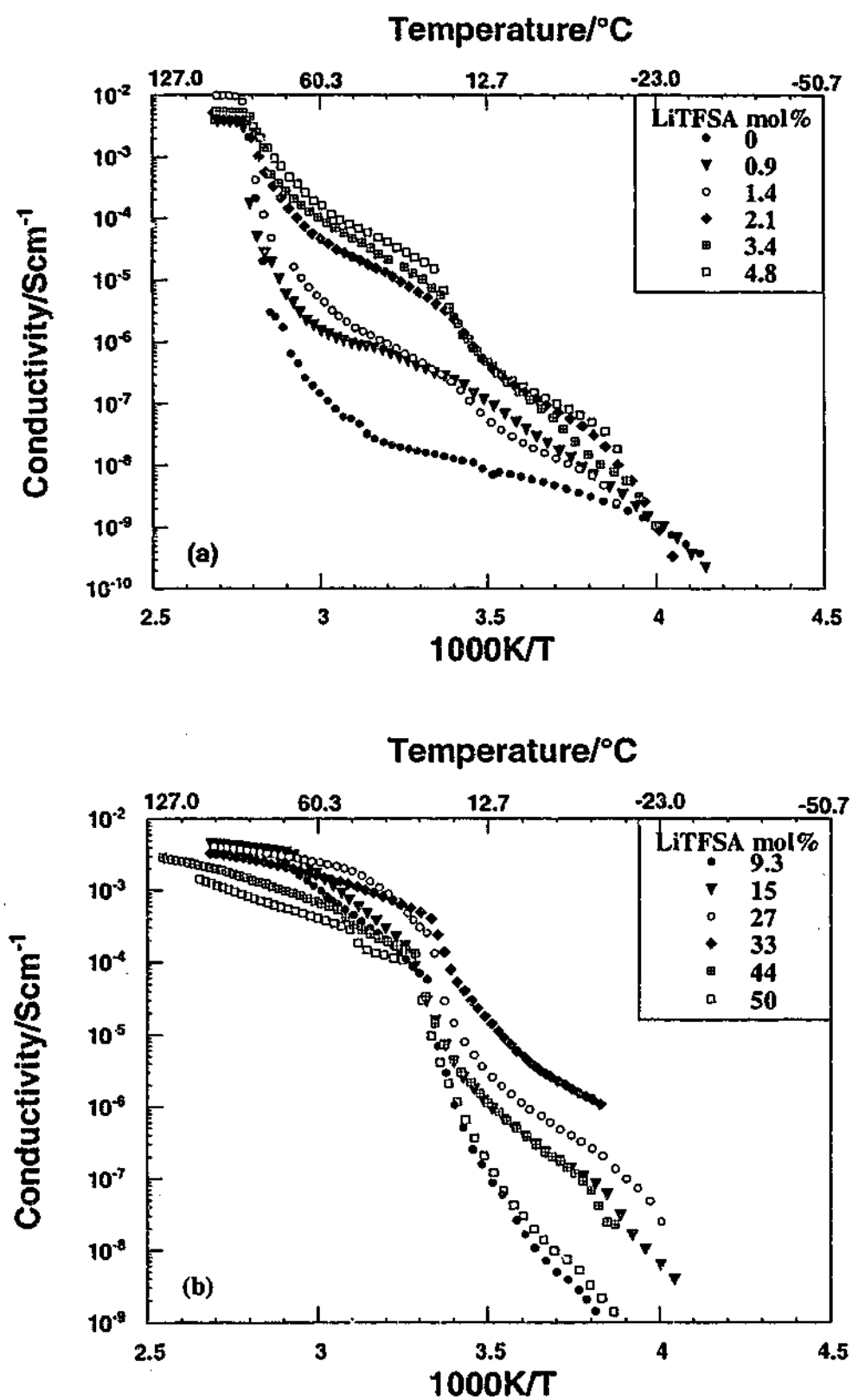
Figure 5.5 Conductivity as a function of inverse temperature for (a) 0 ~ 4.8 mol% LiTFSA doped P12TFSA and (b) 9.3 ~ 50 mol% LiTFSA doped P12TFSA. The conductivity curve for the pure P12TFSA is slightly different from the one observed in section 3.2.1 due to slightly different thermal history of the sample.

Conductivity vs. LiTFSA Concentration

Figure 5.6 presents the compositional dependence of the conductivity at a number of temperatures, allowing a comparison of the conductivity changes in the various phase transition regions.

At 5 °C the samples are all solid, albeit in some cases a solid state mixture, and the stable P12TFSA phase will be phase III according to the phase diagram shown in Figure 5.4. The conductivity increases with doping of LiTFSA, though to a less extent than the increase above 25 °C. This probably suggests that the lithium salt is less soluble in the P12TFSA lattice in phase III and so the number of conducting lithium ions may be relatively small and not changing as more lithium salt is added to P12TFSA. The highest conductivity is observed for the 33 mol% composition.

In the phase II region, at 25 °C, the conductivity is clearly seen to rise dramatically up to 4.8 mol% LiTFSA, whereas smaller increases are seen beyond this point; eventually conductivity decreases again beyond the eutectic composition. The 33 mol% LiTFSA sample exhibits the highest conductivity in the solid phases below the eutectic temperature, which may simply reflect the fact that all of the sample is approaching the molten state at 35 °C.

In the phase I region, at 50°C, the increase as a function of concentration is even more dramatic, four orders of magnitude increase between 0 and 10 mol% LiTFSA, followed by a plateau in conductivity. · Highest conductivity is observed at 27 mol% LiTFSA. The interpretation of the conductivity behavior between 35 °C and final melting is complex, because both the solid phase that remains above 35 °C (Li^+ doped P12TFSA phase for compositions between 9.3 and 33 mol% or LiTFSA rich phase for compositions beyond 33 mol%) and the liquid domains whose volume increase above the eutectic temperature contribute to the conductivity. It is thought that Li^+ ions are the main charge carriers in the P12TFSA rich solid solution phase whilst the conduction in the liquid domains is likely to involve all of the ions to some extent.

At 95 °C, all of the samples are in the molten state and so it is not surprising that there is an insignificant compositional effect on the conductivity. If anything, the conductivity decreases with LiTFSA additions, which can be indicative of a decreasing ionic mobility due to the increased viscosity visually observed with the doping of lithium salts.
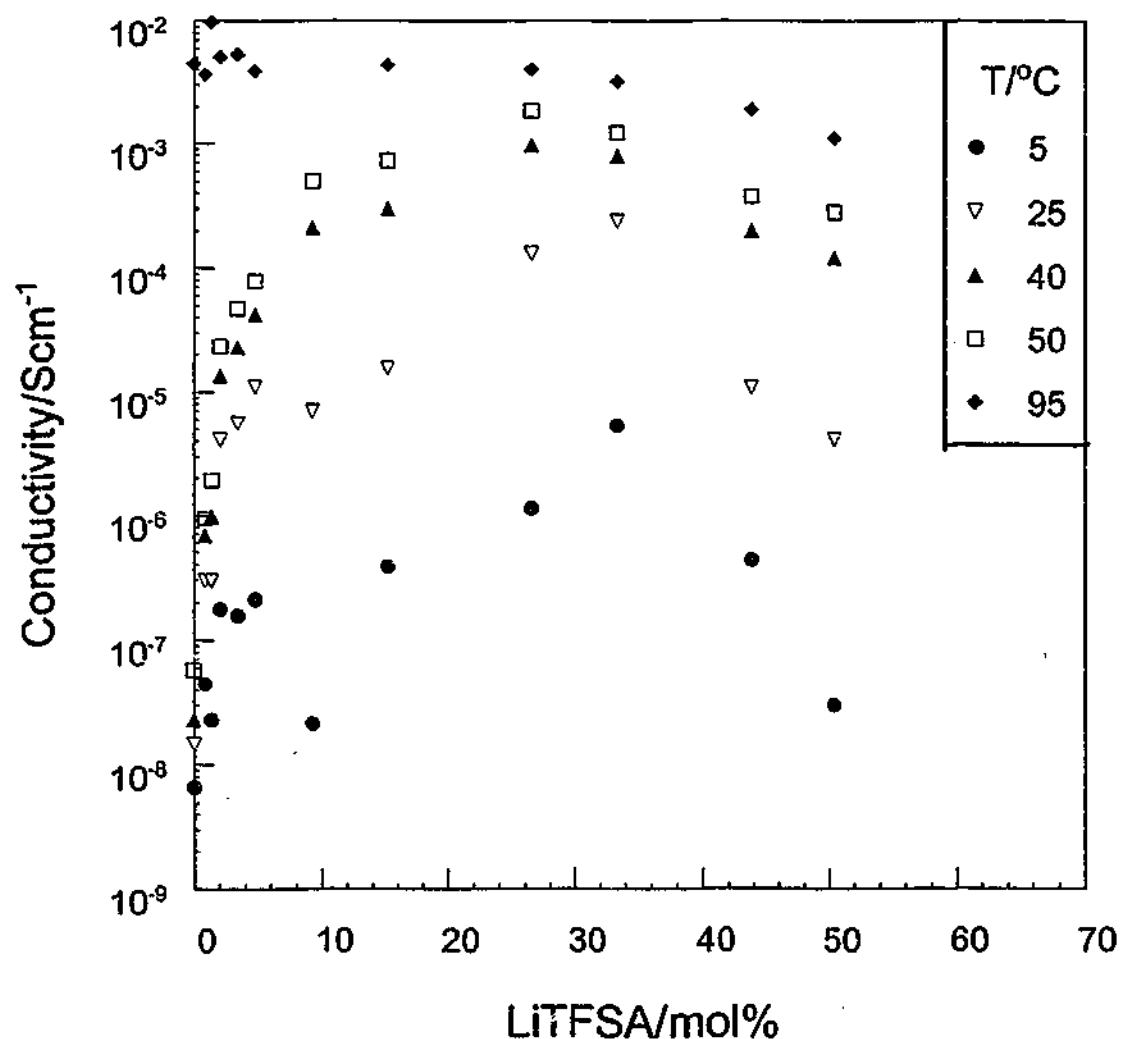
Figure 5.6 Conductivity isotherms as a function of LiTFSA composition for P12TFSA-LiTFSA binary.

Conductivity vs. Time

The stability of conductivity for 0.9 mol% and 4.8 mol% LiTFSA samples was tested at constant temperatures distributed in phases I, II and III, as shown in Figure 5.7. Both samples exhibit a slight decrease in conductivity in the first 50 hours and then approach a

conductivity limit. One exception is that the conductivity for 0.9 mol% LiTFSA at 56 °C increases, probably indicating a homogenizing of the dopant in the sample. The small change in the conductivity over more than one week suggests that the phases are stable at least over this time period.
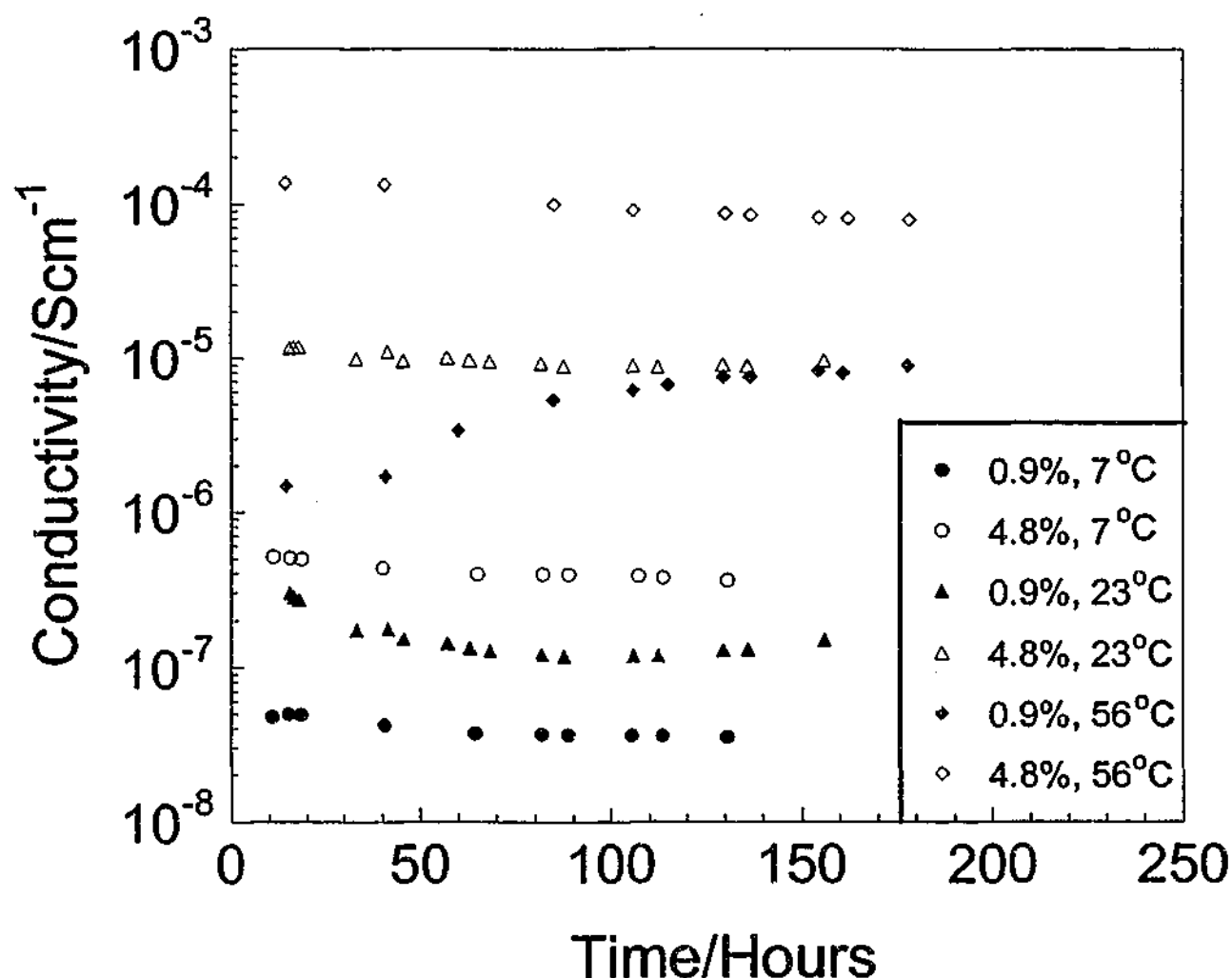
Figure 5.7 Isothermal conductivity as a function of time for 0.9 mol% and 4.8 mol% LiTFSA in P12TFSA.

5.2.3 Nuclear Magnetic Resonance

^{1}H NMR Linewidth for 4.8 mol% LiTFSA in P12TFSA

^{1}H NMR spectra for 4.8 mol% LiTFSA are shown in Figure 5.8. Similar to the ^{1}H NMR spectra observed for pure P12TFSA, 4.8 mol% LiTFSA exhibits a single broad resonance

at –56 °C, in phase III. A sharp line appears at –33 °C. The intensity of the sharp peak increases with temperature at the expense of the broad line.

The temperature dependence of the linewidth and the fraction of the narrow component are shown in Figure 5.9 and Figure 5.10, respectively. The linewidth of the broad line is about 23.2 kHz in phase III. Line narrowing occurs when the temperature gets close to the phase III>>II transition. The linewidth reduces to 12.5 kHz in phase I. These linewidth values and the temperature dependence are very similar to those observed for the pure P12TFSA, as shown in section 3.2.5, suggesting that the cations represented by the broad peak perform similar anisotropic rotational motions to those in pure P12TFSA. These are consistent with the hypothesis that the solid solution phase exhibits the same dynamic rotational behaviors as the pure plastic crystal phases. The slightly broader linewidths observed for 4.8 mol% LiTFSA compared to pure P12TFSA are probably attributed to a less homogeneous environment by doping with the LiTFSA salt, particularly in phase III where a P12TFSA rich phase and a LiTFSA rich phase coexist.

The linewidth of the narrow peak is about 2.8 kHz at –33 °C. It reduces to 1.1 kHz in phase III and remains constant in phase II and phase I. These linewidths are much less than 7 kHz, the calculated value for cationic isotropic rotation from Table 4.3, indicating translational motion. Again, these linewidths are broader than the value of 500 Hz observed for pure P12TFSA. It is very likely that peaks of different chemical shifts which are not discernable result in the relatively broader linewidth, since two narrow peaks are observed for pure P12TFSA versus one less narrow peak for the 4.8 mol% LiTFSA compound.

The fractions of the mobile cations in 4.8 mol% LiTFSA and pure P12TFSA are compared in Figure 5.10. The numbers of mobile cations exhibit an increase in phase III and another sharp rise near the melting points for both samples. The number of diffusing cations in phase III and II for 4.8 mol% LiTFSA is nearly one order of magnitude higher than that for pure P12TFSA. According to the discussion in section 3.3.2 that the cationic diffusion is associated with vacancies, the larger number of diffusing cations seems to indicate that more vacancies are formed by doping with LiTFSA salt. This is not unexpected, because

the dopant normally results in defects [163]. Thus at least some of the conductivity enhancement observed will be attributed to a larger number of cationic (P12$^+$) vacancies.
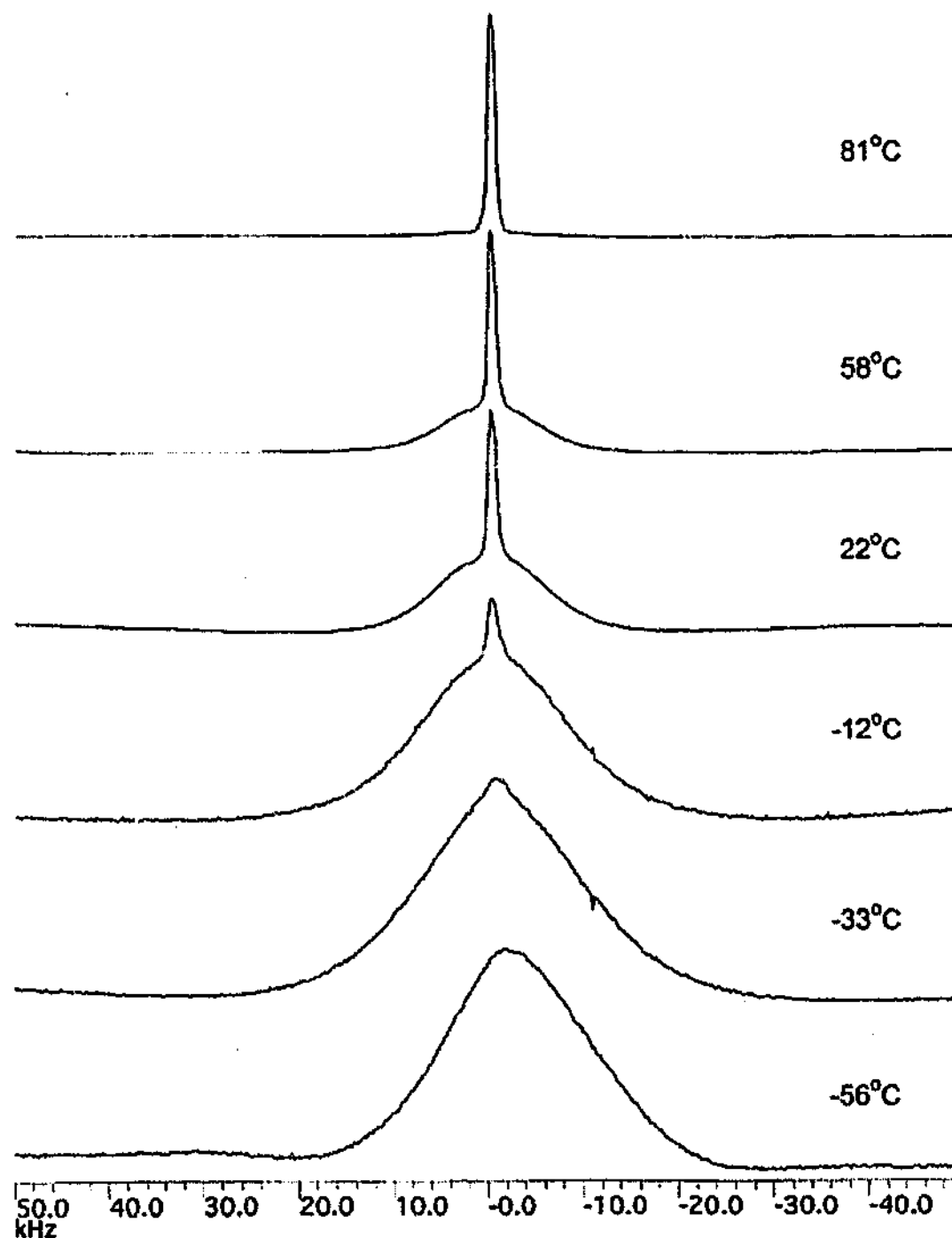
Figure 5.8 ^{1}H NMR spectra for 4.8 mol% LiTFSA in P12TFSA as a function of temperature.
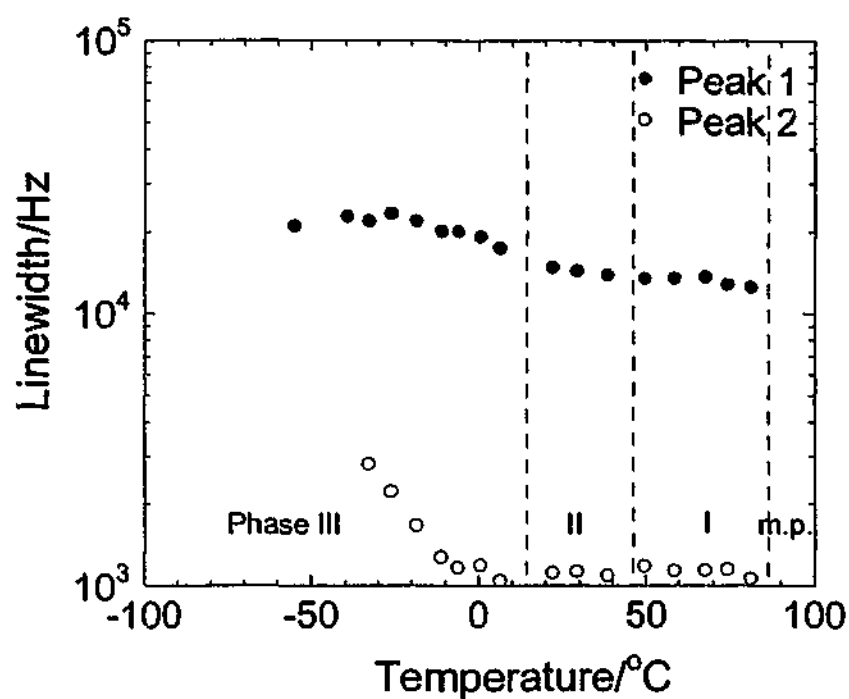
Figure 5.9 Temperature dependence of ^{1}H NMR Linewidth for 4.8 mol% LiTFSA in P12TFSA.
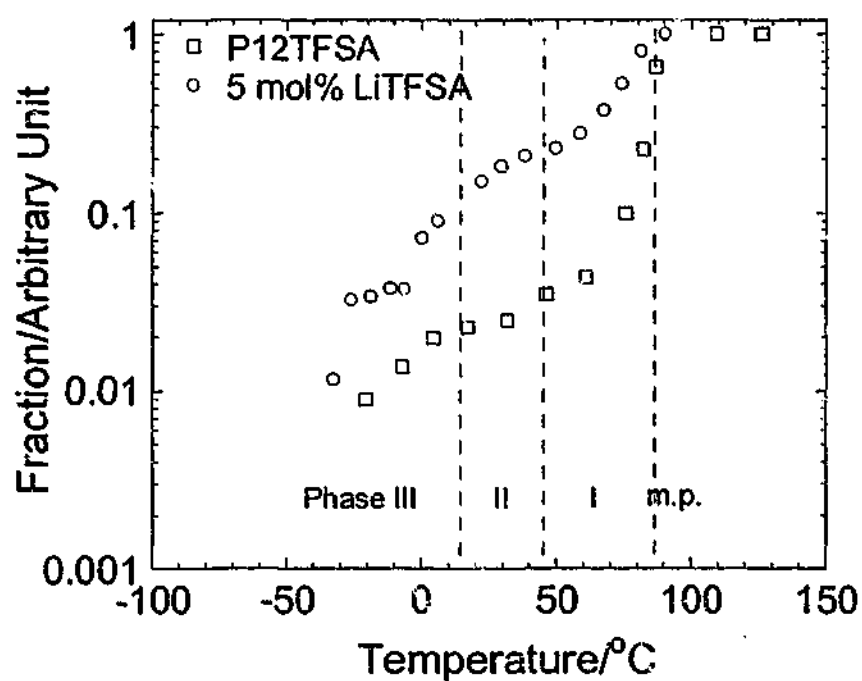
Figure 5.10 Fractions of narrow peak area of ^{1}H NMR as a function of temperature for 4.8 mol% LiTFSA in P12TFSA and pure P12TFSA. Dashed lines indicate the phase transition temperatures of 4.8 mol% LiTFSA in P12TFSA.

^{1}H NMR Spin-lattice Relaxation for 4.8 mol% LiTFSA in P12TFSA

The magnetizations of the broad and narrow peaks are analyzed separately. Similar to pure P12TFSA, mono-exponential behavior was observed for both components and single T_1s were obtained for the broad and narrow peaks respectively with correlation coefficient R>0.99 in most curve fits. The T_1s obtained are shown in Figure 5.11.

There is a discontinuity in T_1 between the low and high temperature ranges for the broad component, suggesting a change in the relaxation mechanism. According to the linewidth analyses above, the cations represented by the broad peaks rotate anisotropically in phase III, which could be associated with a rotation or inversion of the ring plus the CH_3 group rotation. The narrower linewidth in phases II and I suggests that a new anisotropic rotational motion commences. It is very likely that the low temperature rotational motion still remains at higher temperature. For an anisotropic rotation, the relaxation mechanism is dominated by intraionic dipolar interactions according to Table 4.3, which are ^{1}H-^{1}H dipolar interactions. Therefore, T_1 over the whole temperature range can be expressed as:

$$1/T_1^H = 1/T_1^H{}_{rot1} + 1/T_1^H{}_{rot2}$$

Equation 5.1

where subscripts rot1 and rot2 indicate the two rotation mechanisms, respectively. $1/T_1^H{}_{rot1}$ or $1/T_1^H{}_{rot2}$ is attributed to the dipolar interactions between like nuclei, expressed as Equation 2.27 in section 2.1.5. Equation 5.1 can be written as Equation 3.2 and Equation 3.3. The activation energies E_a and correlation times τ of these rotations can then be obtained by curve fit, as shown in Figure 5.12. Two sets of E_a's and τ_o's corresponding to two rotational mechanisms are obtained, as listed in Table 5.1

As to the narrow component which indicates the diffusing $P12^+$ cations, since diffusing ions normally participate in isotropic rotational motion as well, due to lower energy barrier of rotation than diffusion, intraionic dipolar interactions are averaged out. Interionic dipolar interactions mainly account for the relaxation mechanism. Interionic ^{1}H-^{1}H, ^{1}H-^{19}F and ^{1}H-^{7}Li dipolar interactions are all possible contributors to the spin-lattice relaxation. Since the number of Li^+ ions is much smaller than the numbers of $P12^+$ and TFSA⁻ ions and

hence the numbers of ^1H and ^{19}F nuclei, ^1H-^7Li dipolar interactions can be ignored. Only ^1H-^1H and ^1H-^{19}F dipolar interactions are considered. The T_1 can be expressed as:

$$1/T_1{}^H{}_{dif} = 1/T_1{}^{H-H}{}_{dif} + 1/T_1{}^{H-F}{}_{dif}$$

Equation 5.2

where superscripts H-H and H-F indicate contributions from ^1H-^1H and ^1H-^{19}F dipolar interactions respectively. $1/T_1{}^{H-H}{}_{dif}$ and $1/T_1{}^{H-F}{}_{dif}$ are expressed as Equation 2.27 and Equation 2.32 in section 2.1.5 due to the dipolar interactions between the like and unlike nuclei, respectively. The T_1s obtained are all on the high temperature side of the minimum, so $\omega_H\tau \ll 1$ is assumed. By comparing Equation 2.15 with Equation 2.27, Equation 2.17 with Equation 2.32, Equation 5.2 can be simplified as:

$$\frac{1}{T_1{}^H} = 10 \times (\frac{M_2{}^{H-H}}{3} + \frac{M_2{}^{H-F}}{2})\tau = C\tau_0 \exp(\frac{Ea}{RT})$$

Equation 5.3

Although at low temperature the sample may be composed of two phases, a P12TFSA rich phase and a LiTFSA rich phase according to the phase diagram in Figure 5.4, the P12TFSA rich phase is the major phase over all the temperature range studied according to the lever rule. Therefore, $M_2{}^{H-H}$, $M_2{}^{H-F}$ and C are assumed to have similar values to those for pure P12TFSA. They are 2.3×10^8 s^{-2}, 1.2×10^8 s^{-2} and 1.4×10^9 s^{-2}, respectively as shown in Page 120. $1/T_1{}^H$ exhibit different temperature dependences over different temperature ranges, probably suggesting different activation energies. τ_0 and E_a can be obtained by curve fit using Equation 5.3, as shown in Figure 5.13. The E_a and τ_0 values obtained from this fitting are listed in Table 5.1.
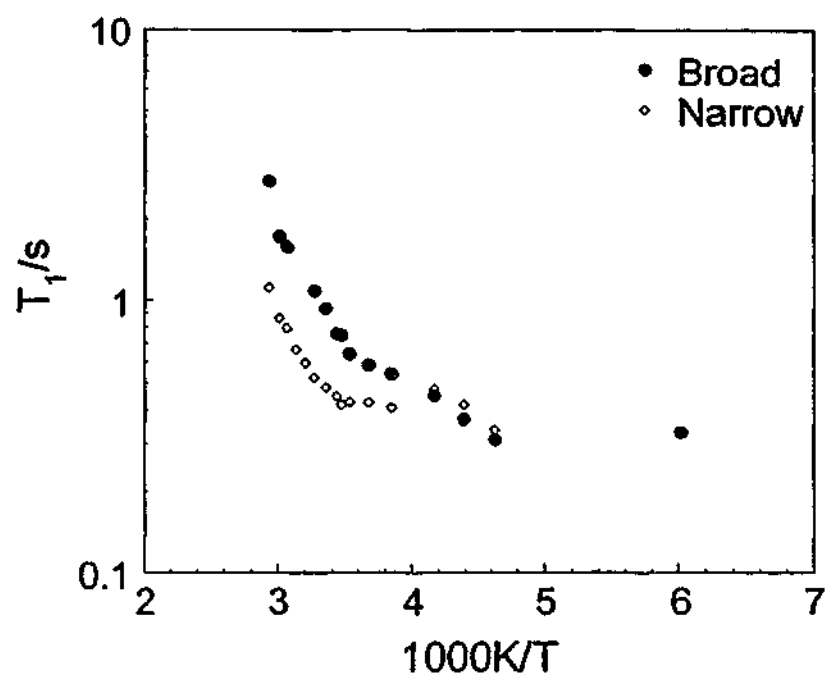
Figure 5.11 Temperature dependence of ^{1}H NMR spin-lattice relaxation time T_1 for 4.8 mol% LiTFSA in P12TFSA.
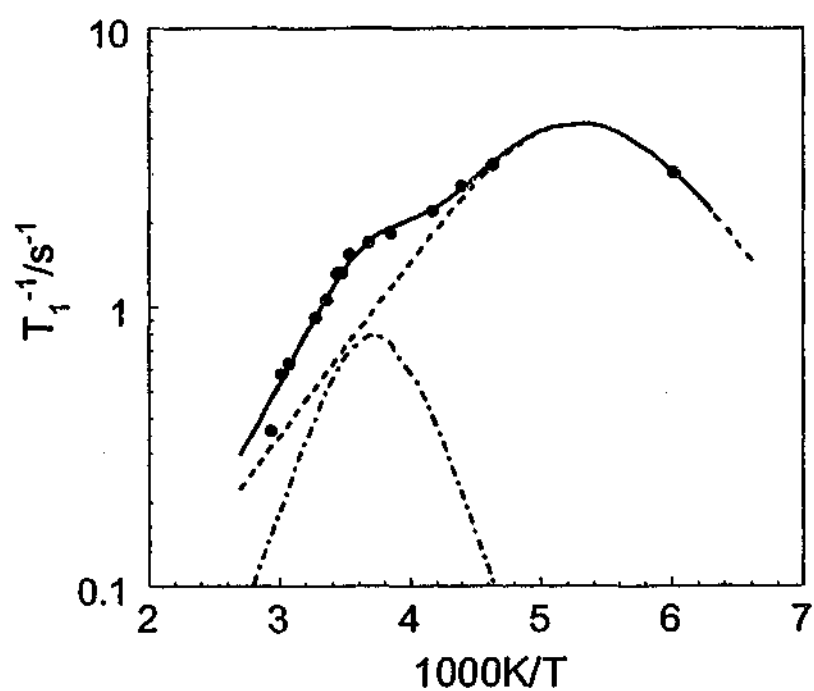
Figure 5.12 Curve fit of T_1^{-1} of the broad ^{1}H NMR for 4.8 mol% LiTFSA in P12TFSA. The solid circles are the experimental data. The two dashed lines are the calculated values for two rotational mechanisms, respectively. The solid line is the sum of the two calculated values.

- 200 -
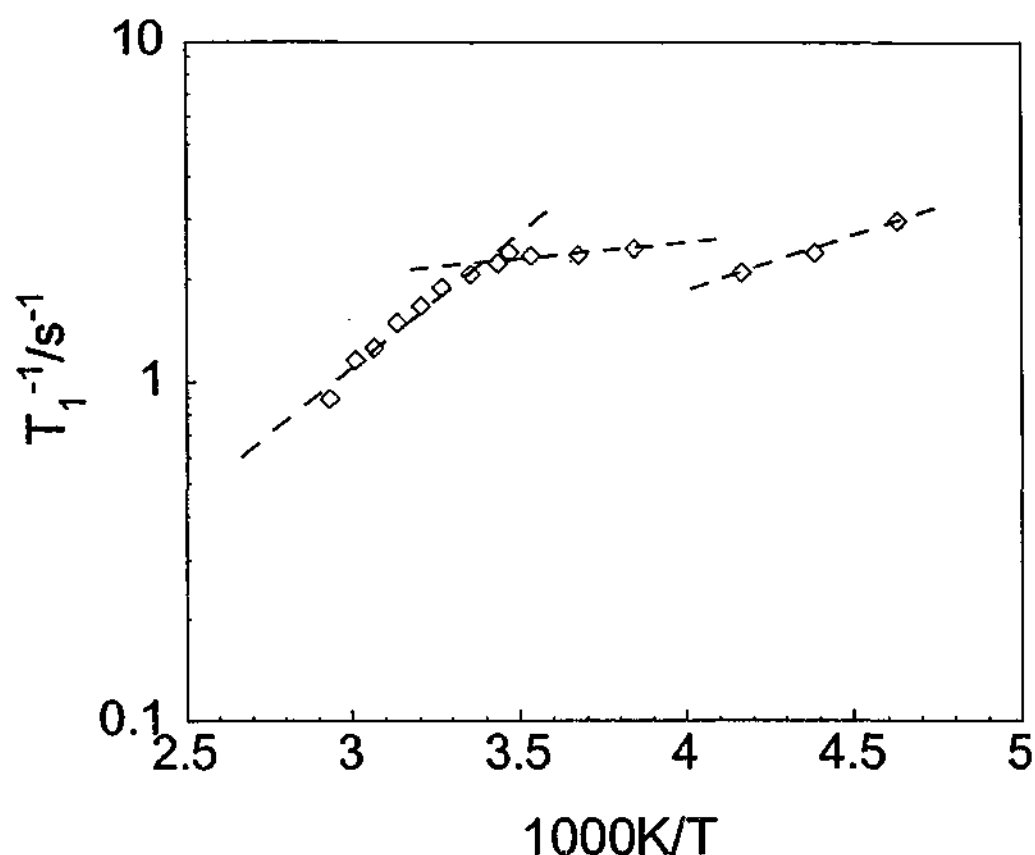
Figure 5.13 Curve fit of T_1^{-1} of the narrow ^{1}H NMR for 4.8 mol% LiTFSA in P12TFSA. The diamonds are experimental values. The dashed lines are calculated values.

The correlation times of P12$^+$ cationic motion calculated from τ_o and E_a in Table 5.1 are shown in Figure 5.14. The correlation times for the P12$^+$ cation diffusion at 30 °C and 80 °C are 7.8×10^{-10} s and 5.9×10^{-10} s, respectively. Diffusion coefficients D are estimated to be 2.1×10^{-10} m^{2}s^{-1} and 2.8×10^{-10} m^{2}s^{-1}, respectively, by using Equation 3.8. These data coincide well with those measured by gradient field NMR techniques [293], which again indicates the reliability of T_1 measurements and analyses in this study, at least for the diffusion behavior.

The effects of doping LiTFSA salt on the motion of P12$^+$ cation are shown in Figure 5.14. The broad peaks for pure P12TFSA and 4.8 mol% LiTFSA exhibit similar linewidth range and similar T_1 temperature dependence, suggesting that the same rotational mechanisms occur in these two samples. This is confirmed by the similar DSC traces which indicate the same plastic crystal behaviors for these two samples. However, doping seems to change

- 201 -

the correlation times and alter the activation energies for both rotational motions. Doping with LiTFSA salt also seems to increase the diffusion rate of $P12^+$ ions. This effect is more obvious below 14 °C, in phase III. The possible reason is that in phase III, 4.8 mol% LiTFSA is composed of two solid phases, a P12TFSA rich phase and a LiTFSA rich phase. Consequently, defects are created in the forms of vacancies or phase boundaries, which provide diffusion pathways for $P12^+$ cations. In contrast, the sample is a homogenous solid solution above 14 °C, which can be regarded as the analogue to the pure P12TFSA. Therefore the difference in the diffusion coefficient between these samples is less than in phase III.

Table 5.1 Activation energies (E_a), correlation times at the limit of infinite temperature (τ_o) and motional constants (C) evaluated for cationic motion from ^{1}H NMR relaxation time T_1 for 4.8 mol% LiTFSA in P12TFSA. [a] Calculated from second moment.

Motion	Temperature/°C	$C/10^8\ s^{-2}$	$E_a/kJmol^{-1}$	τ_o/s	Correlation coefficient
Rotation I		60.2±11	12.1±4	$(1.4\pm0.2)\times10^{-13}$	0.998
Rotation II		10.5±6	25.7±9	$(3.3\pm0.6)\times10^{-15}$	
Diffusion	T<-25	14^a	6.3±0.5	$(6.2\pm0.2)\times10^{-11}$	0.996
	-25 ~ 14	14^a	1.3±0.2	$(9.4\pm0.6)\times10^{-10}$	0.941
	T>14	14^a	14.2±0.9	$(4.7\pm0.2)\times10^{-12}$	0.984
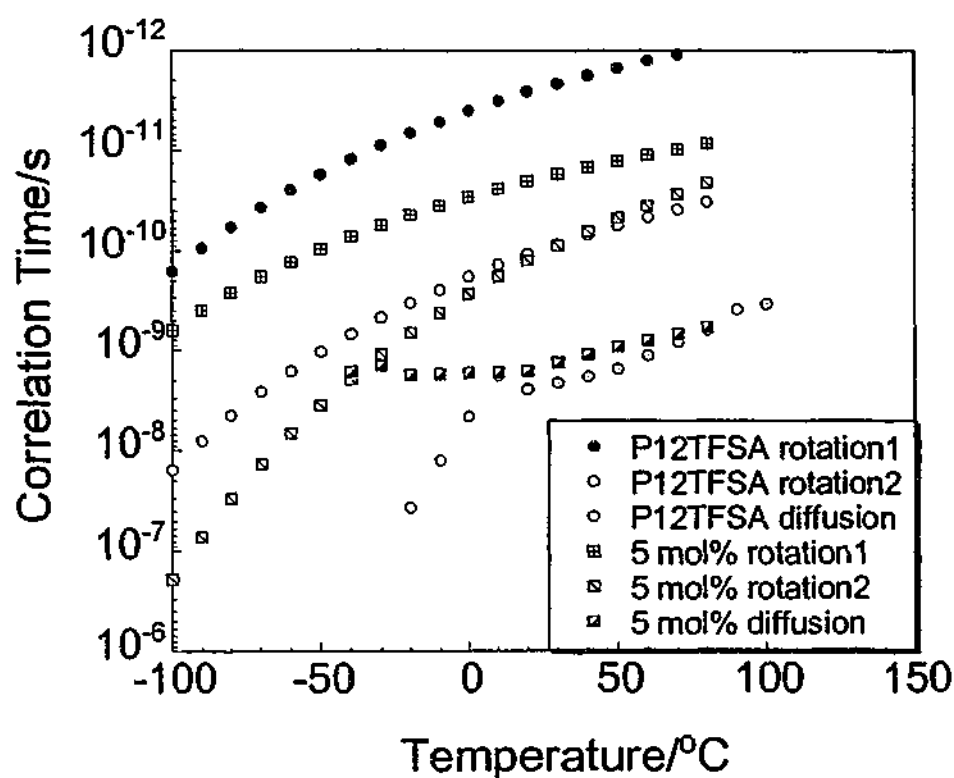
Figure 5.14 Comparison of the correlation times of $P12^+$ cation for pure P12TFSA and 4.8 mol% LiTFSA in P12TFSA. Data are calculated from activation energy E_a and correlation times at the limit of infinite temperature τ_0 in Table 3.3 and Table 5.1.

^{19}F NMR Linewidth for 4.8 mol% LiTFSA in P12TFSA

^{19}F NMR spectra are shown in Figure 5.15. Similar to the spectra for P12TFSA, 4.8 mol% LiTFSA exhibit a broad bottom at low temperature. This broad bottom can be deconvoluted into two peaks of different chemical shifts, indicating at least two different sites for F atoms. A narrow line appears at –63 °C. The intensity of the narrow peak increases with temperature.

The linewidth of each component is shown in Figure 5.16. The linewidth of the broad peak reduces from 11 kHz at –80 °C to 6.4 kHz at 17 °C. Similar to the linewidth analyses for P12TFSA, the broad bottom can be assigned to the positionally ordered anions, which rotate anisotropically at –80 °C and undergo isotropic rotation above –20 °C. In the case of the narrow peaks, substantial further line narrowing occurs in phase III, from 1.2 kHz at – 63 °C to about 200 Hz at 10 °C. The linewidths of this peak remain relatively constant in phase II and phase I. The narrow peaks can be attributed to the diffusing anions.
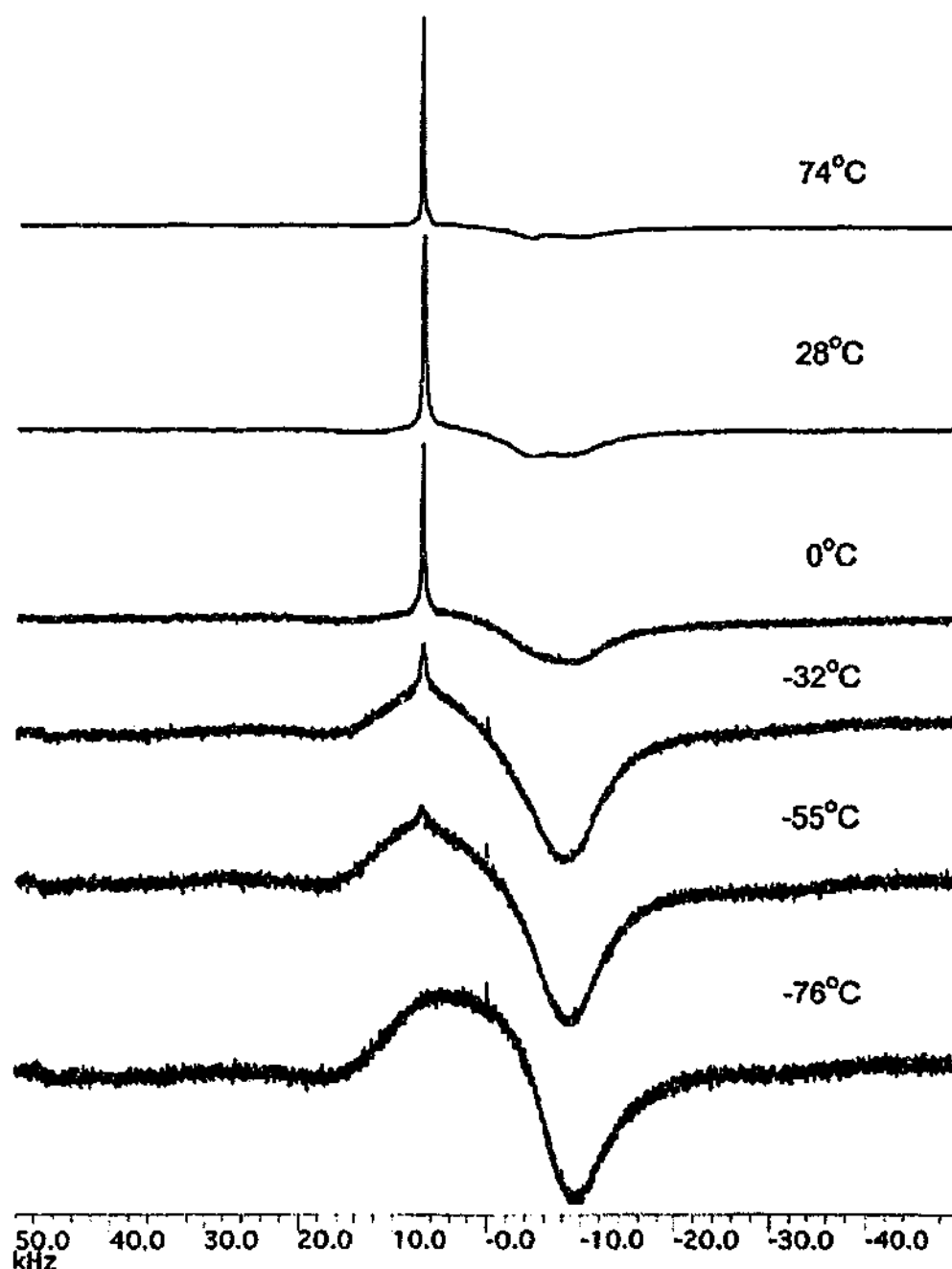
Figure 5.15 ^{19}F NMR spectra for 4.8 mol% LiTFSA in P12TFSA as a function of temperature. The peak at about −10 kHz comes from background.

Due to the relatively smaller broad peak compared to that for pure P12TFSA or P11TFSA, the background brings about a larger error in assessing the broad peak area and so the fraction of the narrow peak area can not be estimated accurately. Moreover, the diffusion coefficient of TFSA⁻ anions can not be directly measured by gradient field NMR below 90 °C due to the serious interference from T_2 relaxation time [293]. However, it could be

- 204 -

postulated that doping of the LiTFSA salt results in a larger number and/or higher diffusion coefficient of the TFSA⁻ anions. This idea seems reasonable, because if there is some association between P12⁺ cations and TFSA⁻ anions in the diffusive motion in pure P12TFSA, this association may still exist in 4.8 mol% LiTFSA. As the number of diffusing P12⁺ is increased by doping with LiTFSA, the number of diffusing population of TFSA⁻ could also be increased. The observations that (1) the narrow peak is first observed at temperature as low as –55 °C compared to –26 °C for pure P12TFSA; and (2) the narrow peak linewidth of 200 Hz is much smaller than the 400 Hz for pure P12TFSA also support the idea that anionic motion is enhanced upon doping with LiTFSA.
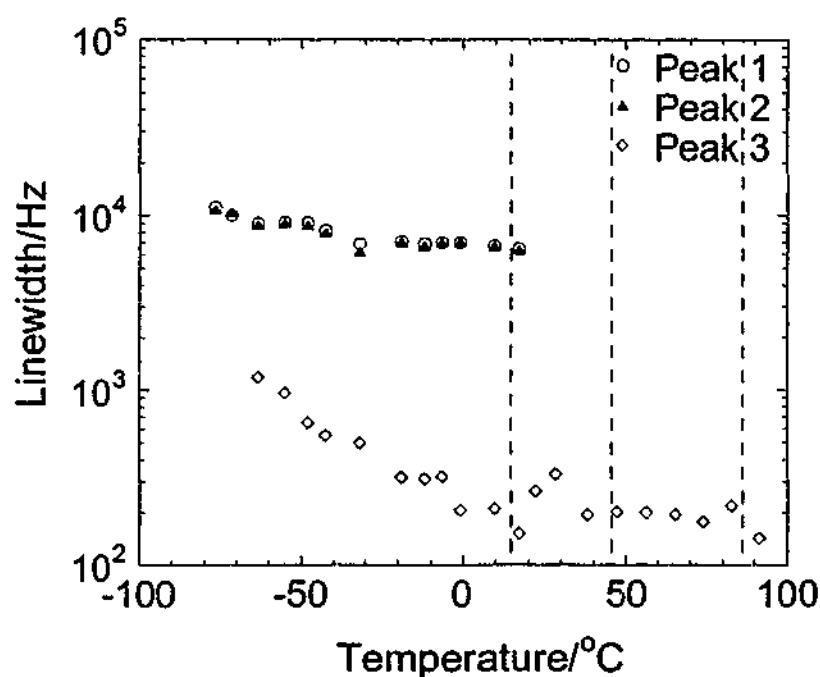
Figure 5.16 ¹⁹F NMR linewidth of 4.8 mol% LiTFSA in P12TFSA as a function of temperature. Dashed lines indicate phase transition temperatures.

⁷Li NMR Linewidth for 4.8 mol% LiTFSA in P12TFSA

Temperature dependent ⁷Li NMR spectra for 4.8 mol% LiTFSA are presented in Figure 5.17. At –105 °C, in phase IV, the spectrum displays a single broad resonance. With increasing temperature, a narrower line appears on the top of the broad bottom. The intensity of the narrow peak increases with temperature whilst that of the broad line decreases. Considering that ⁷Li has a spin quantum number of 3/2, the broad component

could arise from the $|\pm 3/2 \rangle \leftrightarrow |\pm 1/2 \rangle$ quadrupolar satellite transitions whilst the $|1/2 \rangle \leftrightarrow |-1/2 \rangle$ transition could account for the central sharper line. However, this interpretation is not supported by a comparison of the peak areas of the broad and narrow components, because if the broad peak is due to quadrupolar satellites, the ratio of the broad component to the narrow component should be close to 3:2, expected theoretically from respective transition probabilities, as observed in ^{23}Na NMR for Na_3PO_4 [201]; whilst the ratio of the broad to narrow peak area measured is changing with temperature, according to Figure 5.19. Therefore, in a similar way to the ^{1}H and ^{19}F NMR spectra observed in this study, this "narrow line on top of broad peak" should be attributed to Li^+ ions at different sites where dipolar interactions act to different extents.

The broad line exhibits a linewidth of about 3.6 kHz at -105 °C, shown in Figure 5.18. This is a typical value for lithium ions in a rigid lattice, as observed in other electrolyte systems. For example, the ^{7}Li rigid lattice linewidths for a series of silicate, borate and phosphate glasses, estimated from second moment measurements, range from 3 kHz to 6 kHz [298]. Lithium salt doped PEO polymers exhibit rigid lattice linewidths of about 6 to 7 kHz [299]. ^{7}Li-^{7}Li, ^{7}Li-^{1}H and ^{7}Li-^{19}F dipolar interactions in the P12TFSA-LiTFSA system are all possibly responsible for the broad linewidth. The linewidth of the narrow peak is about 300 Hz in phase III, indicative of translational motion. This residual linewidth may result from: (1) the dipolar interactions which are not totally averaged out; and/or (2) the inhomogeneous environments, because of the coexistence of two solid phases in phase III or the inhomogeneity of the magnetic field. At 16 °C where phase III to phase II transition occurs, the broad line becomes narrower and finally disappears, indicating that all of the Li^+ ions become mobile in phases II and I. The narrow line shows a sharp narrowing to 80 Hz, suggesting that Li^+ ions are more mobile or are in more homogeneous environments. Figure 5.19 indicates that the number of mobile Li^+ ions increases substantially through this transition. This supports the proposal that Li^+ ions are significantly more "soluble" in phase II. All the Li^+ ions are incorporated into the P12TFSA network and become very mobile. The linewidth remains 80 Hz in phase I. Compared to the linewidth value of 68 Hz measured for 0.1 M LiCl solution which mainly results from the magnetic inhomogeneity, the linewidth of 80 Hz for the solid 4.8 mol%

LiTFSA sample indicates that Li^+ ions are very mobile and the sample is homogenous in phase II and phase I.
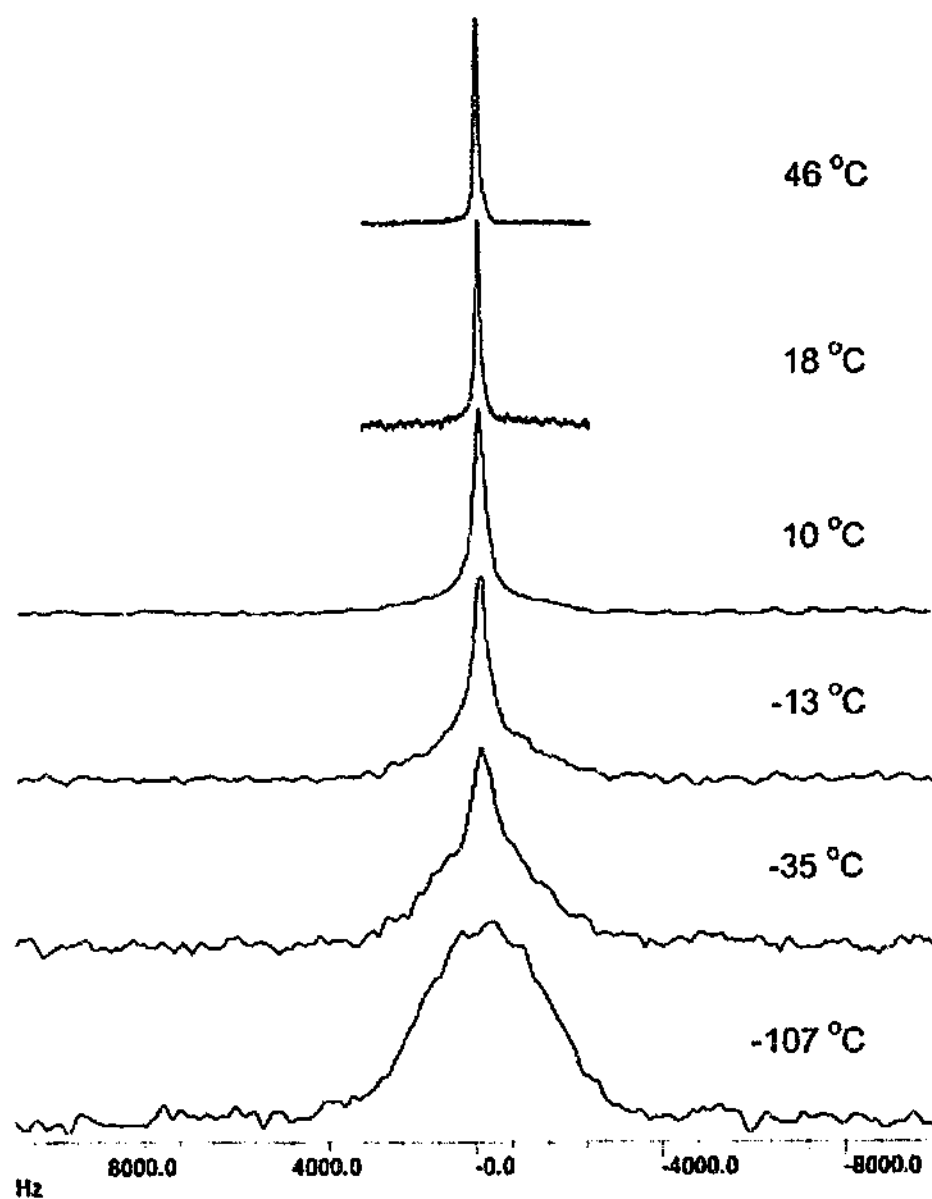
Figure 5.17 ^{7}Li NMR spectra for 4.8 mol% LiTFSA in P12TFSA.
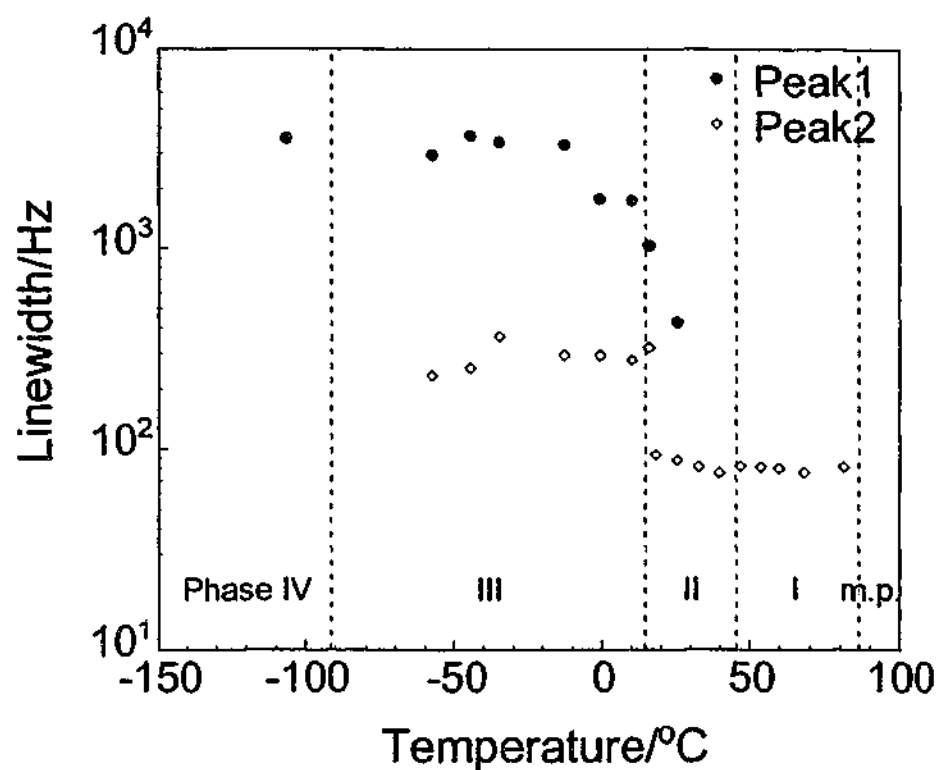
Figure 5.18 ^{7}Li NMR linewidth for 4.8 mol% LiTFSA in P12TFSA as a function of temperature.
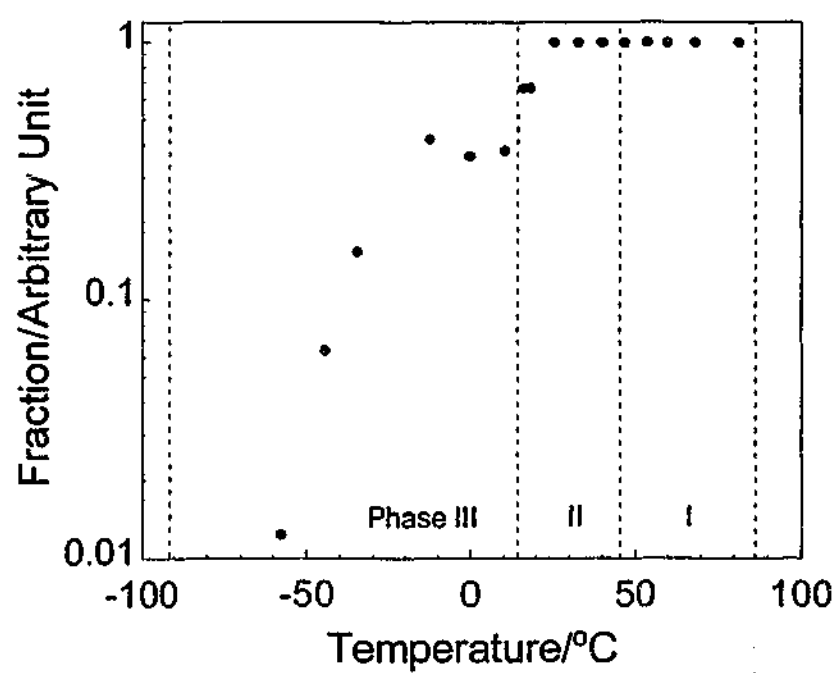
Figure 5.19 Fraction of ^{7}Li NMR narrow peak area for 4.8 mol% LiTFSA in P12TFSA as a function of temperature.

^{7}Li NMR Spin-lattice Relaxation for 4.8 mol% LiTFSA in P12TFSA

^{7}Li NMR spin-lattice relaxation could be a complicated process, because ^{7}Li-^{7}Li, ^{7}Li-^{1}H and ^{7}Li-^{19}F dipolar interactions as well as the quadrupolar interaction could all contribute to ^{7}Li spin-lattice relaxation. The quadrupolar relaxation is bi-exponential. The magnetization as a function of recovery time τ is given by [204]:

$$\frac{M_o - M_z}{2M_o} = \frac{4}{5}\exp(-\frac{\tau}{T_{1a}}) + \frac{1}{5}\exp(-\frac{\tau}{T_{1b}})$$

Equation 5.4

where T_{1a} and T_{1b} are two distinct spin-lattice relaxation times; M_o and M_z are the equilibrium magnetization and the magnetization at recovery time τ, respectively, as defined in section 2.1.5; τ is the time interval between the 180° and 90° pulses. Since the experimental data normally show very small deviations from mono-exponential behavior, a single exponential function is generally used [300]. According to Equation 2.36, a simple expression of T_1 is given as:

$$\frac{1}{T_1{}^{Li}} = C\left(\frac{\tau}{1 + \omega_{Li}{}^2\tau^2} + \frac{4\tau}{1 + 4\omega_{Li}{}^2\tau^2}\right)$$

Equation 5.5

where

$$C = \frac{3}{40}\frac{2I+3}{I^2(2I-1)}\left(1 + \frac{\eta^2}{3}\right)\left(\frac{e^2qQ}{\hbar}\right)^2$$

Equation 5.6

where τ is correlation time; I is 3/2 for ^{7}Li; η is the asymmetry parameter, which is assumed to be 0 here; $\dfrac{e^2qQ}{\hbar}$ is the nuclear quadrupole coupling constant (QCC) as defined in section 2.1.3; ω_{Li} is the angular frequency of ^{7}Li, which is 7.32×10^8 s^{-1}.

If dipolar interactions dominate in the spin-lattice relaxation, according to Equation 2.27, T_1 has the same form as Equation 5.5 for ^{7}Li-^{7}Li dipolar interactions, where

$$C = \left(\frac{\mu_o}{4\pi}\right)^2 \frac{2\gamma_{Li}^4 \hbar^2 I(I+1)}{5r^6}$$

Equation 5.7

If the spin-lattice relaxation is dominated by ^{7}Li-^{1}H or ^{7}Li-^{19}F dipolar interactions, according to Equation 2.32,

$$\frac{1}{T_1^{Li}} = C\left(\frac{\tau}{1+(\omega_{Li}-\omega_S)^2\tau^2} + \frac{3\tau}{1+\omega_{Li}^2\tau^2} + \frac{6\tau}{1+(\omega_{Li}+\omega_S)^2\tau^2}\right)$$

Equation 5.8

where

$$C = 2\left(\frac{\mu_o}{4\pi}\right)^2 \frac{\gamma_{Li}^2\gamma_S^2\hbar^2 S(S+1)}{15r^6}$$

Equation 5.9

where τ is correlation time; r is the distance between the interacting nuclei; S is ½ for both ^{1}H and ^{19}F; γ_{Li} is 1.04×10^8 rads^{-1}T^{-1}; γ_H is 2.67×10^8 rads^{-1}T^{-1}; γ_F is 2.52×10^8 rads^{-1}T^{-1} and ω_s is 1.884×10^9 s^{-1} for ^{1}H or 1.772×10^9 s^{-1} for ^{19}F.

The magnetizations for the broad and narrow components are analyzed separately. Both exhibit a mono-exponential behavior. The temperature dependent spin lattice relaxation time T_1 is shown in Figure 5.20. The T_1s of the broad peaks show a relatively larger error than the narrow ones due to their smaller intensity. The curve fit correlation coefficients for the narrow component are all greater than 0.994. Only the T_1s of the narrow component are further analyzed here in order to obtain the activation energy E_a and correlation time τ. According to Figure 5.20, two minima are obtained, suggesting different diffusion mechanisms and activation energies in different temperature ranges. These

coincide with the two different linewidths below and above the phase III>>II transition. Since the contributions from ^{7}Li-^{7}Li, ^{7}Li-^{1}H and ^{7}Li-^{19}F dipolar interactions as well as the quadrupolar interaction are difficult to separate, each of the four mechanisms is assumed to be dominant. The fits of Equation 5.5 and Equation 5.8 to T_1 data are shown in Figure 5.21. Only one dominant relaxation mechanism is assumed in each fit. Since homonuclear dipolar interaction and quadrupolar interaction have similar frequency dependence, Figure 5.21 (a) applies to both ^{7}Li-^{7}Li dipolar interaction and quadrupolar interaction. The parameters obtained from the fits are listed in Table 5.2.
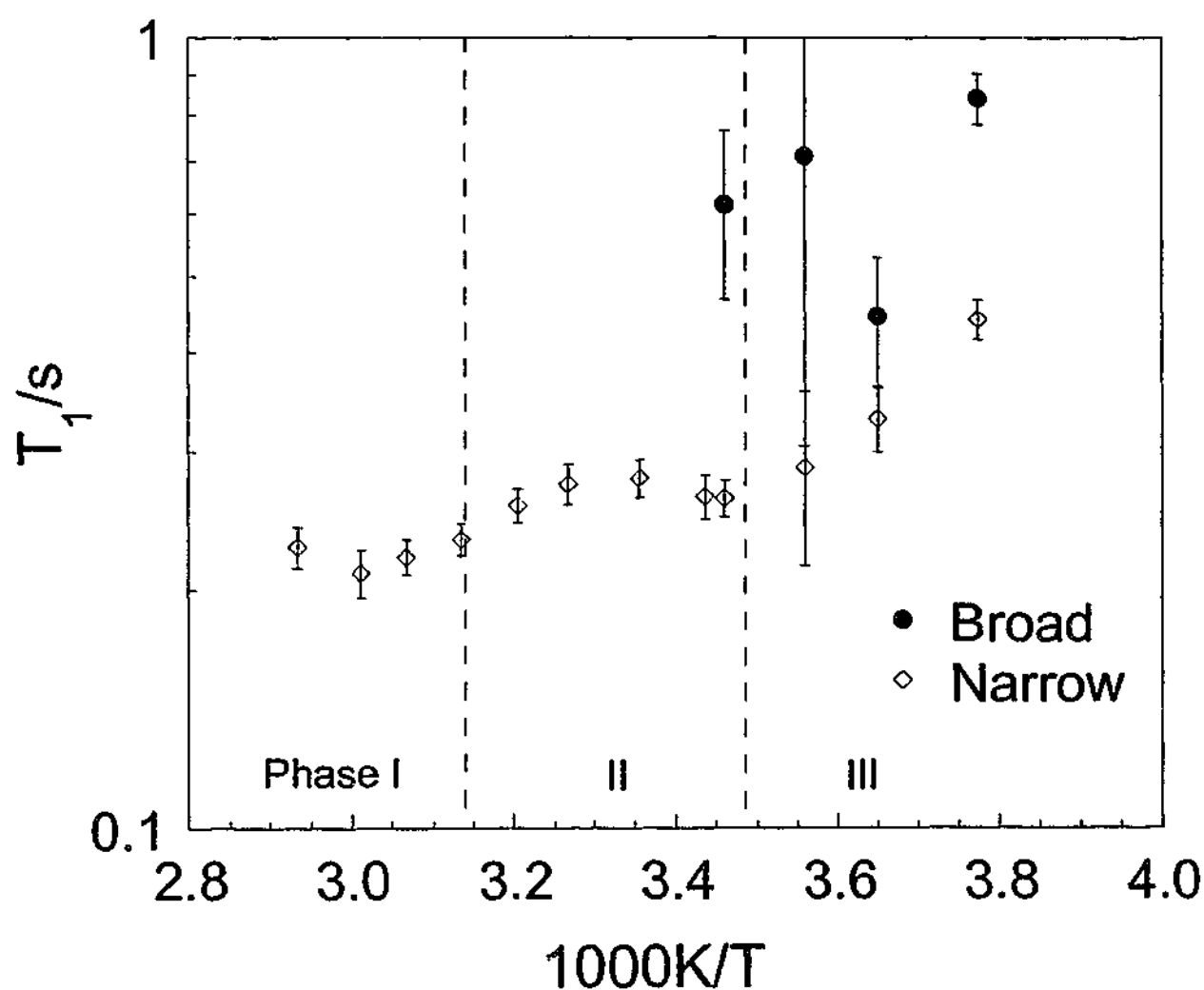
Figure 5.20 Temperature dependence of ^{7}Li NMR spin-lattice relaxation time T_1 for 4.8 mol% LiTFSA in P12TFSA.
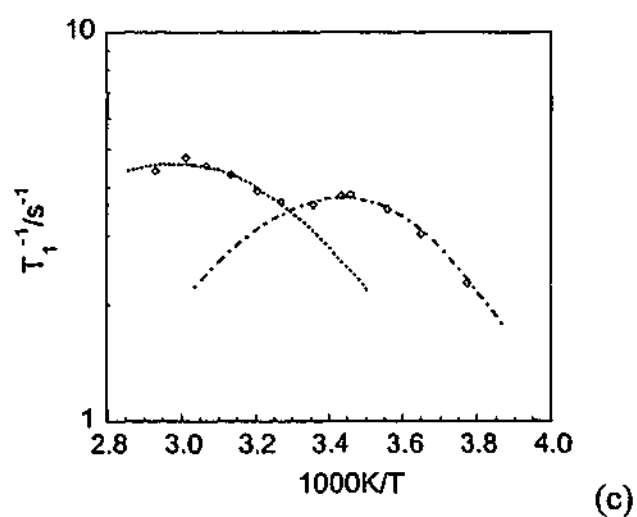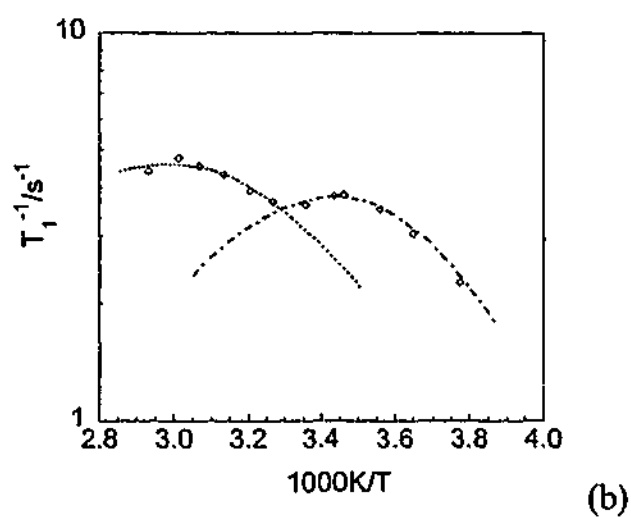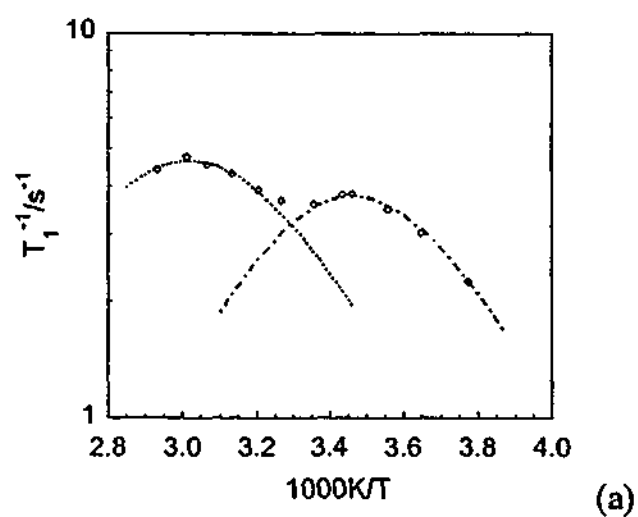
Figure 5.21 Curve fit of T_1^{-1} of the ^{7}Li NMR narrow peak for 4.8 mol% LiTFSA in P12TFSA by different relaxation mechanisms: (a) Li-Li dipolar interaction or quadrupolar interaction using Equation 5.5; (b) Li-H dipolar interaction using Equation 5.8; (c) Li-F dipolar interaction using Equation 5.8.

Table 5.2 Activation energies (E_a), correlation times at the limit of infinite temperature (τ_0) and motional constants (C) evaluated for Li^+ diffusion from ^7Li NMR relaxation time T_1 for 4.8 mol% LiTFSA in P12TFSA.

Temperature	Relaxation Mechanism	$C/10^8\,s^{-2}$	$E_a/kJmol^{-1}$	τ_0/s	Correlation Coefficient
T<30 °C	^7Li-^7Li dipole or quadrupole	19.4±0.3	31.9±2	$(1.4\pm0.2)\times10^{-15}$	0.994
	^7Li-^1H dipole	12.0±0.2	29.6±3	$(4.6\pm0.5)\times10^{-15}$	0.993
	^7Li-^{19}F dipole	11.5±0.1	29.8±3	$(4.4\pm0.9)\times10^{-15}$	0.994
T>30 °C	^7Li-^7Li dipole or quadrupole	23.8±0.5	30.6±4	$(1.3\pm0.3)\times10^{-14}$	0.975
	^7Li-^1H dipole	14.5±0.3	24.3±7	$(1.6\pm0.3)\times10^{-13}$	0.935
	^7Li-^{19}F dipole	14.0±0.3	24.3±7	$(1.6\pm0.3)\times10^{-13}$	0.933

Motion of Ions for 4.8 mol% LiTFSA in P12TFSA

The E_a and τ_0 obtained by T_1 measurements as shown in Table 5.2 enable the correlation time for Li^+ ion diffusion to be estimated. The diffusion of Li^+ ions is also compared with the motion of $P12^+$ cations in Figure 5.22. One of the features is that the values obtained by assuming that each of ^7Li-^7Li (or quadrupolar interactions), ^7Li-^1H or ^7Li-^{19}F dipolar interaction is the dominant relaxation mechanism are very close over all of the temperature range displayed. The correlation time of Li^+ ionic diffusion exhibits a small increase at about 20 °C. Combined with the sharp line narrowing from 300 Hz to 80 Hz at 14 °C in

Figure 5.18, these changes again support the postulate that the solubility of Li^+ ions in P12TFSA increases at this phase transition, and that Li^+ ions are all incorporated into the P12TFSA network. As the sample transforms from a two-phase region into a single solid solution phase, Li^+ ions are in more homogeneous environments. It is interesting to note that the diffusion of Li^+ ions and one of the $P12^+$ cation rotations exhibit similar temperature dependence, probably indicative of the association between the $P12^+$ cationic rotation and Li^+ ionic diffusion. The correlation times of $P12^+$ cationic diffusion are also close to those of Li^+ ions in phase II and phase I.
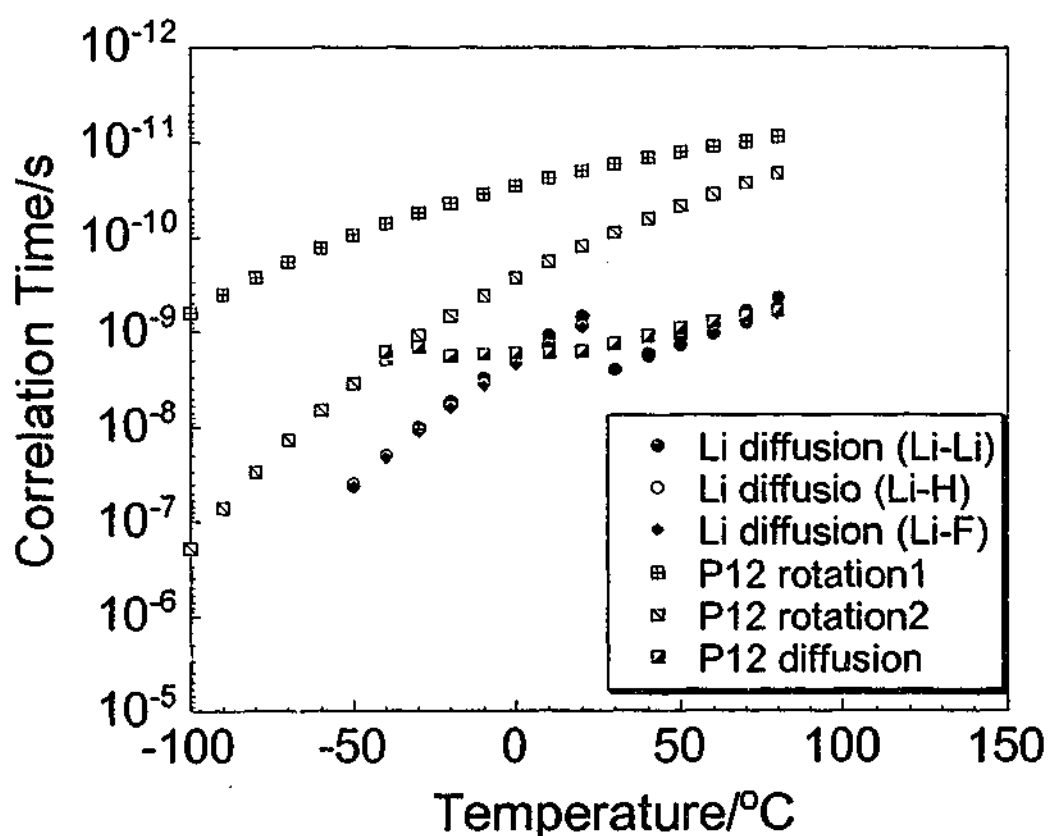
Figure 5.22 Correlation times of Li^+ ions and $P12^+$ cations for 4.8 mol% LiTFSA in P12TFSA as a function of temperature. Data are calculated from activation energy E_a and correlation times at the limit of infinite temperature τ_0 in Table 5.1 and Table 5.2. The solid circles, open circles and diamonds are the results calculated by assuming that either ^7Li-^7Li (or quadrupolar interactions), ^7Li-^1H or ^7Li-^{19}F dipolar interactions are the dominant relaxation mechanism, respectively.

The fraction of the mobile P12$^+$ cations and Li$^+$ ions are compared in Figure 5.23. The fraction of mobile Li$^+$ ions is significantly higher than that of P12$^+$ cations over all the temperature range investigated. All the Li$^+$ ions become mobile at 25 °C whilst the fraction of diffusing P12$^+$ cations is 0.18. It is very likely that not all the diffusing P12$^+$ cations contribute to the conductivity, because P12$^+$ cations and TFSA$^-$ anions may be associated in the diffusion, which will not contribute as much to the conductivity. This proposal is supported by the fact that the conductivity calculated from the diffusion coefficient values measured by gradient field NMR is higher than the conductivity measured [293].
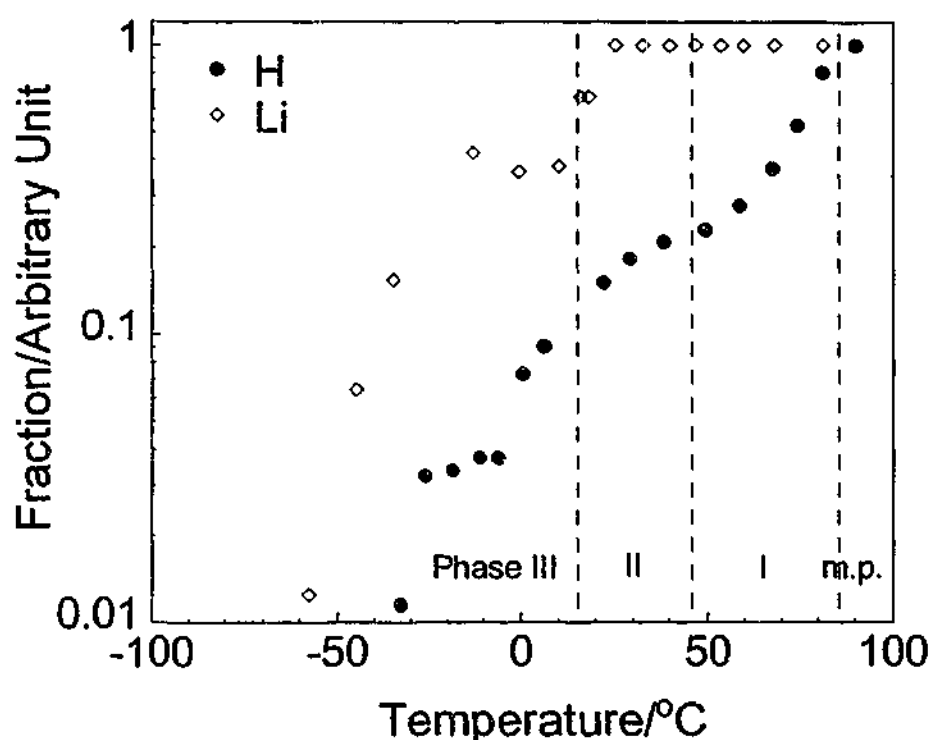
Figure 5.23 The fraction of narrow components of ^{1}H and ^{7}Li NMR peaks as a function of temperature for 4.8 mol% LiTFSA in P12TFSA. These narrow components represent the mobile ions as discussed in text.

^{7}Li NMR Linewidth for 9.3 mol% LiTFSA in P12TFSA

^{7}Li NMR spectra for 9.3 mol% LiTFSA are shown in Figure 5.24. The temperature dependence of linewidth is shown in Figure 5.25. At –70 °C, a single broad peak is observed with linewidth of 3.6 kHz, indicative of immobile Li$^+$ ions. In a similar way to the Li$^+$ ion behavior observed for 4.8 mol% LiTFSA, a narrow line appears in phase III

- 215 -

with linewidth of 270 Hz, suggesting the diffusing Li$^+$ ions. The narrow peak exhibits a further line narrowing to about 80 Hz above 18 °C whilst the broad bottom totally disappears, indicating that all the ions become mobile in phase II. Above 30 °C, two narrow peaks are clearly discernable until only a single narrow resonance is observed beyond 72 °C.
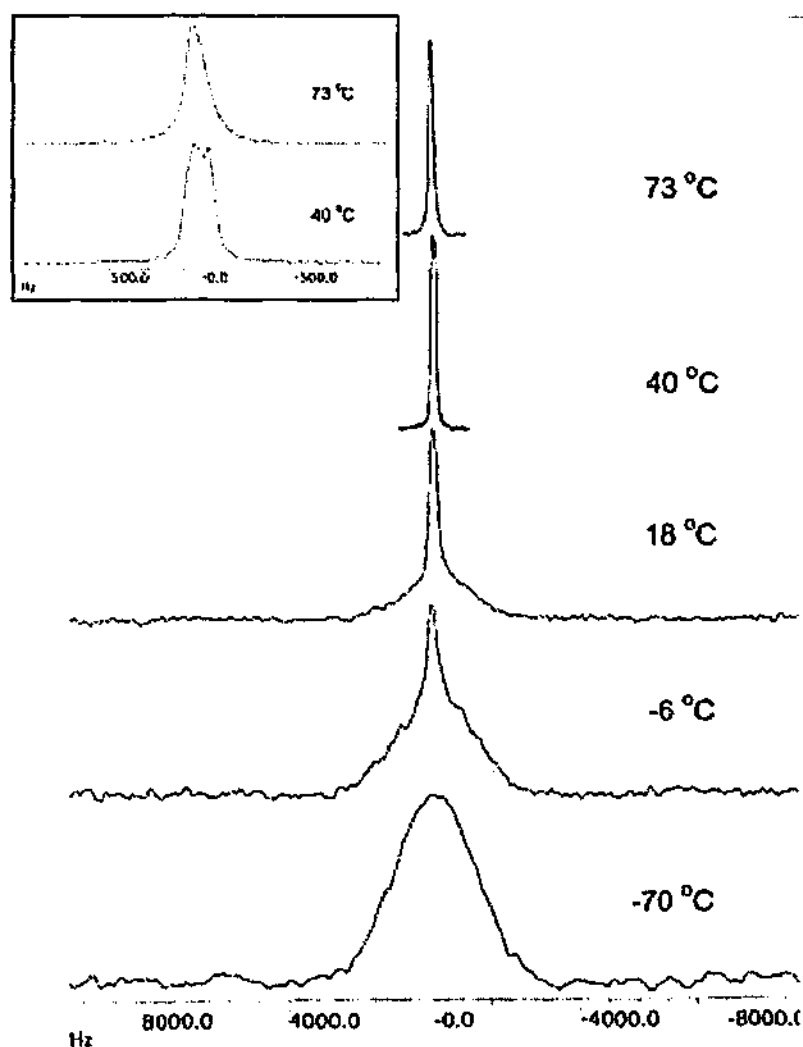
Figure 5.24 ^{7}Li NMR spectra for 9.3 mol% LiTFSA in P12TFSA. The inset expands the frequency axis to clearly show the splitting above the eutectic temperature.
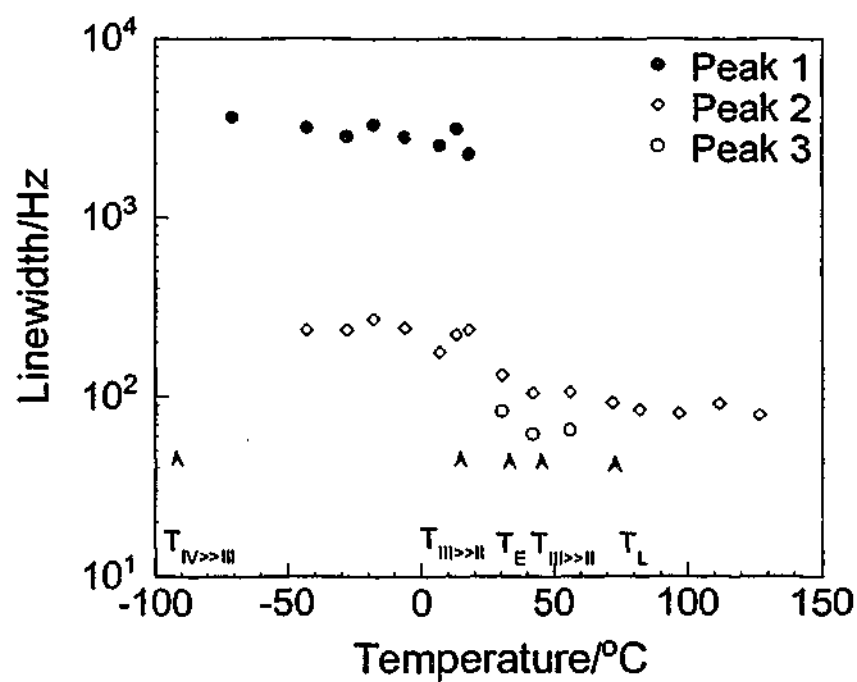
Figure 5.25 Temperature dependence of ^{7}Li NMR linewidth for 9.3 mol% LiTFSA in P12TFSA. Peak 1 is assigned to the broad component. Peak 2 and peak 3 are assigned to the solid phase (low field narrow peak) and liquid phase (high field narrow peak), respectively.
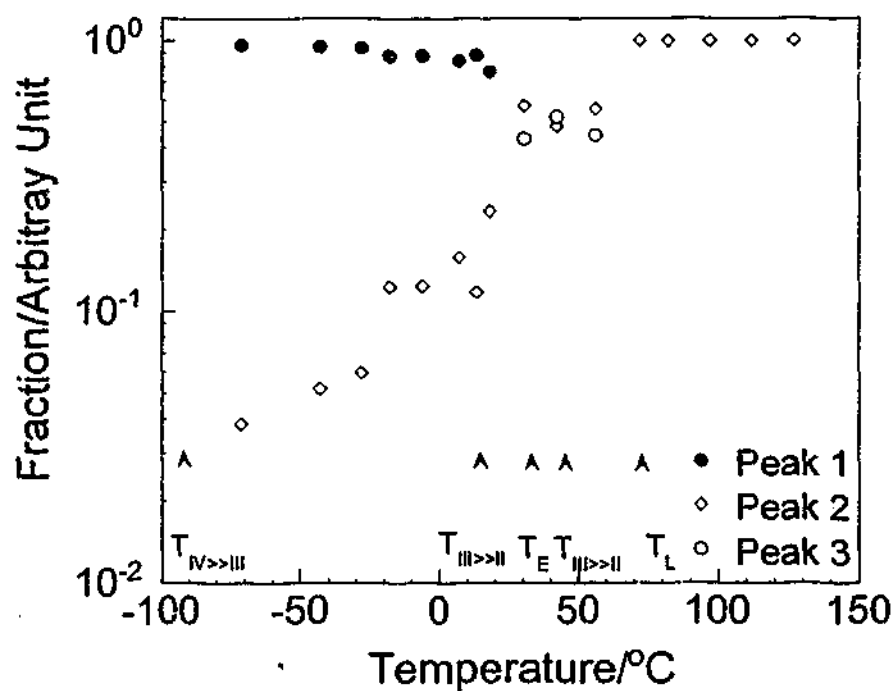
Figure 5.26 Fraction of ^{7}Li NMR peak areas for 9.3 mol% LiTFSA in P12TFSA as a function of temperature. The assignments of the peaks refer to those in Figure 5.25.

The two narrow peaks observed can be assigned to the Li$^+$ ions in a liquid phase represented by the high field resonance and in a solid phase indicated by the low field resonance, respectively. The latter disappears beyond the liquidus point when all the species are in the melt. These assignments are supported by the observation for the 33 mol% LiTFSA compound, as shown in Figure 5.27, that the peak is observed at high field above the eutectic temperature when all the sample melts. The fraction of each of the component is shown in Figure 5.26, which indicates the amount of each phase. It is interesting to note that the linewidths of these two peaks are comparable, indicating the liquid-like mobility for Li$^+$ ions in the solid solution.

^{7}Li NMR Linewidth for 33 mol% LiTFSA in P12TFSA
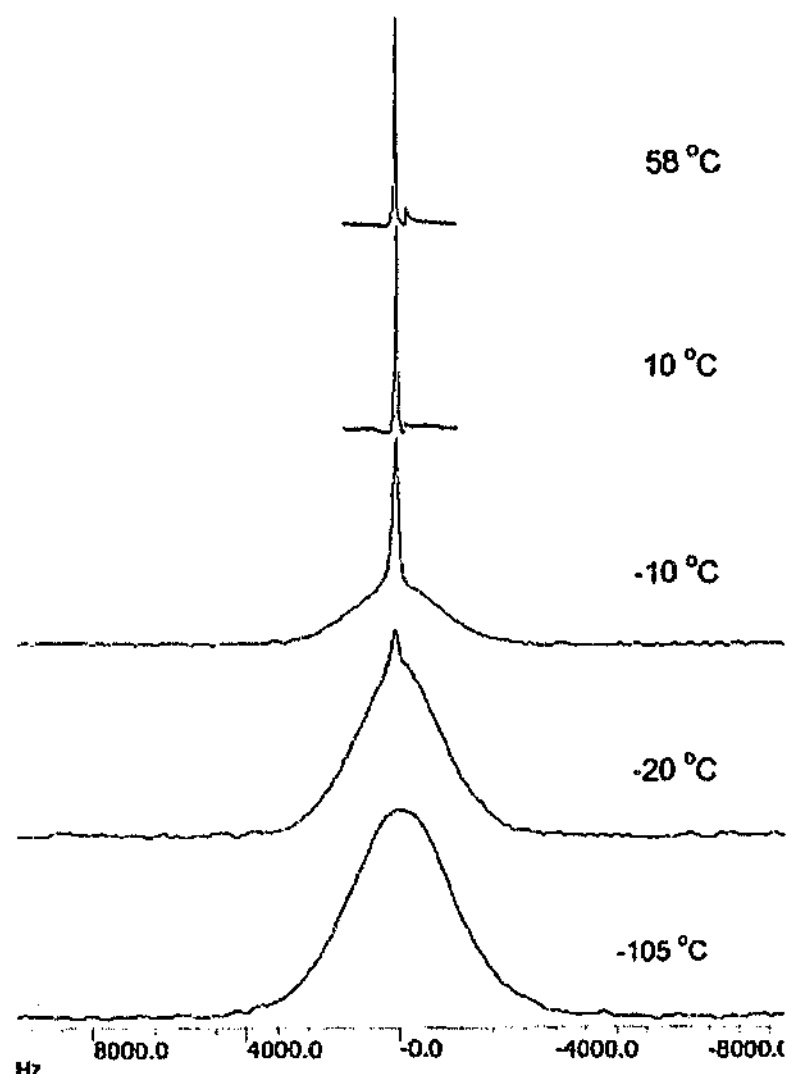
Figure 5.27 ^{7}Li NMR spectra for 33 mol% LiTFSA in P12TFSA.

Li$^+$ ions in 33 mol% LiTFSA are rigid at temperatures as low as −105 °C, indicated by the single broad line, about 3.6 kHz wide as shown in Figure 5.27. A narrow line, about 250 Hz wide, appears and increases gradually in intensity with temperature, suggesting that more Li$^+$ ions become mobile with temperature. This narrow resonance exhibits a sharp line narrowing to 76 Hz at about −3 °C whilst the broad peak disappears. In contrast to the 4.8 mol% and 9.3 mol% LiTFSA samples, all the Li$^+$ ions in the 33 mol% sample become mobile below the phase III>>II transition temperature, according to Figure 5.29. Above −3 °C, the linewidth is further narrowed until the eutectic temperature is reached, as shown in Figure 5.28.
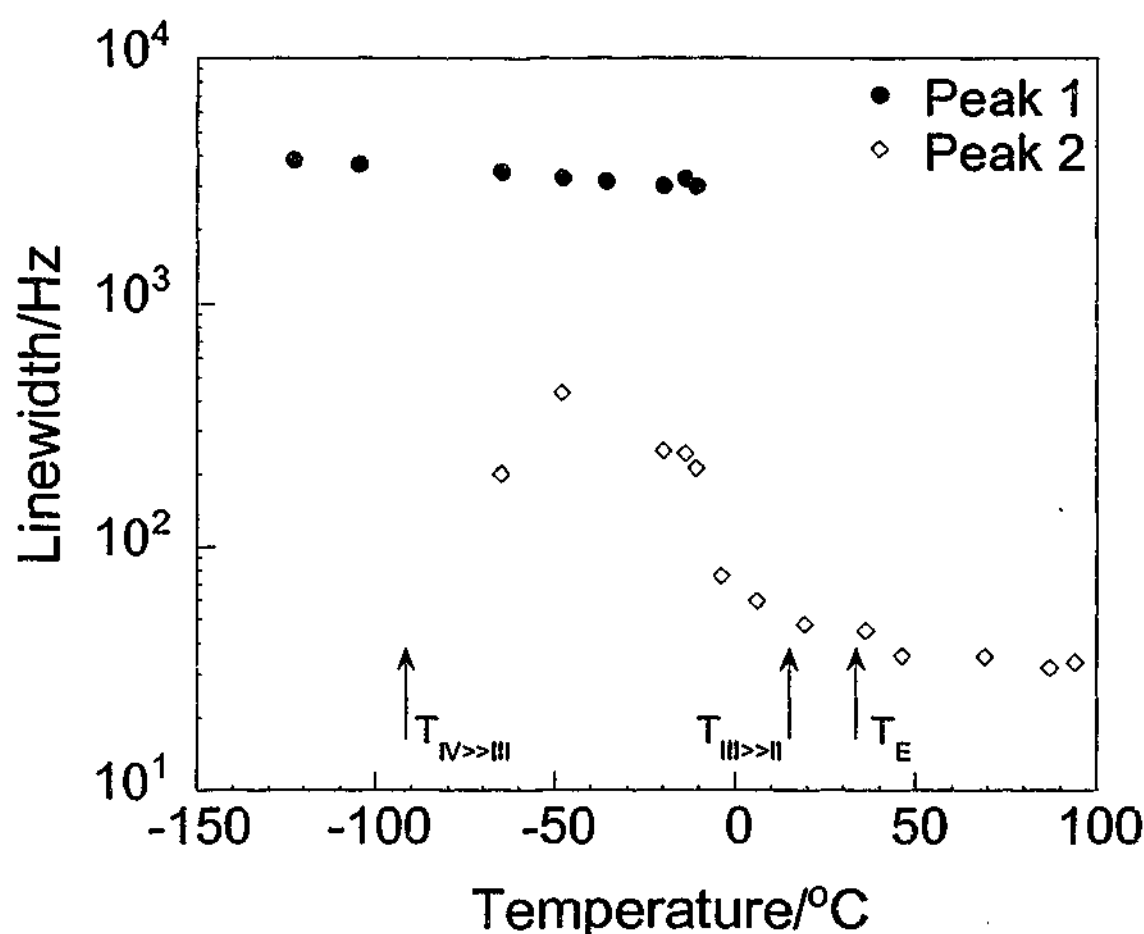
Figure 5.28 Temperature dependence of ^{7}Li NMR linewidth for 33 mol% LiTFSA in P12TFSA.
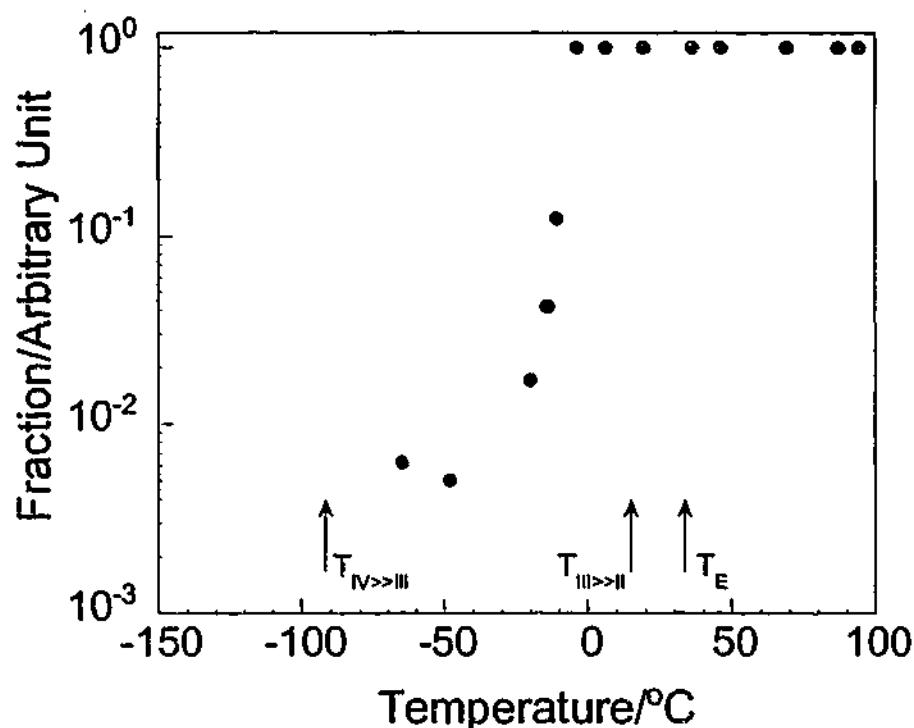
Figure 5.29 Fraction of the ^{7}Li NMR narrow peak area for 33 mol% LiTFSA in P12TFSA as a function of temperature.

5.2.4 Conduction Models

Ionic motion and conduction process in different phases can be summarized as follows:

Compositions of 0 ~50 mol% in Phase III

The phase transformation data for this system indicates that, in all compositions studied, the materials are completely solid in phase III. Beyond about 1.5% LiTFSA two solid phases are present, a P12TFSA rich phase and a LiTFSA rich phase. At this stage the second phase has not been isolated in its pure state. ^{1}H and ^{19}F NMR indicate that the numbers of diffusing P12$^+$ cations and TFSA$^-$ anions are increased for 4.8 mol% LiTFSA composition compared to the pure P12TFSA. Doping of LiTFSA salt in this composition also results in higher diffusion coefficients, at least for P12$^+$ ions. The increase in both the number of charge carriers and diffusion rate may be attributed to the defects formed due to the coexistence of the two phases. ^{7}Li NMR for 4.8 mol%, 9.3mol% and 33 mol% compositions exhibit similar features: all the Li$^+$ ions are distributed between two

environments, a rigid one and a mobile one. However, the Li^+ ions in the P12TFSA rich phase and the LiTFSA rich phase can not be distinguished from NMR spectra or spin lattice relaxation measurements. The fraction of mobile Li^+ ions is significantly higher than that of mobile $P12^+$ ions whilst the diffusion rate of Li^+ ions is slower than that of $P12^+$ cations for 4.8 mol% LiTFSA.

The conductivity exhibits a sharp increase when the LiTFSA salt is doped though to less extent than in phase II and phase I. The highest conductivity is obtained for 33 mol% composition. The possible factors affecting the conductivity are: the amount of the two phases, the ionic mobility within each phase, the fraction of charge carriers within each phase, the defects brought about by the coexistence of two phases, etc. As the LiTFSA concentration increases, the amount of the LiTFSA rich domain increases at the expense of the P12TFSA rich domain. The conductivity drops at LiTFSA concentrations beyond 33 mol%, probably suggesting a less conductive LiTFSA rich phase. The highest conductivity which occurs at 33 mol% composition is the result of all these possible effects.

Compositions between 0 ~ 4.8 mol% LiTFSA in Phase II and Phase I

Above 14 °C, the phase III>>II transition temperature, compositions with LiTFSA content up to 4.8 mol% transform into a single solid solution phase. This is indicated by: (1) these compositions exhibit solid-solid phase transition behavior similar to pure P12TFSA and lack eutectic melting transitions; (2) ^7Li NMR spectra for 4.8 mol% LiTFSA display a single narrow resonance, indicative of a relatively homogenous environment in contrast to the two narrow peaks for 9.3 mol% LiTFSA which is composed of a solid phase and a liquid phase; (3) structurally, P12TFSA exhibits substantial volumetric expansion and increases in both the number and size of vacancies during the phase III>>II transition, which could facilitate the incorporation of the small Li^+ ions into the P12TFSA lattice.

The solid solution phase displays similar plastic crystal behavior to pure P12TFSA, as indicated by the fact that the $P12^+$ cations and TFSA⁻ anions still perform rotational motion according to the linewidths of the broad ^1H and ^{19}F NMR peaks, although the incorporation of Li^+ ions may alter the rotational rate and/or energy barrier to the rotation. The fractions of mobile $P12^+$ cations and TFSA⁻ anions are larger than observed in pure P12TFSA.

Doping of LiTFSA also enhances the diffusion coefficient of P12$^+$ cations. The mismatched sizes of the small Li$^+$ ion (0.7Å in radius) and the substituted P12$^+$ cations (3.1Å in radius) may account for the diffusion behavior. The disparity in size and shape of the Li$^+$ and the P12$^+$ cations, indicated in Figure 5.30, could create a significant disruption of the crystal lattice which may allow an increase in ion mobility.

All Li$^+$ ions become mobile and the correlation time is comparable to that of P12$^+$ cations. There may be some association between the Li$^+$ ionic diffusion and the rotation of P12$^+$ cations, both of which exhibit close values of activation energy. It is also expected that strong interactions could occur between the oxophilic Li$^+$ cation and the sulphonyl oxygen atoms of the TFSA$^-$ anion, as indicated in Figure 5.30. The motion of the Li$^+$ ions could be closely associated with the motion of TFSA$^-$ anions as well.
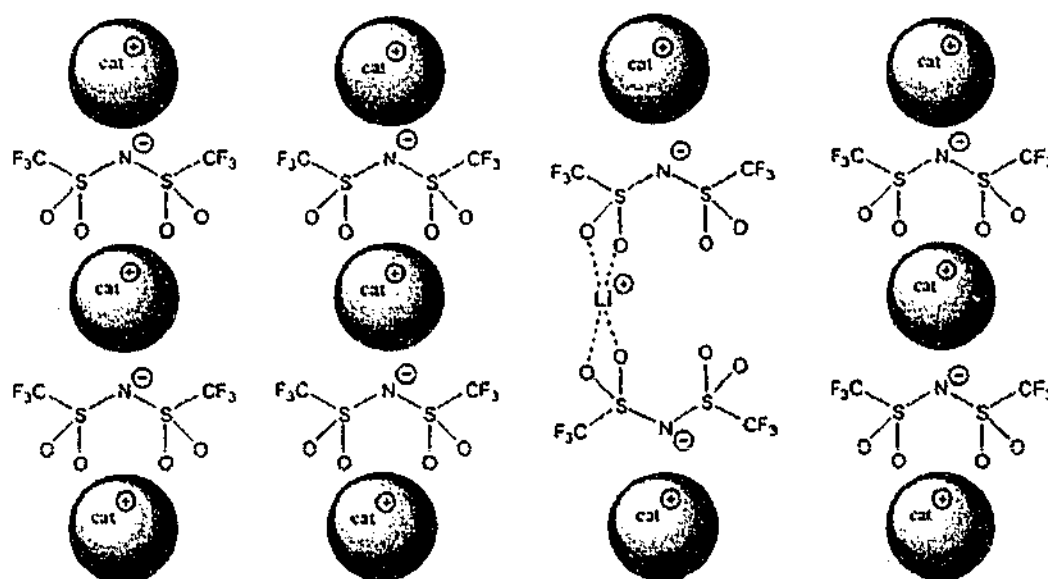
Figure 5.30 Schematic representation of the site substitution of the cation for Li$^+$ and the consequent lattice disruption resulting from doping of the LiTFSA salt.

According to the analyses above, the increase in conductivity by four orders of magnitude for 4.8 mol% LiTFSA in phase II with regard to the pure P12TFSA may be attributed to all these three ions, although each individual contribution is difficult to identify at this stage. The conductivity calculated from the diffusion coefficients of P12$^+$ cations and TFSA$^-$ anions is higher than the conductivity measured [293], which suggests that, similar to that in P12TFSA, these P12$^+$ and TFSA$^-$ ions may undergo local translational motion, which

- 222 -

does not contribute to the conductivity. The lithium solid state NMR spectra suggest that all the lithium ions have liquid like transport properties, and hence are at least a contributor to this fast ion conduction. All the compositions between 1.4 mol% and 4.8 mol% exhibit similar slope $d\ln\sigma/d(1/T)$ below their liquidus temperature, indicative of the same ionic transport mechanism.

Compositions of 9.3 ~ 33 mol% in Phase II and Phase I

33 mol% LiTFSA composition represents another interesting limit. Gradient field NMR measurements show that, above the eutectic temperature, the diffusion coefficients of both $P12^+$ cations and TFSA$^-$ anions in the liquid 33 mol% LiTFSA sample are smaller than those for the solid state 4.8 mol% composition [293]. The difference in the transport mechanism between the liquid and solid state accounts for the different diffusion coefficients. In the liquid state, the ionic transport may involve the collective rearrangement of small sections of the material whilst a vacancy mechanism may account for the ionic diffusion in the solid state [293].

For the compositions between 9.3 mol% and 33 mol% LiTFSA, the conduction mechanism involves two phases above 33 °C: the solid solution phase and the liquid phase. The possible factors affecting the conductivity include: the amount of each phase, the diffusion coefficient and the fraction of the mobile ions within each phase, possible defects such as the phase boundary, etc. Again, it is complicated to assess the contribution from each ion. For example, the ionic mobility is less in the liquid phase, but all the ions could be involved in the diffusion. The ^{7}Li NMR on the other hand clearly show two distinct narrow lines in the 9.3% sample, one of which was associated with the melt and the other with the conductive doped solid phase II, suggesting that Li$^+$ ions exhibit liquid-like mobility in the solid state. The overall result of all these effects is that the highest conductivity is obtained for 27 mol% composition at 40 °C and 50 °C.

5.3 Conclusions

P12TFSA-LiTFSA binary system displays relatively classic phase behavior: eutectic temperature is 33 °C (±3 °C) with eutectic composition at about 33 mol% LiTFSA; the solubility limit on the P12TFSA end is between 4.8 mol% and 9.3 mol% LiTFSA, which is closely associated with the microstructure of P12TFSA. The doping of the LiTFSA up to 4.8 mol% results in substitution of the $P12^+$ cations with Li^+ in the lattice and formation of a solid solution, which exhibit similar plastic crystal behavior to that of pure P12TFSA. A four order of magnitude increase in conductivity between 0 and 4.8 mol% LiTFSA is obtained. In the case of the solid solution phase, doping of LiTFSA results in the higher number of more mobile $P12^+$ cations and $TFSA^-$ anions probably due to the discontinuity of the lattice structure. However, the diffusion of $P12^+$ cations and $TFSA^-$ anions may involve local translational motion and hence not contribute directly to conductivity. All the Li^+ ions exhibit liquid-like transport behavior, which may be facilitated by the rotation of the matrix cation and/or anion, similar to the process for Li_2SO_4 [170, 172].

Compared with LiTFSA containing PEO polymer electrolytes, lithium doped P12TFSA is as conductive as solid polymer electrolytes, but at substantially lower lithium ion concentration. For example, 1 molkg^{-1} LiTFSA in PEO achieves conductivity of about 10^{-5} Scm^{-1} at 25 °C [301] whereas equivalent conductivity in P12TFSA requires less than 0.1 mol kg^{-1} LiTFSA. The doped P12TFSA can therefore be classified as a new class of fast ion conductor.

Chapter 6   Lithium Doped N-methyl-N-methylpyrrolidinium bis(trifluoromethanesulfonyl)amide Salt Mixtures

6.1   Introduction

In chapter 5, it was found that in LiTFSA doped P12TFSA mixtures, the small Li^+ ions substitute for the $P12^+$ cations in the lattice structure and exhibit liquid-like transport behavior through the P12TFSA network. The conductivity is enhanced by three orders of magnitude by doping with 5 mol% lithium salt. However, there is some concern about the thermal stability of some of the mixtures. As the eutectic temperature for P12TFSA-LiTFSA is at about 33 °C, the fluctuation in ambient temperature could easily bring about the transformation from the liquid state to the metastable solid phase and thus result in thermal instability for any sample potentially containing eutectic domain. This is reflected by the poor reproducibility of the DSC traces especially for the compositions close to the eutectic.

In this chapter, LiTFSA salt is doped into P11TFSA salt to test the hypothesis that the small lithium ions could be similarly mobile in the P11TFSA network while the thermal stability could be improved. The phase behavior, ionic motion and conductivity are studied for compositions ranging from 0 to 50 mol% LiTFSA.

6.2   Results and Discussion

6.2.1   Thermal Analysis

The DSC traces for a number of P11TFSA-LiTFSA compositions ranging from 0 to 51 mol% LiTFSA are shown in Figure 6.1.

When 0.6 – 2.7 mol% LiTFSA is doped, the final melting is broadened and shifted to lower temperature. This is quite typical for a doped sample. Three solid-solid phase transitions

appear at −38 (± 3) °C, 26 (± 2) °C and 81 (± 2) °C, respectively. The solid-solid phase transitions suggest that these LiTFSA doped P11TFSA compositions remain the plastic crystal behavior. All these three solid-solid phase transitions remain the same shapes and occur at the same temperatures as those for pure P11TFSA. Analogous to the LiTFSA doped P12TFSA solid solution phase, as discussed in section 5.2.1, these similar DSC traces may suggest a solid solution of the LiTFSA salt in the P11TFSA matrix. The similar thermal properties indicate that the solid solution may exhibit similar plastic crystal behavior to pure P11TFSA.

When 5 mol% LiTFSA is doped, all three solid-solid phase transitions still appear, albeit with smaller transition enthalpies. Two additional peaks are observed, one at 57 °C and another weak one at −52 °C. The final liquidus peak is further broadened and depressed.

The 57 (± 2) °C and the −52 (± 2) °C transitions are present for all the compositions between 7 mol% and 51 mol%. Both of the peaks are quite sharp. For both transitions, the enthalpy changes exhibit a LiTFSA content dependence, increasing with doping of LiTFSA up to 33 mol% and decreasing beyond 33 mol%. For the 33 mol% composition, the DSC trace exhibits no more transitions above 57 °C and the sample was visually observed to have melted at this temperature, suggesting that the peak at 57 (± 2) °C represents a eutectic transition and the eutectic composition is close to 33 mol%. The −52 (± 2) °C transition is probably related to the eutectic transition, as it only appears in those mixtures which exhibit eutectic transition.

Another feature of these mixtures is that the solid-solid phase transitions observed for pure P11TFSA are still present, in particular for the low LiTFSA concentration compositions. For example, the peak at about −38 (± 3) °C is observed up to 33 mol% and can not be discerned beyond 33 mol%. The 26 (± 2) °C transition appears for all the compositions up to 50 mol%. The transition at 81 (± 2) °C is observed up 27 mol%. The enthalpy changes of all these three transitions decrease with increasing the amount of doped LiTFSA salt.

All the transitions discussed above exhibit good reproducibility, even for the mixtures close to the eutectic composition. Compared to P12TFSA-LiTFSA mixtures, the chances of forming the metastable solid phases from the liquid eutectic domain due to temperature

fluctuation around room temperature are reduced, as the eutectic temperature is well above room temperature.

The thermal properties and possible metastable states are further studied by quenching the melts using liquid nitrogen and recording the DSC traces from -120 °C to 30 °C. Selected DSC traces are shown by the dotted lines in Figure 6.1. For the compositions between 0 and 2.7 mol% LiTFSA, the quenching procedure does not change the thermal features of the solid-solid transitions. In the case of 5 to 15 mol% LiTFSA compositions, the -52 (±2) °C transition disappears after quenching whilst the -38 (± 3) °C and 26 (± 2) °C transitions remain the same. These suggest that the -52 °C transition may be related to the phase which can only be formed at a relatively slow cooling rate. For the compositions between 26 mol% to 50 mol%, a glass transition is observed followed by a devitrification exotherm at -22 (± 2) °C. It is thought that the molten domain is trapped as an amorphous phase by quenching which transforms into supercooled liquid at the glass transition and then is devitrified. The glass transition temperature increases gradually with LiTFSA concentration from -56 °C for 26 mol% to -22 °C for 50 mol%. T_g increasing with the concentration of doped lithium salts has also been reported for organic salts [302]. As found for the P12TFSA-LiTFSA binary, the metastable states observed in P11TFSA-LiTFSA system are mainly due to the eutectic domain. The transitions related to the plastic crystal behavior exhibit less dependence on the thermal history than the eutectic domain related transitions.

The phase transitions are summarized in Figure 6.2. Similar to the phase diagram of P12TFSA-LiTFSA mixtures, Figure 6.2 also represents a classic binary system. The eutectic transition is clearly shown at 57 (± 2) °C and the eutectic composition is about 33 mol%. The -52 (± 2) °C transition, as discussed above, is related to the eutectic formation and can only be formed at a slow cooling rate. A possible explanation is that this transition is related to the interfaces of inserted P11TFSA rich phase and LiTFSA rich phase. In a quenching procedure, the inserting distribution of these two phases is not allowed to form, which accounts for the absence of the -52 (± 2) °C transition.
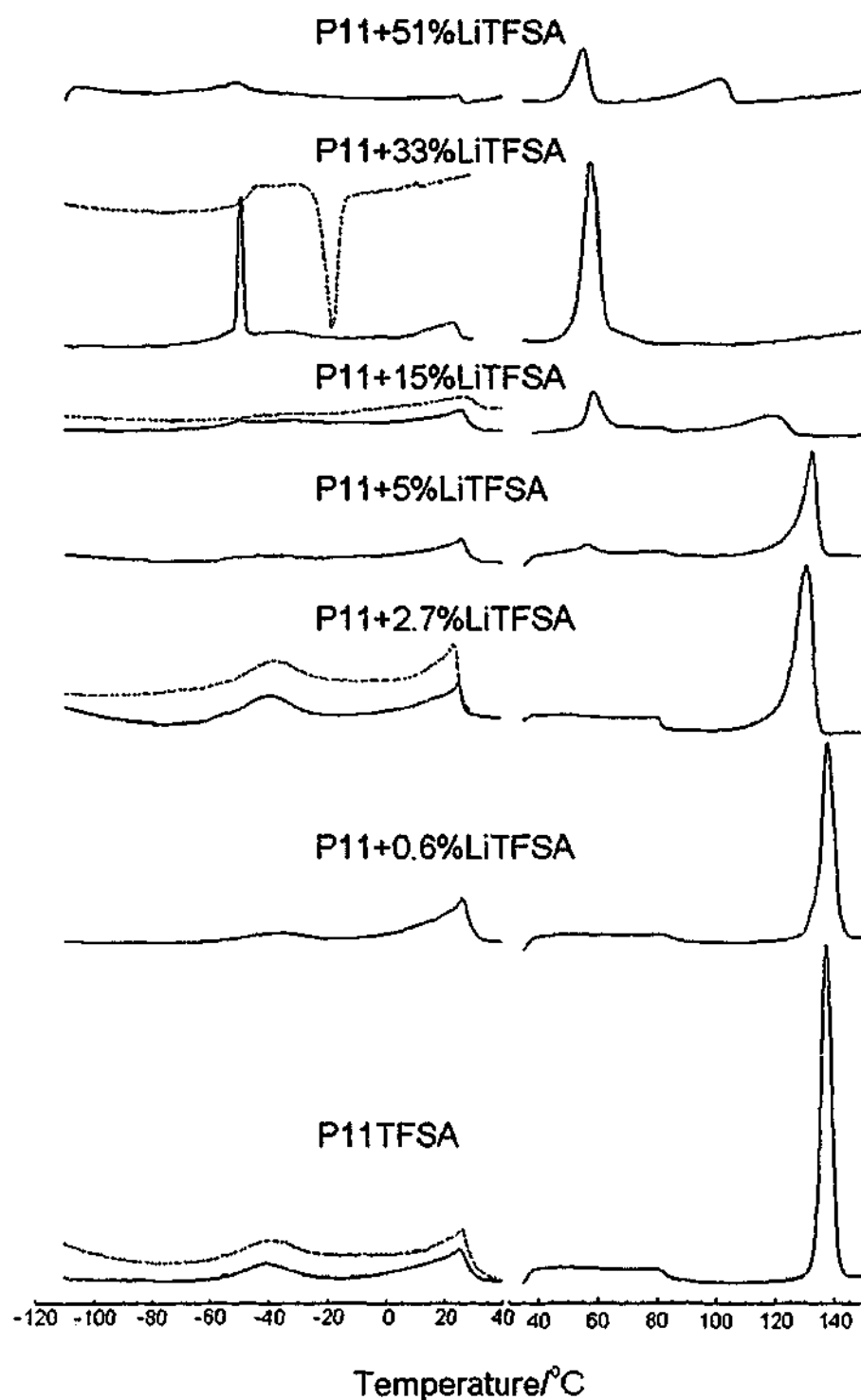
Figure 6.1 DSC traces for P11TFSA-LiTFSA mixtures at compositions indicated. These measurements were performed by heating in two different temperature ranges: -120 °C ~ 40 °C and 30 °C ~ 150 °C at 20 °Cmin⁻¹. Dotted lines indicate that samples have been quenched from molten state.

A solid solution phase is present at the P11TFSA rich end. The solubility limit of LiTFSA is between 2.7 mol% and 5 mol%. This value is less than that for P12TFSA, indicating that

Li$^+$ ion is less soluble in P11TFSA. This is not unexpected, because as discussed in section 5.2.1, the solubility is related to the lattice volume or vacancies in the parent lattice structure. Chapter 4 shows that P11TFSA exhibits less volumetric expansion as well as less vacancy volume due to smaller vacancy size and lower vacancy number. Therefore, incorporation of Li$^+$ ions is less favored into the P11TFSA matrix than into P12TFSA.
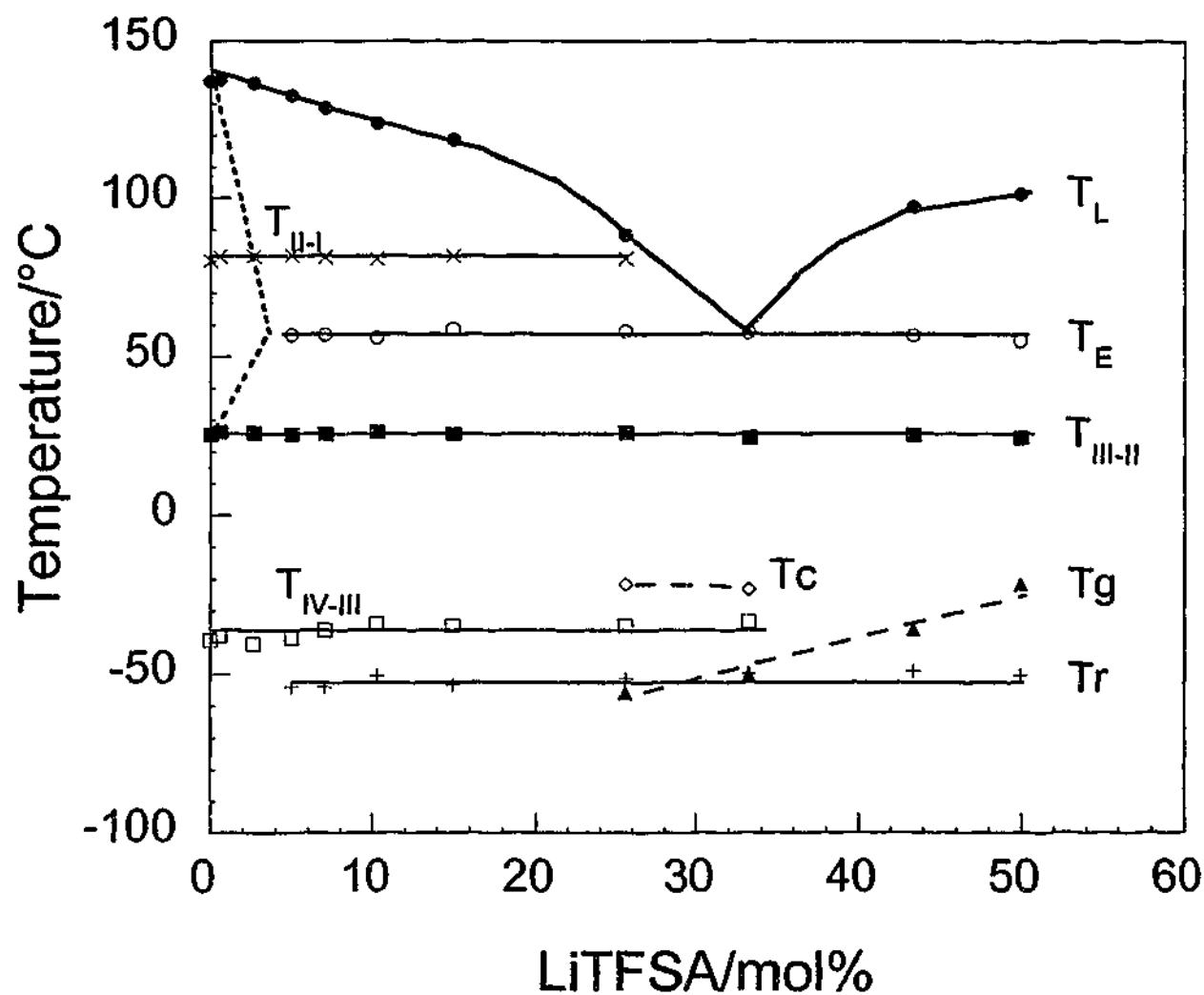
Figure 6.2 Partial phase diagram for P11TFSA-LiTFSA binary, indicating solid-solid phase transitions $T_{IV\text{-}III}$, $T_{III\text{-}II}$ and $T_{II\text{-}I}$, liquidus temperature T_L, eutectic temperature T_E, a transition temperature Tr, glass transition T_g and devitrification temperature T_C. T_g and T_C are the onset temperatures. The rest are peak temperatures. Solid and dashed lines indicate equilibrium and metastable phase transitions, respectively. Doted lines are tentatively drawn to indicate the solid solution region.

It is interesting to note that when a P11TFSA rich phase is present either as a single phase in the solid solution region or in coexistence with the other phase (a LiTFSA rich solid phase below 57 °C or a liquid phase above 57 °C), the solid-solid phase transitions at –38 (± 3) °C, 26 (± 2) °C and 81 (± 2) °C still remain, suggesting that the plastic crystal behavior of P11TFSA may not be altered by introducing another phase or another salt. The phase III>>II and II>>I transitions occur at relatively constant temperatures. This is in contrast to the depressed liquidus temperature for a doped molten phase. Doping into a molten state results in a decrease in the free energy of the melt and hence a depressed liquidus temperature. The constant phase III>>II and II>I transition temperatures observed here possibly indicate that the free energies of the plastic crystal phases are less influenced by doping with the LiTFSA salt than those of the molten phase [297].

6.2.2 Nuclear Magnetic Resonance

^{1}H NMR

^{1}H NMR spectra for 5 mol% LiTFSA in P11TFSA are shown in Figure 6.3. A single broad resonance is observed at low temperatures. A narrow line appears on top of the broad peak at about 0 °C. The intensity of the narrow line increases with temperature whilst that of the broad bottom gradually decreases.

Temperature dependence of the linewidth is shown in Figure 6.4. The linewidth of the broad peak is about 22.6 kHz in phase IV. According to Table 4.3, this linewidth is less than the value of 50 kHz when only the CH_3 groups are involved in rotation while the ring is static and greater than the value of 7 kHz when the ring is involved in isotropic rotation, indicating that cations are rotating anisotropically. No obvious discontinuity in linewidth is observed at the phase IV>>III transition temperature, probably suggesting that the cationic rotation mechanism does not change during this weak phase transition. A slight decrease to 18 kHz occurs at about 5 °C which is in the broad phase III>>II transition range, indicating that a change occurs in the rotational motion for the cations during this phase transition. A further line narrowing occurs in phase II. The linewidth is reduced to 11.7 kHz in phase I, indicative of another anisotropic rotation.

- 230 -
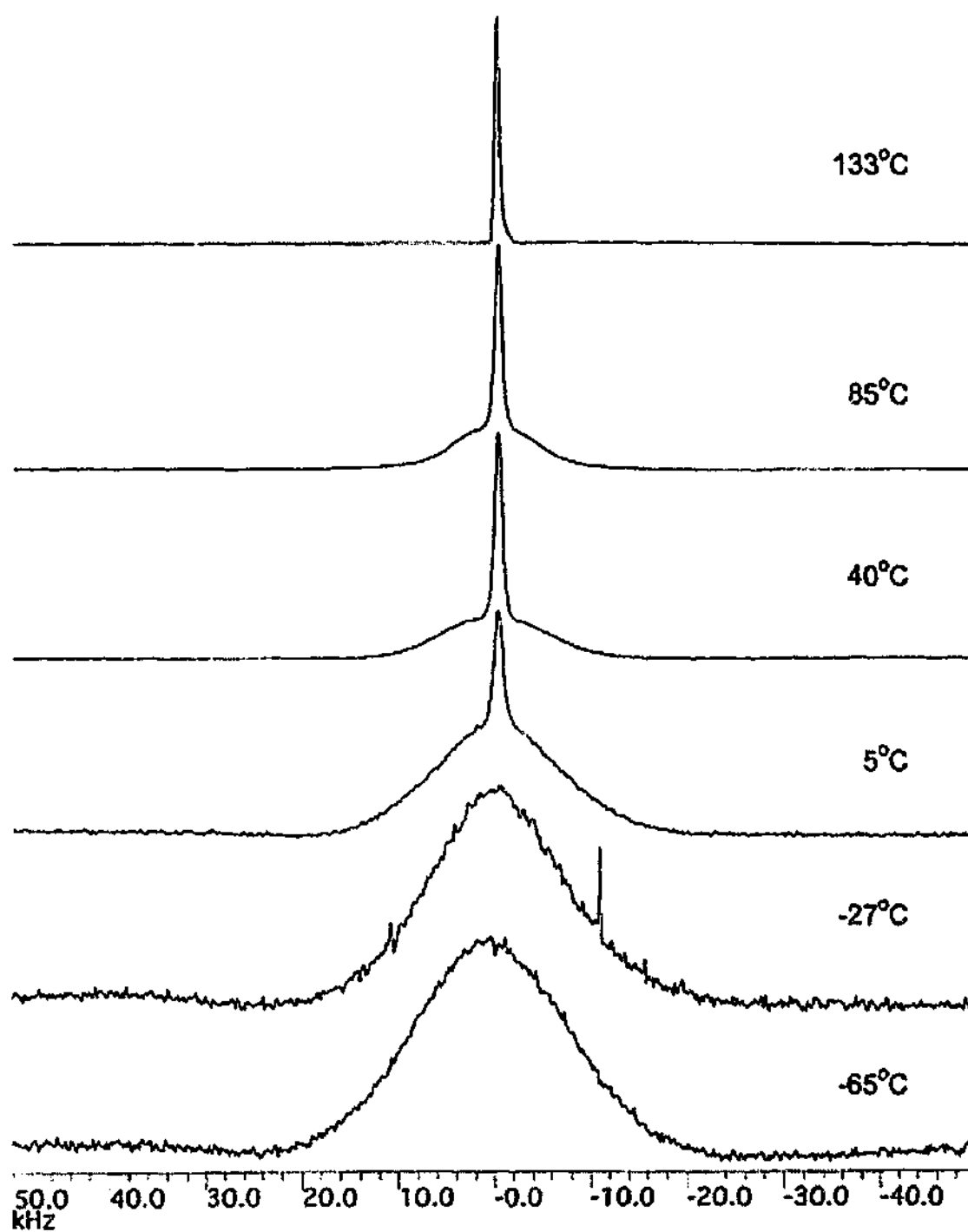
Figure 6.3 ^{1}H NMR spectra of 5 mol% LiTFSA in P11TFSA. The spikes at –27 °C are not part of original signal, but occur during transformation of data between software.

These linewidth values and temperature dependence are very similar to those for pure P11TFSA by comparing with Figure 4.9. For example, for pure P11TFSA, the linewidth is 22.6 kHz in phase III and 11.7 kHz in phase I. A slight decrease from 22.6 kHz to 18 kHz

at about 0 °C is also observed in pure P11TFSA. This implies that doping of 5 mol% LiTFSA does not change the rotational mechanism for the P11$^+$ cations over the entire temperature range investigated, although the rotational frequency or activation energy may be altered. This is consistent with the observation in DSC traces that the solid-solid phase transitions of 5 mol% LiTFSA remain the same shapes and occur at the same temperatures as those for the pure P11TFSA. The evidence from NMR and DSC suggests that the ionic rotational motion and plastic crystal phase behavior are not changed by doping with the lithium salt at the dopant level. The same phenomenon is also observed for LiTFSA doped P12TFSA.
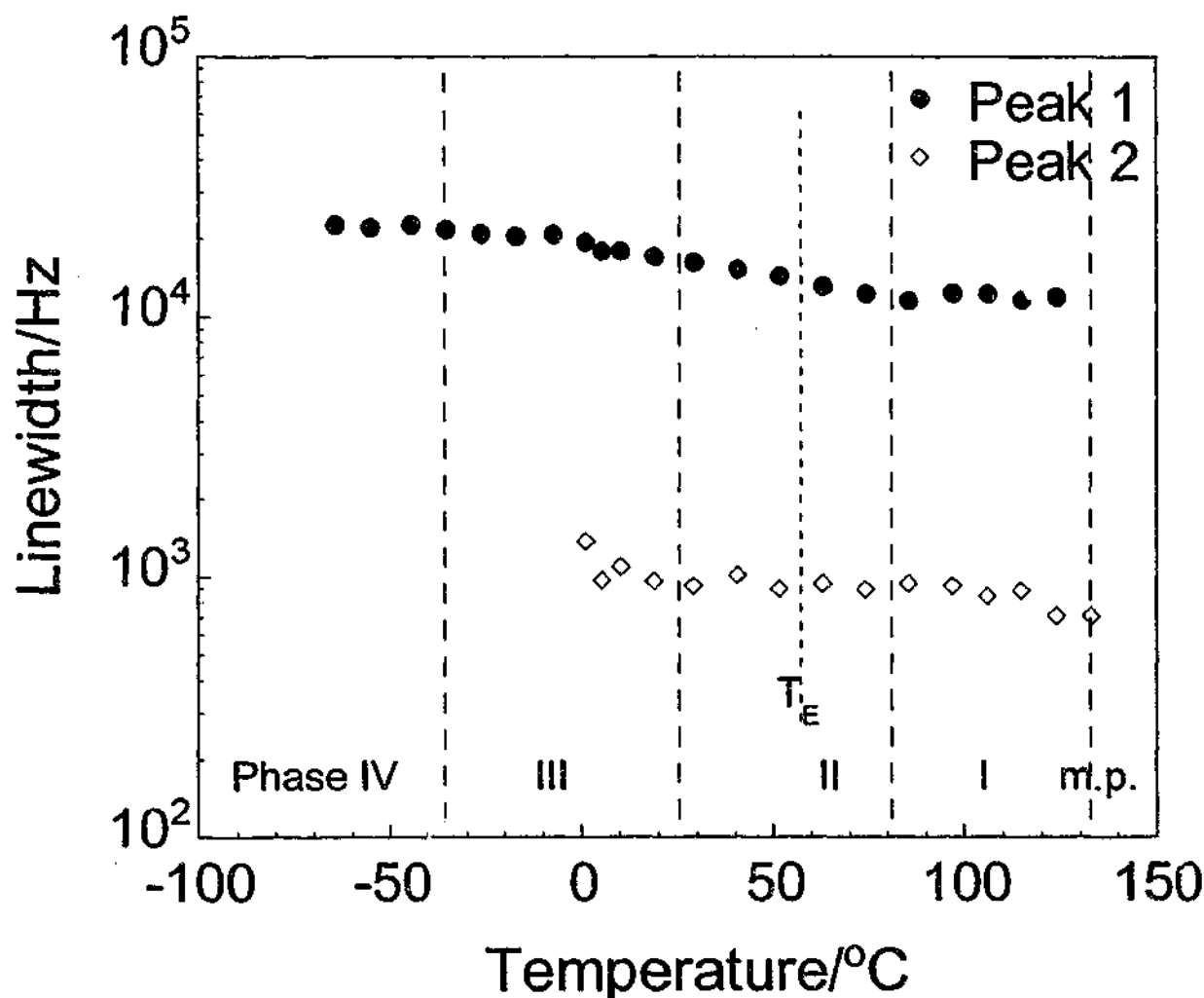
Figure 6.4 ^{1}H NMR linewidth for 5 mol% LiTFSA in P11TFSA as a function of temperature.

In the case of the narrow peak, the linewidth is 1.3 kHz at 0 °C. It remains a relatively constant value of about 900 Hz in phases II and I until it decreases to 700 Hz near the melting point. These linewidths are much smaller than 7 kHz, the calculated linewidth value for isotropically rotating cations according to Table 4.3, indicative of diffusing P11$^+$ cations. Cationic diffusion in 5 mol% LiTFSA is detected at temperatures as low as 0 °C. This is in contrast to pure P11TFSA as shown in Figure 4.9, where the cationic diffusion can only be detected near the melting point. The diffusion can be detected in the form of the narrow NMR peak only when (1) the diffusion rate is high enough (comparable to $M_2^{-1/2}$) to cause a line narrowing, and (2) the number of the diffusing ions is high enough so that the narrow resonance is not "drowned" by the broad peak. The NMR studies in this project suggest that the observation limit for the fraction of mobile ions is about 0.01. Therefore, the appearance of the narrow peak implies that doping with LiTFSA salt results in P11$^+$ cations diffusing in larger numbers and/or with higher diffusion coefficient.

^{19}F NMR

^{19}F NMR spectra for 5 mol% LiTFSA in P11TFSA are shown in Figure 6.5. Broad peaks are observed at low temperatures. Similar to those observed for pure P11TFSA as shown in , the broad peaks can be deconvoluted into three peaks of different chemical shift, indicative of at least three different F sites. A narrow line appears on top of the broad bottom at −70 °C. The intensities of the broad peaks decrease gradually while that of the narrow peak increases with temperature.

The linewidth as a function of temperature is shown in Figure 6.6. Peak 1 indicates the broad resonance centred at about 28 kHz. This peak contributes about 15% to the overall peak area. The linewidth is about 19 kHz in phase IV. It decreases gradually in phases III and II and reaches 7 kHz in phase I. According to Table 4.4, the linewidth values expected for rigid anions, anions with rotating CF$_3$ groups and isotropically rotating anions are about 27, 17 and 8 kHz, respectively. Therefore, the anions represented by peak 1 are not static in phase IV, but involve in some motion unidentified at this point. These anions participate in isotropic rotation in phase I. Peak 2 and peak 3 exhibit similar linewidth and temperature dependence over all the temperature range studied, probably indicative of the

anions doing similar rotational motions at different sites. The linewidth at −77 °C is about 13 kHz and reduces to 8 kHz in phase II. Again, the linewidth range is similar to that for pure P11TFSA by comparing with Figure 4.12, probably suggesting that doping of LiTFSA salt does not change the anionic rotational mechanism.
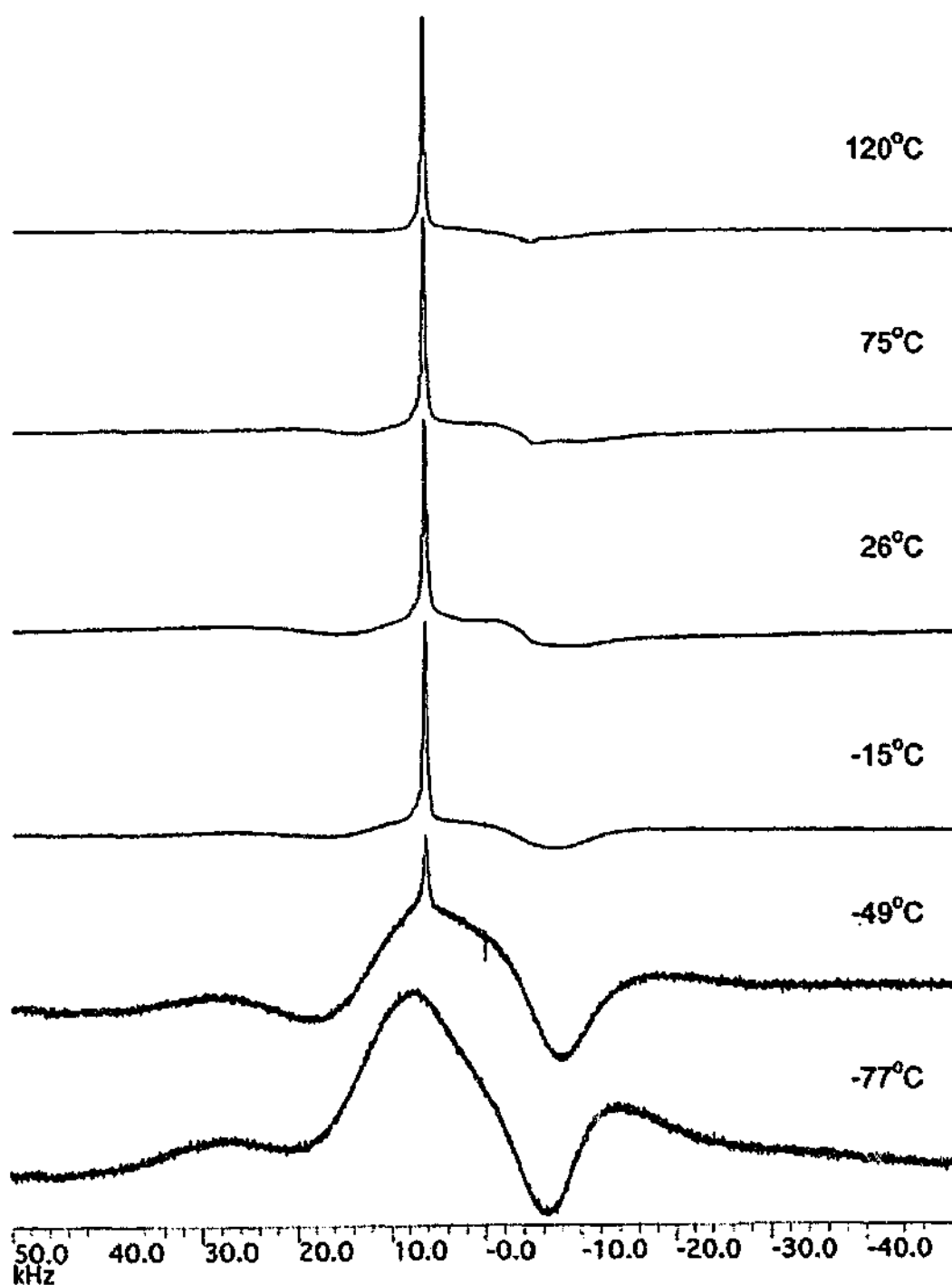
Figure 6.5 ^{19}F NMR spectra for 5 mol% LiTFSA in P11TFSA. The peak at about −7 kHz comes from background.

The linewidth of the narrow peak is 1.8 kHz at −70 °C, much less than the calculated value of 8 kHz for the isotropic rotation, suggesting the diffusing anions. It is in the range of 300 ~ 400 Hz in phases III, II and I. Again, in contrast to the pure P11TFSA where the anionic diffusion can only be detected near the melting point according to Figure 4.12, the anionic diffusion in 5 mol% LiTFSA can be observed by NMR at temperatures as low as −70 °C. This indicates that doping with LiTFSA salt also improves the number and/or the diffusion coefficient of diffusing anions.
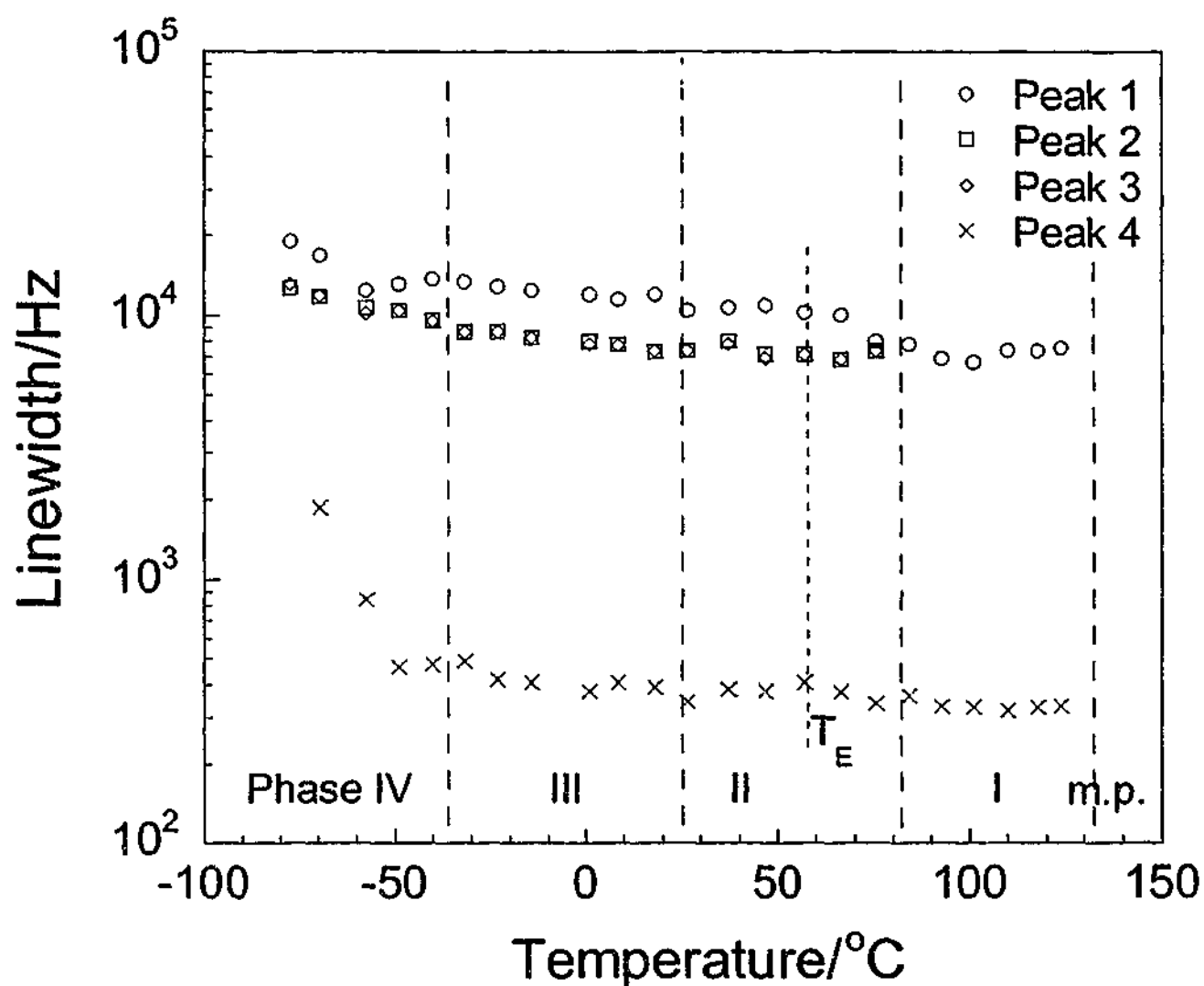
Figure 6.6 ^{19}F NMR linewidth as a function of temperature for 5 mol% LiTFSA in P11TFSA.

^{7}Li NMR

^{7}Li NMR spectra for 5 mol% LiTFSA are shown in Figure 6.7. Similar to those for LiTFSA doped P12TFSA, the spectra display a single broad resonance in phase IV. A narrow line appears on top of the broad peak above 0 °C. The intensity of the narrow line increases with temperature while that of the broad line decreases until the broad bottom disappears above 25 °C. As discussed in ^{7}Li NMR Linewidth for 4.8 mol% LiTFSA in P12TFSA, the broad and narrow peaks are not the satellites and center peaks caused by quadrupolar interactions, but indicate the Li$^+$ ions at different sites where the Li$^+$ ions experience different extents of dipolar interactions. Otherwise, the ratio of the broad and narrow peak area should be the same with temperature [201].
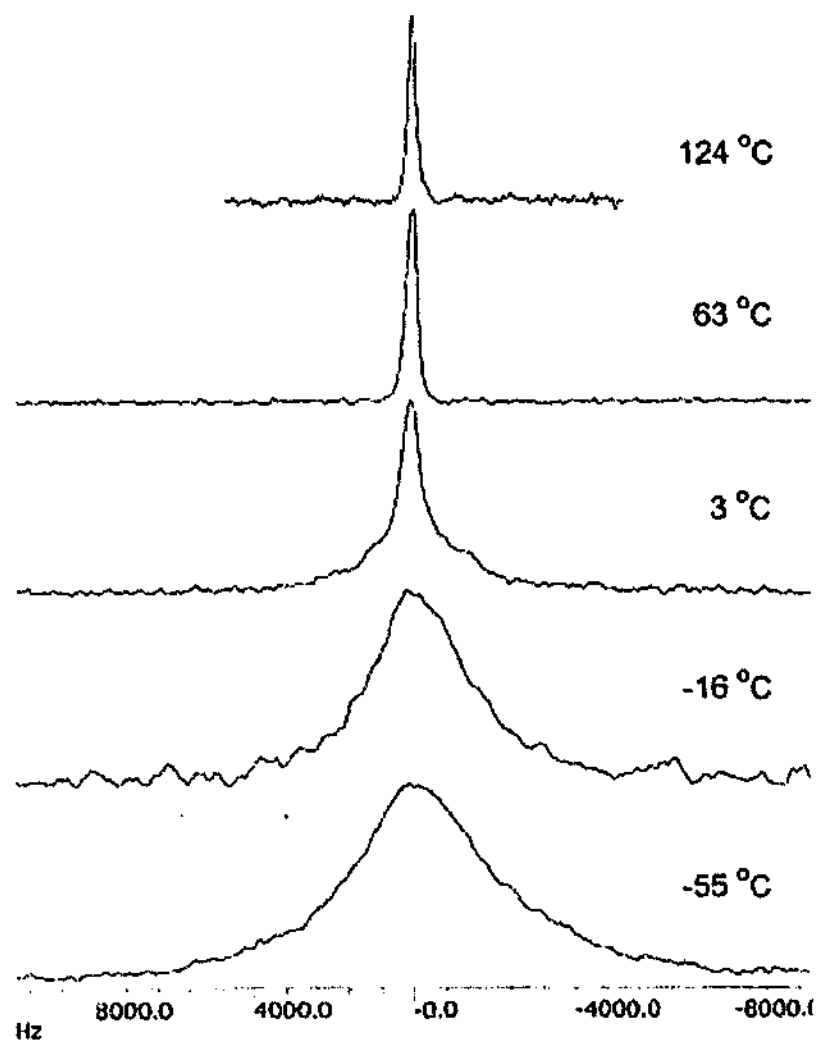
Figure 6.7 ^{7}Li NMR spectra for 5 mol% LiTFSA in P11TFSA.

Changes in the linewidth with temperature are shown in Figure 6.8. The linewidth of the broad peak is about 3.9 kHz in phase IV, which is in the typical linewidth range for Li^+ ions in the rigid lattice [298, 299]. ^7Li-^7Li, ^7Li-^1H and ^7Li-^{19}F dipolar interactions are the possible contributors to this broad linewidth. The line exhibits a narrowing through the phase IV>>III transition to 2.7 kHz in phase III. This line narrowing could be associated with changes in the surrounding environments, either the onset of the TFSA⁻ (or P11⁺) motion or a change in the P11TFSA lattice. Both of the reasons are possible. The former is supported by the ^{19}F NMR which indicates a line narrowing at this temperature. The later is revealed by the volumetric expansion experiment, which shows that volumetric expansion of the P11TFSA network starts to occur at this temperature, as shown in section 4.2.3. The distances between the Li^+ ions and surrounding ions are increased. As a result, the dipolar interactions with the surrounding nuclei are weakened.

The linewidth of the narrow line is 450 Hz at 0 °C, suggesting that the Li^+ ion possesses translational mobility. The linewidth decreases gradually and reaches 350 Hz at 20 °C. This is in contrast to ^7Li NMR for 5 mol% LiTFSA doped P12TFSA, where the linewidth shows a sharp decrease in a narrow temperature range at phase III>>II transition, as shown in Figure 5.18. The difference probably provides additional evidence that the motion of the Li^+ ions is related to the microstructure of the parent salt, because both the volumetric expansion and vacancy size exhibit sharp increases at phase III>>II transition for P12TFSA while the changes in the volumetric expansion and vacancy parameters are relatively steady for P11TFSA at phase III>>II transition.

Above 26 °C where the phase III>>II transition peak position is in DSC, the broad bottom of the NMR spectrum disappears, implying that all the Li^+ ions become mobile in phase II. This probably suggests that the solubility of Li^+ ions is increased in phase II and that most of the Li^+ ions become soluble in the P11TFSA matrix. Compared to the linewidth value of 80 Hz for 4.8 mol% LiTFSA in P12TFSA in phase II, the linewidth of about 350 Hz here in phase II is much broader. This probably indicates that the Li^+ ions are less mobile in the P11TFSA network than in P12TFSA matrix. In phase I, the narrow peak exhibits a further line narrowing to about 100 Hz at the melting point. This line narrowing indicates

that all the species start to become mobile near the liquidus temperature, so that the dipolar interactions with the surrounding nuclei are further averaged out.

The fraction of mobile Li^+ ions is indicated in Figure 6.9. The fraction of diffusing $P11^+$ cations and $TFSA^-$ anions are also displayed for comparison. The diffusion behaviors of Li^+ ions and $P11^+$ cations seem to exhibit some similarity in that (1) the diffusions of both ions become detectable by NMR at about 0 °C; (2) the number of the diffusing ions increases substantially during the phase III>>II transition for both species. However, the diffusion of $TFSA^-$ anions is observed at much lower temperature than the cations. There is probably a relatively large error in estimating the fraction of the diffusing $TFSA^-$ anions due to the interference from the background on the broad peaks, so the fraction of the diffusing anions is not analyzed in detail here.

In summary, the solubility of Li^+ ions in P11TFSA probably increases in phase II and thus more Li^+ ions become incorporated into the P11TFSA matrix. All the Li^+ ions are mobile in the P11TFSA network, although they are less mobile than in P12TFSA. Substitution of the $P11^+$ cations with the small Li^+ ions probably introduces disruption in the lattice structure and thus provides more transport volume for the parent ions. As a result, more $P11^+$ cations and $TFSA^-$ anions participate in the diffusional motion than in pure P11TFSA. It should be noted that the fraction of the mobile Li^+ ions is much higher than that of $P11^+$ cations over all the temperature range below the melting point. In addition, the $P11^+$ cations and the $TFSA^-$ anions could still be associated in the diffusional process. Therefore, the doped Li^+ ion is one of the main contributors to the improved conductivity.
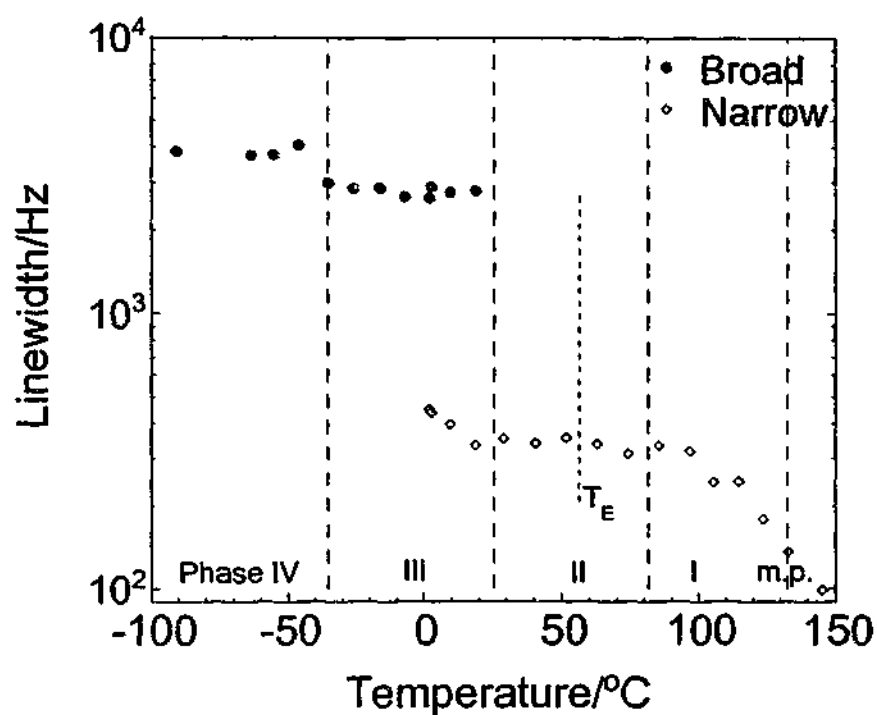
Figure 6.8 ^{7}Li NMR linewidth as a function of temperature for 5 mol% LiTFSA in P11TFSA.
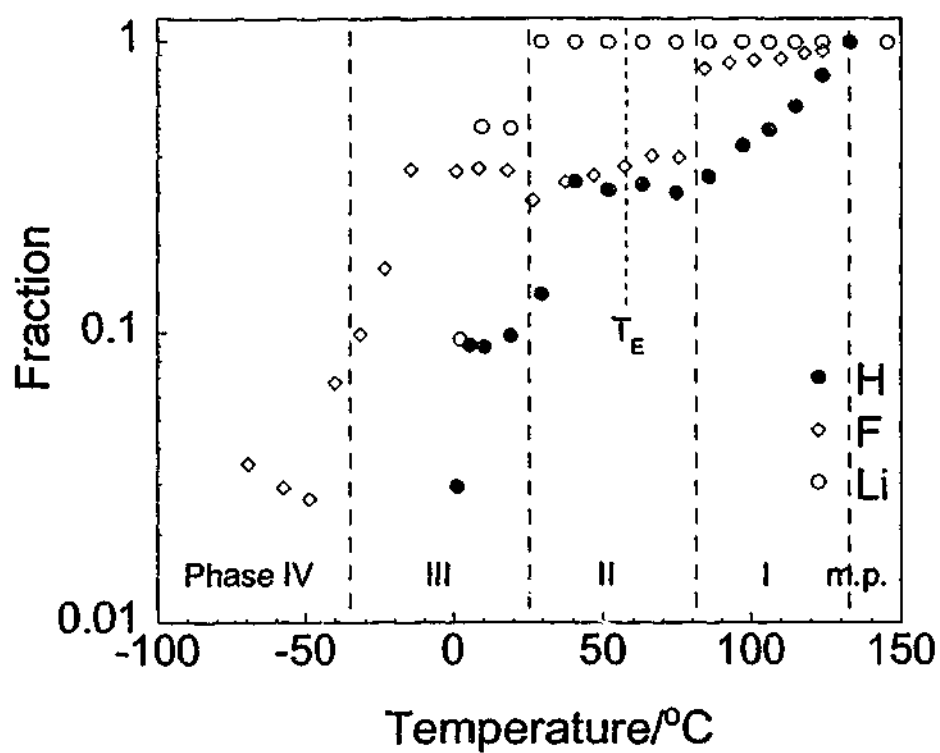
Figure 6.9 Fraction of narrow peak area of ^{1}H, ^{19}F and ^{7}Li NMR for 5 mol% LiTFSA in P11TFSA.

6.2.3 Conductivity

Temperature dependence of conductivity data for P11TFSA-LiTFSA system with the LiTFSA content ranging from 0 to 51 mol% is shown in Figure 6.10.

0.6 mol% and 1.0 mol% compositions exhibit similar conductivity values in phase III. A divergence occurs from 12 °C, in the broad phase III>>II transition range. In the case of the 2.7 mol% and 5.0 mol% compositions, obvious "knees" are observed in the range of 0 °C ~ 14 °C, as shown in Figure 6.10 (a). The conductivity for 5 mol% LiTFSA is three orders of magnitude higher than that of the pure P11TFSA at 26 °C. The possible reasons for the enhanced conductivity in phase II are: (1) The number of mobile Li^+ ions increases, as the solubility of Li^+ ions in the P11TFSA network is improved through the phase III>II transition. This is supported by the ^7Li NMR results for 5 mol% LiTFSA which show that the fraction of mobile Li^+ ions is greatly increased in this temperature range. (2) The mobility of Li^+ ions is enhanced by being incorporated into the P11TFSA matrix. The narrower ^7Li NMR linewidth (340 Hz) in phase II compared to 450 Hz at 0 °C supports this idea. (3) The increased number and/or diffusion coefficient of $P11^+$ cations or $TFSA^-$ anions through the phase III>>II transition may also contribute to the increase in the conductivity. ^1H NMR for 5 mol% LiTFSA shows a substantial increase in the fraction of the diffusing $P11^+$ ions and a decrease in the linewidth in this temperature range.

In phase I, all the compositions between 0 and 5 mol% LiTFSA exhibit a rapid increase in conductivity below the melting point. The slope of $d\ln\sigma/d(1/T)$ in the transition range decreases with increasing LiTFSA concentration. The sharp increase in conductivity indicates that the samples are mainly composed of the solid solution phase until the liquidus temperature.

The compositions between 26 mol% to 51 mol% also exhibit a sharp conductivity increase in the broad phase III>>II transition range, as shown in Figure 6.10 (b). The highest conductivity at 26 °C is 2.4×10^{-5} Scm^{-1}, obtained at 33 mol%. This value is more than one order of magnitude higher than that of 5 mol% LiTFSA. All the compositions between 9.3 mol% to 51 mol% show another "knee" at about 45 °C, which may be attributed to the

eutectic transition, where part of the sample transforms from solid state into liquid state. Above the eutectic temperature, the conductivity increases steadily with temperature, as reflected by a relatively constant slope of $d\ln\sigma/d(1/T)$ until beyond the final liquidus temperature for the compositions between 9.3 mol% ~ 51 mol%. This contrasts with the rapid increase near the melting point for the compositions of 0 ~ 5 mol% LiTFSA. The difference should be attributed to that the liquidus temperatures for the compositions of 9.3 mol% ~ 51 mol% are greatly depressed and broadened and that the liquid domain expands gradually above the eutectic temperature, as indicated from the phase diagram.

LiTFSA composition dependence of conductivity at various temperatures is present in Figure 6.11.

At 5 °C, all the compositions are solid. The solubility of Li^+ ions in P11TFSA is estimated to be less than 5 mol%. For the compositions between the solubility and 51 mol%, two phases are present, the P11TFSA rich phase and the LiTFSA rich phase. The LiTFSA rich phase is not clearly identified at this point. Figure 6.11 indicates that doping with a small amount of lithium salt improves the conductivity. For example, the conductivity is increased by one order of magnitude for 5 mol% LiTFSA. The doped Li^+ ions are of course one of the contributors to the conductivity. The fraction of mobile Li^+ ions is estimated to be in the range of 0.1 – 0.5 at this temperature according to Figure 6.9. $P11^+$ and $TFSA^-$ ions are the possible contributors to the conductivity as well. According to the ^1H and ^{19}F NMR analyses, doping with lithium salt results in higher numbers of diffusing $P11^+$ cations and $TFSA^-$ anions compared to pure P11TFSA where the diffusion of either $P11^+$ cations or $TFSA^-$ anions can only be detected just below the melting point. However, further doping beyond 26 mol% leads to a decrease in conductivity. The conductivity of 50 mol% LiTFSA is even smaller than that of the pure P11TFSA. The possible reason is that the LiTFSA rich phase is less conductive than the P11TFSA rich phase. The LiTFSA rich phase expands gradually with doping of the lithium salt, and thus results in the decrease in the overall conductivity.
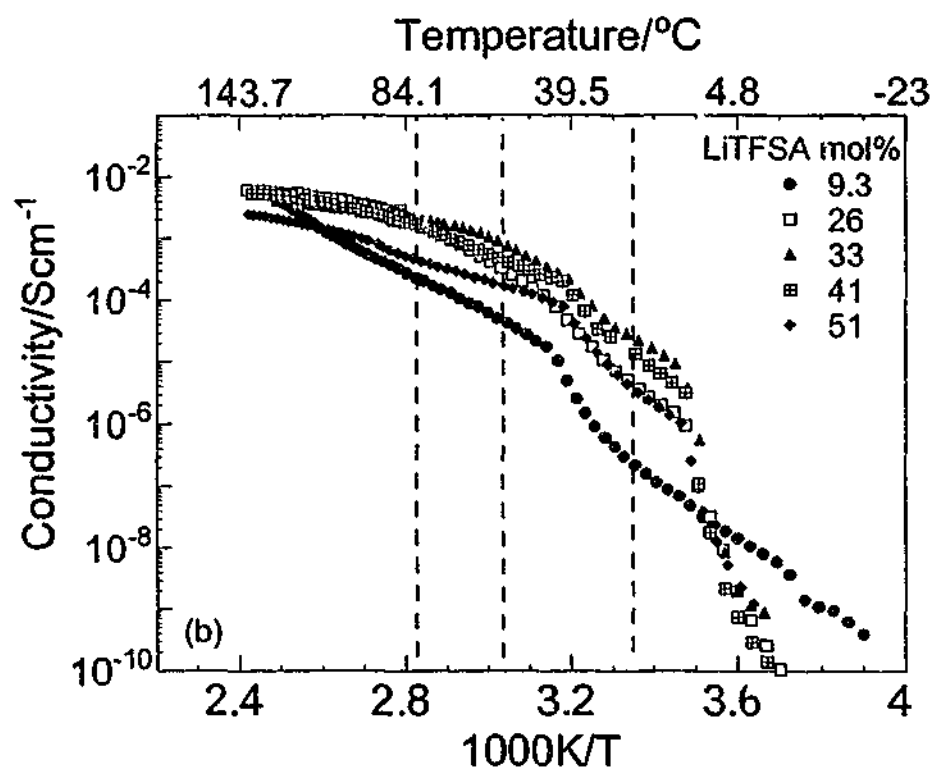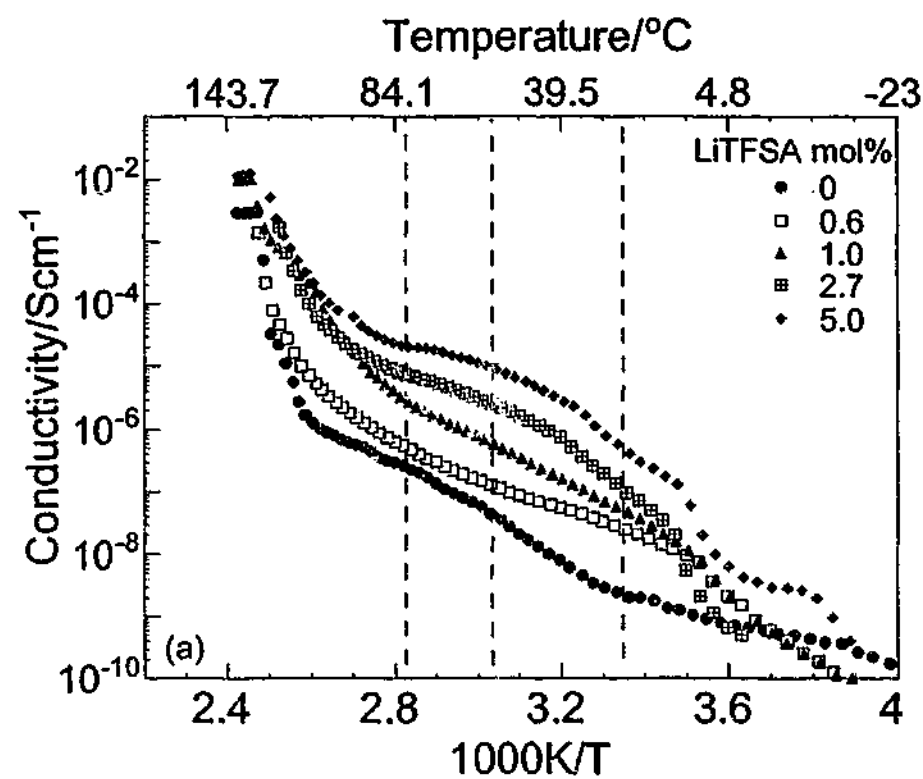
Figure 6.10 Conductivity as a function of temperature for (a) 0 ~ 5.0 mol% and (b) 9.3 ~ 51 mol% LiTFSA doped P11TFSA. The dashed lines indicate the common phase transition temperatures of III>>II, II>>I and the eutectic temperature.

At 45 °C, all the compositions are still in the solid state. The effect of salt on conductivity is greater than at 5 °C. Doping of 5 mol% LiTFSA leads to an increase in the conductivity by more than two orders of magnitude. For compositions with low LiTFSA content, Li^+ ion is thought to be a major, if not sole, contributor to the increase in conductivity. As the solubility of Li^+ ions in P11TFSA is increased through the phase III>>II transition, more Li^+ ions become incorporated in the P11TFSA network. The Li^+ ions in the P11TFSA matrix are very mobile. The diffusion of $P11^+$ cation and $TFSA^-$ anions may also be improved in the solid solution phase. The increased number of diffusing $P11^+$ cations in the solid solution phase is clearly shown by ^1H NMR. It is thought that, in the P11TFSA matrix, substitution of the $P11^+$ cation (2.7 Å in radius) with the small Li^+ ion (0.7 Å in radius) introduces vacancy-like discontinuity in the lattice, which may facilitate the diffusion of the $P11^+$ or $TFSA^-$ ions.

For compositions beyond 9.3 mol%, the conduction mechanism is more complicated, as another solid phase, a LiTFSA rich phase, coexists with the P11TFSA solid solution phase. The overall conductivity is related to the amount of the two phases, the conduction mechanism within each phase and the effect of phase boundaries. It seems that the LiTFSA rich phase may also become more conductive than that at 5 °C, which partly accounts for the substantial increase in conductivity. As a result of all these effects, the highest conductivity of 3.5×10^{-4} Scm^{-1} is observed at 33 mol% LiTFSA. It is interesting to note that doping with 5 mol% LiTFSA improves the conductivity by more than two orders of magnitude on the base of the pure P11TFSA whilst the conductivity for 33 mol% LiTFSA is less than two orders of magnitude higher than that of 5 mol% LiTFSA. This comparison implies that the LiTFSA doped P11TFSA solid solution phase is more conductive.

At 65 °C and 100 °C, substantial increase in conductivity by doping with a small amount of LiTFSA salt is still observed. Doping with 5 mol% LiTFSA improves the conductivity by about two orders of magnitude versus the pure P11TFSA at these two temperatures. The increase should mainly be attributed to the Li^+ doped P11TFSA solid solution, as the P11TFSA rich phase is the dominant phase at both temperatures according to the phase diagram. Beyond 5 mol% LiTFSA, a liquid phase coexists with a solid phase (a P11TFSA

rich phase for 5 mol% ~ 33 mol% compositions or a LiTFSA rich phase for 33 mol% ~ 51 mol% compositions). These two phases as well as the phase boundaries should all contribute to the total conductivity. The highest conductivity is observed for 33 mol% composition at 65 °C and 26 mol% at 100 °C.
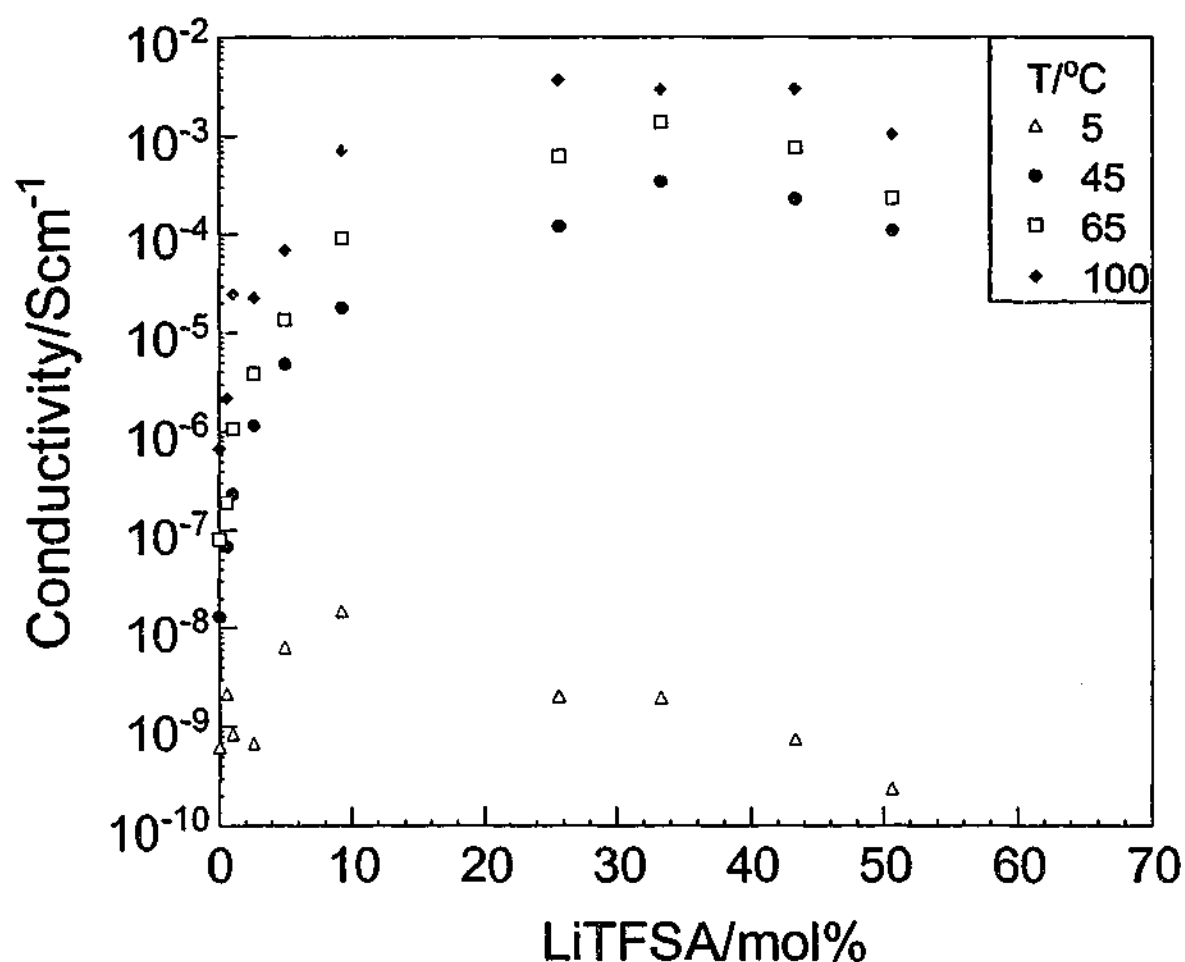
Figure 6.11 Conductivity isotherms as a function of LiTFSA composition for P11TFSA-LiTFSA binary.

6.3   Conclusions

P11TFSA-LiTFSA mixtures present relatively classic phase behavior for a binary system. The eutectic temperature is observed at 57 (± 2) °C with eutectic composition at about 33 mol% LiTFSA. The phase diagram of P11TFSA-LiTFSA bears some similarities to that of P12TFSA-LiTFSA in: (1) eutectic composition is about 33 mol% LiTFSA for both

systems; and (2) both systems exhibit a significant solid solution phase at low lithium salt concentration.

The solubility of the lithium salt in the solid solution is associated with the microstructure of the parent salt. For example, the solubility of the lithium salt into the parent salt for both systems increases through the phase III>>II transition where volumetric expansion occurs, which favors the incorporation of the Li^+ ions into the parent salt. The solubility limit of lithium salt in P11TFSA is between 2.7 mol% and 5 mol%, as compared to the value of between 4.8 mol% and 9.3 mol% for P12TFSA-LiTFSA system. The smaller solubility limit in P11TFSA is consistent with less lattice expansion or vacancy volume observed in the parent salt.

Doping with lithium salt does not change the plastic crystal behaviors of the parent salt. This is reflected by that the solid-solid phase transitions of pure P12TFSA or P11TFSA still remain in the lithium salt doped samples. The rotational mechanisms of the parent ions, as indicated by the NMR linewidths, are not changed by doping with the lithium salt.

Doping of a small amount of LiTFSA salt results in a substantial increase in conductivity. For example, the conductivity is increased by two orders of magnitude by doping with 2.7 mol% LiTFSA into P11TFSA. When the concentrations of LiTFSA are within the solubility limit, these compositions can be regarded as the analogues to the pure P1xTFSA (x=1 or 2), where some of the $P1x^+$ cations are substituted by the Li^+ ions while the rotational motions of $P1x^+$ cations and $TFSA^-$ anions still remain. All the Li^+ ions exhibit liquid like mobility through the parent network and therefore are important charge carriers in the conductivity. The translational motion of the small Li^+ ions may be associated with the rotational motion of the parent ions in the same way as in Li_2SO_4 [171, 172] and Na_3PO_4 [201]. The mismatched sizes of the small Li^+ ion and the substituted $P1x^+$ cation may cause discontinuity in the crystal lattice and allow the diffusion of the parent ions.

Compared to P12TFSA-LiTFSA system, the eutectic temperature for P11TFSA-LiTFSA is enhanced to 57 °C, which brings about better thermal stability for the whole system as reflected by the improved reproducibility in the DSC traces even for the components close

to eutectic composition. This is of significance for the P11TFSA-LiTFSA mixtures in the practical use as electrolyte materials.

Chapter 7 Conclusions

Chapters 3-6 present the studies of the P1xTFSA salts and the LiTFSA-P1xTFSA binary systems. The conclusions of these studies are summarized as the followings.

7.1   Pure P1xTFSA Salt

Phase behavior, ionic motion, microstructure, mechanical properties and conduction mechanisms of the pure P1xTFSA salts have been studied. These studies have achieved better understanding of the P1xTFSA salts as plastic crystals.

1. Both of the P12TFSA and P11TFSA salts have been shown to be plastic crystals. Their phase behavior shows several solid-solid phase transitions. These solid-solid phase transitions are related to the rotational motion of the ions. The rotational motions of both the $P1x^+$ cations and $TFSA^-$ anions are observed in NMR studies and dielectric responses.

2. The solid-solid phase transition entropies in the P1xTFSA salts should be attributed to the changes in lattice structure; vacancy formation, expansion or redistribution; and ionic rotational mechanisms. Most of the phase transitions in P11TFSA and P12TFSA are found to be broad, indicating that the transformations in these salts are progressive procedures rather than sudden changes. P11TFSA exhibits less volume expansion, less vacancy volume and less significant diffusion in the solid state than P12TFSA, indicative of less degree of freedom in the solid state for P11TFSA. These coincide with the fact that the fusion entropy of P11TFSA is higher than that of P12TFSA.

3. Vacancies are found to be important features for P11TFSA and P12TFSA. The vacancy concentration in P11TFSA is 0.27 % at room temperature. Vacancies seem to be closely associated with ionic or molecular rotation, although it is hard to define the cause-effect relationship. It is thought that the less hindered rotation and the formation of a larger number of vacancies result from the same microstructural features: the intermolecular or interionic distance is relatively long; and the intermolecular or interionic interactions are weak. When the structure of a material has the potential to permit the ionic or molecular

- 247 -

rotation, it could also allow the formation of a larger number of vacancies. In addition, vacancies encourage the rotation, as the rotation of the molecules or ions in the vicinity of vacancies is less hindered. On the other hand, the rotation leads to increased vacancy formation entropy, decreased vacancy formation free energy and thus benefits vacancy formation. Therefore, higher vacancy concentration is one of the important properties of plastic crystals, at least for P11TFSA and P12TFSA salts.

4. Both P11TFSA and P12TFSA exhibit good plasticity. The plasticity is related to the vacancy number and mobility, as plastic deformation occurs by the slip of crystalline planes, which is associated with the motion of dislocations and essentially the self diffusion of vacancies. The dislocation traces of P12TFSA are clearly observed by SEM.

5. A vacancy mechanism is thought to be responsible for the conduction. No obvious associations are found between ionic rotation and diffusion whereas the conductivity exhibits similar temperature dependence to that of volumetric expansion, which is related to the volume of vacancies. The cations and anions may be associated in a Schottky mechanism in diffusion, as the translational motions of cations and anions exhibit close association. It is thought that for plastic crystals containing molecules or comparable sized ions, a vacancy mechanism is more likely to account for the diffusion of the molecules or ions. The paddle wheel mechanism seems more suitable to describe those plastic crystals where a small ion (or molecule) can be attached to another rotating ion (or molecule) and be transported. Extended defects, such as dislocations and grain boundaries, could also contribute to the conductivity by providing diffusion tunnels in the P1xTFSA salts.

7.2   Lithium Salt Doped P1xTFSA Mixture

Based on the understanding of the plastic crystal behavior for P12TFSA and P11TFSA salts, LiTFSA salt has been doped into these two salts in order to produce fast Li^+ ion conductors. The phase behavior, ionic motion and conductivities for the compositions ranging from $0 \sim 50$ mol% LiTFSA have been studied for both systems.

1. P12TFSA-LiTFSA and P11TFSA-LiTFSA binary systems exhibit complicated phase behavior. The liquidus temperature is depressed and broadened by doping with LiTFSA salt. Each system displays a eutectic phase transition. The eutectic temperatures are 33 (± 2) °C for P12TFSA-LiTFSA binary and 57 (± 2) °C for P11TFSA-LiTFSA binary. The eutectic composition is at 33 mol% LiTFSA for both systems. The plastic crystal behavior of the pure P12TFSA or P11TFSA still remains even though another new salt or another phase is introduced. The phase behavior for LiTFSA-P12TFSA mixtures close to their eutectic composition is influenced by the temperature fluctuation around room temperature. The thermal behavior for the LiTFSA-P11TFSA mixtures is less influenced by the temperature fluctuation. 33 mol% composition displays the highest conductivity at room temperature in both systems: 2.5×10^{-4} Scm^{-1} for 33 mol% LiTFSA-P12TFSA and 2.4×10^{-5} Scm^{-1} for 33 mol% LiTFSA-P11TFSA. The conduction mechanism in the two-phase region involves the motions of the three species in two phases and thus is complicated.

2. An important feature of both binary systems is the LiTFSA doped P11TFSA or P12TFSA solid solution phase. The solubility of LiTFSA salt in the P11TFSA or P12TFSA salt depends on the microstructure of the parent salt. The solubility increases with the lattice expansion or vacancy formation of the parent salt. The solubility limit in P12TFSA is higher than in P11TFSA.

These LiTFSA doped P1xTFSA solid solutions can be regarded as the P1xTFSA analogues. The crystal lattice structures of the parent salts are retained while some of the P1x$^+$ cations are substituted by the small Li$^+$ ions. The plastic crystal phase behavior remains. The parent ions still participate in rotational motion, although the rotational frequency and energy barrier could be changed. The substitution of the P1x$^+$ cations with the small Li$^+$ ions leads to discontinuity in the crystal lattice, which may account for the diffusion of both P1x$^+$ cations and TFSA$^-$ anions in larger numbers and/or with higher diffusion coefficients. Li$^+$ ions are shown to be important charge carriers. All the Li$^+$ ions are incorporated into the parent salts in higher temperature phases and are involved in the diffusion. The transport of Li$^+$ ions displays liquid like mobility through the P1xTFSA network. The translational motion of the Li$^+$ ions seems to show some association with the rotational motion of the parent ions. It is thought that the rotational motion of the parent

ions may facilitate the diffusion of Li^+ ions. As a result, doping with LiTFSA salt at as small an amount as 5 mol% could lead to an increase in conductivity by three orders of magnitude. The composition of 5 mol% LiTFSA in P12TFSA, which is believed to be completely solid at room temperature, exhibits conductivity of about 1.2×10^{-5} Scm^{-1}. Therefore, these LiTFSA doped P1xTFSA plastic crystals can be regarded as a new class of fast Li^+ conductor.

These mixtures in the single solid solution phase region normally exhibit good reproducibility in phase behavior, regardless of the thermal history. These mixtures also display relatively constant conductivities over a one week period, suggesting that the phases are relatively stable. It is also expected that the good plasticity is less altered by doping with a small amount of lithium salt. Therefore, these mixtures have good potential to be used as solid state electrolyte materials for lithium batteries.

7.3   Future Work

More work is needed to further understand the ionic motions. It is important to measure the diffusion coefficient of the Li^+ ions, which could provide direct evidence of the high mobility of Li^+ ions. By comparing the diffusion coefficient of Li^+ ions with those of the $P1x^+$ cations and $TFSA^-$ anions, the transference numbers of each ion can be obtained. This can be done by field gradient ^7Li NMR measurements. In addition, ^{19}F NMR T_1 and T_2 relaxation measurements are helpful to assess the rotational and hopping frequencies of the $TFSA^-$ anions. By comparing the correlation times and activation energies of the rotational and translational motions of the $P1x^+$ cations, $TFSA^-$ anions and the Li^+ ions, a clearer picture of the associations between the rotational and translational motions of the three ionic species could be obtained. This work has not been done in this study due to the interference from the background in ^{19}F NMR. ^{13}C NMR could also be useful to study the rotational mechanisms of the $P1x^+$ and $TFSA^-$ ions.

It is interesting to test the performance of these mixtures as solid state electrolyte materials in lithium batteries. A sample of 5 mol% LiTFSA in P12TFSA has been assembled in a lithium battery as a preliminary test. After charging, the cell voltage is in the normal range

for a lithium cell, indicating that Li^+ ions are conductive in the electrolytes. More work is needed to make full assessments about the stability of the electrolytes, energy density, power density, interfacial behavior, lifetime, etc.

Since it has been found in this study that the $P1x^+$ cations and the $TFSA^-$ anions also participate in the diffusion, it is of interest to employ some molecular plastic crystals as the parent materials. The doped Li^+ ions are very mobile through the parent network whilst the parent molecules do not contribute to the conductivity, even though they involve in the diffusion. A higher t_{Li}^+ would then be expected. The requirement for the plastic crystal molecules is that, the interactions between the molecules and the Li^+ ions should be weak enough to allow a high diffusional mobility for the Li^+ ions while the associations between the anions of the lithium salts and the plastic crystal molecules should be strong. The mobility of the anions could thus be restricted. This could also be achieved by doping with new lithium salts, where the degree of dissociation of the anions and Li^+ ions should be high while the anion is bulky and immobile. Recently, Angell et al. have reported a new lithium salt, lithium bis(perfluoropinacolato)borate $LiB[OC(CF_3)_2]_4$ [303]. The negative charge on the anion is delocalized, as there are eight CF_3 groups with strong electron-withdrawing ability. The Li^+ ions and the anions appear to be fully dissociated in PC solvent. If a lithium salt like this is doped into molecular plastic crystals, the mobility of the anions should be restricted, as bigger vacancies are needed for the anionic diffusion. The Li^+ ions could be dissociated easily with the anions and become very mobile through the molecular network.

The thermodynamic and kinetic properties of the P1xTFSA salts are worthy of further study. The observation of a possible glass transition in P12TFSA indicates that these plastic crystals could be compared dynamically with a large number of materials exhibiting glass transitions, either an orientational glass transition or a structural glass transition. These materials could be unified within a common mathematical framework. Within this framework, some perplexing aspects of the present salts, such as the relatively low solid-solid phase transition entropy changes, could be better understood. The dynamics of the present systems could also be compared with those of other conductors within this

- 251 -

framework. Some puzzles, such as the different degree of deviation from the Arrhenius behavior observed for Li_2SO_4, Na_3PO_4, P1xTFSA, etc, could be solved. The study of the thermodynamic and relaxation behaviors for P11TFSA and P12TFSA could be complicated. Both salts exhibit several plastic crystal phases. Each phase could produce a corresponding meta-stable glassy state. The salts would need to be treated by different thermal processes to allow each of the phases to present and to be identified. Heat capacity and dielectric measurements within each of the phases and through the phase transitions would be very informative.

In conclusion, the studies of this project reveal that plastic crystals could provide high conductivity and good mechanical flexibility. They have great potential to be used as highly effective solid state electrolyte materials in the lithium battery industry. The thermodynamic and kinetic properties, molecular motions, microstructures, and the practical applications of plastic crystals are a new exciting area to be explored.

Appendix A Crystal Lattice Studies by XRD

Determination of the lattice structures at various temperatures for P11TFSA and P12TFSA has been attempted by X-Ray Diffraction (XRD).

A single crystal of P11TFSA was obtained at −150 °C. The crystal lattice structure was investigated by single crystal X-ray diffraction at −150 °C[*]. The lattice parameters are listed in Table AP- 1. Each unit cell contains four cations and four anions. The position of each of the atoms is shown in the reference [295].

It was difficult to grow single crystals of P11TFSA and P12TFSA at room temperature. Therefore powder X-ray diffraction was employed to study the lattice structures of P11TFSA and P12TFSA at various temperatures. The powder XRD patterns are shown in Figure AP- 1 and Figure AP- 2. A program TREOR90 (VERSION 90 C1 31) was used in indexing. There has been difficulty in indexing the powder X-ray patterns at temperatures other than 20 °C probably due to the relatively poor resolution of the instrument below room temperature.

Two sets of crystal data were obtained for P11TFSA and one set for P12TFSA at 20 °C, as shown in Table AP- 1. Among the two sets of the indexed crystal lattice parameters for P11TFSA, the one where β angle is 97° has some consistence with the one at −150 °C. Both are monoclinic. The β angles are close. The cell constants "b" and "c" are the same. This result suggests that the lattice structure change in P11TFSA occurs by expansion in the "a" direction when temperature increases.

All the parameters obtained from the powder XRD are yet to be confirmed.

---

[*] This work was mainly carried out by Dr. Craig Forsyth using single crystal X-Ray diffraction. Details about this work are in Reference [295].
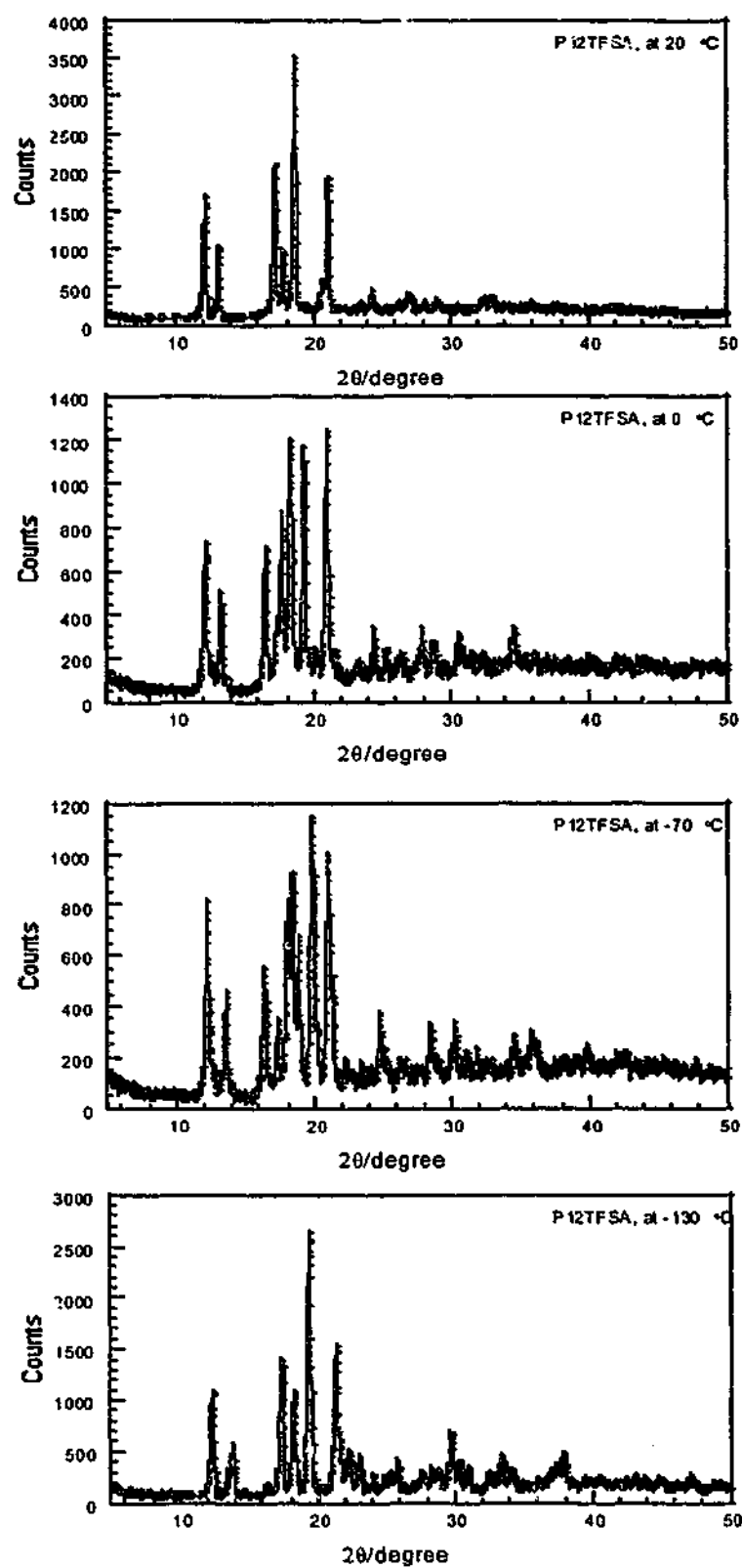
Figure AP- 1 Powder X-ray diffraction pattern for P12TFSA at various temperatures. $\lambda(CuKa_1=1.54060$ Å).
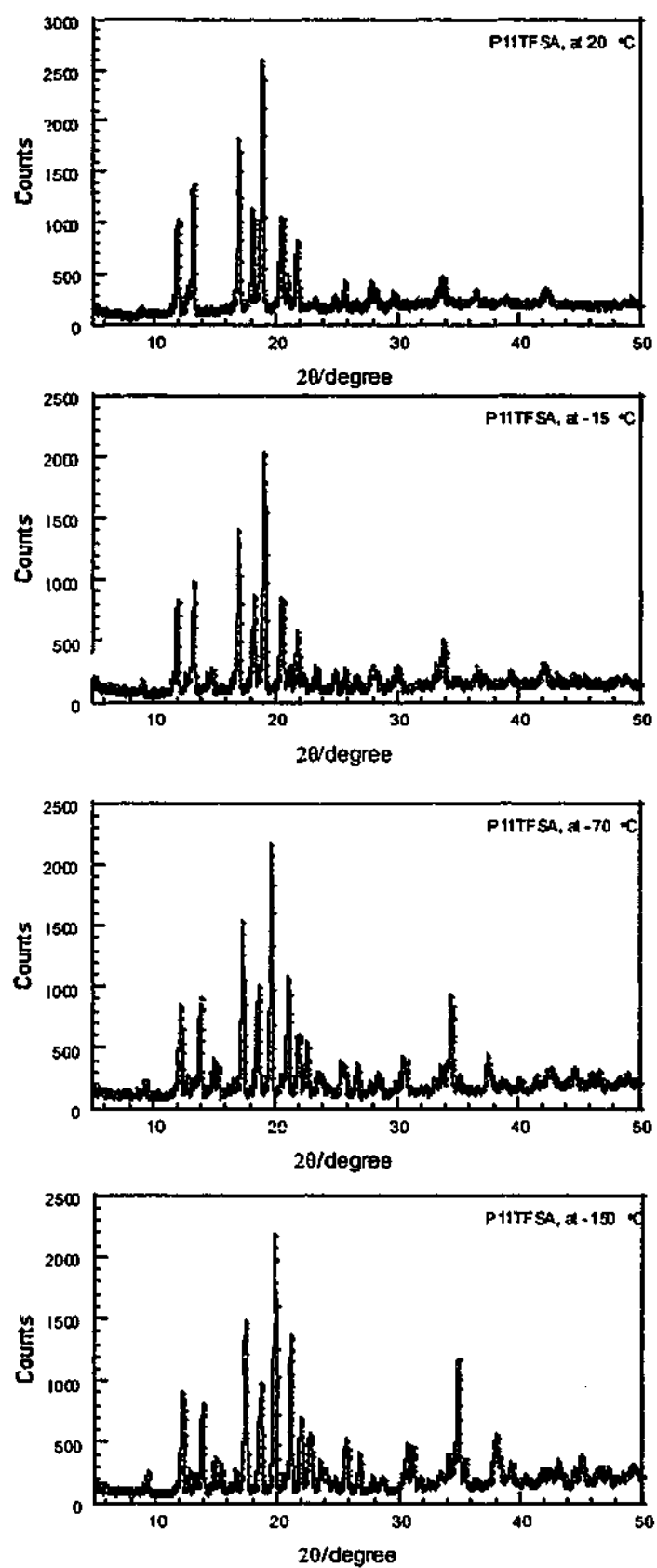
Figure AP- 2 Powder X-ray diffraction pattern for P11TFSA at various temperatures.
λ(Cu*Ka*₁=1.54060 Å).

Table AP- 1 Possible lattice parameters for P11TFSA and P12TFSA. [a,b] two possible results for P11TFSA obtained by powder XRD. [c] possible result for P12TFSA obtained by powder XRD. [d] Obtained by single crystal XRD [295].

Lattice Parameter	P11TFSA -150 °C [d]	P11TFSA 20 °C [a]	P11TFSA 20 °C [b]	P12TFSA 20 °C [c]
a (Å)	12.8083(3)	13.408(9)	15.06(1)	15.42(2)
b (Å)	13.8305(4)	13.834(6)	13.834(6)	14.74(3)
c (Å)	8.5034(2)	8.691(6)	8.691(6)	8.52(2)
α (°)	90.000	90.00	90.00	90.00
β (°)	98.785(2)	97.03(7)	117.92(6)	117.9(2)
γ (°)	90.000	90.00	90.00	90.00
V (Å^3)	1488.66	1599.96	1599.96	1713.49

Appendix B   A Table of The Summary of The Ammonium Salts Reviewed

Table AP- 2 The lattice structures, the activation energies of ionic rotation and diffusion (Ea_{rot} and Ea_{dif}, respectively), the correlation times of rotation and diffusion at the melting point (τ_{rot} and τ_{dif}, respectively), the activation energies of conductivity (Ea_{σ}) for some ammonium salts in phase I.

Compound	Lattice structure	Cation rotation		Cation diffusion		Anion rotation		Anionic Diffusion		Ea_{σ} /kJmol^{-1}	Ref.
		Ea_{rot} /kJmol^{-1}	τ_{rot} /s	Ea_{dif} /kJmol^{-1}	τ_{dif}/s.	Ea_{rot} /kJmol^{-1}	τ_{rot} /s	Ea_{dif} /kJmol^{-1}	τ_{dif} /s		
NH_4Cl	NaCl	20		120					1.6×10^{-7}		[234]
NH_4Br	NaCl	10		120					1.8×10^{-7}		[234]
NH_4NO_3	CsCl			51		rot				67	[214]
CH_3NH_3I	CsCl			35	5.0×10^{-8}						[304]
				43						51	[287]

Compound	Lattice structure	Cation rotation		Cation diffusion		Anion rotation		Anionic Diffusion		Ea_o /kJmol^{-1}	Ref.
		Ea_{rot} /kJmol^{-1}	τ_{rot} /s	Ea_{dif} /kJmol^{-1}	τ_{dif}/s.	Ea_{rot} /kJmol^{-1}	τ_{rot} /s	Ea_{dif} /kJmol^{-1}	τ_{dif} /s		
CH_3NH_3Br	CsCl	20		51	1.1×10^{-8}						[58]
$CH_3NH_3ClO_4$	NaCl			49	1.1×10^{-8}						[219]
				29	2.7×10^{-8}						[220]
$CH_3NH_3NO_3$	CsCl			29	9.7×10^{-8}					45	[220, 221]
$(CH_3NH_3)_2SO4$	Hexagonal	17		76	1.0×10^{-8}						[227]
$C_3H_7NH_3Cl$	Tetragonal	20		40						37	[228]
$C_4H_9NH_3Cl$	Tetragonal	5.1	8.9×10^{-13}	64	2.8×10^{-7}				1.2×10^{-7}	45	[59]
$C_5H_{11}NH_3Cl$	Tetragonal	6	1.6×10^{-12}	50,44						46	[229]

Compound	Lattice structure	Cation rotation		Cation diffusion		Anion rotation		Anionic Diffusion		Ea_σ /kJmol^{-1}	Ref.
		Ea_{rot} /kJmol^{-1}	τ_{rot} /s	Ea_{dif} /kJmol^{-1}	τ_{dif}/s.	Ea_{rot} /kJmol^{-1}	τ_{rot} /s	Ea_{dif} /kJmol^{-1}	τ_{dif} /s		
$C_6H_{13}NH_3Cl$	Tetragonal	5.1	3.5×10^{-12}	60						48	[230]
$C_7H_{15}NH_3Cl$	Tetragonal	5.8	6.5×10^{-12}	75	1.0×10^{-7}			45	5.5×10^{-8}	54	[230]
$C_8H_{17}NH_3Cl$	Tetragonal	5.4	4.4×10^{-12}	70						57	[230]
$C_9H_{19}NH_3Cl$	Tetragonal	5.5	4.3×10^{-12}	80	1.2×10^{-7}			40	1.1×10^{-7}	57	[230]
$C_{10}H_{21}NH_3Cl$	Tetragonal	6.0	2.2×10^{-12}	90	1.6×10^{-7}			50	1.3×10^{-7}	64	[230]
$(C_2H_5)_2NH_2Br$	Tetragonal	18		51						58	[231]
$(C_3H_7)_2NH_2Br$	Tetragonal	12		60						61	[231]
$(C_4H_9)_2NH_2Br$	Tetragonal	14		69							[231]

Compound	Lattice structure	Cation rotation		Cation diffusion		Anion rotation		Anionic Diffusion		Ea $_\sigma$ /kJmol^{-1}	Ref.
		Ea$_{rot}$ /kJmol^{-1}	τ_{rot} /s	Ea$_{dif}$ /kJmol^{-1}	τ_{dif}/s.	Ea$_{rot}$ /kJmol^{-1}	τ_{rot} /s	Ea$_{dif}$ /kJmol^{-1}	τ_{dif} /s		
$(CH_3)_2NH_2ClO_4$	Tetragonal	14.6		37.6		11.9					[233] [232]
$(CH_3)_3NHClO_4$	Tetragonal	rot		57.9		40.7					[226] [2²2]
$(CH_3)_3NHBF_4$		rot		21		rot		dif			[57]
$(CH_3)_4NClO_4$		24.2									[226]
$(CH_3)_4SCN$	CsCl	21		110	rot					100	[222]
$(CH_3)_3NCH_2CH_3ClO_4$	CsCl	27		60							[53]
$(CH_3)_3NCH_2CH_3PF_6$	CsCl	19		56		5		53			[53]

Compound	Lattice structure	Cation rotation		Cation diffusion		Anion rotation		Anionic Diffusion		Ea $_\sigma$ /kJmol^{-1}	Ref.
		Ea$_{rot}$ /kJmol^{-1}	τ_{rot} /s	Ea$_{dif}$ /kJmol^{-1}	τ_{dif}/s.	Ea$_{rot}$ /kJmol^{-1}	τ_{rot} /s	Ea$_{dif}$ /kJmol^{-1}	τ_{dif} /s		
$(CH_3)_3NCH_2CH_3NO_3$	NaCl	13				rot					[53]
PyrrolidiniumClO$_4$	CsCl	7		48							[55]
PyrrolidiniumPF$_6$	CsCl	7		45, 42	1.2×10^{-7}	10		25	1.1×10^{-7}		[55]
PiperidiniumClO$_4$	CsCl	10		61		Rot					[52]
PiperidiniumPF$_6$	CsCl	17		61, 57	1.8×10^{-7}	15		44, 39	1.0×10^{-7}		[54]
PiperidiniumNO$_3$	NaCl	25				rot					[52]

Appendix C Publications

List of publications and Patents:

1.   D.R. MacFarlane, J. Huang, and M. Forsyth, *Lithium-doped plastic crystal electrolytes exhibiting fast ion conduction for secondary batteries.* Nature (London), 1999. **402**: p. 792-794.

2.   M. Forsyth, J. Huang, and D.R. MacFarlane, *Lithium-doped n-methyl-n-ethylpyrrolidinium bis(trifluoromethanesulfonyl)amide fast-ion conducting plastic crystals.* J. Mater. Chem., 2000. **10**: p. 2259-2265.

3.   J. Huang, M. Forsyth, and D.R. MacFarlane, *Solid state lithium ion conduction in pyrrolidinium imide-lithium imide salt mixtures.* Solid State Ionics, 2000. **136-137**: p. 447-452.

4.   J. Golding, N. Hamid, D.R. MacFarlane, M. Forsyth, C. Forsyth, C. Collins and J. Huang, *N-methyl-n-alkylpyrrolidinium hexafluorophosphate salts: Novel molten salts and plastic crystal phases.* Chem. Mater., 2001. **13**: p. 558-564.

5.   D.R. MacFarlane, M. Forsyth, and J. Huang, *Ion conductive material having a dopant ion in an organic matrix phase.*, in *PCT Int. Appl.* 2001: Australia. p. 21pp.

6.   C.M. Forsyth, D.R. MacFarlane, J.J. Golding, J. Huang, J. Sun and M. Forsyth, *Structural characterization of novel ionic materials incorporating the bis(trifluromethylsulphonyl)amide anion.* Chem. Mater., 2002. **14**: p. 2103-2108.

7.   A.J. Hill, J. Huang, J. Efthimiadis, P. Meakin, M. Forsyth and D.R. MacFarlane, *Microstructural and molecular level characterisation of plastic crystal phases of pyrrolidinium trifluoromethanesulfonyl salts.* Solid State Ionics, 2002. **154-155**: p. 119-124.

Papers in Preparation

1. J. Huang, M. Forsyth, D.R. MacFarlane, et al., *Solid state lithium ion conductor based on n-methyl-n-methylpyrrolidinium bis(trifluoromethanesulfonyl)amide-lithium bis(trifluoromethanesulfonyl)amide mixtures.* In preparation.

2. J. Huang, M. Forsyth, and D.R. MacFarlane, *N-methyl-n-propylpyrrolidinium hexafluorophosphate-lithium hexafluorophosphate mixtures: Thermal properties, ionic motion and conductivity.* In preparation.

3. J. Huang, D.R. MacFarlane, M. Forsyth, et al., *A study of conduction mechanism of plastic crystalline phases of pyrrolidinium bis(trifluoromethanesulfonyl)amide salts.* In preparation.

4. J. Huang, D.R. MacFarlane, and M. Forsyth, *A study of the plastic crystalline phase of n-methyl-n-ethylpyrrolidinium bis(trifluoromethanesulfonyl)amide: Mechanical properties, microstructure and ionic motion.* In preparation.

5. J. Huang, D.R. MacFarlane, and M. Forsyth, *A study of n-methyl-n-methylpyrrolidinium bis(trifluoromethanesulfonyl)amide: Mechanical properties, microstructure, ionic motion and conductivity.* In preparation.

References

1. F. Beck and P. Ruetschi, *Rechargeble batteries with aqueous electrolytes.* Electrochim Acta, 2000. **45**: p. 2467-2482.

2. J.R. Owen, *Rechargeable lithium batteries.* Chem. Soc. Rev., 1997. **26**: p. 259-267.

3. B. Scrosati, *Recent advances in lithium ion battery materials.* Electrochim Acta, 2000. **45**: p. 2461-2466.

4. A.R. West, *Crystalline solid electrolytes I: general considerations and the major materials.*, in *Solid State Electrochemistry*, P. Bruce, G., Editor. 1995, Cambridge University Press. p. 7-42.

5. H. Gerischer, *Principles of electrochemistry*, in *The CRC handbook of solid state electrochemistry*, P.J. Gellings and H.J.M. Bouwmeester, Editors. 1997, CRC Press. p. 9-73.

6. K. Hayamizu, Y. Aihara, et al., *Pulse-gradient spin-echo ^1H, ^7Li, and ^{19}F NMR diffusion and ionic conductivity measurements of 14 organic electrolytes containing $LiN(SO_2CF_3)_2$.* J. Phys. Chem. B, 1999. **103**: p. 519-524.

7. A. Webber, *Conductivity and viscosity of solutions of $LiCF_3SO_3$, $Li(CF_3SO_2)_2N$, and their mixtures.* J. Electrochem. Soc., 1991. **138**: p. 2586-2590.

8. C. Julien, *Solid State Batteries*, in *The CRC handbook of solid state electrochemistry*, P.J. Gellings and H.J.M. Bouwmeester, Editors. 1997, CRC Press. p. 371-406.

9. G.-y. Adachi, N. Imanaka, and H. Aono, *Fast Li^+ conducting ceramic electrolytes.* Adv. Mater., 1996. **8**: p. 127-135.

10. S. Chandra, *Superionic solids: principles and applications.* 1981: North-Holland Publishing Company. 404.

11. J.M. Chezeau and J.H. Strange, *Diffusion in molecular crystals.* Phys. Reports, 1979. **53**: p. 1-92.

12. M. Jansen, *Volume Effect or Paddle-Wheel Mechanism -- Fast Alkali-Metal Ionic Conduction in Solids with Rotationally Disordered Complex Anions.* Angew. Chem. Int. Ed. Engl., 1991. **30**: p. 1547-1558.

13. H. Kawai and J. Kuwano, *Lithium ion conductivity of A-site deficient perovskite solid solution $La_{0.67-x}Li_{3x}TiO_3$.* J. Electrochem. Soc., 1994. **141**: p. L78-L79.

14. L. Latie, G. Villeneuve, et al., *Ionic conductivity of oxides with general formula $Li_xLn_{1/3}Nb_{1-x}Ti_xO_3$ (Ln=La, Nd).* J. Solid State Chem., 1984. **51**: p. 293-299.

15. J.L. Souquet, *Ionic transportation in glassy electrolyts*, in *Solid state electrochemistry*, P. Bruce, G., Editor. 1995, Cambridge University Press. p. 74-94.

16. C.A. Angell, *Mobile ions in amorphpous solids*. Annu. Rev. Phys. Chem., 1992. **45**: p. 693-717.

17. P.G. Bruce and C.A. Vincent, *Polymer Electrolytes*. J. Chem. Soc. Faraday Trans., 1993. **89**: p. 3187-3203.

18. W. Meyer, H., *Polymer electrolytes for lithium-ion batteries*. Adv. Mater., 1998. **10**: p. 439-448.

19. P.G. Bruce and F.M. Gary, *Polymer electrolytes II: physical principles*, in *Solid State Electrochemistry*, P. Bruce, G., Editor. 1995, Cambridge University Press. p. 119-162.

20. K. Ito, M. Yoshizawa, and H. Ohno. *Ionic conductivity of a series of molten-salt type polymer electrolytes*. in *The sixth international symposium on polymer electrolytes*. 1998. Japan: Meisei-Planning and Printing Co., Ltd.

21. H. Ohno and K. Ito, *Room-temperature molten salt polymers as a matrix for fast ion conduction*. Chem. Lett., 1998: p. 751-752.

22. E.I. Cooper and C.A. Angell, *Ambient Temperature Plastic Crystal Fast Ion Conductors*. Solid State Ionics, 1986. **18&19**: p. 570-576.

23. J. Timmermans, *Plastic Crystal: A Historical Review*. J. Phys. Chem. Solids, 1961. **18**: p. 1-8.

24. G.W. Smith, *Liquid-like Solids*. Intern. Sci. Tech., 1967. **61**: p. 72-80.

25. C.A. Angell, *Relaxation in liquids, polymers and plastic crystals-strong/fragile patterns and problems*. J. Non-Cryst. Solids, 1991. **131-133**: p. 13-31.

26. G.W. Smith, *Orientational Order and Melting*. Comments Solid State Phys., 1978. **9**: p. 21-35.

27. B. Wunderlich, *Metastable mesophases*. Macromol. Symp., 1997. **113**: p. 51-65.

28. L. Pauling, *Rotational motion of molecules in crystals*. Phys. Rev., 1930. **36**: p. 430-443.

29. J. Timmermans, *A new mesomorphic state. Plastic organic crystals*. J. Chim. Phys., 1938. **35**: p. 331-344.

30. C.A. Fyfe, *Solid State NMR for Chemists*. 1983, Ontario, Canada: C. F. C. Press.

31. C. Brot and B. Lassier-Govers, *Rotational Diffusion and Reorientations in Molecular Crystals*. Ber. Bunsenges. Phys. Chem., 1976. **80**: p. 31-41.

32. D.R. MacFarlane, P. Meakin, et al., *Structural studies of ambient temperature plastic crystal ion conductors*. J. Phys.: Condens. Matter, 2001. **13**: p. 8257-8267.

33. D.R. MacFarlane and M. Forsyth, *Plastic crystal electrolyte materials: new perspectives on solid state ionics*. Adv. Mater. (Weinheim, Ger.), 2001. **13**: p. 957-966.

34. H. Ishida, Y. Furukawa, et al., *Phase transitions and ionic motions in solid Trimethylammonium Iodide studied by ^1H and ^{127}I NMR, electric conductivity, X-ray diffraction and thermal analysis.* Ber. Bunsenges. Phys. Chem., 1996. **100**: p. 433-439.

35. L.M. Amzel and L.N. Becka, *A Model for The Evaluation of Thermodynamic Properties for The Solid-Solid and Melting Transitions of Molecular Crystals.* J. Phys. Chem. Solids, 1969. **30**: p. 521-538.

36. J.A. Pople and F.E. Karasz, *A Theory of Fusion of Molecular Crystals I. The Effects of Hindered Rotation.* J. Phys. Chem. Solids, 1961. **18**: p. 28-39.

37. J.M. Bruce, *Self-Diffusion and Point Defects Studies in Plastic Crystals,* in *Dept. of Pure and Applied Chem.* 1986, Univ. of Strathclyde. p. 232.

38. G.W. Smith, *Proton Magnetic Resonance Studies of Pentaerythritol.* J. Phys. Chem. Solids, 1969. **50**: p. 3595-3605.

39. G.W. Smith, *Proton Magnetic Resonance Studies of Solids Tetramethyls of Silicon, Germanium, Tin, and Lead.* J. Chemical Physics, 1965. **42**: p. 4229-4243.

40. K. Moriya, T. Matsuo, and H. Suga, *Phase transition and freezing of disordered ionic orientation in cesium nitrite crystal.* Chem. Phys. Letters, 1981. **82**: p. 581-585.

41. K. Moriya, T. Matsuo, et al., *Calometric and dielectric studies of phase transitions in $TiNO_2$ crystal.* Chem. Lett., 1977. **12**: p. 1427-1430.

42. K. Moriya, T. Matsuo, and H. Suga, *Phase transition and freezing of ionic disorder in cesium and thallium nitrite crystals.* J. Phys. Chem. Solids, 1983. **44**: p. 1103-1119.

43. K. Moriya, T. Matsuo, and H. Suga, *Orientational and positional disorder of ions and its freezing in the cesium nitrite-thallium nitrite system.* J. Phys. Chem. Solids, 1983. **44**: p. 1121-1132.

44. K. Moriya, T. Matsuo, and H. Suga, *Thermodynamic properties of alkali and thallium nitrites: the ionic plastically crystalline state.* Thermochim. Acta, 1988. **132**: p. 133-140.

45. K. Moriya, T. Matsuo, and H. Suga, *Calorimetric and dielectric studies of phase transitions in rubidium nitrite.* Bull. Chem. Soc. Jpn., 1988. **61**: p. 1911-1916.

46. K. Moriya and H. Suga, *Orientational disorder and its ordering process.* Kagaku (Kyoto), 1983. **38**: p. 599-601.

47. S.C. Mraw, R.J. Boak, and L.A. Staveley, *A calorimetric investigation of the polymorphism of potassium nitrite.* J. Chem. Thermodyn., 1978. **10**: p. 359-368.

48. S.C. Mraw and L.A. Staveley, *A calorimetric investigation of the polymorphism of cesium nitrite.* J. Chem. Thermodyn., 1976. **8**: p. 1001-1007.

49. H. Honda, M. Kenmotsu, et al., *Dynamics of Nitrite ions in ionnic plastic crystal $RbNO_2$ studied by N and Rb NMR.* Ber. Bunsenges. Phys. Chem., 1995. **99**: p. 1009-1014.

50. H. Honda, S. ishimaru, et al., *Dynamics of nitrite ions in the ionic plastic crystal TlNO$_2$ studied by ^{15}N and ^{205}Tl NMR.* Z. Naturforsch, 1995. **50a**: p. 871-875.

51. K. Moriya, T. Matsuo, and H. Suga, *Calorimetric, thermoanalytical and dielectric studies of phase transitions in ammonium nitrite.* Solid State Commun., 1988. **66**: p. 533-535.

52. H. Ono, S. Ishimaru, et al., *New Mesophases in Ionic Crystals: Piperidinium Perchlorate and Nitrate Studied by ^1H, ^2H, ^{14}N and ^{35}Cl NMR.* Chem. Phys. Letters, 1997. **275**: p. 485-490.

53. H. Ono, S. Ishimaru, et al., *Molecular Motions in Highly Disordered Solid Phases of $[(CH_3)_3NCH_2CH_3]X$ (X=ClO$_4^-$, PF$_6^-$, NO$_3^-$) Studied by ^1H, ^{19}F and ^{14}N NMR, powder X-Ray Diffraction and Differential Scanning Calorimetry.* Bull. Chem. Soc. Jpn., 1997. **70**: p. 2963-2972.

54. H. Ono, S. ishimaru, et al., *Ionic Plastic Phase in Piperidinium Hexafluorophosphate Studied by Solid NMR, X-Ray Diffraction and Thermal Measurements.* Ber. Bunsenges. Phys. Chem., 1998. **102**: p. 650-655.

55. H. Ono, S. lshimaru, et al., *^1H, ^2H, ^{19}F, ^{31}P and ^{35}Cl NMR Studies on Molecular Motions in Ionic Plastic Phases of Pyrrolidinium Perchlorate and Hexafluorophosphate.* Bull. Chem. Soc. Jpn., 1999. **72**: p. 2049-2054.

56. H. Honda, M. Kenmotsu, et al., *^{15}N and ^{133}Cs Solid NMR Studies on Ionic Dynamics in Plastic CsNO$_2$.* Z. Naturforsch, 1996. **51a**: p. 761-768.

57. H. Ishida, N. Hayama, and R. Ikeda, *Phase transitions and ionic motions including self-diffusion in solid trimethylammonium tetrafluoroborate studied by ^1H and ^{19}F.* Chem. Lett., 1992: p. 1333-1336.

58. M. Tansho, D. Nakamura, and R. Ikeda, *Cationic self-diffusion in the metastable ionic-plastic phase of CH$_3$NH$_3$Br studied by ^1H NMR.* Ber. Bunsenges. Phys. Chem., 1991. **95**: p. 1643-1646.

59. M. Hattori, S.-i. Fukada, et al., *Studies of the anisotropic self-diffusion and reorientation of butylammonium cations in the rotator phase of butylammonium chloride using ^1H magnetic resonance, electrical conductivity and thermal measurements.* J. Chem. Soc. Faraday Trans., 1990. **86**: p. 3777-3783.

60. G.J. Kabo, V.V. Diky, et al., *Thermodynamic properties, conformational composition, and phase transitions of cyclopentanol.* J. Chem. Thermodyn., 1995. **27**: p. 953-967.

61. G.J. Kabo, A.V. Blokhin, et al., *Heat Capacities and Enthalpies of Thransitions of 1-methylcyclopentanol and 1-chloro-1-methylcyclopentane in the Condensed State.* Thermochim. Acta, 1996. **290**: p. 13-30.

62. G.J. Kabo, A.V. Blokhin, et al., *Thermodynamic properties and phase transitions of 1-methylcyclohexanol and 1-chloro-1-methylcyclohexane.* Thermochim. Acta, 1998. **313**: p. 111-124.

63. R. Wagner, I,, R. Bau, et al., *Disorder and polymorphism in tetramethylammonium metaperiodate.* Inorg. Chem., 1997. **36**: p. 2564-2569.

64. H. Honda, N. Onoda-Yamamuro, et al., *Dielectric study on ionic orientational disorder in low-temperature phases of ionic plastic crystal KNO_2.* Ber. Bunsenges. Phys. Chem., 1998. **102**: p. 148-151.

65. M. Postel and J.G. Riess, *Plastic Phases in Globular Phosphorus Componds: A New Structureal Criterion for Plastic Behaviour.* J. Chemical Physics, 1977. **81**: p. 2634-2637.

66. A. Kubo, A. Yogo, et al., *Deuterium NMR Study of the Glassy Crystal Pentachloro toluene. Hadamard Quadrupole-Order Exchange NMR.* J. Phys. Chem., 1996. **100**: p. 15933-15941.

67. G.J. Kabo, A.V. Blokhin, et al., *Thermodynamic properties of adamantane and the energy states of molecules in plastic crystals for some cage hydrocarbons.* Thermochim. Acta, 2000. **345**: p. 125-133.

68. G.J. Kabo, A.A. Kozyro, et al., *Solid State Transitions of the cyclohexane derivatives and the model of energy states of molecules in plastic crystals.* Mol. Cryst. Liq. Cryst., 1999. **326**: p. 333-355.

69. V.V. Diky, N.V. Martsinovich, and A.G. Kabo, *Calculation of pseudorotational moments of intertia of cyclopentane derivatives using molecular mechanics method.* J. Phys. Chem. A, 2001. **105**: p. 4969-4973.

70. G.B. Guthrie and J.P. McCullough, *Some Observations on Phase Transformations in molecular crystals.* J. Phys. Chem. Solids, 1961. **18**: p. 53-61.

71. R.J. Webb, M.D. Lowery, et al., *Ferrocenium Hexafluorophosphate: Molecular Dynamics in the solid state.* Inorg. Chem., 1992. **31**: p. 5211-5219.

72. M.B. Charapennikau, A.V. Blokhin, et al., *Thermodynamic properties and the plastic crystal state of 2-methy-2-adamantanol.* Thermochim. Acta, 2002. **382**: p. 109-118.

73. J.E. Lennard-Jones and A.F. Devonshire, *Critical and co.ovrddot.operative phenomena. IV. Theory of disorder in solids and liquids and the process of melting.* Proc. Roy. Soc., 1939. **A170**: p. 464-484.

74. F. Affouard, J.F. Willart, and M. Descamps, *Orientationally disordered crystals: from the onset of slow dynamics to the glass transition.* J. Non-Cryst. Solids, 2002. **307-310**: p. 9-15.

75. J.W. Perram, E. Prastgaard, and S.E. R., *Lattice Model for ordering in two-dimensional plastic crystals.* Physica A, 2000. **279**.

76. C.A. Angell, L.E. Busse, et al., *Glasses and glassy crystals from molecular and molecular ionic systems.* J. Chim. Phys. Phys.-Chim. Biol., 1985. **82**: p. 267-74.

77. J.F. Willart and M. Descamps, *Relaxation and structural frustration in an orientational glassy crystal.* Prog. Theor. Phys. Suppl., 1997. **126**: p. 239-243.

78. H. Suga, *Slow relaxation processes in glassy crystals.* AIP Conf. Proc., 1992. **256**: p. 20-9.

79. K. Adachi, H. Suga, and S. Seki, *Phase changes in crystalline and glassy-crystalline cyclohexanol.* Bull. Chem. Soc. Jpn., 1968. **41**: p. 1073-1087.

80. T. Hiramoto, M. Nishii, et al., *Radiation-induced polymerization of cyclohexene sulfide in the solid state.* J. Polym. Sci., Polym. Chem. Ed., 1973. **11**: p. 2257-2263.

81. A. Gonthier-Vassal and H. Szwarc, Chem. Phys. Letters, 1986. **129**: p. 5.

82. I. Kishimoto, J.J. Pinvidic, et al., *Phase transition and glass transitions in isocyanocyclohexane studied by a polaro-calorimeter.* Proc. Jpn. Acad., Ser. B, 1991. **67**: p. 66-71.

83. M. Mizukami, H. Fujimori, and M. Oguni, *Possible emergence of plural sets of a- and b-glass transitions in orientationally disordered crystal, cyclohexanol.* Solid State Commun., 1996. **100**: p. 83-88.

84. G.P. Singh, R. Vacher, and R. Calemczuk, *Dielectric evidence for existence of two-level systems in cyclohexanol, a "glassy crystal" system.* J. Phys., Colloq., 1982. **C9**: p. 525-527.

85. D. Ceccaldi, F. Denoyer, et al., *Diffuse x-ray scattering by glassy crystalline cyclohexanol: preliminary results.* J. Phys., Lett. (Orsay, Fr.), 1980. **41**: p. L365-L368.

86. D. Andre, D. Ceccaldi, and H. Szwarc, *Glassy crystals. III: X-ray determination of the structures of the plastic and glassy crystalline phases of cyclohexanol.* J. Phys. C, 1984. **45**: p. 731-737.

87. A. Dworkin, A.H. Fuchs, et al., *Glassy crystals. Part I. NMR line-width measurements, thermally stimulated depolarization currents, and enthalpy analyses of some cyclic alcohols.* J. Phys., Lett., 1982. **43**: p. 21-27.

88. T. Wasiutynski, J. Sciesinski, and E. Sciesinska, *Kinetics of irreversible transformations in a glassy crystal studied by infrared spectroscopy.* Phase Transitions, 2001. **73**: p. 523-532.

89. E. Bonjour, R. Calemczuk, et al., *Low temperature thermal properties of cyclohexanol: a glassy crystal system.* J. Phys., Colloq., 1981. **C6**: p. 63-65.

90. P.L. Kuhns and M.S. Conradi, *NMR study of molecular motions in cyclohexanol, a glass-forming rotor crystal.* J. Chem. Phys., 1984. **80**: p. 5851-5858.

91. T. Eguchi, G. Soda, and H. Chihara, *On the state of aggregation of cyclohexanol in a glassy crystalline state.* J. Non-Cryst. Solids, 1976. **21**: p. 143-145.

92. O.R. Andersson, Russell G.; Baeckstroem, Gunnar., *Thermal conductivity of crystalline and glassy crystal cyclohexanol under pressure.* Mol. Phys., 1989. **66**: p. 619-635.

93. D.M. Synderman, J.M. Adams, et al., *Solid Phases and Phase Transitions of Cycloheptane.* J. Phys. Chem., 1994. **98**: p. 6234-6236.

94. K. Adachi, H. Suga, and S. Seki, *Calorimetric study of the glassy state. VII. Phase changes between the crystalline phases of cycloheptanol with various degrees of stability.* Bull. Chem. Soc. Jap., 1972. **45**: p. 1960-1972.

95. J. Haines and D.F.R. Gilson, *A vibrational spectroscopic investigation of solid 1,3,5-cycloheptatriene.* Phase Transitions, 1990. **21**: p. 1-9.

96. Y. Huang, D.F.R. Gilson, and I.S. Butler, *Vibrational spectroscopic studies of phase transitions in solid cyclooctane.* J. Phys. Chem., 1991. **95**: p. 5051-5054.

97. M. Shablakh, L.A. Dissado, and R.M. Hill, *Structure and dipole relaxation mechanisms in the cyclic alcohols cyclopentanol to cyclooctanol.* J. Chem. Soc. Faraday Trans., 1983. **79**: p. 369-417.

98. O. Andersson and R.G. Ross, *Thermal conductivity, heat capacity, and phase diagram of cyclooctanol in liquid, solid, and glassy crystal states under high pressure.* Mol. Phys., 1990. **71**: p. 523-539.

99. K. Adachi, H. Suga, and S. Seki, *Calorimetric study of the glassy state. VI. Phase changes in crystalline and glassy-crystalline 2,3-dimethylbutane.* Bull. Chem. Soc. Jpn., 1971. **44**: p. 78-89.

100. M. El Adib, M. Descamps, and N.B. Chanh, *X-ray kinetic study of glassy crystal formation in adamantane derivatives: time-temperature-transformation curves and crystal size effect.* Phase Transitions, 1989. **14**: p. 85-96.

101. M. Foulon, J.P. Amoureux, et al., *Different aspects of an interesting glassy crystal: 1-cyanoadamantane.* J. Phys. C, 1984. **17**: p. 4213-4229.

102. M. Foulon, J.P. Amoureux, et al., *Evidence of a "glassy crystal" phase obtained by the quenching of the plastic phase of the cyanoadamantane.* J. Phys. C, 1983. **16**: p. L265-L269.

103. Y. Guinet and J.L. Sauvajol, *Temperature dependence of the Raman-active modes in the low-temperature phase of 1-cyanoadamantane.* J. Phys. C: Solid State Phys., 1988. **21**: p. 3827-42.

104. J. Lefebvre, J.P. Rolland, et al., *Coherent neutron scattering on the 'glassy crystal' of cyanoadamantane.* J. Phys. C, 1985. **18**: p. 241-55.

105. M. Descamps, M. Bee, et al., *Dynamics and kinetics in glassy crystal cyanoadamantane.* Quasielastic Neutron Scattering Proc., 1994: p. 107-127.

106. M. Descamps, G. Odou, and J.C. Caucheteux, *First observation of molecular and volume relaxation in glassy crystal cyanoadamantane.* J. Phys., Lett., 1985. **46**: p. 261-5.

107. R. Decressain, E. Cochin, and L. Carpentier, *Dynamics NMR investigations of a glassy crystal confined in porous materials.* J. Phys. IV, 2000. **10**: p. r7/299-Pr7/303.

108. J.P. Bonnet, M. Boissier, et al., *"Glassy" and plastic crystals of cyanoadamantane: a Brillouin scattering investigation.* J. Phys., Lett., 1985. **46**: p. 617-21.

109. M. Descamps, C. Caucheteux, et al., *Local molecular order in the glassy crystalline phase of cyanoadamantane: diffuse x-ray scattering analysis.* J. Phys., Lett., 1984. **45**: p. 719-727.

110. M. Descamps, C. Caucheteux, and G. Odou, *Local order and nonequilibrium behavior in glassy crystal cyanoadamantane.* J. Phys., Colloq., 1985. **C8**: p. 329-333.

111. M. Descamps and C. Caucheteux, *The mechanisms of annealing and glass-like transition in a glassy plastic phase: cyanoadamantane.* Stud. Phys. Theor. Chem., 1987. **46**: p. 333-339.

112. L. Bistricic, G. Baranovic, and V. Volovsek, *Low-temperature Raman spectra of 2-adamantanone in different phases.* J. Mol. Struct., 1999. **482-483**: p. 661-664.

113. M. Descamps, J.F. Willart, and O. Delcourt, *Molecular and structural relaxations in a glassy crystal.* Physica A (Amsterdam), 1993. **201**: p. 346-362.

114. J.P. Amoureux, R. Decressain, et al., *Molecular motions in glassy crystal cyanoadamantane: a proton spin-lattice relaxation study.* J. Phys. II, 1992. **2**: p. 249-259.

115. M. Bee, P. Derollez, et al., *Molecular motions in the glassy crystalline phase of 1-cyanoadamantane.* Physica B (Amsterdam), 1992. **180-181**: p. 655-657.

116. M. Bee, P. Derollez, and M. Descamps, *Relaxations near the glass transition of a molecular crystal.* J. Non-Cryst. Solids, 1994. **172-174**: p. 520-530.

117. K. Pathmanathan and G.P. Johari, *Molecular relaxations in a rigid molecular glassy crystal.* J. Phys. C: Solid State Phys., 1985. **18**: p. 6535-6545.

118. J.P. Rolland and J.L. Sauvajol, *Raman studies of orientational glassy phase: the 1-cyanoadamantane glassy crystal phase.* J. Phys. C: Solid State Phys., 1986. **19**: p. 3475-3486.

119. M. Descamps and J.F. Willart, *Slow non-equilibrium process in a glassy crystal.* J. Non-Cryst. Solids, 1994. **172-174**: p. 510-519.

120. J.F. Willart, M. Descamps, and J.C. van Miltenburg, *Structural signature of the configurational entropy change during the glass formation of plastic crystal cyanoadamantane.* J. Chem. Phys., 2000. **112**: p. 10992-10997.

121. F. Affouard and M. Descamps, *Two-step rotational relaxation in glassy crystal cyanoadamantane.* Phys. Rev. B: Condens. Matter Mater. Phys., 1999. **59**: p. R9011-R9014.

122. M. Descamps, J.F. Willart, et al., *The implication of the lattice in the nonequilibrium behavior of a glassy crystal.* J. Phys. I, 1992. **2**: p. 813-827.

123. M. Descamps and C. Caucheteux, *Kinetics of ordering and cluster stability: nondiffusive transformation in a glassy crystal.* Dyn. Ordering Processes Condens. Matter, [Proc. Int. Symp.], 1988: p. 257-262.

124. M. Descamps, J.F. Willart, et al., *Metastable state in glassy crystal cyanoadamantane: experiments and simulations.* J. Non-Cryst. Solids, 1998. **235-237**: p. 559-566.

125. F. Affouard, A. Hedoux, et al., *Indication for a change of dynamics in plastic crystal chloroadamantane: Raman scattering experiment and molecular dynamics simulation.* J. Phys.: Condens. Matter, 2001. **13**: p. 7237-7248.

126. N.T. Kawai, D.F.R. Gilson, and I.S. Butler, *Phase transitions in adamantane derivatives: 1-fluoroadamantane.* Can. J. Chem., 1991. **69**: p. 1758-1765.

- 271 -

127. E.F. Westrum and S. Henriquez, *Interphase transitions and thermophysics of ortho- and meta-carboranes*. Mol. Cryst. Liq. Cryst., 1976. **32**: p. 31-35.

128. M. Winterlich, H. Zimmermann, and R. Bohmer, *Phase transition kinetics and reorientational dynamics of the plastic crystal meta-carborane studied by deuteron NMR*. J. Non-Cryst. Solids, 2002. **307-310**: p. 442-448.

129. K. Saito, H. Kobayashi, et al., *Anomalous lattice heat capacity of orientationally glassy crystal of p-chloronitrobenzene at low temperatures*. Solid State Commun., 2001. **118**: p. 611-614.

130. B. Sundqvist, O. Andersson, et al. *Fullerenes under pressure: Structure, order, and disorder*. in *High Pressure Sci. Technol., Proc.* 1996.

131. T. Matsuo, H. Suga, et al., *The heat capacity of solid C60 fullerene*. Solid State Commun., 1992. **83**: p. 711-15.

132. B. Kuchta, L. Firlej, et al., *A computer simulation study of short-range order in metastable hcp. phase of solid nitrogen*. J. Low Temp. Phys., 2001. **122**: p. 211-219.

133. O. Haida, H. Suga, and S. Seki, *Calorimetric study of the glassy state. XII. Plural glass-transition phenomena of ethanol*. J. Chem. Thermodyn., 1977. **9**: p. 1133-1148.

134. O. Haida, H. Suga, and S. Seki, *Realization of glassy liquid and glassy crystal of ethanol*. Proc. Jap. Acad., 1972. **48**: p. 683-686.

135. M.A. Ramos, Q.-W. Zou, et al., *Low-temperature thermal properties of molecular glasses*. Czech. J. Phys., 1996. **46**: p. 2235-2236.

136. T. Eguchi, G. Soda, and H. Chihara, *Molecular motions in polymorphic forms of ethanol as studied by nuclear magnetic resonance*. Mol. Phys., 1980. **40**: p. 681-696.

137. S. Benkhof, A. Kudlik, et al., *Two glass transitions in ethanol: a comparative dielectric relaxation study of the supercooled liquid and the plastic crystal*. J. Phys.: Condens. Matter, 1998. **10**: p. 8155-8171.

138. K. Morishige and K. Kawano, *Freezing and melting of methanol in a single cylindrical pore: Dynamical supercooling and vitrification of methanol*. J. Chem. Phys., 2000. **112**: p. 11023-11029.

139. M. Barrio, J. Font, et al., *Glassy state in 2-amino-2-methyl-1,3-propanediol plastic crystal*. J. Therm. Anal., 1994. **41**: p. 1171-5.

140. M. Barrio, J. Font, et al., *Polymorphism in 2-amino-2-methyl-1,3-propanediol plastic crystal*. J. Phase Equilib., 1991. **12**: p. 409-15.

141. A.H. Fuchs, J. Virlet, et al., *Glassy crystals. V: structural and dynamic studies of large amplitude molecular motions*. J. Chim. Phys. Phys.-Chim. Biol., 1985. **82**: p. 293-303.

142. K. Binder, *From orientational glasses to structural glasses: What computer simulations have contributed to understand experiments*. J. Non-Cryst. Solids, 2002. **307-310**: p. 1-8.

143. H. Szwarc and C. Bessada, *Glassy crystals: correlation between molecular symmetry and glass transition.* Thermochim. Acta, 1995. **266**: p. 1-8.

144. H. Suga, *Thermodynamic aspects of glassy crystals. Approaching the equilibrium glass.* Ann. N. Y. Acad. Sci., 1986. **484**: p. 248-263.

145. C. Bessada, A.H. Fuchs, et al., *Dynamics of glassy crystals. A critical review of some current phenomenological hypotheses about molecular glasses.* Stud. Phys. Theor. Chem., 1987. **46**: p. 317-323.

146. J.-i. Koga and T. Odagaki, *Stochastic Orientation Relaxation of a Plastic Crystal.* J. Phys. Chem. B, 2000. **104**: p. 3808-3811.

147. R. Brand, P. Lunkenheimer, and A. Loidl, *Relaxation dynamics in plastic crystals.* J. Chem. Phys., 2002. **116**: p. 10386-10401.

148. C.A. Angell, A. Dworkin, et al., *Strong and Fragile Plastic Crystals.* J. de Chimie Physique, 1985. **82**: p. 773-777.

149. C.A. Angell, *Perspective on the glass transition.* J. Phys. Chem. Solids, 1988. **49**: p. 863-871.

150. O. Yamamuro, M. Ishikawa, et al., *Thermodynamic approach to glass transitions of plastically crystalline Cyanoadamantane and Isocyanocyclohexane.* J. Phys. Soc. Jp., 1999. **68**: p. 2969-2976.

151. C.A. Angell, *The amorphous state equivalent of crystallization: new glass types by first order transition from liquids, crystals, and biopolymers.* Solid State Sci., 2000. **2**: p. 791-805.

152. S. Mrowec, *Defects and Diffusion in Solids An Introduction.* Materials Science Monographs, ed. C. Laird. Vol. 5. 1980, Warszawa: Polish Scientific Publishers. 466.

153. J.N. Sherwood, *Lattice Defects, Self-Diffusion, and the Plasticity of Plastic Crystals*, in *The Plastically Crystalline State*, J.N. Sherwood, Editor. 1979, Wiley-Interscience. p. 39-84.

154. R.H. Baughman and D. Turnbull, *Vacancy Formation Parameters in Organic Crystals.* J. Phys. Chem. Solids, 1971. **32**: p. 1375-1394.

155. A.V. Chadwick, *Point defects and diffusion in molecular solids.* NATO Advanced Study Institutes Series, Series B, Physics, 1983. **97**: p. 285-320.

156. J.N. Sherwood, *Lattice Defects in Organic Crystals.* Mol. Cryst. Liq. Cryst., 1969. **9**: p. 37-57.

157. D. Lightbody, J.N. Sherwood, and M. Eldrup, *Vacancy formation energies in plastic crystals using positron annihilation techniques.* Mol. Cryst. Liq. Cryst., 1983. **96**: p. 197-210.

158. H.M. Hawthorne and J.N. Sherwood, *Lattice defects in plastic organic solids Part 1. --Self-diffusion and plastic deformation in pivalic acid, hexamethylethane and cyclohexane.* Trans. Faraday Soc., 1970. **66**: p. 1783-1791.

159. M. Eldrup, D. Lightbody, and J.N. Sherwood, *The vacancy formation energy in crystalline adamantane determined by positron annihilation techniques.* Chem. Phys. Lett., 1980. **70**: p. 487-491.

160. J.R. Green and D.R. Wheeler, *X-ray investigation of some plastic crystals. II Density of vacancies in cyclohexane, cyclohexanol, and dl-camphene.* Mol. Cryst. Liq. Cryst., 1969. **6**: p. 13-21.

161. H.M. Hawthorne and J.N. Sherwood, *Lattice defects in plastic organic solids. 2. Anomalous self-diffusion in succinonitrile.* Trans. Faraday Soc., 1970. **66**: p. 1792-1798.

162. M. Meyer and C. Marhic, *Molecular Dynamics study of Molecular Rotational Processes in the High Temperature phase of Adamantane.* Stud. Phys. Theor. Chem., 1987. **46**: p. 719-724.

163. W. Callister, D., *Materials Science and Engineering: An Introduction.* 1997: John Wiley & Sons, Inc. 852.

164. G.J. Ogilvie and P.M. Robinson, *Comments on "lattice defects in plastic organic solids".* Mol. Cryst. Liq. Cryst., 1971. **12**: p. 379-384.

165. B.S. Shah and J.N. Sherwood, *Lattice Defects in Plastic Organic Crystals part 6. -- Dislocation Etching in Adamantane.* Trans. Faraday Soc., 1971. **67**: p. 1200-1202.

166. J. Sun, D.R. MacFarlane, and M. Forsyth, *Conductive plastic crystal phases of the 1-alkyl-2-methyl-pyrrolinium TFSA salts.* Solid State Ionics, 2002. **148**: p. 145-151.

167. L. Nilsson, J.O. Thomas, and B.C. Tofield, *The structure of the high-temperature solid electrolyte lithium sulphate at 908K.* J. Phys. C: Solid State Phys., 1980. **13**: p. 6441-6451.

168. A. Lunden, *Evidence for and against the paddle wheel mechanism of ion transport in superionic sulphate phases.* Solid State Commun., 1988. **65**: p. 1237-1240.

169. R. Aronsson, B. Jansson, et al., *Fast Ion conductors with rotating sulphate ions.* J. De Phys., 1980. **C6**: p. 35-37.

170. A. Lunden, *Enhancement of cation Mobility in Some sulphate phases due to a paddle-wheel mechanism.* Solid State Ionics, 1988. **28-30**: p. 163-167.

171. A. Lunden, *Cation transport mechanisms in high temperature rotator phases of sulfates.* J. Solid State Chem., 1993. **107**: p. 296-298.

172. A. Lunden, *On the paddle-wheel mechanism for cation conduction in lithium sulphate.* Z. Naturforsch, 1995. **50a**: p. 1067-1076.

173. P. Depondt and W. Breymann, *Orientational-translation and orientation-orientation correlations in neopentane plastic crystals. Computer simulation.* Mol. Phys., 1996. **87**: p. 1015-1037.

174. S. Galam and P. Depondt, *Rotational State and Self-dilution vs. Translational disorder in plastic Neopentane.* Europhys. Lett., 1988. **5**: p. 43-47.

175. E.A. Secco, *Fast cation conductivity by percolation in alkali sulfate compositions.* Solid State Ionics, 1988. **28-30**: p. 168-172.

176. E.A. Secco, *Ion transport in sulfates: Percolation Mechanism versus paddle-Wheel Mechanism.* Solid State Commun., 1988. **66**: p. 921-923.

177. E.A. Secco, *Comments on electrical conductivity and phase diagram of the system Li_2SO_4-Li_3PO_4.* Solid State Ionics, 1991. **45**: p. 335-336.

178. E.A. Secco, *Paddle-wheel versus percolation model.* Solid State Ionics, 1993. **60**: p. 233-235.

179. E.A. Secco, *Paddle Wheel Mechanism in Lithium Sulfates: Arguments in Defense and Evidence Against.* J. Solid State Chem., 1992. **96**: p. 366-375.

180. A. Lunden, *Paddle-wheel versus percolation model, revisited.* Solid State Ionics, 1994. **68**: p. 77-80.

181. A. Lunden, *On the ionic conductivity and phase transition in the Li_2SO_4-Li_2WO_4 system and their relation to ion transport mechanism.* J. Solid State Chem., 1991. **90**: p. 179-184.

182. B. Jansson and C.A. Sjoblom, *Thermal expansion of alkali metal sulfate mixtures.* Z. Naturforsch, 1970. **25a**: p. 1115-1119.

183. R. Kaber, L. Nilsson, et al., *A single-crystal neutron diffraction study of the structure of the high-temperature rotor phase of lithium sulphate.* J. Phys.: Condens. Matter, 1992. **4**: p. 1925-1933.

184. L. Borjesson and L.M. Torell, *Reorientational motion in superionic sulfates: A raman Linewidth study.* Phys. Rev. B, 1985. **32**: p. 2471-2477.

185. A. Kvist and A. Lunden, *Electrical conductivity of solid and molten Li_2SO_4.* Z. Naturforsch, 1965. **20a**: p. 235-238.

186. R. Tarneberg and A. Lunden, *Ion diffusion in the high temperature phases Li_2SO_4, $LiNaSO_4$, $LiAgSO_4$ and $Li_4Zn(SO_4)_3$.* Solid State Ionics, 1996. **90**: p. 209-220.

187. A. Lunden, *Isotopic effect during electrolytic transport of lithium ions in solid lithium sulfate.* Z. Naturforsch, 1960. **15a**: p. 365.

188. A. Lunden, *Isotope transfer, external transfer, and self-diffusion of Li in solid Li_2SO_4 at 600-700°.* Z. Naturforsch, 1962. **17a**: p. 142-146.

189. R. Aronsson, L. Borjesson, and L.M. Torell, *Low frequency Raman Scattering in superionic Li_2SO_4.* Phys. Lett., 1983. **98A**: p. 205-207.

190. R.W. Impey, M.L. Klein, and I.R. McDonald, *Structural and dynamic properties of lithium sulfate in its solid electrolyte form.* J. Chem. Phys., 1985. **82**: p. 4690-4698.

191. B.E. Mellander and D. Lazarus, *Electric conductivity and activation volume for a-Li_2SO_4.* Phys. Rev. B, 1985. **31**: p. 6801-6803.

192. R.W. Impey, M.L. Klein, and I.R. McDonald, *Structure of the fast-ion conducting phase of solid lithium sulfate.* J. Phys. C, 1984. **17**: p. 3941-3944.

193. M.A.K.L. Dissanayake, M.A. Careem, et al., *Ionic conductivity of solid solutions of lithium sulfate (a-Li$_2$SO$_4$) with lithium tungstate (Li$_2$WO$_4$): strong evidence for the paddle wheel mechanism of ion transport.* Solid State Ionics, 1991. **48**: p. 277-281.

194. R. Tarneberg and B.E. Mellander, *Ion Transport in High Temperature Rotator Phase Solid Electrolytes.* Solid State Ionics, 1997. **98**: p. 175-183.

195. R.P. Gunawardane, M.A.K.L. Dissayake, and F.P. Glasser, *Phase Equiiria in the system Li$_2$SO$_4$-Li$_2$WO$_4$.* Br. Ceram. Trans. J., 1989. **88**: p. 45-46.

196. M. Touboul, N. Sephar, and M. Quarton, *Electrical Conductivity and Phase Diagram of the System Li$_2$SO$_4$-Li$_3$PO$_4$.* Solid State Ionics, 1990. **38**: p. 225-229.

197. M. Touboul and M. Quarton, *Reply to the comments on electrical conductivity and phase diagram of the ststem Li$_2$SO$_4$-Li$_3$PO$_4$.* Solid State Ionics, 1991. **45**: p. 337-338.

198. D. Wilmer, R.D. Banhatti, et al., *Anion reorientation in Na$_3$PO$_4$.* Physica B., 1998. **241-243**: p. 338-340.

199. D. Wilmer, K. Funke, et al., *Anion reorientation in an ion conducting plastic crystal -- coherent quasielestic neutron scattering from sodium ortho-phosphate.* Physica B., 1999. **266**: p. 60-68.

200. M. Witschas, H. Eckert, et al., *Anion rotation and cation diffusion in low temperature sodium orthophosphate: results from solid state NMR.* J. Phys. Chem. A, 2001. **105**: p. 6808-6816.

201. M. Witschas, H. Eckert, et al., *Anion Rotation and Cation Transport in the Rotor Phase α-Sodium Orthophosphate: Paddle-Wheel Mechanism Redefined in View of New Experimental Results.* Zeitschrift fur Physikalische, 2000. **214**: p. 643-673.

202. R.D. Banhatti, M. Witschas, et al. *Studies of ion dynamics in a-Na$_3$PO$_4$: Paddle-wheel mechanism better defined.* in *Solid State Ionics.* 1998. Singapore: World Scientific.

203. K. Funke, D. Wilmer, et al., *Interplay between anion rotation and cation transport in plastic high-temperature phase of sodium ortho-phosphate.* Mater. Res. Soc. Symp. Froc., 1998. **527**: p. 469-480.

204. M. Witschas and E. Hellmut, *^{31}P and ^{23}Na solid state NMR studies of cation Dynamics in HT-Sodium Orthophosphate and the solid solutions (Na$_2$SO$_4$)$_x$-(Na$_3$PO$_4$)$_{1-x}$.* J. Phys. Chem. A, 1999. **103**: p. 10764-10775.

205. Y. Furukawa, H. Nagase, et al., *Cationic self-diffusion in ionic plastic phases of thallium nitrite and nitrate and in Thallium thiocyanate.* Bull. Chem. Soc. Jap., 1991. **64**: p. 3105-3108.

206. M. Kenmotsu, H. Honda, et al., *Ionic dynamics in plastic crystal KNO$_2$ studied by [39]K and ^{15}N NMR.* Z. Naturforsch, 1993. **49a**: p. 247-252.

207. Y. Furukawa and H. Kiriyama, *magnetic relaxation of thallium nuclei and ionic motion in solid thallium(I) nitrite*. Chem. Phys. Lett., 1982. **93**: p. 617-620.

208. R. Feyerherm, M.F. Collins, and G.P. Johari, *Neutron diffraction study of orientational freezing in TlNO₂ and CsNO₂*. Phys. Rev., 1998. **57**: p. 11125-11131.

209. G. Dosseh, C. Fressigne, and A.H. Fuchs, *Premelting in Orientationally Disordered Molecular Crystals A Re-appraisal*. J. Phys. Chem. Solids, 1992. **53**: p. 203-209.

210. G. Dosseh and A.H. Fuchs, *The sites of premelting in Organic Compound*. Z. Naturforsch, 1991. **46a**: p. 917-919.

211. J. Bleay, P.W. Salthouse, and J.N. Sherwood, *Self-diffusion in crystalline adamantane*. Phil. Mag., 1977. **36**: p. 885-892.

212. M. Brissaud-Lancin, M. Meyer, and J. Philibert, *Self-diffusion in the plastic phase of pivalic acid (2,2-dimethyl-propanoic acid). I. Diffusion coefficients and isotope effects*. J. Phys. Chem. Solids, 1982. **43**: p. 97-103.

213. S. Stapf and R. Kimmich, *Translational versus rotational molecular dynamics in plastic crystals studied by NMR relaxometry and diffusometry*. Mol. Phys., 1997. **92**: p. 1051-1060.

214. R.N. Brown and A.C. McLaren, *On the mechanism of the thermal transformations in solid ammonium nitrate*. Proc. Roy. Soc. A., 1962. **266**: p. 329-343.

215. R. Wasylishen, E., *Motion of the nitrate ion in the solid I and II phases of ammonium nitrate using nitrogen NMR*. Spectrochimica Acta, 1983. **40A**: p. 115-116.

216. S. Albert and H.S. Gutowsky, *Nuclear relaxation and spin exchange in ammonium hexafluorophosphate (NH₄PF₆)*. J. Chem. Phys., 1973. **59**: p. 3585-3594.

217. D.E. O'Reilly, E. Mark Peterson, and T. Tsang, *Nuclear magnetic resonance and nonexponential spin-lattice relaxation in ferroelectric ammonium fluoroberyllate*. Phys. Rev., 1967. **160**: p. 333-342.

218. Y. Furukawa and H. Kiriyama, *Molecular motion in ammonium Hydrogendifluoride studied by pulse NMR*. Bull. Chem. Soc. Jpn., 1979. **52**: p. 339-343.

219. S. Jurga and H.W. Spiess, *Interrelation between molecular motions and phase transitions in monomethylammonium perchlorate: a study by DSC, proton and deuteron NMR*. Z. Naturforsch, 1985. **40a**: p. 602-610.

220. H. Ishida, R. Ikeda, and D. Nakamura, *premelting state of methylammonium nitrate and perchlorate as revealed by ¹H NMR studies*. Chem. Lett., 1982: p. 1943-1946.

221. H. Ishida, R. Ikeda, and D. Nakamura, *Self-diffusion of methylammonium cations in the high-temperature solid phase of CH₃NH₃NO₃*. 1985.

222. T. Tanabe, D. Nakamura, and R. Ikeda, *Novel ionic plastic phase of [(CH₃)₄]SCN ontainable above 455K studied by proton magnetic resonance, electrical conductivity and thermal measurements*. J. Chem. Soc. Faraday Trans., 1991. **87**: p. 987-990.

- 277 -

223. S. Sato, M. Kondo, et al., *Ionic dynamics in [(CH₃)₄N]SbF₆ crystals as studied by the temperature dependence of ^1H and ^{19}F NMR spin-lattice relaxation times.* Ber. Bunsenges. Phys. Chem., 1989. **93**: p. 450-454.

224. H. Ishida, K. Takagi, and R. Ikeda, *An ionic plastic Phase of 1,1-Dimethylhydrazinium Tetrafluoroborate Revealed by ^1H and ^{19}F NMR and Thermal Measurements.* Chem. Lett., 1992: p. 605-608.

225. M. Gosniowska, Z. Ciunik, et al., *Structure and phase transitions in tetremethylammonium tetrabromoindate (III) and tetraethylammonium tetrabromoindate (III) crystals.* J. Molecular Structure, 2000. **555**: p. 243-255.

226. S. Jurga, *Molecular motions and polymorphic phase transitions in (CH₃)₄NClO₄ and (CH₃)₃NHClO₄ as studied by NMR.* Phys. Stat. Sol. (a), 1984. **81**: p. 77-85.

227. H. Ishida, N. NMatsuhashi, et al., *^1H nuclear magnetic resonance studies on cationic reorientation and translational self-diffusion in two solid phases, including a new high-temperature phase of methylammonium sulphate.* J. Chem. Soc. Faraday Trans. 1, 1989. **85**: p. 111-120.

228. S.-i. Fukada, H. Yamamoto, et al., *Hydrogen-1 nuclear magnetic resonance, differential thermal analysis, X-ray powder diffraction and electrical conductivity studies on the motion of cations, including self-diffusion in crystals of propylammonium chloride and brpmide as well as thier N-deuterated analogues.* J. Chem. Soc. Faraday Trans., 1, 1987. **83**: p. 3207-3222.

229. S. Iwai, R. Ikeda, and D. Nakamura, *^1H nuclear magnetic resonance, differential scanning calorimetry, and electrical conductivity studies on the phase transitions of pethylammonium chloride and the cation self-diffusion in its rotator phase.* Can. J. Chem., 1988. **66**: p. 1961-1969.

230. S. Iwai, M. Hattori, et al., *Ionic dynamics in the rotator phase of n-alkylammonium chlorides (C₆-C₁₀), studied by ^1H nuclear magnetic resonance, electrical conductivity and thermal measurements.* J. Chem. Soc. Faraday Trans., 1993. **89**: p. 827-831.

231. T. Shimizu, S. Tanaka, et al., *New rotator phase revealed in di-n-alkylammonium bromides studied by solid-state NMR, powder XRD, electric conductivity and thermal measurements.* J. Chem. Soc. Faraday Trans., 1997. **93**: p. 321-326.

232. S. Jurga, G.S. Harbison, et al., *Static and MAS ^{35}Cl NMR and Molecular Motions of ClO₄⁻ Ions in the Various Phases of Multimethylammonium Perchlorates.* Ber. Bunsenges. Phys. Chem., 1986. **90**: p. 1153-1159.

233. S. Jurga and H.W. Spiess, *Phase transitions and molecualr motion in dimethylammonium perchlorate as revealed by DSC, proton and deuteron NMR.* Ber. Bunsenges. Phys. Chem., 1985. **89**.

234. M. Tansho, Y. Furukawa, et al., *Cationic self-diffusion in the highest-temperature solid phases of ammonium chloride and bromide studied by ^1H NMR.* Ber. Bunsenges. Phys. Chem., 1992. **96**: p. 550-553.

235. D.R. MacFarlane, P. Meakin, et al., *Pyrrolidinium Imides: A New Family of Molten Salts and Conductive Plastic Crystal Phases.* J. Phys. Chem. B, 1999. **103**: p. 4164-4170.

236. J. Sun, D.R. MacFarlane, and M. Forsyth, *Hydroxide-doped plastic crystal electrolytes based on pyrrolidinium imide salts.* Solid State Ionics, [Proc. Asian Conf.], 7th, 2000: p. 663-667.

237. J. Sun, D.R. MacFarlane, and M. Forsyth, *N,N-dimethylpyrrolidinium hydroxide:a highly conductive solid materila at ambient temperature.* J. Mater. Chem., 2001. **11**: p. 2940-2942.

238. J. Golding, N. Hamid, et al., *N-Methyl-N-alkylpyrrolidinium Hexafluorophosphate Salts: Novel Molten Salts and Plastic Crystal Phases.* Chem. Mater., 2001. **13**: p. 558-564.

239. S. Forsyth, J. Golding, et al., *N-methyl-N-alkylpyrrolidinium tetrafluoroborate salts: ionic solvents and solid electrolytes.* Electrochim. Acta, 2001. **46**: p. 1753-1757.

240. J. Efthimiadis, S.J. Pas, et al., *Structure and transport properties in an N,N-substituted pyrrolidinium tetrafluoroborate plastic crystal system.* Solid State Ionics, 2002. **154-155**: p. 279-284.

241. J. Nowinski, L.,, P. Lightfoot, and P. Bruce, G., *Structure of LiN(CF₃SO₂)₂, a novel salt for electrochemistry.* J. Mater. Chem., 1994. **4**: p. 1579-1580.

242. P. Bonhote, A.-P. Dias, et al., *Hydrophobic, highly conductive ambient-temperature molten salts.* Inorg. Chem., 1996. **35**: p. 1168-1178.

243. K. Naoi, M. Mori, et al., *The surface film form on a lithium metal electrode in a new imide electrolyte, lith.   bis(perfluoroethylsulfonylimide) [LiN(C₂F₅SO₂)₂].* J. Electrochem. Soc., 1999. **146**: p. 462-469.

244. N. Boden, *NMR Studies of Plastic Crystals*, in *The Plastically Crystalline State*, J.N. Sherwood, Editor. 1979, Wiley-Interscience.

245. T.C. Farrar and E.D. Becker, *Pulse and Fourier Transform NMR: Introduction to Theory and Methods.* 1971, New York, USA: Academic press, Inc.

246. E. Fukushima and S.B.W. Roeder, *Experimental Pulse NMR: A Nuts and Bolts Approach.* 1981, Massachusette, USA: Addison-Wesley Publishing Company, Inc.

247. B.C. Gerstein and C.R. Dybowski, *Transient Techniques in NMR of Solids: An Introduction to Theory and Practice.* 1985, Oriando, USA: Academic Press, Inc.

248. A. Abragam, *The Principles of Nuclear Magnetism.* 1961: Oxford University Press.

249. J.K. Choi, *Nuclear Magnetic Resonance Studies of Hydrogen-Bonding and Molecular Dynamics in Some Organic Plastical Crystals*, in *Dept. of Chem.* 1972, Nothern Illinois University. p. 154.

250. T.C. Moore, *Nuclear Magnetic Resonance of Plastic Crystals, Liquid Crystals and Model Bioligical Membranes.* 1981, The University of Texas at Austin. p. 238.

251. J.H. Van Vleck, *the dipolar broadening of magnetic resonance line in crystal.* Phys. Rev., 1948. **74**: p. 1168-1183.

252. R.A. Petrick, *Dielectric and Acoustic Studies*, in *The plastically Crystalline State*, J.N. Sherwood, Editor. 1979, Wiley-Interscienc. p. 123-145.

253. M. Szostak, M., G. Wojcik, et al., *^1H-NMR, dielectric and calorimetric studies of molecular motions in m-nitroaniline crystals.* Chem. Phys., 1998. **229**: p. 275-284.

254. A.S. Nowick, V. Vaysleyb, and I. Kuskovsky, *Universal Dielectric Response of Variously Doped CeO_2 Ionically Conducting Ceramics.* Physical Review B, 1998. **58**: p. 8398-8406.

255. J.M. Adams, D.M. Snyderman, and M.S. Conradi, *The solid phases of cyclooctanone studied by thermal, nuclear magnetic resonance, and dielectric techniques.* J. Phys. Chem., 1993. **97**: p. 11092-11095.

256. J.P. Sethna, *Glassy crystals. Low-frequency and low-temperature properties.* Ann. N. Y. Acad. Sci., 1986. **484**: p. 130-49.

257. J.F. Willart, M. Descamps, et al., *High and low frequency .beta. relaxation in a glassy crystal.* Non Equilib. Phenom. Supercooled Fluids, Glasses Amorphous Mater., Proc. Workshop, 1996: p. 327-328.

258. C.P. Smyth, *Dielectric Evidence of Molecular Rotation in Solids.* J. Phys. Chem. Solids, 1961. **18**: p. 40-45.

259. A.K. Jonscher, *The universal dielectric response: A review of data and their new interpretation.* Physics of Thin Film, 1980. **11**: p. 205-317.

260. D.P. Almond, A.R. West, and R.J. Grant, *Temperature dependence of the AC conductivity of Na β-alumina.* Solid State Commun., 1982. **44**: p. 1277-1280.

261. A.K. Jonscher, *The 'universal' dielectric response.* Nature, 1977. **267**: p. 673-679.

262. D. Chandra, J. Helms, H., and A. Majumdar, *Ionic conductivity in ordered and disordered phases of plastic crystals.* J. Electrochem. Soc., 1994. **141**: p. 1921-1927.

263. J. Helms, H., A. Majumdar, and D. Chandra, *AC conductivities of Neopentyiglycol and 2-Amino-2-methyl-1,3-Propanediol.* J. Electrochem. Soc., 1993. **140**: p. 1048-1055.

264. D.P. Almond, C.C. Hunter, and A.R. West, *The extraction of ionic conductivities and hopping rates from ac conductivity data.* J. Mater. Sci., 1984. **19**: p. 3236-3248.

265. D.P. Almond, G.K. Duncan, and A.R. West, *The determination of hopping rates and carrier concentrations in ionic conductors by a new analysis of AC conductivity.* Solid State Ionics, 1983. **8**: p. 159-164.

266. A.V. Vaysleyb, *Dynamic cluster model of the AC conductivity of crystalline materials and glasses.* Phys. Rev. B, 1998. **58**: p. 8407-8410.

267. J.R. Macdonald, *Impedance Spectroscopy: Emphasizing solid materials and systems*, ed. J.R. Macdonald. 1987: John Wiley & Sons, Inc. 346.

268. K. Nairn, M., *Lithium ion conducting composites*, in *Department of Materials Engineering*. 2000, Monash University. p. 275.

269. E. Hampton, N.C. Lockhart, and J.N. Sherwood, *Temperature dependence of self-diffusion in adamantane*. Chem. Phys. Lett., 1973. **21**: p. 191-193.

270. A.V. Chadwick and J.W. Forrest, *Radiotracer studies of self-diffusion in the plastic solids norbornylene and norbornane*. J. Chem. Soc. Faraday Trans. 1, 1978. **74**: p. 2562-2569.

271. E.M. Hampton and J.N. Sherwood, *Isotope-mass-effect and self-diffusion in crystalline naphthalene*. J. Chem. Soc. Faraday Trans. 1, 1975. **71**: p. 1392-1395.

272. R. Freer and J.N. Sherwood, *Diffusion in organic liquids. Part 2. Isotope-mass effects in self-diffusion in benzene and cyclohexane*. J. Chem. Soc. Faraday Trans. 1, 1980. **76**: p. 1030-1037.

273. R. Freer, P.W. Salthouse, and J.N. Sherwood, *Isotope mass effects for self-diffusion in single crystals of pivalic acid*. Philos. Mag. A, 1982. **45**: p. 205-212.

274. M. Eldrup, D. Lightbody, and J.N. Sherwood, *The temperature dependence of positron lifetimes in solid pivalic acid*. Chem. Phys., 1981. **63**: p. 51-58.

275. T. Goworek, *Defects in molecular solids: Positron studies*. Phys. State Solids (a), 1987. **102**: p. 511-526.

276. R. Folland, R.L. Jackson, et al., *Self-diffusion in a series of plastic organic solids studied by NMR*. J. Phys. Chem. Solids, 1973. **34**: p. 1713-1726.

277. A.R. Britcher and J.H. Strange, *On self-diffusion in plastic crystals*. Mol. Phys., 1979. **37**: p. 181-189.

278. J.M. Spaeth, *Recent developments in magnetic resonance studies of defects in ionic crystals*. J. de Physique, 1980. **Colloque C6**: p. C6-13.

279. M. Meyer and C. Marhic, *Molecular dynamics simulation of vacancy properties in plastic adamantane*. Physica B+C, 1985. **131**: p. 249-55.

280. M. Schmidt and F. Maurer, H. J.;, *Isotropic pressure-densified atactic poly(methyl methacrylate) glasses: free volume properties from equation-of-state data and positron annihilation lifetime spectroscopy*. macromolecules, 2000. **33**: p. 3879-3891.

281. R.N. West, *Positron studies of condensed matter*. Adv. Phys., 1973. **22**: p. 263-383.

282. P. Meakin, *A study of the properties of plasticised polymer electrolytes*, in *School of Chemistry*. 2000, Monash University: Melbourne. p. 188.

283. J.R. Macdonald, *CNLS (Complex Nonlinear Least Squares) Immittance Fitting Program LEVM Manual*. Vol. Version 7.11. 1999: J. Ross Macdonald and Solartron Group Limited.

284. A.L. Van Geet, *Calibration of the methanol and glycol Nuclear Magnetic Resoance Thermometers with a static Thermistor Probe.* Analytical Chemistry, 1968. **40**: p. 2227-2229.

285. H. Every, D.R. MacFarlane, et al., J. Mater. Chem., submitted.

286. J. Efthimiadis, S.J. Pas, et al., *Structure and transport properties in a N,N-substituted pyrrolidinium tetrafluoroborate plastic crystal system.* Intern. Conference on Solid State Ionics, 2001: p. 297.

287. H. Ishida, R. Ikeda, and D. Nakamura, *Pre-melting State of Methylammonium Iodide as revealed by Proton Magnetic Resonance.* Phys. State Solids (a), 1982. **70**: p. K151-153.

288. Y. Kume, R. Ikeda, and D. Nakamura, *Phase transitions of methylammonium hexahalotellurates(IV) as revealed by the nuclear quadrupole resonance of halogens.* J. Phys. Chem., 1978. **82**: p. 1926-1930.

289. Y. Kume, R. Ikeda, and D. nakamura, *Structural phase transition in various methylammonium hexahalometallates(IV) as studied by the NQR of halogens.* J. Magn. Res., 1979. **33**: p. 331-344.

290. J. Efthimiadis, M. Forsyth, and D.R. MacFarlane, *In-situ surface characterisation and microstructural study by Scanning Electron Microscopy of the N-methyl-N-alkylpyrrolidinium tetrafluoroborate organic salts.* in preparation.

291. C.J. Craven, G. Dosseh, et al., *Grain boundary premelting in crystalline benzene as studied by proton NMR.* J. Phys., 1990. **51**: p. 2489-2499.

292. C.I. Ratcliffe, *^2H NMR line-shape studies of dimethylammonium chloride, bromide and iodide.* J. Phys. Chem., 1990. **94**: p. 152-157.

293. H. Every, *An NMR diffusion study of the transport properties in novel electrolytes*, in *Department of Materials Engineering.* 2001, Monash University: Melbourne. p. 207.

294. T. Kobayashi, Y. Fujiyoshi, and N. Uyeda, *The observation of molecular orientations in crystal defects and the growth mechanism of thin phthalocyanine films.* Acta Cryst., 1982. **A38**: p. 356-362.

295. C.M. Forsyth, D.R. MacFarlane, et al., *Structural characterization of novel ionic materials incorporating the bis(trifluromethylsulphonyl)amide anion.* Chem. Mater., 2002. **14**: p. 2103-2108.

296. H.S. Gutowsky and G.E. Pake, *Structure Investigations by Means of Nuclear Magnetism II. Hindered Rotation in Solids.* J. Chemical Physics, 1950. **18**: p. 162-170.

297. C.A. Angell, *Origin and control of low-melting behavior in salts, polysalts, salt solvates and glassformers.* NATO Science Series, II: Mathematics, Physics and Chemsitry, 2002. **52 (Molten Salts: From Fundamentals to Applications)**: p. 305-320.

298. E. Gobel, W. Muller-Warmuth, et al., *^7Li NMR Spectra, Nuclear Relaxation and Lithium Ion Motion in Alkali Silicate, Borate and Phosphate Glasses.* J. of Magnetic Resonance, 1979. **36**: p. 371-387.

299. J.P. Donoso, T.J. Bonagamba, et al., *Nuclear Magnetic Relaxation Study of poly(ethylene oxide)-Lithium Salt Based Electrolytes.* J. Chemical Physics, 1993. **98**: p. 10026-10036.

300. A. Geiger and H.G. Hertz, *Nuclear Magnetic Resonance by Intermolecular Quadrupole Interaction, Determination of the Correlation Time.* Advances in molecular Relaxation Processes, 1976: p. 293-326.

301. S. Sylla, J.-Y. Sanchez, and M. Armand, *Electrochemical study of linear and crosslinked PEO-based polymer electrolyts.* Electrochim Acta, 1992. **37**: p. 1699-1701.

302. A. Noda, A. Nishimoto, and M. Watanabe. *Polymer electrolyts prepared by in situ polymerization of vinyl monomers in room temperature molten salts.* in *The sixth international symposium on polymer electrolytes.* 1998. Japan: Meisei-planning and printing Co., Ltd.

303. M. Videa, W. Xu, et al., *High Li$^+$ self-diffusivity and transport number in novel electrolyte solutions.* J. Electrochem. Soc., 2001. **148**: p. A1352-A1356.

304. H. Ishida, R. Ikeda, and D. Nakamura, *^1H NMR studies on the reorientational motions of cations in four solid phases of methylammonium iodide and the self-diffusion of ions in its highest-temperature solid phase.* Bull. Chem. Soc. Jap., 1986. **59**.